Dry Sliding Wear and High Pressure Torsion of Cold Sprayed Aluminum-Alumina Composites

J. Michael Shockley

Department of Mining and Materials Engineering
McGill University, Montreal
April 2015

A thesis submitted to McGill University in partial fulfillment
of the requirements for the degree of Doctor of Philosophy.

Contents

Abstract

The cold spray process was used to consolidate Al coatings and Al-Al_2O_3 composite coatings. Cold spray feedstock was prepared by admixing commercially pure, gas atomized aluminum powder with 0, 10, and 50 wt.% Al_2O_3 of angular or spherical morphology. The cold spray deposition was carried out in such a manner that "thick" coatings (greater than 500 µm thick) were obtained. Prior to deposition of composite coatings, the ideal cold spray deposition parameters were studied for pure aluminum coatings to optimize the deposition efficiency and quality of coating. Once the deposition conditions were selected, Al-Al_2O_3 composites were cold sprayed as well.

The cold sprayed deposits were characterized in terms of the recovery of Al_2O_3 as a function of feedstock Al_2O_3 content, as well as microhardness. It was found that recovery of Al_2O_3 was significantly higher for angular Al_2O_3 than spherical Al_2O_3, with 10 and 50 wt.% Al_2O_3 in the feedstock resulting in coating concentrations of 10 and 22 wt.% angular Al_2O_3 and 3 and 11 wt.% spherical Al_2O_3, respectively. Yet regardless of particle morphology, similar quantities of Al_2O_3 led to similar coating hardness.

The coatings were subjected to reciprocating dry sliding wear experiments using a custom-built *in situ* tribometer on which a transparent sapphire counterface was equipped; this was used to directly observe activity occuring at the sliding interface and understand its link to actively measured friction forces. Once the tests were completed, the wear tracks and counterfaces were characterized *ex situ* using surface metrology and electron microscopy techniques to measure wear rate and the morphology of "third bodies" formed at the sliding interface.

Cross-sectioning was carried out using various techniques to observe the microstructural, mechanical, and chemical changes that occurred as a result of the sliding process.

The combined *in situ* and *ex situ* analysis revealed detailed mechanistic explanations of the phenomena resulting in the observed friction and wear behavior. From the standpoint of friction and wear, the pure aluminum coatings had high wear rates and friction forces that fluctuated significantly. Much of this behavior was linked to physical changes observable *in situ* in the transfer film such as plastic flow and material detachment. In contrast, the lower wear rates and stabler friction forces in 22 wt.% angular Al_2O_3 composites and 11 wt.% spherical Al_2O_3 composites were linked to a stable transfer film that exhibited little physical change over time. Further contrasts were visible in the microstructural features and morphologies of material in and near the wear track, as well as the hardness measured by nanoindentation.

The same materials were subjected to high pressure torsion (HPT) to observe the microstructural changes and mechanical (torque) response due to compressive loading (0.5 and 1.0 GPa) and shear strain. Plastic flow patterns in the matrix were observed and were dependent on the particle morphology. The presence of sharp corners and flat edges of the angular Al_2O_3 particles resulted in microcracking in the aluminum matrix, which was not visible for the spherical alumina morphology. A unit cell finite element model was developed to observe the micromechanical stress and strain contours in the matrix material in the vicinity of the hard particles, providing some explanation of the microstructural features observed.

Résumé

Des revêtements en Al et Al-Al_2O_3 ont été déposés par projection à froid. Les matières premières ont été préparées en mélangeant mécaniquement de l'aluminium atomisé en poudre, de qualité commerciale, avec de l'alumine en poudre de morphologie anguleuse ou sphérique, à des fractions de masse de 0%, 10%, et 50 %. L'épaisseur des revêtements ainsi obtenus avaient une épaisseur minimale de 500 µm. Avant le dépôt des revêtements composites, les paramètres de projection ont été étudiés pour l'aluminium pur afin d'optimiser l'efficacité du dépôt et la qualité du revêtement.

La dureté des revêtements et la récupération de l'alumine dans les dépôts ont été caractérisées. La récupération d'alumine était plus élevée pour la morphologie anguleuse des particules d'alumine que pour celle sphérique. Pour des fractions de masse d'alumine de 10% et 50 % dans les matières premières, la quantité d'alumine dans les revêtements était respectivement de 10% et 22 % pour la morphologie anguleuse et de 3% et 11 % pour la sphérique. Néanmoins quel que soit la morphologie des particules, une même quantité d'alumine dans le revêtement a donné une dureté similaire.

Des essais de frottement en cinématique alternative ont été réalisés avec un tribomètre in-situ de type bille-plan, de construction hors-série. La bille en saphir transparent a permis de visualiser directement le contact lors du frottement, ainsi que le comportement du troisième corps, et d'y relier les forces de frottement en temps réel. Après les essais, le matériau superficiel à l'interface du contact a été analysé par des techniques de métrologie de surface et par microscopie électronique pour mesurer la quantité d'usure et pour analyser la morphologie

des surfaces. Des coupes des échantillons en section transversale au niveau des traces de frottement ont permis d'étudier les changements microstructuraux, mécaniques, et chimiques créés lors du frottement.

Le couplage des analyses in-situ et post mortem ont révélé des mécanismes fins des phénomènes mis en jeu au cours du frottement et de l'usure. Les revêtements en aluminium pur ont révélé un taux d'usure ainsi que des forces de frottement élevées présentant beaucoup de fluctuations. Ce comportement a été relié aux changements physiques observés in-situ dans le film de transfert adhérant à la bille, tel que le fluage plastique et le détachement de particules. Par contre, les taux d'usure étaient beaucoup moins élevés pour les composites en Al-Al_2O_3 contenant 22 % d'alumine anguleuse ou 11% de sphérique. Le film de transfert semblait stable, montrant peu de changements physiques lors du frottement. Des différences à une échelle plus locale entre les deux types de revêtements, en termes de microstructure, de morphologie, et de nano-dureté, ont été observées et reliées au comportement tribologique.

Les mêmes revêtements ont été soumis à des essais de torsion sous pression élevée (high pressure torsion, HPT) pour observer les changements de microstructure et la réponse mécanique au cisaillement couplé à une charge de compression de 0,5 et 1,0 GPa. Il a été mis en évidence par l'analyse des microstructures après essai, une déformation plastique qui dépendait de la morphologie des particules d'alumine. Les angles aigus de l'alumine anguleuse ont causé la formation des micro-fissures dans l'aluminium, ce que n'était pas visible dans les échantillons avec l'alumine sphérique. Un modèle par éléments finis a été développé pour observer les régions de contraintes et de déformation dans la matrice d'aluminium, autour des particules d'alumine, ce qui a permis de commencer à expliquer les changements de microstructure observés.

Acknowledgements

This thesis work was completed with the help and support of many people and organizations, to all of whom I am deeply gracious. I first thank my supervisor Prof. Richard Chromik for offering me this position and trusting me with what turned out to be a rewarding and exciting project. I also thank my co-supervisor Dr. Sylvie Descartes of LaMCoS, INSA-Lyon for her expertise and vision. Both of my supervisors showed a degree of professionalism and patience that I know not all PhD students are lucky enough to get. Hats off to you both.

Thanks are also due to the diverse personalities at McGill including Dina, Holger, Pantcho, Yinyin, Lisa, Praveena, Matthew, Yaoyao, Rosen, Jason, Fanchao, and the many others who helped support and shape this project. I also acknowledge the technical support at McGill including Nicolas Brodusch, Florence Paray, Monique Riendeau, Pierre Vermette, and Robert Paquette. I must also thank Pedro Marzano and Walker Nickerson, undergraduate students who helped me in the lab.

At LaMCoS, INSA-Lyon, I offer thanks to Pierre, Serge, Ghassen, Marion, Vincent, and the other folks who helped me feel at home. I must also acknowledge the invaluable technical support at LaMCoS from Edouard Régis, Claude Godeau, and Lionel Lafarge. Thanks also go to the CLYM (Center Lyonnais de Microscopie) for the access to the FIB/SEM (Zeiss NVision 40) and to N. Blanchard, A. Descamps-Mandine, Th. Douillard, and B. Van De Moortèle for the technical help. I also thank Chrisophe Desrayaud at École des Mines de Saint-Etienne for helpful conversations regarding finite element modelling.

There are many funding sources without which this project would not have been possible. I first acknowledge Canadian funding sources including the McGill Engineering Doctoral Award (MEDA) and the late Gerald G. Hatch for funding the named fellowship I received. I also acknowedge the Rio Tinto Alcan Graduate Fellowship. Further acknowledgements are due to the financial support from the Canadian Foundation for Innovation (CFI) project no. 8246 for the cold spray equipment, the CFI Leader's Opportunity Fund project no. 13029 for the *in situ* tribometer, and the Natural Sciences and Engineering Research Council (NSERC) Discovery Grants Program for the operational funding of this project. I also aknowledge the partial financial support from several sources in the French government, including ”Région Rhône-Alpes” (within the context SRESR 2007-2010) via MaCoDev (”Matériaux et Conception pour un Développement durable”) research cluster grant n° 08 013 865 01, the 2013 Programme Avenir Lyon St-Etienne doctoral mobility scholarship, and finally the support for the CLYM by the CNRS, le Grand Lyon, and the Conseil Régional Rhône-Alpes.

On a final note, I thank my friends and family for being there for me throughout this journey. I especially thank my parents, Jim and Cindy, and my brother John. I finally thank Kaitlyn O'Shaughnessy for her companionship, encouragement, friendship, support, and good humor. I couldn't have done it without you.

Preface

This thesis comprises work completed over the period of September 2010 to December 2014, during which time the author was enrolled as a PhD student supervised by Prof. Richard Chromik at McGill University. A portion of this work, notably the HPT and FIB cross-sectioning, was completed in Lyon, France at LaMCoS, INSA-Lyon during a research exchange from September to December 2013. The work in Lyon was performed under the supervision of Dr. Sylvie Descartes, who co-supervised the rest of the thesis work starting in July 2012.

In keeping with the manuscript format of this thesis, chapters 4 through 8 were adapted from manuscripts published, or to be submitted for publication, in peer reviewed academic journals. The manuscripts were produced in collaboration with a number of people from different groups and facilities. Their titles and coordinates are the following, along with a breakdown of the contributions of each author in the order they are listed in the publication. Authors with no listed specification are from the Department of Mining and Materials Engineering, McGill University.

- **Chapter 4**: *In Situ* Tribometry of Cold Sprayed Al-Al_2O_3 Coatings, *Surface and Coatings Technology* **215** (2013) 350–356.

  J.M. Shockley performed the dry sliding wear experiments, the post-wear analysis, and the writing of the whole manuscript. H.W. Strauss constructed and programmed the *in situ* tribometer. R.R. Chromik supervised the project and edited the manuscript. N. Brodusch and R. Gauvin assisted in the electron microscopy work on the SU-8000 SEM. E. Irissou and J.-G. Legoux from National Research Council - Boucherville were responsible for the deposition of the coatings and the initial microstructural analysis.

- **Chapter 5**: Third Body Behavior During Dry Sliding of Cold-Sprayed Al-Al_2O_3 Composites: *In Situ* Tribometry and Microanalysis, *Tribology Letters* **54** (2014) 191–206, DOI 10.1007/s11249-014-0326-z.

  J.M. Shockley performed the dry sliding wear experiments, performed or assisted with the post-wear analysis, and wrote the whole manuscript. S. Descartes from LaMCoS, INSA-Lyon performed the FIB cross-sectioning portion of the post-wear analysis and edited the manuscript. E. Irissou and J.-G. Legoux from National Research Council - Boucherville were responsible for the deposition of the coatings and the initial microstructural analysis. R.R. Chromik (with S. Descartes) supervised the project and edited the manuscript.

- **Chapter 6**: The influence of Al_2O_3 particle morphology on the cold spray coating formation and dry sliding wear behavior of Al-Al_2O_3, *Surface and Coatings Technology* (2015), DOI 10.1016/j.surfcoat.2015.01.057.

  J.M. Shockley and P. Vo deposited the cold spray coatings. J.M. Shockley performed the dry sliding wear experiments, performed or assisted with the post-wear analysis, and wrote the whole manuscript. P. Vo and E. Irissou from National Research Council - Boucherville supervised the cold spray deposition. S. Descartes and R.R. Chromik supervised the project and edited the manuscript.

- **Chapter** 7: Significance of Al_2O_3 particle morphology in the microstructure evolution of cold-sprayed Al-Al_2O_3 during unconstrained high-pressure torsion, manuscript, intended for publication.

  J. M. Shockley performed the high pressure torsion experiments and post-wear analysis, and wrote the whole manuscript. S. Descartes and R.R. Chromik supervised the project and edited the manuscript.

- **Chapter 8**: High pressure torsion of cold-sprayed Al-Al_2O_3 composites in the unconstrained condition, manuscript, intended for publication.

J. M. Shockley performed the high pressure torsion experiments and post-wear analysis, and wrote the whole manuscript. S. Descartes and R.R. Chromik supervised the project and edited the manuscript.

Chapter 1

Introduction

The low density, high thermal conductivity, and inherent corrosion resistance of aluminum and many of its alloys make them attractive as coating materials. However, the tribological performance of these materials in terms of friction and wear is too poor for many applications, unless the alloy is chosen judiciously or the matrix is reinforced using hard secondary phases such as Al_2O_3 or SiC particles [1]. Such aluminum metal matrix composite (Al-MMC) materials have become popular as bulk materials for their enhanced stiffness and wear resistance compared to the unreinforced matrix material [1–3]. For coating applications, Al-MMC materials may be deposited by various techniques and, among them, the cold spray process has been noted for its rapid deposition of coatings with low porosity and high purity [4–8]. The production of so-called “thick” tribological MMC composite coatings by way of cold spray has been investigated in recent years [9–23].

The goals of the present thesis were to develop an understanding of the role of Al_2O_3 particles, in terms of concentration and morphology, on the cold spray deposition and dry sliding wear behavior of Al-Al_2O_3 composites. The approach used here falls into the study of process-structure-property-performance relationships that are central to the field of materials engineering. First, the cold spray process is stochastic in that it relies on the interaction of many thousands of individual particles in a high speed gas stream to consolidate and form a coating upon impact with a substrate. The structure of the coating, in terms of Al_2O_3 content and distribution, is dictated by the recovery of Al_2O_3 into the coating during cold spray, and this in turn influences the coating mechanical properties. Finally, the performance during dry sliding in terms of friction and wear rate are influenced by the presence of Al_2O_3 particles as well. Al-MMC materials typically exhibit dry sliding wear rates that are significantly lower than the unreinforced metal [24–26], depending on the kinematics of the sliding system [27, 28]. In a study on a cold sprayed Al-Al_2O_3 composite, the decrease in wear rate was found to extend up to five orders of magnitude, with little influence of post-deposition heat treatment [11]. Notably, tribological studies of metallic materials have found that wear rates may not correlate only with bulk strength and hardness, but also with the formation of third bodies such as the mechanically mixed layer (MML) [24, 26, 29]. The action of material mixing and transfer between surfaces is central to the metallic wear process. This has been evidenced by microstructural studies of MMLs, which are often found to be nanostructured and contain material from both of the mechanically contacting faces [29–32]. Furthermore, sudden changes in friction or wear behavior may be attributed to detachment of transfer material during the wear process [32, 33]. The presence of hard particles in Al-MMC materials influences the mechanisms of mixing and transfers during sliding, which in turn influence the friction and wear rates [25, 34]. Thus it may be conceived that to characterize the tribological behavior, a new set of process-structure-properties-performance relationships may be uncovered, in this case in terms of the third body material. The sliding process influences the structure and properties of the third bodies through plastic deformation and chemical reactions, and then this affects the friction and wear behavior.

Thus a large part of this thesis is dedicated to analysis of the third bodies generated during dry sliding against cold sprayed Al and Al-Al_2O_3. A tool used to do so was *in situ* tribometry, which provided novel insights on the behavior at the sliding interface by permitting direct observation of the behavior of third bodies through the transparent sapphire counterface. After the test was over, *ex situ* analysis of the third body material revealed details about its morphology, microstructure, and the hardness of the third bodies relative to the underlying undeformed coating. This analysis provided a thorough mechanistic understanding, in terms of third bodies, of the effect of Al_2O_3 content and morphology on the friction and wear behavior observed during dry sliding.

The final part of this thesis is dedicated to high pressure torsion (HPT) experiments on the Al-Al_2O_3 coatings that had been studied by dry sliding wear. In the HPT technique, a disk of material (in this case, cold sprayed Al-Al_2O_3) is placed between two anvils, then compressively loaded and subjected to shear by rotating one or both of the anvils. In doing so, severe plastic deformation in shear is induced throughout the bulk of the sample. Ordinarily, HPT is used as a materials processing technique to achieve grain refinement and the corresponding enhancement of mechanical properties [35]. However, there has been a growing field of research in which HPT is used to study tribological mechanisms [36, 37]. One of the major driving forces for the formation of third body material is severe plastic deformation that occurs at the sliding interface; this can be studied in a more controlled manner by HPT, in which the level of strain can be estimated [35, 36]. Therefore, in order to attempt to reveal mechanisms behind third body formation during dry sliding, HPT experiments were carried out followed by microstructural analysis.

Organization of thesis

This work is divided into ten chapters. The present chapter seeks to familiarize the reader with the basic context of the project and outline the rest of the thesis.

In Chapter 2, a brief literature review is presented covering five interconnected topics: aluminum matrix composites, cold spray, tribology, materials tribology of aluminum matrix composites, and high pressure torsion (HPT). The first section covers aspects of aluminum matrix composites (Al-MMCs) such as the basic definitions, the industrial consolidation routes, the various choices of materials, and general mechanical properties. This will serve to contextualize the second section, which covers the cold spray process and its use in the deposition of Al-Al_2O_3, which is the material system of interest for this thesis. The third section covers basic topics of tribology, such as friction, wear, and the logical frameworks of the third body, the tribological circuit, and the velocity accommodation modes (VAMs). The third section will also introduce the various systems of tribometry. The fourth section will survey the literature concerning tribological studies of aluminum and Al-MMC materials, using concepts from the previous three parts. Finally, the fifth part will review HPT as a materials processing technique and its applications to tribological studies.

In Chapter 3, an overview of experimental techniques is provided. As this is a manuscript-based thesis, each chapter is intended to stand alone as a published journal paper. Therefore, the specific experimental techniques for each chapter may be found as a section within that chapter. Chapter 3 instead serves to offer more a detailed overview of each technique than what was appropriate for a journal publication.

In Chapter 4, one cold sprayed Al and two Al-Al_2O_3 coatings with angular Al_2O_3 were subject to *in situ* tribometry and *ex situ* characterization of wear track microstructural features. This paper represented the first time that an *in situ* tribometry technique was used to study Al-MMC composites and it revealed that there were contrasting dynamic behaviors observable in the transfer film. These were correlated to the friction coefficient, wear rate, and microstructural changes in the wear track, where a mechanically mixed layer (MML) was observed to develop. This analysis of third body behavior was discussed in light of previous studies on cold sprayed Al-Al_2O_3.

In Chapter 5, the two coatings from Chapter 4 with the most contrasting friction, wear, and transfer film behavior were subject to a more detailed analysis than in Chapter 4. Dynamic changes visible in the transfer film when viewed *in situ* were correlated to specific friction events, and observations of the surface morphologies of transfer films were performed. The wear tracks and transfer films were subject to focused ion beam (FIB) cross-sectioning to study the extreme near-surface microstructural features at high magnification. The mechanical properties of the features in the wear tracks were also explored with nanoindentation. The results were brought together to derive the tribological circuit, which is a logical framework for describing any tribological system. Finally, to help describe the evolution of microstructural features, a discussion was developed to contextualize these results to previous tribology and severe plastic deformation (SPD) research on Al-MMC materials.

As Chapters 4 and 5 utilized coatings that had been already cold sprayed by our collaborators at NRC-Boucherville for another study, it became necessary to deposit new coatings for our subsequent studies. Using a different cold spray sytem (Plasma Giken PCS-800) than that which was used to deposit the coatings used in Chapters 4 and 5, various deposition conditions were utilized to optimize the cold spray deposition of pure aluminum.

In Chapter 6, five coatings were cold sprayed using deposition conditions derived in Chapter 6 using the following admixed feedstocks: pure Al, 10 wt.% spherical Al_2O_3, 50 wt.% spherical Al_2O_3, 10 wt.% angular Al_2O_3, and 50 wt.% spherical Al_2O_3. The deposition behavior in terms of deposition efficiency and recovery of Al_2O_3 particles was determined from powder flow rate measurements during cold spray and microstructural analysis. Then dry sliding wear tests were performed on the obtained coatings, from which friction behavior, *in situ* tribometry observations, wear rate, and third body morphologies were observed. A discussion of the effect of Al_2O_3 morphology on the cold spray deposition behavior and dry sliding wear behavior was developed.

In Chapter 7, two coatings from Chapter 6 of similar Al_2O_3 content but differing Al_2O_3 morphologies were subjected to HPT. As these were found in Chapter 6 to have different friction and wear behavior, they provided excellent candidates to study their mechanical response to severe plastic deformation under conditions of compressive loading and shear. The von Mises stress (proportional to the shear stress) was calculated during torsion and microstructural analysis was performed on the materials post-HPT. Finite element modelling was used to help understand the microstructural features were observed. The differing damage mechanisms observed in the microstructure were discussed in light of the cold spray deposition behavior and tribological behavior.

In Chapter 8, four coatings from Chapter 6 were subjected to HPT. Microstructural analysis was performed on the materials post-HPT, and a full discussion of the microstructural features observed was developed in light of the cold spray deposition behavior and tribological behavior.

Finally, overall conclusions of this thesis and recommendations for future work are discussed in the final chapter. Three appendices were included: the standard operating procedure developed for the HPT test apparatus, samples of MATLAB code (one used to calculate wear rate, the other used to derive stress-strain curves from HPT tests), and a sample input for ABAQUS finite element modelling software.

Chapter 2

Literature review

2.1 Aluminum matrix composites (Al-MMCs)

2.1.1 Definition of a metal matrix composite (MMC)

A composite material consists of two or more physically or chemically distinct materials combined to attain properties not available in either material alone [38]. Typically, a secondary phase such as a fiber or particulate is arranged homogeneously within a continuous matrix of another material [38]. When the continuous phase is a metal, the material system is called a metal matrix composite (MMC). By definition, conventional composite materials consist of at least two phases that remain chemically distinct throughout the processing life of the material [3]. A small distinction is drawn for *in situ* composite materials, in which at least one secondary phase changes in chemical composition during processing but remains distinct from the matrix. Both definitions exclude materials where the multiple phases dissociate from the same melt as consequences of chemical processes, such as aluminum-silicon alloys and cast irons, even though they bear some semblance in form and properties to composites [3]. This distinction is not universal, as some sources do consider aluminum-silicon alloys and cast irons to be composite materials [1]. For the sake of this thesis, the former definition will be respected.

A further distinction lies between distinction of discontinuously reinforced particulate MMCs and dispersion strengthened metal alloys. In composite materials, the reinforcing phase bears a significant part of the stress when physically loaded; this is in contrast to dispersion strengthened metal where the small quantity (less than 5 vol.%) of dispersoids primarily serves to disrupt dislocation motion or grain boundary sliding in the load bearing metal [3]. Thus, in spite of their similarities to MMCs, dispersion strengthened metal alloys will be considered a separate topic and will not be explored here.

2.1.2 Consolidation routes of MMCs

Whether for tribological or for structural applications, most MMCs with hard reinforcements are prepared by way of liquid state or solid state processes [38]. The liquid state methods involve molten metals which may either be combined with loose reinforcements and then cast, or forced into reinforcement preforms by way of squeezing or infiltration methods [2,38]. An alternative liquid state method is spray casting, where fully molten metal is atomized and slowly deposited onto a cooled substrate to form a bulk component [2]. A similar route is thermal spray, where solid metal and reinforcement powder particles are passed through a plasma or electric arc heat source in which they soften or melt, and then accelerate at high velocities (200-700 m/s) toward a substrate where they quench and form a coating [2]. Important differences between spray casting and thermal spray are in the particle velocities and the quenching rates, which are both orders of magnitude higher in the latter. Furthermore, the high quenching rates result in characteristic “pancaked” microstructures in thermal spray coatings which contain high levels of porosity and residual stresses [39]. These microstructural features lead to accelerated crack growth and particle pullout, which lead to poorer wear performance in thermally sprayed tribological composite coatings compared to other methods [39]. However, increased development of thermal spray process control measures has improved performance in recent years [39].

Solid state methods are generally used for bulk components rather than coatings. Most common solid state forming methods involve powder metallurgical techniques, where metallic and reinforcement powders are mixed together, pressed, and sintered. In most cases there is absolutely no melting of components, but rather they diffuse together at elevated temperature [2]. There is some advantage to this as very precise control over powder quantities can be achieved, and the thermal stresses are lower since processing occurs at a much lower temperature [38]. However, this technique is quite expensive compared to other techniques and generally the geometry of the sintered component must be somewhat simple [38].

The consolidation route for the Al-MMC coatings in this thesis is cold spray, which combines principles of the thermal spray process and the solid state methods mentioned above. The cold spray process is overviewed in Section 2.2.

2.1.3 Examples of Al-MMCs

Interest in metal matrix composites originates from the limited properties of commercially available lightweight metals, namely aluminum, titanium and magnesium [40]. While steel matrix composites do exist and are commercially available, the vast majority are based on aluminum matrices and to a lesser extent on titanium or magnesium matrices [40]. Aluminum is particularly attractive as a matrix metal thanks to its low density, low cost, high machinability, and inherent corrosion resistance [41]; aluminum and its alloys are therefore the most common matrix metals for MMCs. Alloys must be selected such that there is high compatibility between the matrix alloying elements and reinforcement phases, as otherwise it could result in the creation of undesirable tertiary phases during processing or use [42]. For instance, molten aluminum reacts with SiC to form Al_4C_3, a brittle phase which is considered detrimental to the properties of the composite [43]. In many cases Al_2O_3 is preferable as it is stable in most aluminum alloys. However, when Al_2O_3 is used to reinforce magnesium alloys or aluminum alloys containing magnesium, it can react to form MgO or $MgAl_2O_4$, again undesirable as reinforcements [43].

Bulk MMC materials may have secondary phases present as continuous long fibers, as

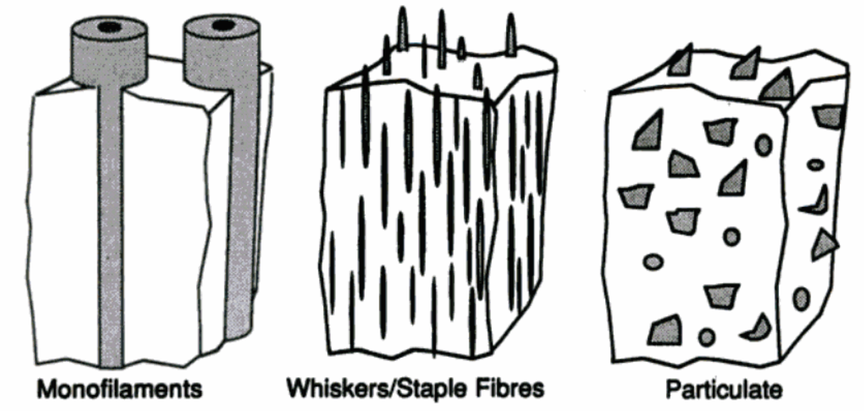

Figure 2.1 – Schematic depiction of the three types of secondary phase morphologies in metal matrix composites [44].

short fibers, or as roughly equiaxed particulates (see Figure 2.1). The choice of morphology is dependent on the desired properties of the composite and on the processing route [3].

2.1.4 Mechanical properties of MMCs

MMCs form a class of material in which the useful properties of the metal matrix such as high ductility, high thermal conductivity, high fracture toughness, and strength isotropy are enhanced by properties of the secondary phase [40]. For bulk materials, engineering purposes for such enhancements fall into several categories: stiffness enhancement, strength enhancement, increased creep resistance, increased wear resistance, density reduction, and thermal expansion control [41]. The degree of enhancement in any of these categories depends on the physical properties of the secondary phases, their morphology, orientation, and volume fraction within the metal matrix, and the state of the interface between the two.

Generally speaking, in a metal matrix containing a significant quantity (greater than 5 vol. %) of a stiff reinforcement, the reinforcing phase will bear a significant portion of the load. In doing so, the total stress on the matrix is reduced and the higher modulus of the reinforcing phase will increase the total composite modulus. This is highly advantageous for applications where stiffness is critical, such as for aligned components in a satellite or where dynamic stability improves with stiffness, such as in a drive shaft or bicycle [3, 41]. There are very few other means of improving specific stiffness in metallic systems than by incorporating stiff reinforcements; microstructural control and minor additions of alloying elements have little if any influence on specific stiffness [41].

MMC materials may exhibit anisotropy in the stiffness, strength, creep, and tribological behavior depending on the orientation of reinforcement material. This is particularly notable in continuous reinforced MMCs, which although are not a focus of this thesis, provided an ideal example of the difficulty of predicting the stiffness of MMC materials. When continuous reinforced MMCs are loaded longitudinally, the fibers and matrix experience equal strain. In this loading orientation, the maximum degree of load sharing is experienced and hence the composite response is stiffer and stronger than in transverse loading.

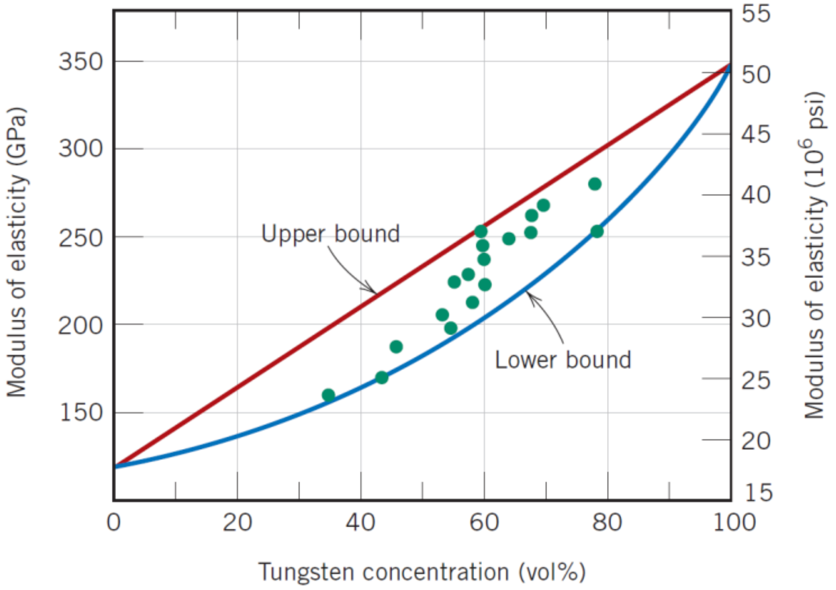

Figure 2.2 – Voigt and Reuss bounds (upper and lower, respectively) for the elastic modulus of a copper matrix reinforced with varying concentrations of tungsten particles [45].

The stiffness of a fiber-reinforced composite in longitudinal loading may be accurately calculated by the rule of mixtures as it corresponds to the Voigt model of equal strain, the theoretical maximum bound for the modulus [46] (see Equation 2.1). In the Voigt model, the composite modulus is the average of the matrix modulus and the fiber reinforcement modulus weighted according to volume fraction (see Figure 2.2) [46].

$$E_c = E_{Matrix}V_{Matrix} + E_{Reinforcement}V_{Reinforcement} \tag{2.1}$$

$$E_c = (\frac{V_{Matrix}}{E_{Matrix}} + \frac{V_{Reinforcement}}{E_{Reinforcement}})^{-1} \tag{2.2}$$

Calculation of the stiffness in transverse loading for a fiber reinforced composite, or for any direction of a particulate reinforced composite, is far more complex – it is certainly less than that calculated by the Voigt model, but generally not so low as the minimum theoretical bound calculated by the Reuss model of equal stress (see Equation 2.2) [38]. Many predictive models have been developed for these more complex scenarios, each of which places values between the Voigt and Reuss bounds [46] (see Figure 2.2). In this thesis, the Hertzian contact pressure is a key parameter used to contextualize the contact condition (as explained in Section 2.3.5). As the elastic modulus of each contacting body is necessary for this calculation, the elastic modulus of the particulate reinforced Al-Al_2O_3 materials in this study must be determined. Rather than attempt to estimate the modulus using one of the many existing models (such as the Halpin-Tsai model [47]), the Voigt and Reuss bounds in Equations 2.1 and 2.2 were used to predict the upper and lower bounds of elastic modulus, and then used to calculate the corresponding upper and lower bounds of Hertzian contact pressure. This was calculated for each Al-Al_2O_3 material based on its measured content of Al_2O_3 particles.

2.2 Cold spray

2.2.1 Context and bonding mechanisms

The cold spray process, sometimes referred to as gas dynamic cold spray or kinetic metallization, is a material deposition process. Described in the simplest of terms, the cold spray process operates by entraining feedstock powders, which are generally metals or mixes of metals with other phases, into a high velocity stream of gas. Upon impact with a substrate, the metallic powder particles deform and coating buildup takes place through a combination of mechanical interlocking and metallurgical bonding [4–6, 8, 48].

The earliest meaningful research in cold spray is attributed to the work of Dr. Anatolii Papyrin at the Institute of Theoretical and Applied Mechanics of the Russian Academy of Sciences, Novosibirsk in the 1980s [5]. In the midst two-phase flow studies of supersonic gas ($v > 330$ m/s) with entrained solid particles (Ø = 1-50 µm), it was discovered that some metallic particles were adhering to the test apparatus and forming a dense layer. This behavior was surprising because generally, particles travelling at high velocities (10-100 m/s) are associated with erosive wear upon impact with a surface [5, 49]. Above a certain critical velocity, the kinetic energy during impact was high enough to cause the particles to stick to the surface [5].

A large amount of cold spray research has been dedicated to understanding the mechanisms of adhesion and the parameters influencing the critical velocity. It is widely accepted that during impact of a metal particle with a stationary surface at sufficiently high velocities, localized deformation at the interface results in thermal softening and adiabatic shear instabilities in the material [48, 50]. This generates a shear load, accelerating thermally softened material at the interface away in a behavior called jetting (see Figure 2.3). This flow of material carries away oxide layers and other impurities, resulting in intimate contact and metallurgical bonding of the heated, clean metal surfaces. The jetting behavior, and subsequent bonding, is maximum at the region oriented 45° to the direction of deposition, potentially leaving some surfaces unbonded [51, 52]. Furthermore, the degree of bonding depends on the kinetic energy of the particles, with more bonding occurring at higher velocities [48, 50–52]. Therefore it is believed that the total coating adhesion is a combination of metallurgical bonding and conformal adhesion.

2.2.2 Cold spray compared to conventional thermal spray

At its roots, cold spray is an outgrowth of the various thermal spray techniques, where material is sprayed in its molten or near-molten state toward a substrate, on which it quenches and

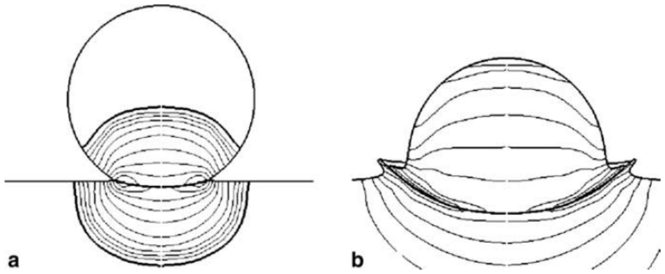

Figure 2.3 – Pressure fields during impact: initial contact (a) and during the jetting process (b) [50].

forms a coating. Although there are many mature and commonly used thermal spray processes, the high temperatures utilized therein present limitations to the coating quality and available materials. Cold spray offers an alternative to traditional thermal spray techniques through the following advantages. First, in thermal spray, the act of projecting molten metallic or ceramic particles through a gas stream creates opportunity for oxidation and other chemical reactions which can lead to the formation of undesirable phases. By maintaining particles well under their melting points, the chemical reactivity of materials undergoing cold spray is significantly lower (see Figure 2.4). This makes cold spray suitable for oxidation sensitive materials such as Al, Ti, or MCrAlY. Second, in thermal spray the fast cooling rate associated with the quenching process at impact leads to limitations in the types of coating microstructures that can be produced. Although significant microstructural changes can occur during cold spray as well, particularly grain refinement, the deposited material very rarely passes through the liquid phase. Third, thermal spray produces coatings that may contain high levels of porosity, the control of which may be difficult. As cold spray relies primarily on kinetic energy, not thermal energy, to produce coatings through plastic deformation, the resulting composites are typically very dense. Finally, the high temperatures during thermal spray can induce significant microstructural changes or melting in the substrate, limiting the materials that can be used. The lower temperatures during cold spray allow for coating deposition on heat sensitive materials such as aluminum and magnesium alloys.

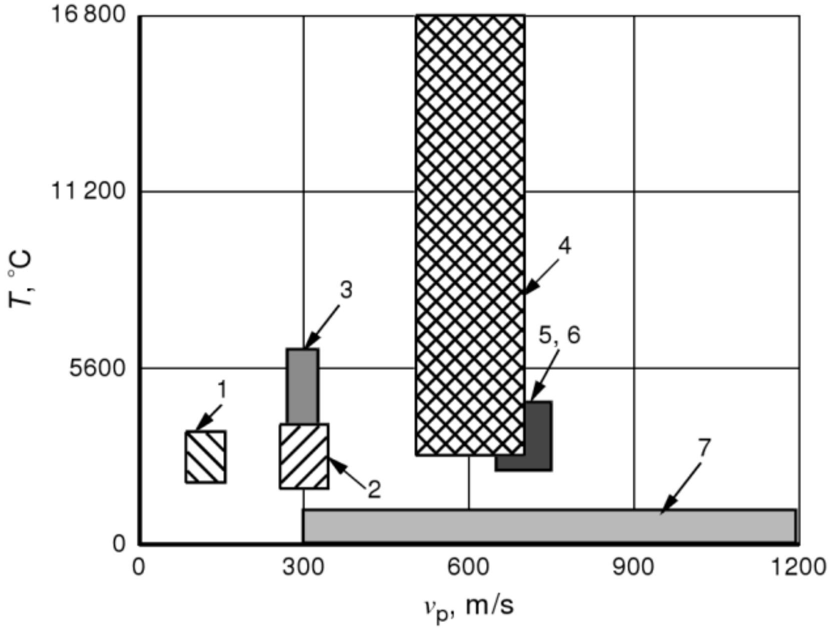

Figure 2.4 – Diagram of jet temperatures (T) and particle velocities (v_p) used in thermal spray and cold spray methods. 1 - low velocity gas-plasma; 2 - high velocity gas plasma; 3 - electric-arc; 4 - plasma; 5,6 - detonation and high velocity oxy-fuel (HVOF); and 7 - cold spray [5].

2.2.3 Cold spray equipment and technology

To obtain the high velocities needed during cold spray, a converging-diverging nozzle is used in conjunction with a preheated and prepressurized gas source (see Figure 2.4). A pressurized gas stream, which may be compressed air or more commonly an inert gas such as nitrogen or helium, is sent through an electric heater, in which it heats to a pre-selected temperature. This is directed into a de Laval-type nozzle of the desired geometry and material. In the narrowest portion of the nozzle, the gas velocity reaches the speed of sound and continues to accelerate as it passes through the divering part of the nozzle. Meanwhile, a separate portion of the gas is sent through a powder feeder system, which injects powder either into the converging or the divering section of the nozzle, at which point it becomes entrained in the high velocity gas and accelerates.

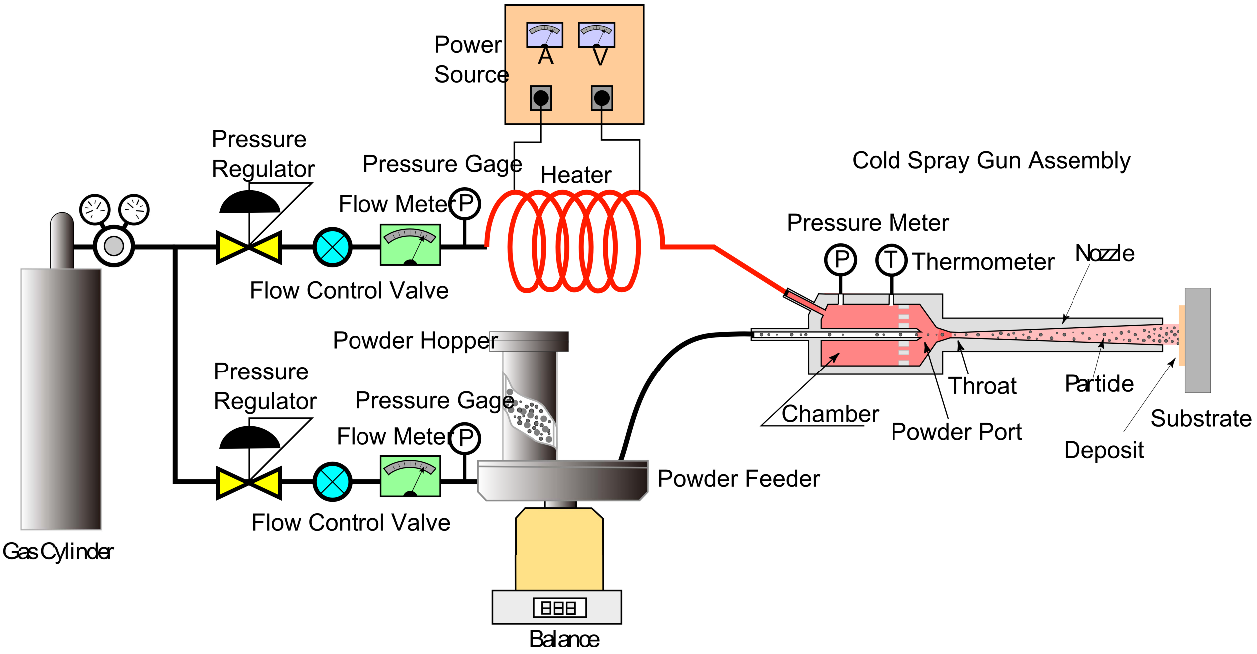

Figure 2.5 – Schematic diagram of a Plasma Giken cold spray system (courtesy of Plasma Giken Co., Ltd.) [53].

2.2.4 Cold spray of Al-MMC materials

The inherent corrosion resistance of pure aluminum has made it an important coating material in the aerospace industry; for instance, thermal sprayed aluminum coatings have been used to prevent stress corrosion cracking in aluminum alloy 7075-T6 structural elements [54], and similar techniques have been applied to corrosion-prone magnesium alloys [11, 55, 56] . However, due to its affinity for oxygen, aluminum has a tendency for in-flight oxidation during thermal spray process, leading to porosity and poor cohesion between coating layers [54]. These defects can detrimental to the corrosion protection under cyclic loading, and the heat transfer associated with thermal spray processes can be detrimental to the properties of the underlying structural alloy. The cold spray process has been investigated as an alternative means of depositing pure aluminum coatings, and its corrosion protection in the as-sprayed state has been shown to be improved over thermal sprayed aluminum in the as-sprayed state [9, 11, 54, 57]. The interest in cold spray deposition of Al-Al_2O_3 arises partly from the poor tribological behavior, in terms of friction and wear, of pure aluminum coatings. The tribological behavior of Al-MMC materials has been shown to be generally improved over the unreinforced matrix material (see Section 2.4). Thus research questions were established as to how the presence of Al_2O_3 particles would influence the coating formation behavior and coating properties of Al-Al_2O_3, whether cold sprayed Al-Al_2O_3 could exhibit similar corrosion protection behavior as cold sprayed pure Al coatings, and then the extent to which the tribological behavior could be improved (this last point is covered in Section 2.4) [9, 11].

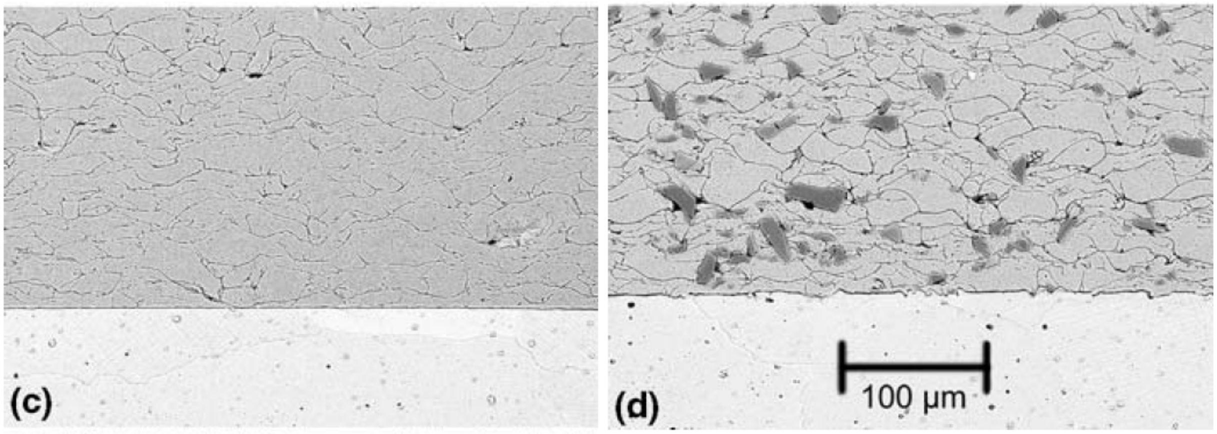

Figure 2.6 – Etched microstructures of cold sprayed Al (c) Al-Al_2O_3 (d) coatings [9].

Hard ceramic phases such as Al_2O_3 and SiC are not believed to participate in the adiabatic shear instability associated with bonding during cold spray [9, 58]. Indeed, when cold sprayed alone, ceramic particles will only act erosively to roughen and peen the substrate surface. Yet when cold sprayed along with ductile metal powders, some ceramic particles are recovered in the coating (see Figure 2.6). This is attributed to a "wedging" effect during impact, where the ceramic particle can get caught up among the uneven surface while the coating is formed. When the relative concentrations of Al and ceramic phases are measured, the recovered Al_2O_3 concentration is generally lower than that in the initial feedstock (see Figure 2.7) [9, 11, 58]. This has been shown in at least two studies (see Figure 2.7). The maximum recoverable Al_2O_3 concentration has been shown to be on the order of 25 wt.% when feedstock concentrations were at 75 wt.% [9]. Coating hardness increases as a function of Al_2O_3 content as well (see Figure 2.8) due to load bearing by Al_2O_3 particles. The corrosion resistance in a salt spray bath found no measurable differences between cold sprayed Al and Al-Al_2O_3 in the as-sprayed condition [9, 11].

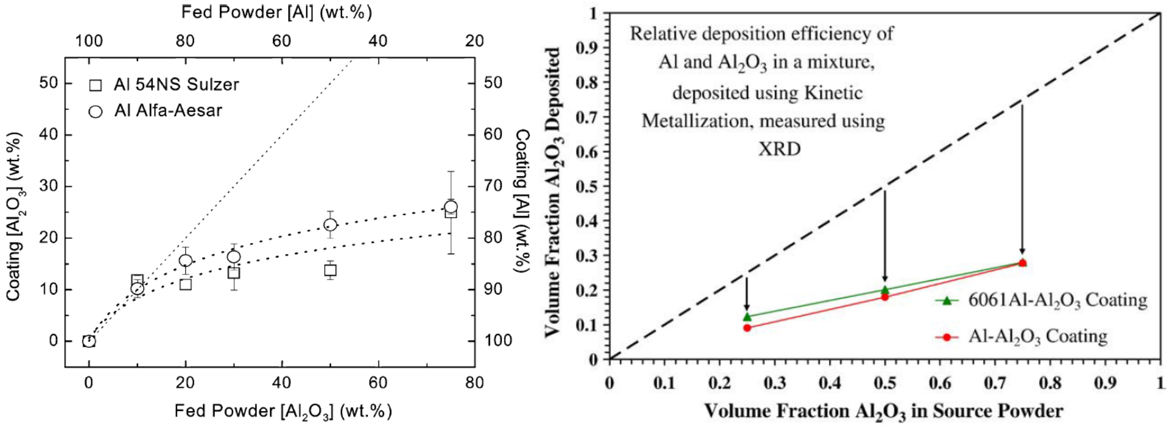

Figure 2.7 – Recovery of Al_2O_3 in coatings as a function of feeder powder content; [9] (left) and [11] (right).

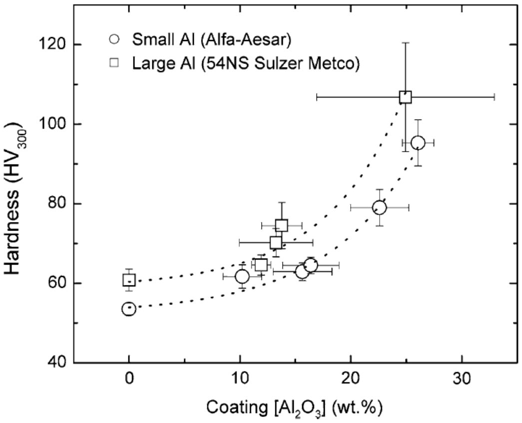

Figure 2.8 – Microhardness values of Al-Al_2O_3 coatings as a function of coating Al_2O_3 content [9].

Deposition of MMC coatings is commonly achieved by admixing (mechanically stirring) metal and ceramic powders to create blended feedstock in the mass or volume fraction desired [4, 9, 11]. Then the powder blend is injected into the nozzle. Additional techniques of dual-powder feeding have been investigated (see Figure 2.9) where ceramic powders were injected separately, either in the diverging section of the nozzle or directly into the gas plume outside the nozzle [58]. However the highest recovery of ceramic particles was found to come admixed powders, so in spite of a tendency for ceramic particles to erode nozzles, admixing was found to be preferable to downstream injection [58].

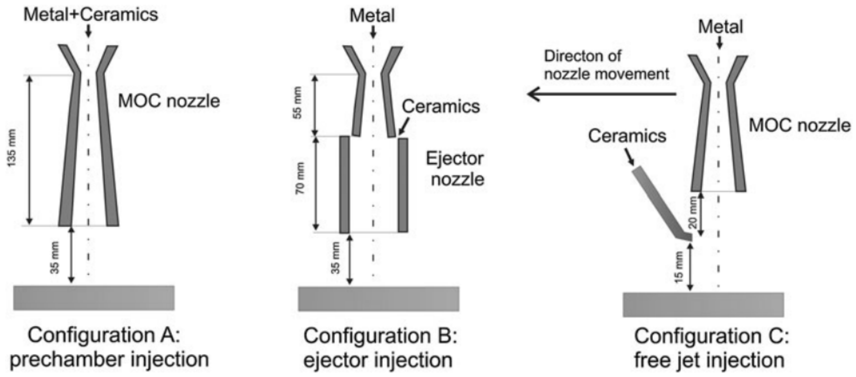

Configuration A: prechamber injection

Configuration B: ejector injection

Configuration C: free jet injection

Figure 2.9 – Configurations for depositing MMC materials by cold spray [58]. Configuration A, where an admixed powder is injected in the prechamber, is the most common and was used for the work in this thesis.

2.3 Selected tribological phenomena

The wide field of tribology is associated with topics as diverse as lubrication, abrasion, and erosion. The tribological experiments in this manuscript consist entirely of dry sliding wear, so only the tribological phenomena associated with this will be discussed here.

2.3.1 Friction and wear

Wear and friction are system responses to surfaces in relative motion. Friction is the reaction force parallel to the direction of movement, while wear is the removal of material from one or both surfaces [59]. Importantly, neither friction nor wear performance is uniquely a function of material properties. Tribological performance is a highly complex phenomenon influenced by surface morphology, applied loads, velocity of motion, contaminants or lubricants on the surface, temperature, atmospheric conditions, and other factors [49, 60].

Friction may be simply expressed as the coefficient of friction (COF or μ) which is the ratio of the tangential reaction force, F_T, to the applied normal load, F_N (see Equation 2.3). Friction is classically attributed to adhesion and deformation surface interactions, μ_a and μ_d, respectively [60].

$$\mu = \frac{F_T}{F_N} = \mu_a + \mu_d \tag{2.3}$$

Wear can be divided into at least five categories including adhesive, abrasive, fatigue, erosive, and chemical wear [49]. Adhesive wear is the dominant wear mechanism for aluminum materials in dry sliding wear, and it arises from the fact that two nominally smooth surfaces in contact will have a true contact area much smaller than the nominal contact area due to micro- and nano-scale asperities [61]. Bonding occurs between a fraction of the asperities due to the concentrated stresses, and then those bonds are sheared during sliding [49]. The force required to shear the interfacial bonding in dry sliding is the adhesive force (Equation 2.4 where μ_a is the adhesive COF, A_r is the real contact area, τ_a is the interfacial shear strength and p_r is the real pressure) [60]. Lowering the interfacial adhesive shear strength is one strategy for lowering the adhesive component to the coefficient of friction [60]. Lubricating media, whether solid or liquid, lower friction and wear partly by this mechanism. Lowering the contact area is another means of lowering the adhesive forces, as it directly determines the number of interacting asperities. From this logical standpoint it is evident that it is the hardness of the asperities, and not necessarily the hardness of the bulk material, that determines the contact area and thus the adhesion [62].

$$\mu_a = \frac{A_r \tau_a}{F_N} = \frac{\tau_a}{p_r} \tag{2.4}$$

In a fraction of asperities the interfacial shear will cause cohesive failure within one of the asperities rather than adhesive failure between the asperities [63]. This causes a particle to detach, generating an adhesive wear particle of (typically) equiaxed morphology [49]. The depth of the site of failure is proportional to the load applied to the surface. At low stresses the wear debris will be fine particles, while gross material removal called galling wear may occur at stresses above a certain threshold [1].

$$v = \frac{kF_N x}{H} \tag{2.5}$$

The simplest quantitative relation of adhesive wear is Archard's equation (Equation 2.5) where v represents the wear volume, F_N the applied load, x the total sliding distance, and H the hardness of the surface being worn [49]. The parameter k is a fitting variable interpreted as the probability of a wear particle being formed during an asperity encounter [49]. The term k varies according to the sliding system and is empirically derived. Equation 2.5 has been found to be accurate in many sliding wear tribological systems, particularly those involving metals [64].

However, at the basis of the Archard equation is the assumption that material that is detached will immediately form a wear debris particle. This assumption ignores the many phenomena that can occur at the sliding interface, where a piece of detached material could remain inside the contact, where it could deform, or chemically react, or roll, or indeed be ejected from the contact (and later perhaps recirculate back into the contact!) [65]. A more robust and complete theory is the logical framework provided by the concepts of the third body [66] and the tribological circuit [67].

2.3.2 Third bodies

Third bodies develop due to deformation-induced physical, chemical, and microstructural changes of material at the sliding interface, and often exhibit distinct properties compared to the unworn first bodies [29, 66]. During the sliding wear process, material accumulation on one or more surfaces is common [64]. Transfer film is any amount of worn material which attaches and moves along with the sliding surface, while the tribofilm is the stationary surface along which the transfer film slides. Tribofilms may consist of anything from a thin molecular layer of lubricant additives (e.g., ZDDP) to a plastically deformed layer in dry sliding wear systems. In either case, if a stable transfer film forms, then the actual sliding interface exists between the transfer film and tribofilm. The chemistries and structures of the transfer film and tribofilm vary depending on the tribological environment and this in turn influences the observed friction and wear [64]. The formation of stable tribological films is key to the friction and wear reduction properties of most solid lubricants [68], yet it is also observed in some metallic systems.

2.3.3 The tribological circuit

The phenomena of material transfer, mechanical mixing, and wear debris formation are largely third body material flows, and the magnitude of these flows influences the overall performance of the sliding system in terms of friction and wear [67]. The material flows in a sliding system may be described using the tribological circuit (see Fig. 2.10) [67]. The first bodies are contacting and are in relative motion to one another; third bodies form at the sliding interface. The source flow, Qs, represents detachment or transformation of first body material to become the third bodies; the internal flow, Qi, is movement of material across the interface; the ejection flow, Qe, is material ejected from the interface; the recirculation flow, Qr, is ejected material that has been reintroduced to the interface; and the wear flow, Qw, is material permanently removed from the sliding system. When applied to metallic systems, the phenomena of third body formation, mechanical mixing, and wear debris formation [69–71] may be readily assigned theoretical counterparts in the tribological circuit.

The material flows described by the tribological circuit have been used to produce newer quantitative wear models [65] that take into account the formation of third bodies, which are ignored in Archard's equation (Equation 2.5). These models indicate that there tends to be a stable quantity of third body present for a given tribosystem, and this has been verified through experiments [65]. A more complete picture of tribological behavior of a sliding system, in relation to wear, may be gathered by monitoring the wear rate and the third body material.

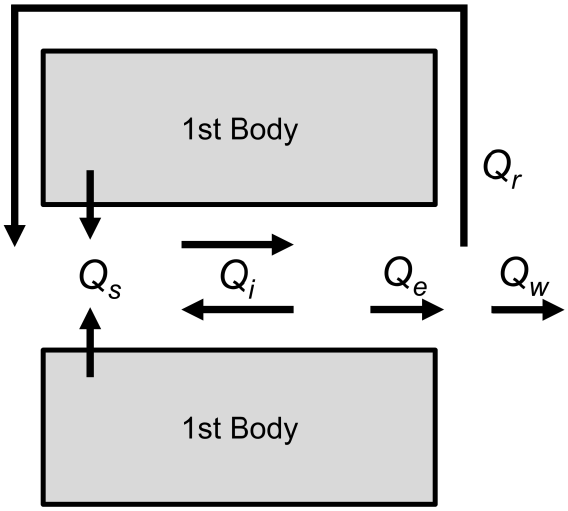

Figure 2.10 – The tribological circuit [67].

2.3.4 Velocity accommodation modes (VAMs)

The surface adaptation to relative motion during dry sliding may be classified according the so-called velocity accommodation modes (VAMs) [72]. This analysis permits description of the locations and mechanisms by which relative motion is manifested at the sliding interface. Classically, the mechanisms of elastic deformation, fracture, shear, and/or rolling may take place in some combination of the first bodies, third bodies, and the interfaces in between; each combination represents a VAM [72]. A shift in VAM may influence the material flows in the tribological circuit and hence the friction and wear of the sliding system.

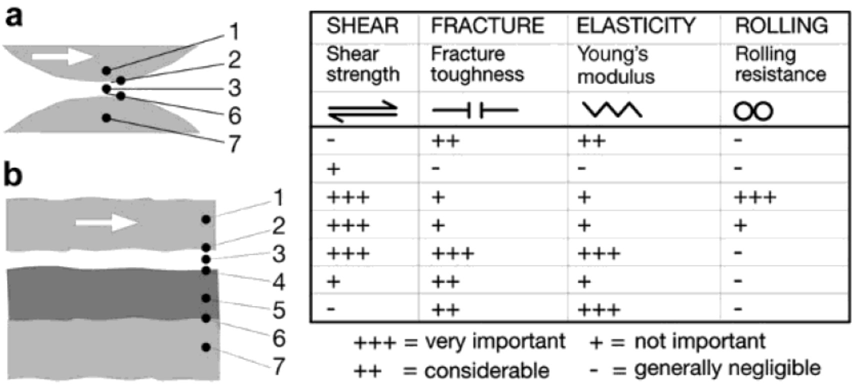

SHEAR	FRACTURE	ELASTICITY	ROLLING
Shear strength	Fracture toughness	Young's modulus	Rolling resistance
⇌	⊣ ⊢	⋀⋀⋀	∞
-	++	++	-
+	-	-	-
+++	+	+	+++
+++	+	+	+
+++	+++	+++	-
+	++	+	-
-	++	+++	-

+++ = very important + = not important
++ = considerable - = generally negligible

Figure 2.11 – Velocity accommodation modes in two sliding couples, (a) uncoated and (b) coated (image from [64]).

2.3.5 Contact between solid surfaces

The subject of contact mechanics was given an initial rigorous approach by Hertz, the effort of which resulted in the Hertzian theory of non-adhesive elastic contact [73]. A number of analytical solutions to a diverse set of contacts, such as sphere-sphere, sphere-plane, etc. The first concept that must be utilized is that of the reduced modulus, E_r:

$$\frac{1}{E_r} = \frac{1 - v_1^2}{E_1} + \frac{1 - v_2^2}{E_2} \tag{2.6}$$

where E_1, E_2, and v_1 are the elastic modulus and Poisson's ratio of the first and second bodies in contact. For a sphere-plane contact, the contact radius, is then calculated as:

$$a_r = \frac{(3F_nR)^{1/3}}{4E_r} \tag{2.7}$$

where F_n is the normal force and R is the radius of the sphere. Thus the average Hertzian contact stress is

$$P_{avg} = \frac{F_n}{\pi a_r^2} \tag{2.8}$$

and the maximum Hertzian stress is

$$P_{max} = \frac{3}{2}P_{avg} \tag{2.9}$$

which occurs in the center of the contact.

The Hertzian contact pressure is typically only valid during the initial contact of two surfaces. Once sliding begins, the processes such as plastic deformation, transfer, wear debris generation, etc. eliminate the initially smooth contact region, and contact pressures become far more difficult to predict. This is particularly the case during dry sliding wear at macroscopic length scales, where there is almost assuredly a multi-asperity contact. The Hertzian contact pressure remains a valid calculation in some lubrication regimes, or in certain

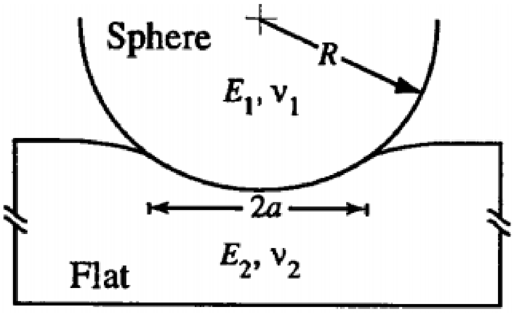

Figure 2.12 – Hertzian contact of a sphere and plane [73].

single-asperity contacts such as microtribology.

2.4 Materials tribology of Al-MMCs

2.4.1 Friction and wear of Al-MMCs

The friction and wear behavior of Al-MMC materials reinforced with hard particles or fibers has been a subject of interest for at least 40 years [74,75]. Relatively soft aluminum-based matrix materials, such as pure Al, Al-4Cu , Al-4Cu-0.75Mg, AA6061, AA2014, Al-10Zn, A356, AA7091, and various other alloys have been paired with comparatively harder reinforcements made most commonly from SiC, Si, or Al_2O_3, but other materials such as MgO, glass beads, Si_3N_4, TiB_2, TiC, sand, B_4N, B_4C, Ni_3Al, and NbC have been explored as well [1,18,24,25,27,34,74–84]. Generally speaking, the presence of hard particles is associated with lower wear rates and lower friction compared to the unreinforced matrix material. One early study explored the influence of concentration and particle size for Al_2O_3 and SiC reinforcements in an AA2014 alloy matrix. It was found that in the ranges of 2-30 wt.% and 1-142 µm particle sizes, the wear rate decreased as reinforcement concentration increased, and at a given weight fraction, wear rate decreased as reinforcement size increased [85]. Similar findings regarding particle concentration were reported in subsequent studies, with the optimum Al_2O_3 particle content for wear resistance falling in the range of 25 - 35% [75,86] (see Figure 2.13). The influence of particle size is not as clear, as some subsequent studies have found that increasing the particle size can lead to slightly higher wear rates [74,87,88]. The friction coefficient was found to be affected by the presence of hard particles as well, with the composite materials exhibiting 30% lower friction coefficients than the aluminum matrix alone [89].

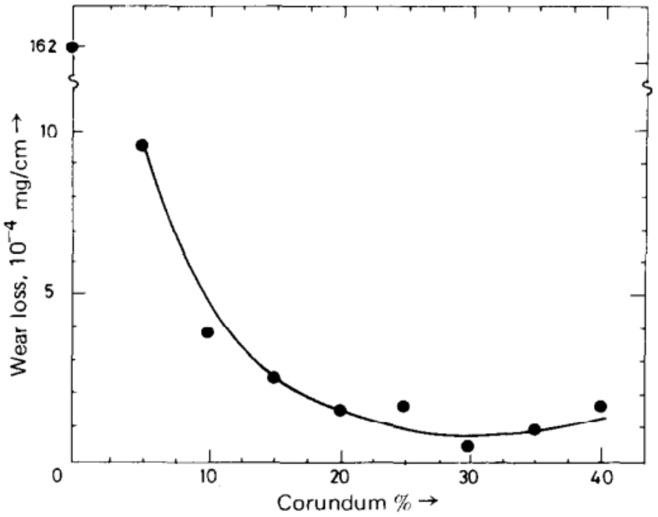

Figure 2.13 – Wear loss as a function of corundum content (wt.%) in a matrix of Al-10wt.%Zn [75].

2.4.2 The mechanically mixed layer (MML)

The general findings of lower wear rates and friction in Al-MMCs compared to the unreinforced matrix alloys has been investigated through surface and subsurface microanalysis. The tribolayer, which may also be referred to as a mechanically mixed layer (MML) [24,26], is a feature very frequently observed during wear of metallic materials, and is closely associated with the behavior of Al-MMC sliding systems [1]. Material transfer between sliding surfaces is a very commonly observed phenomenon, and the high contact stresses at the interface can result in extensive deformation of the transferred material. Thus the material near the interface may extensively work harden, undergo grain refinement, chemically react (e.g., oxidation) or become mechanically milled with other transferred material [1,29,67,76]. If this third body material forms a stable, hard layer of tribofilm, then it can reduce the wear rate and also affect the friction coefficient [90]. Depending on the contact conditions, the depth of plastic deformation typically extends below the tribolayer and into the bulk material, with the degree of deformation varying as a function of depth; the extent of plastic deformation can at times be traced through hardness measurements or grain refinement (see Figure 2.14, left) [1, 24]. In certain regimes of velocity and contact pressure, the tribofilm may not form due to extensive plastic flow and gross material transfer from deep in the material, in which case the formation of a tribofilm is precluded and the presence of hard particles may have little to no influence on the friction and wear rates (see Figure 2.14, right [1, 27, 28]. However, the presence of hard particles can raise the load at which the transition between these regimes occurs [1, 27, 28].

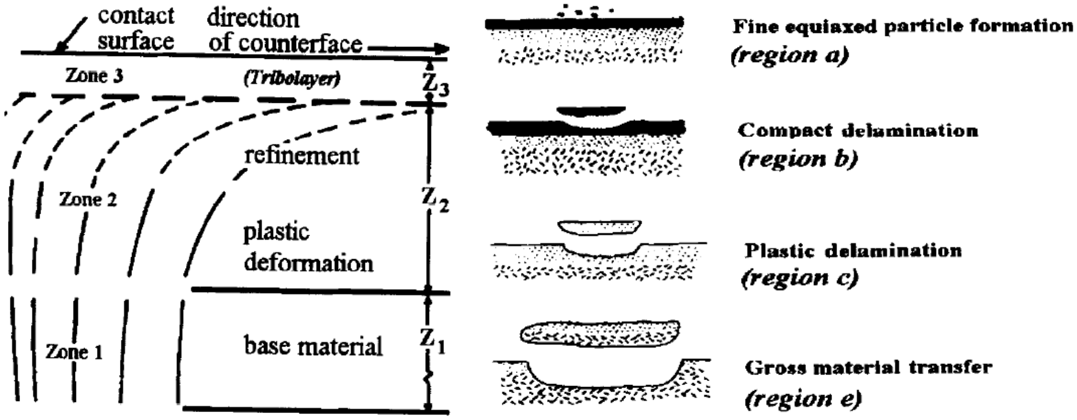

Figure 2.14 – Diagram of the sub-surface zones found beneath wearing surfaces (left) and various wear regimes as related to the tribofilm (right) [1, 91].

The tiny thickness of Al-MMC tribolayers (typically between 2 and 50 µm, depending on the sliding and contact conditions) means they have been difficult to characterize. Although various elemental and chemical techniques (e.g., EDX [Energy-dispersive X-ray spectroscopy microanalysis], XPS [X-ray Photoelectron Spectroscopy], etc.) have detected elevated oxygen content in Al-MMC tribolayers, XRD (X-Ray Diffraction) typically does not detect the presence of crystalline oxides [1, 92]. EDX studies have found that Al-MMC tribolayers are typically rich oxygen, aluminum, fragmented hard particles, and iron (if a steel counterface is used) [1, 25, 28, 93]). Given the importance of Al-MMC tribolayers in dictating friction and wear behavior, they remain somewhat poorly understood in terms of the processes and circumstances under which they form.

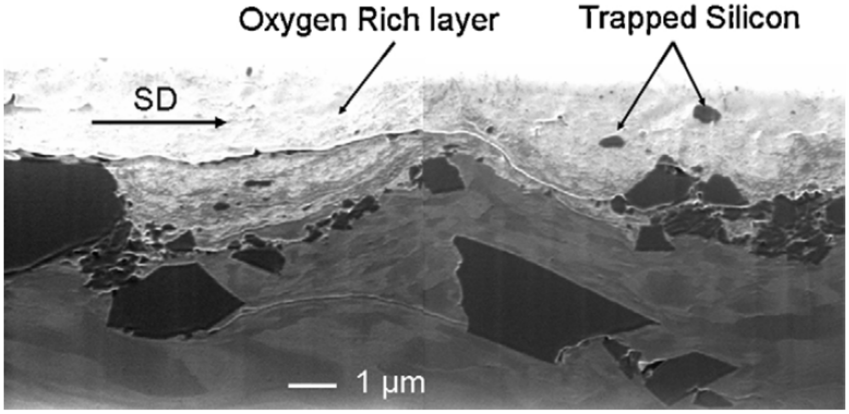

Figure 2.15 – A FIB-cross sectioned tribofilm layer in an Al-Si alloy subjected to dry sliding wear [94].

2.4.3 Tribometry techniques used on Al-MMCs

When conducting any tribological study, it is important to remember that friction and wear rate are not intrinsic material properties, even though they are frequently treated as such in literature and common parlance. The behavior of a tribosystem arises from a combination of material factors and mechanical factors [95]. Comparing results from one tribometry experiment to another must be approached critically and with caution.

The vast majority of older dry sliding wear studies on Al-MMC materials have employed steel counterfaces. The choice of counterface material is important to note because the friction and wear behavior in a sliding system can be influenced by (among a great many other parameters) the counterface hardness, geometry, and chemical reactivity. For instance, given that the most popular Al-MMC reinforcement materials are SiC and Al_2O_3, which have hardness values in excess of 10 GPa, the softer steel counterface may be cut when rubbing on these particles. This may produce debris that could transfer to the opposing surface and/or produce wear debris [1]. In older papers, the typical tribometry setup was either "classical" pin-on-disk, where a (typically) 4 or 6 mm diameter cylindrical pin of Al-MMC material is slid against a steel disk (e.g., [25, 26, 34, 96, 97]), or block-on-ring tests where a block of Al-MMC material is slid on a steel ring (e.g., [27, 28]). These geometries are shown in Figure 2.16. In these geometries, the wear volume is calculated as a function of the change in height/mass of the cylindrical pin [34, 98] or from the width of the scar on the block [99], respectively. The term "pin-on-disk" may also, in contemporary usage, refer to "ball-on-flat" tribometry, where a ball bearing of steel or another material is rubbed against a disk of a material of interest [100]. This test geometry is especially common for tribological studies of coatings [64, 101]. In this scenario, wear volume is measured by observing the wear scar formed on the flat surface and/or the ball material material [101]. The ball-on-flat geometry has become more commonly utilized in tribological studies of aluminum and Al-MMC materials in recent years (e.g., [11, 80, 94, 102–104]).

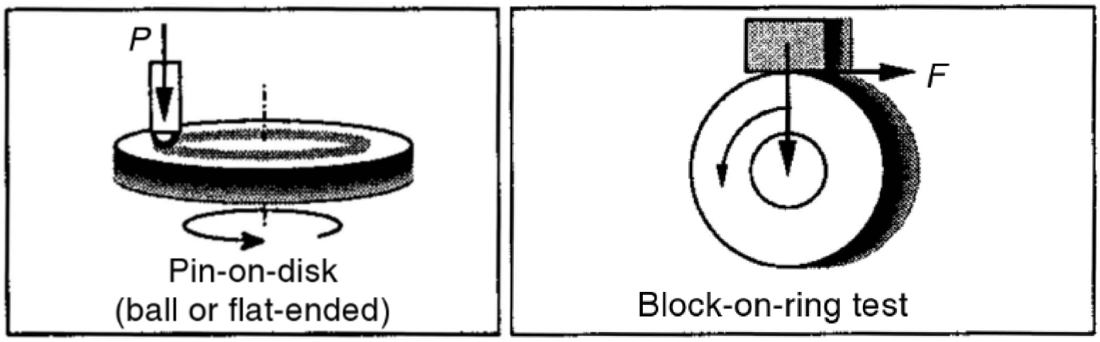

Figure 2.16 – Pin-on-disk and block-on-ring test schematics, two common sliding wear test geometries for Al-MMC materials [100]. The work in thesis uses a reciprocating ball-on-flat geometry (see Figure 3.4).

2.4.4 Dry sliding wear of cold-sprayed Al-Al_2O_3

A study [11] on the coating formation, properties, and corrosion behavior of cold sprayed Al-Al_2O_3, which was already reviewed in Section 2.2, also included dry sliding wear tests. A series of coatings was subjected to wear testing using a ball-on-flat tribometer equipped with a 6 mm diameter ball of 100Cr6 bearing steel pressed against the sample surfaces at using a deadweight load of 3 N (306 gf). The test kinematics were rotational, with a linear speed of 20 cm/s and a total test length of 500 m. Friction measurements found that the presence of Al_2O_3 particles was associated with stable friction coefficients, while the un-reinforced pure Al and AA6061 coatings they tested showed unstable friction, with frequent sharp deviations in the upward direction. Wear rate measurements showed that the presence of Al_2O_3 particles was associated with significant reduction in wear rates (see 2.17) of up to five orders of magnitude. The application of a 2 hour heat treatment at 400°C resulted in very little change in the measured wear rates. Surface analysis of the wear tracks revealed significant changes in morphology (see Figure 2.18). The cold sprayed pure Al coating showed significant plastic flow and evidence of adhesive wear, while the Al-Al_2O_3 composite coating showed significantly smoother features. Significant transfer from the pure Al coating was found on the slider, while the slider showed signs of wear after rubbing against the Al-Al_2O_3 coatings [11]. Little further analysis of the third body behavior was carried out to understand the explanation for these features.

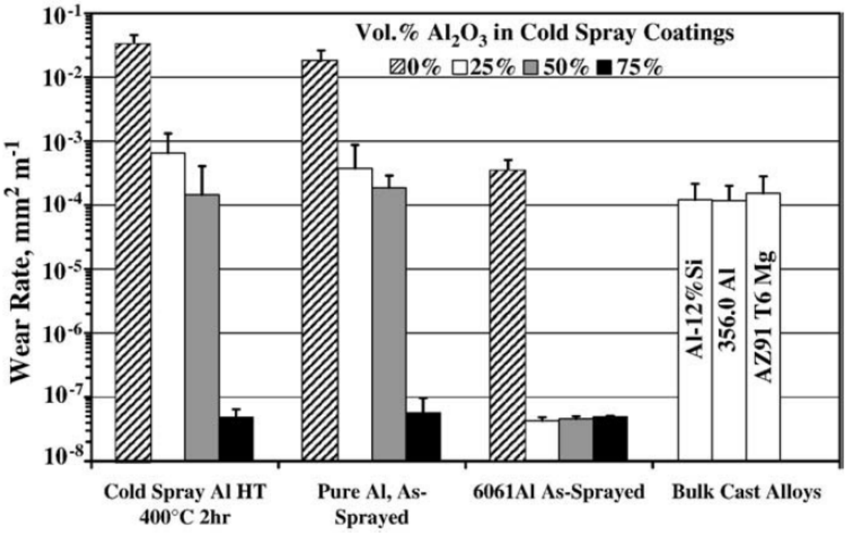

Figure 2.17 – Wear rates for a series of cold sprayed Al-Al_2O_3, in the as-sprayed condition and after a 2 hour 400°C heat treatment, AA6061-Al_2O_3 coatings, and several bulk cast alloys. The content of Al_2O_3 shown here is in the amount in the initial powder, not the coating themselves [11].

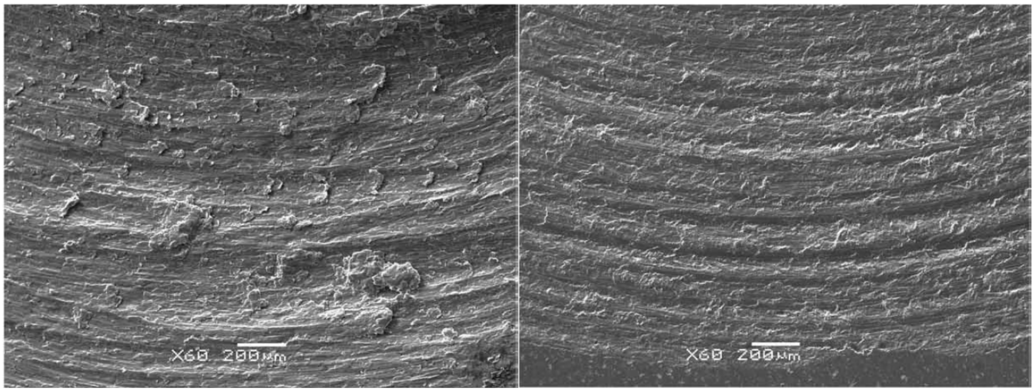

Figure 2.18 – Surfaces of cold sprayed pure Al (left) and Al-Al_2O_3 (right) coatings after dry sliding wear testing [11].

2.5 High pressure torsion (HPT)

2.5.1 Context

HPT is a materials processing technique in which samples are subjected to a compressive force in conjunction with torsional straining. In pioneering experiments by Bridgman in the 1940s, it was found that during torsional straining of a metal bar, applying a compressive load along the axis of rotation allowed the bar to be twisted to higher angles without fracture compared to when no load was applied [105]. To avoid buckling the bars were shortened into disks of material, and Bridgman subsequently constructed the opposed anvil apparatus (see Figure 2.19), which is the precursor to HPT techniques used today [35, 106]. The early use of the opposed anvil apparatus was to study the flow behavior of material under imposed hydrostatic pressure, as it was impossible to apply external hydrostatic pressures on the order of GPa through environmental control alone [106] – the quasi-hydrostatic pressure created by longitudinal compressive loading and the friction between the sample and anvils was a close substitute. Early research showed that deformation-induced grain refinement during HPT could approach grain sizes of 100 nm or smaller [35], and the enhanced mechanical properties of these materials was extensively documented [35, 107]. This drove the development of HPT as a processing tool to produce nanostructured materials through severe plastic deformation (SPD), in the same family as equal channel angular processing (ECAP) [108] and accumulative roll-bonding (ARB) [109].

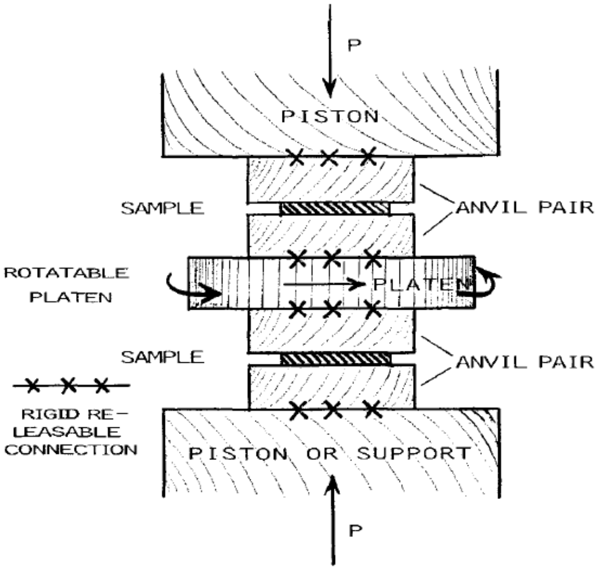

Figure 2.19 – The opposed anvil apparatus developed by Bridgman [106,110].

As the majority of HPT studies focus on the development of nanostructured materials, the change in sample geometry from unconstrained outward flow on the original Bridgman apparatus proved problematic. In the idealized configuration of constrained HPT, the sample is machined to the precise dimensions of a cavity in the lower anvil, and no outward flow is possible (see Figure 2.20) [111]. However, in reality some outward flow always occurs because of machining gaps, and the commonly used configuration today is the quasi-constrained condition [35]. Although the constrained and quasi-constrained configurations are very useful for the study of microstructural evolution during HPT, the friction between the sample and the outer anvil wall introduces extra tangential forces, such that the torque measured during HPT does not necessarily reflect the shear strength of the material itself. This is closer to being the case for the unconstrained condition, and thus the HPT work in this thesis was performed using the unconstrained condition. However, due to outward flow of material in the unconstrained condition, some amount of friction may occur between the sample and the wall, so this could be a source of additional strain beyond the pure shear strain occurring during twisting [112]. Furthermore, hydrostatic pressure may be inconsistent as a function of radius in the unconstrained condition due to the lack of back pressure from the outer anvil wall in the constrained/quasi-constrained conditions.

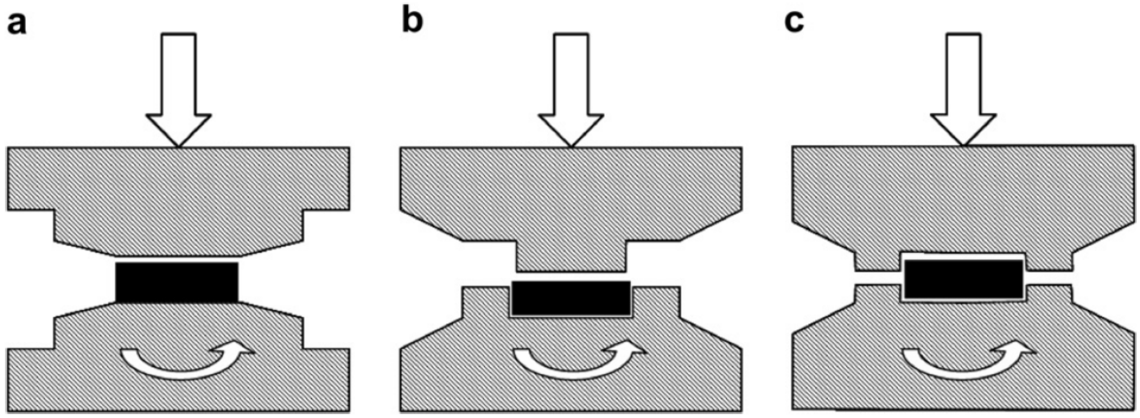

Figure 2.20 – Schematic illustration of HPT for the (a) unconstrained, (b) constrained, and (c) quasi-constrained configuration [111]. The work in this thesis used the unconstrained configuration.

2.5.2 Continuum mechanics models of HPT

The state of stress and strain in the sample may be calculated according to the Fields and Bakofen method, which is used in classical torsion testing [113].The evolution of torque, rotation angle, and sample thickness during HPT may be converted into von Mises equivalent stresses and shear strain at the external radius a by the following equations:

$$\sigma = \sqrt{3}T\frac{(3 + M + N)}{2\pi r^3} \tag{2.10}$$

$$\varepsilon = r\vartheta/\sqrt{3}h \tag{2.11}$$

where ϑ is the rotation angle,T is the measured torque, h is the sample thickness, $M = \delta lnT/\delta ln\dot{\vartheta}$is the rotation rate sensitivity of the torque, and $N = \delta lnT/\delta ln\vartheta$is the rotation sensitivity of the torque. The values of M and N are often estimated as being constants, particularly for high temperature testing of steels (for the sake of estimating rolling load), which is a common application of conventional torsion testing [114]. However, this estimate is inaccurate if the shape of the stress-strain curve is to be determined [114]. When this is the case, the value of N must be calculated on a local basis, because it evolves significantly over the course of the test. For room temperature and quasi-static testing of most materials, M is constant and is generally set to zero [115].

Other strain models have been proposed from that of the Fields and Backofen relation, and these are occasionally applied to HPT data. One popular alternative model is the Eichinger strain model, applied to HPT by Zhilyaev et al. [116]. However, this model has been found to lead to physically unreasonable values of strain [115].

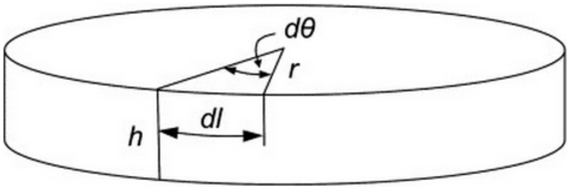

Figure 2.21 – The principle for estimating strain during HPT from the disk radius r and thickness h [117].

2.5.3 HPT of aluminum and Al-MMCs

HPT studies in the constrained condition have been carried out on commercially pure aluminum [117–119], aluminum alloys [120–122], and Al-MMCs [123–125]. The primary focus has been to study SPD-induced microstructural evolution and the enhancement of strength and hardness. As the strain during HPT is directly proportional to the radius, the outer portions of the disk undergo greater strain and harden faster than the inner portions for a given number of rotations. This effect was visible for commercially pure aluminum tested at 1 GPa (see Figure 2.22, left), where the hardness of the outer portions of the disk obtained hardness saturation after only one turn, while roughly four turns were required for the central portion to harden to the same extent. This behavior is similar for most conventional materials of low or moderate stacking fault energy [35]. Interestingly, when a similar test was carried out on high purity aluminum, the opposite behavior is true (see Figure 2.22, right) [117]. This was attributed to the fast recovery rate of the high purity aluminum; the initial increase in dislocation density at small rotations is dynamically recovered in the outer regions of the disk first, so the hardness is lower there compared to the center. In both the commercial and high purity cases, hardness homogeneity was accomplished over the entire specimen after 4-5 rotations. After sufficient rotations to achieve homogeneous mechancial properties, the microstructural features of commercial purity and high purity aluminum showed extensive grain refinement compared to the initial state. For commercially pure aluminum, the grains were relatively equiaxed and have been reported to be on the order of 0.8 µm [118] or 0.5 µm [119] (see Figure 2.23), while for high purity aluminum, slightly higher grain sizes were observed on the order of 1.2 µm [117].

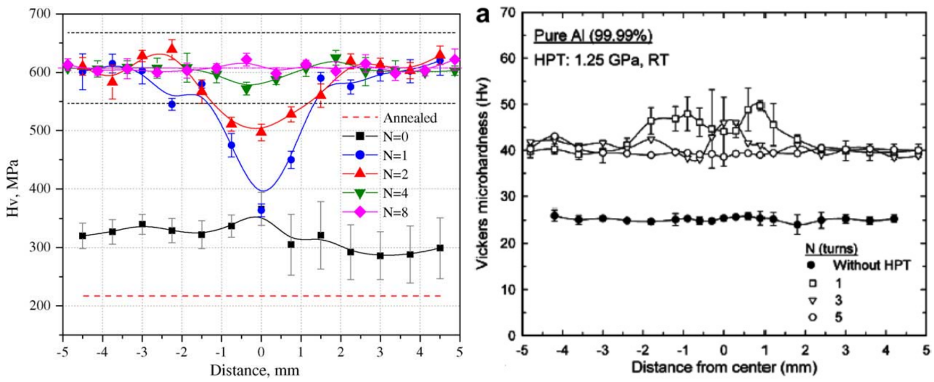

Figure 2.22 – Vickers hardness evolution during HPT as a function of the distance away from the disk center for a number of rotations for commercially purity 99.5% Al at 1 GPa (left, with units in MPa) [118] and high purity 99.99% Al at 1.25 GPa (right, units in HV) [117].

2.5.4 Using HPT to study tribological mechanisms

Various studies have used HPT in the unconstrained condition to study the phenomena of sliding wear. Kuhlmann-Wilsdorf applied HPT to fine stacked foils of silver and copper in order to observe the mechanics of mechanical mixing between the two immiscible metals [126]. This study demonstrated that as the metals were forced to strain together, tongue-like features were observed as the materials mixed into one another (see Figure 2.24), and this

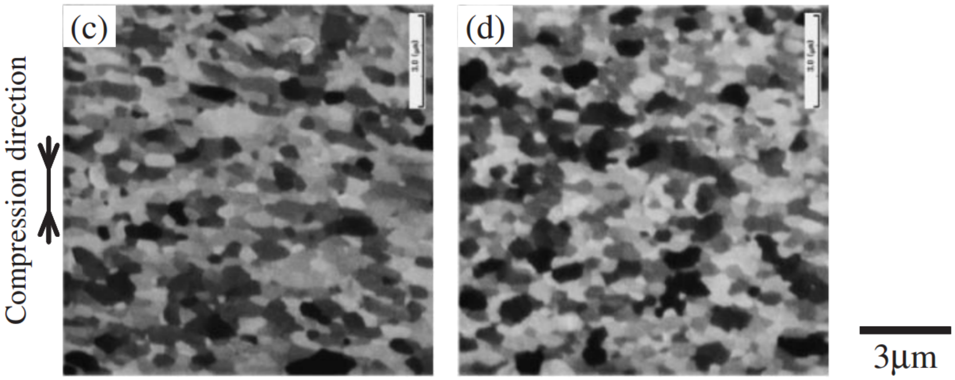

Figure 2.23 – Microstructural features of commercially pure Al after HPT in the shear plane at 1.5 mm (left) and 4.5 mm (right) away from the center a 10 mm diameter disk [119].

was believed to be related to the behavior at a rubbing interface of immiscible metals. In the highly controlled conditions of HPT, the intermixing that would eventually lead to tribolayer formation could be more directly observed than in a tribological contact which may be too small to easily observe.

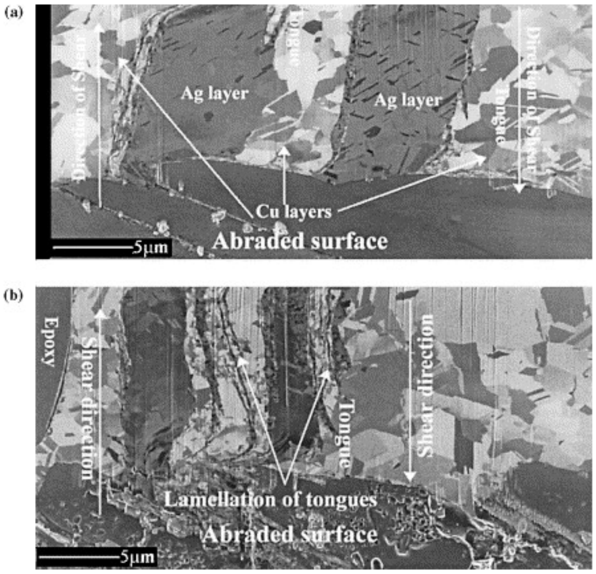

Figure 2.24 – Microstructural features of stacked Ag and Cu foils after (a) zero strain and (b) extensive straining at the edge of an HPT disk [126].

Further studies have been carried out on high-purity iron [36, 112]. It was found that during unconstrained HPT, a rise in the shear stress (see Figure 2.25), calculated using the Fields and Backofen relations from the torque, could be linked to strengthening and grain refinement in the microstructure [112]. Finite element modeling helped identify the local conditions associated with the onset of grain refinement in terms of the degree of strain and strain gradients [36].

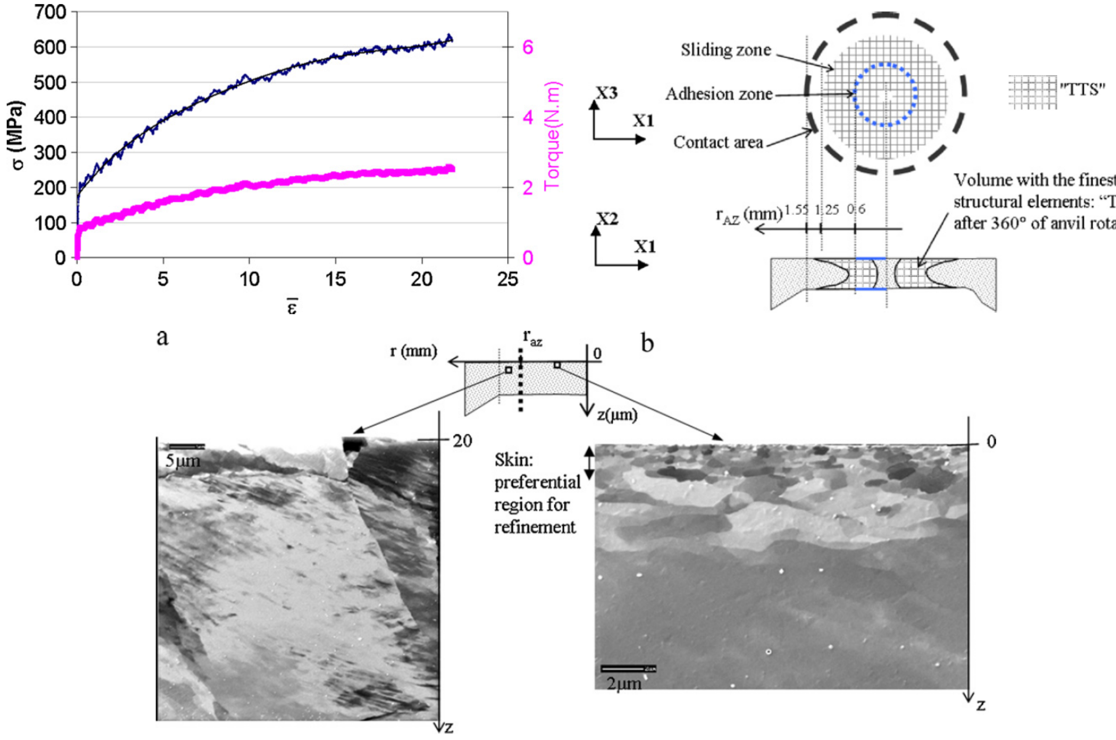

Figure 2.25 – Top left: torque and stress evolution during unconstrained HPT of a high purity iron sample [112]. Top right: zones of microstructural evolution [36]. Bottom: surface grain refinement in the "skin" of the sample within the adhesion zone, which did not occur outside the adhesion zone [36].

2.6 Finite element analysis of Al-MMC materials

In structural mechanics, finite element analysis (FEA) is a numerical technique by which the stresses and strains within a mechanical system may be calculated. This section will provide an overview of a few basic principles of solid mechanics and the application of FEA techniques to the study of Al-MMC materials undergoing deformation.

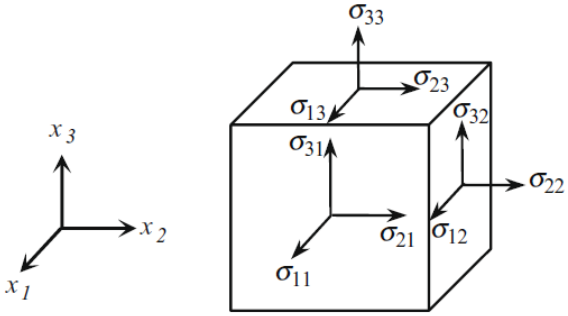

Figure 2.26 – An infinitesimal material element showing the traction vectors on the faces [127].

2.6.1 Mechanics

For an infinitesimal volume element of a material, the stresses acting on that element (see Figure 2.26) can be fully described by the Cauchy stress tensor:

$$\boldsymbol{\sigma} = \sigma_{ij} = \begin{bmatrix} \sigma_{11} & \sigma_{12} & \sigma_{13} \\ \sigma_{21} & \sigma_{22} & \sigma_{23} \\ \sigma_{31} & \sigma_{32} & \sigma_{33} \end{bmatrix} \tag{2.12}$$

where σ_{11}, σ_{22}, and $\sigma_{33}$are normal stress components and the rest are shear components [127]. The Cauchy stress tensor may be split into the hydrostatic and deviatoric components:

$$\boldsymbol{\sigma} = \mathbf{S} + \sigma_{hs}\mathbf{I} \tag{2.13}$$

which are associated with volume change and the plastic flow, respectively. The hydrostatic (or “mean” or “spherical” or “triaxial”) component is calculated from the first invariant of the Cauchy stress tensor multiplied by the identity matrix, **I**:

$$\sigma_{hs}\mathbf{I} = \frac{\mathrm{tr}(\sigma)}{3}\mathbf{I} = \frac{\sigma_{ii}}{3}\mathbf{I} = \frac{(\sigma_{11} + \sigma_{22} + \sigma_{33})}{3} \begin{bmatrix} 1 & 0 & 0 \\ 0 & 1 & 0 \\ 0 & 0 & 1 \end{bmatrix} = \begin{bmatrix} \sigma_{hs} & 0 & 0 \\ 0 & \sigma_{hs} & 0 \\ 0 & 0 & \sigma_{hs} \end{bmatrix} \tag{2.14}$$

and the deviatoric component is calculated by subtracting the hydrostatic component from the Cauchy stress:

$$\mathbf{S} = \boldsymbol{\sigma} - p\mathbf{I} = \begin{bmatrix} \sigma_{11} - \sigma_{hs} & \sigma_{12} & \sigma_{13} \\ \sigma_{21} & \sigma_{22} - \sigma_{hs} & \sigma_{23} \\ \sigma_{31} & \sigma_{32} & \sigma_{33} - \sigma_{hs} \end{bmatrix}. \tag{2.15}$$

The von Mises equivalent stress is a means of calculating the effective plastic stress to multiaxial response:

$$\sigma_{VM} = \frac{1}{\sqrt{2}} \left[(\sigma_{11} - \sigma_{22})^2 + (\sigma_{22} - \sigma_{33})^2 + (\sigma_{33} - \sigma_{11})^2 + 6\left(\sigma_{12}^2 + \sigma_{23}^2 + \sigma_{13}^2\right) \right]^{1/2}. \tag{2.16}$$

When the von Mises equivalent stress exceeds the yield stress determined through uniaxial tension, plastic flow commences [127]. After yield, the total strain of an elastic-plastic material, ε_{ij}, is the sum of elastic and plastic components. The plastic component, ε_{ij}^p, is related to the von Mises equivalent stress through a function in a form of:

$$\sigma_{VM} = h(\int \mathrm{d}\bar{\varepsilon}^p) \tag{2.17}$$

where h is the strain hardening function and $d\bar{\varepsilon}^p$ is the increment of effective plastic strain:

$$\mathrm{d}\bar{\varepsilon}^p = \frac{\sqrt{2}}{3} \left[(\mathrm{d}\varepsilon_{11}^p - \mathrm{d}\varepsilon_{22}^p)^2 + (\mathrm{d}\varepsilon_{22}^p - \mathrm{d}\varepsilon_{33}^p)^2 + (\mathrm{d}\varepsilon_{33}^p - \mathrm{d}\varepsilon_{11}^p)^2 + 6\left(\mathrm{d}\varepsilon_{12}^{p\,2} + \mathrm{d}\varepsilon_{23}^{p\,2} + \mathrm{d}\varepsilon_{13}^{p\,2}\right) \right]. \tag{2.18}$$

The equivalent plastic strain (PEEQ) can therefore be calculated by integrating the incremental plastic strain over the course of time:

$$\bar{\varepsilon}^p = (\int_0^t \frac{\mathrm{d}\bar{\varepsilon}^p}{\mathrm{d}t} \mathrm{d}t). \tag{2.19}$$

One criterion for damage accumulation in ductile solids is the triaxiality factor, η:

$$\eta = \sigma_{hs}/\sigma_{vm} \tag{2.20}$$

where σ_{hs} is the hydrostatic stress and σ_{vm} is the von Mises stress [128]. The stress triaxiality factor is often incorporated into damage criteria in finite element modelling [129]. Plastic strain to failure in positive triaxiality regimes, such as ordinary tensile testing, has been shown to be reduced as the triaxiality factor is increased. In a state of negative triaxiality, where the hydrostatic stress is compressive, the damage mechanisms such as void and microcrack formation can be suppressed [130, 131].

2.6.2 Applications of finite element analysis to Al-MMCs

At its absolute simplest, finite element modelling relies on discretizing a geometric feature in one, two, or three dimensions into a finite number of elements, then defining a set of material properties, physical constraints (boundary conditions), and surface tractions. After these preprocessing steps, a matrix equation is constructed in the form

$$\{P\} = [K]\{u\} \tag{2.21}$$

where $\{P\}$ is the set of loads and reactions at nodal points, $[K]$ represents the stiffness matrix based on the mechanical properties of the materials and the element geometries, and $\{u\}$ represents the nodal displacements to be calculated through the analysis [127]. Once the displacements are known by solving the matrix, the stress and strain fields are back-calculated through the stress-strain and strain-displacement relations. In cases of large displacements, incremental nonlinear techniques are used to break a given step into individual increments, solve the matrix equation, then regenerate the stiffness matrix based on the new geometric conditions [132].

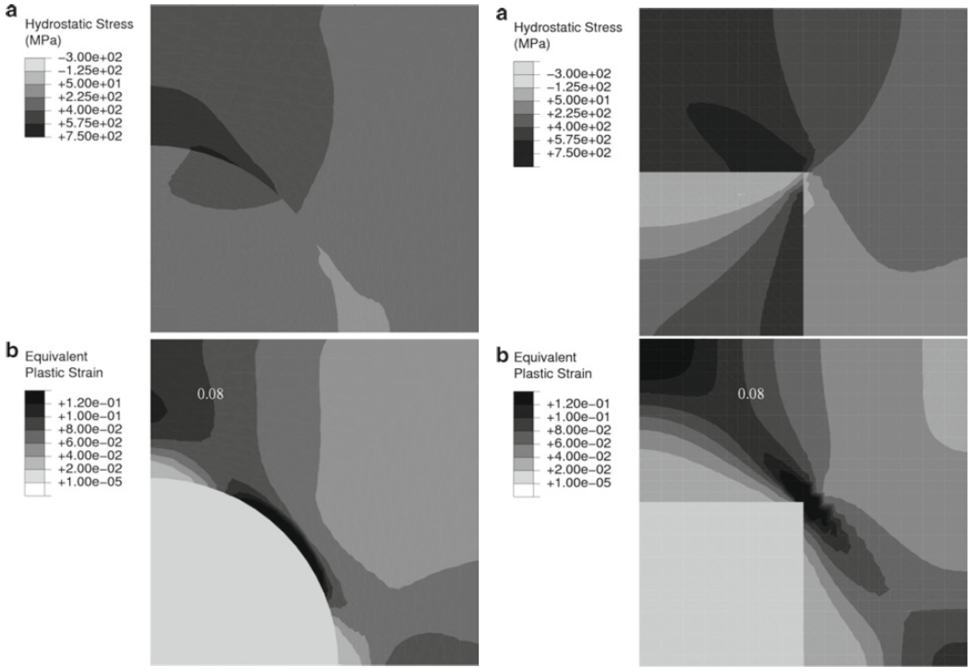

Figure 2.27 – Plots of hydrostatic tension (top) and equivalent plastic strain (bottom) under tensile loading for spherical (left) and square (right) reinforcement morphologies for Al-SiC composites [133].

Finite element analysis techniques have been used to study the role of particle morphology in the tensile behavior of Al-SiC composites [133–136]. At times full 3D models have been developed [136], but frequently 2D models in plane strain (where strain in the z-axis is set to zero) or axisymmetric configurations. The effect of reinforcement particle morphology has been explored by studying the stress distributions in the matrix. In the model shown in Figure 2.27, an axisymmetric configuration was used, and a tensile strain was applied to the top surface while keeping the bottom surface fixed, and the matrix was assumed to adhere perfectly to the particle. The spatial distributions of equivalent plastic strain demonstrate that strain occurs along the 45° direction of maximum shear. For the spherical particle this results in strains remaining in the material very close to the particle, while for the angular particle, the strain takes place largely in the matrix. Stress-strain relations derived from the reaction forces in the model were able to show enhanced strengthening in the angular composite due to matrix yielding at lower tensile strains [133, 134]. In another study, experiments and modelling were carried out on Al-MMC composites made using spherical and conventional angular composites [135]. Experiments demonstrated that higher yield stresses but lower ductilities in tension could be obtained using angular particles instead of spherical (see Figure 2.28). The failure modes were studied and concluded that spherical reinforcements led to failure through matrix debonding at the site of highest hydrostatic tension, at the top of the particle. The angular reinforcements accumulated hydrostatic tension at a higher rate, leading to fracture of the particles themselves and catastrophic failure of the material [135].

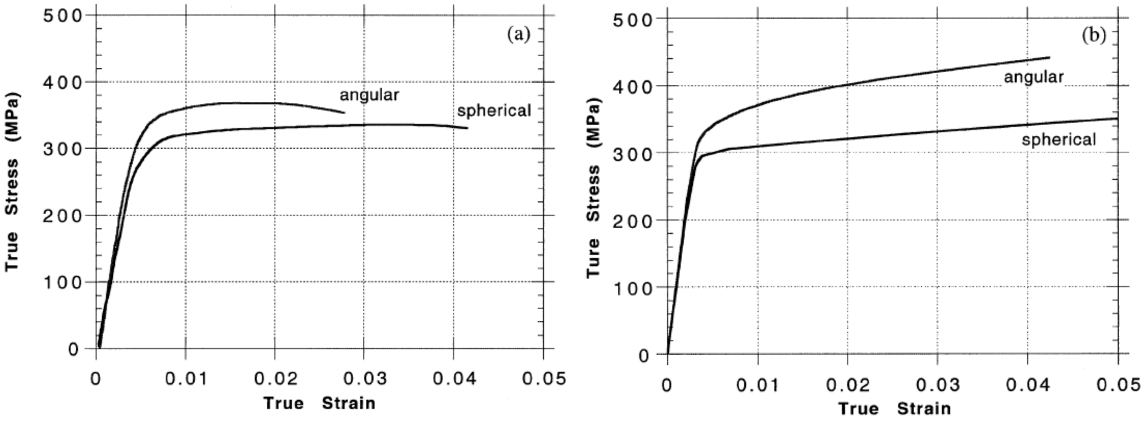

Figure 2.28 – Stress-strain relations derived in tension through experiments (left) and modeling (right) for Al-MMC materials of various reinforcement particle morphologies [135].

Chapter 3

Experimental techniques

As this is a manuscript-based thesis, each chapter is intended to stand alone as a published journal paper. Therefore, the specific experimental techniques for each chapter may be found as a section within that chapter. This chapter serves to offer more a detailed overview of each technique than what was appropriate for a journal publication.

3.1 Cold spray

For the work in chapters 4 and 5, the coatings were deposited by collaborators at NRC-Boucherville. Experimental details such as the choice of cold spray gun, deposition parameters, feedstock powder preparation, powder feed rate, inlet gas temperature, and sample porosity are provided in a previous publication [9]: "Pure Al powders [Alfa-Aesar] and Al-Al_2O_3 powder mixtures were cold sprayed onto mild steel and Al7075 substrates using a low-pressure cold spray system (SST, Centerline, ON, Canada). For all experiments, the inlet nitrogen gas temperature and pressure were fixed at 500° C and 0.62 MPa, respectively. The gun was held by a robot at a constant standoff distance of 1 cm and moved across the substrate surface at a transverse speed of 2 mm/s. The powder was fed at 8-12 g/min using an external powder feeder with nitrogen carrier gas at a flow rate of 3 L/min. Prior to deposition, the substrates were either grit blasted using 24 grit alumina or polished at 1200 grits [9]."

For the work in chapters 6, 7, and 8, four batches of composite feedstock powder were prepared by admixing commercially available spherical Al powder (Valimet H-15, d_{10}= 13.1 µm, d_{50}= 22.6 µm, d_{90}= 43.8 µm) with 10 and 50 wt.% of either angular morphology Al_2O_3 powder (Plasmatec, d_{10} = 14.2 µm, d_{50}= 25.5 µm, d_{90} = 34.2 µm) or a plasma spheroidized spherical morphology Al_2O_3 powder (Tekna, d_{10} = 15.0 µm, d_{50} = 24.3 µm, d_{90} = 39.3 µm). Coatings were deposited onto aluminum alloy AA6061 substrates using a Plasma Giken PCS-800 cold spray system, achieving a thickness of 4-5 mm. A nitrogen carrier gas was used at a 400° chamber temperature and 3 MPa chamber pressure. The 76.2 mm wide substrates were kept stationary and the gun nozzle moved at a 200 mm/s traverse speed with a 1 mm step size. Powder consumption was monitored *in situ* using digital scales upon which the powder hopper was mounted. Deposition efficiency was calculated by dividing the total mass of the deposited coating by the mass of powder sprayed.

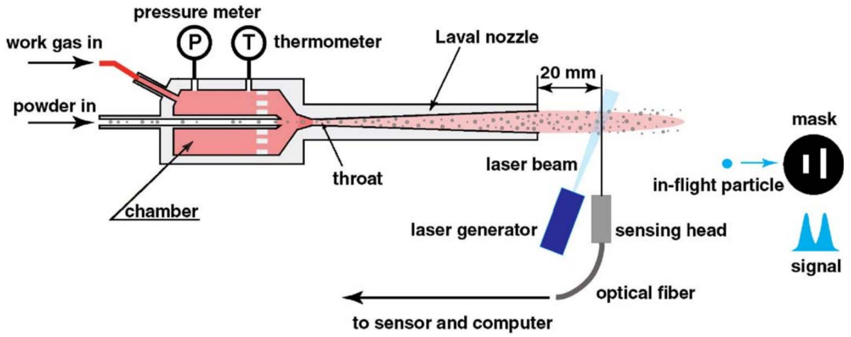

Figure 3.1 – Schematic diagram of the cold spray gun and DPV 2000 / ColdSprayMeter system used in the present study [53].

Powder velocity measurements were conducted using a commercially available ColdSprayMeter system (Tecnar, St-Bruno, QC). This system operates by illuminating a cold spray plume with a monochromatic laser, then focusing a fiber optic sensing head mounted on an X-Y-Z stage to region within the plume (see Figure 3.1). The sensing head is covered with a double-slit mask oriented such that a particle in focus will travel past first one slit then the other, with each passing resulting in a detectable light signal peak from the laser lumination. The resulting double peak in the signal is accepted as a particle if it meets a certain number of signal processing criteria [137]. From the distance between peaks, a time-of-flight measurement can be made of the particle velocity, and other parameters such as particle diameter can be calculated from the signal as well [137].

3.1.1 Confirming aluminum critical velocity and choosing deposition parameters

A batch of pure spherical aluminum powder (Valimet Al H-15), that had been previously opened several times over the course of roughly a year, showed unusually low deposition efficiencies in the spray parameter window recommended by Plasma Giken. Upon raising the nitrogen carrier gas temperature outside this window, deposition was successful. In contrast, a freshly opened batch of powder of the same lot showed successful deposition behavior in the recommended spray parameter window. It was expected, and later confirmed, that the older powder ("O-Al") had oxidized due to exposure to atmospheric oxygen and humidity. The newly-opened powder ("N-Al") had been kept sealed under the original inert atmosphere imposed by the manufacturer. To explore the deposition behavior associated with the new and old powders, a small study was carried out to measure the powder critical velocity. The oxygen content in the powders as measured by inert gas fusion was 0.231 wt.% for N-Al and 0.673 wt.% for O-Al.

Powders O-Al and N-Al were cold sprayed onto mild steel substrates using a commercially available system (PCS-1000, Plasma Giken). The inlet nitrogen gas pressure was fixed at 3 MPa, while the gas temperature was varied between 200, 300, 400, 500, and 600° C. Powder was fed into the gun from an external hopper at a rate of 13.3 ± 2.0 g/min (n=4) through a low temperature nitrogen gas line pressurized to 3.3 MPa. The 76.2 mm wide substrates were held by a robotic arm at a constant standoff distance of 5 cm from the nozzle and moved at a traverse speed of 200 mm/s. Each coating was deposited in 10 passes, with each pass consisting of 56 traverses separated by a step of 1 mm. Particle velocity measurements were taken at the center of the gas plume using a time-of-flight particle diagnostic system (see

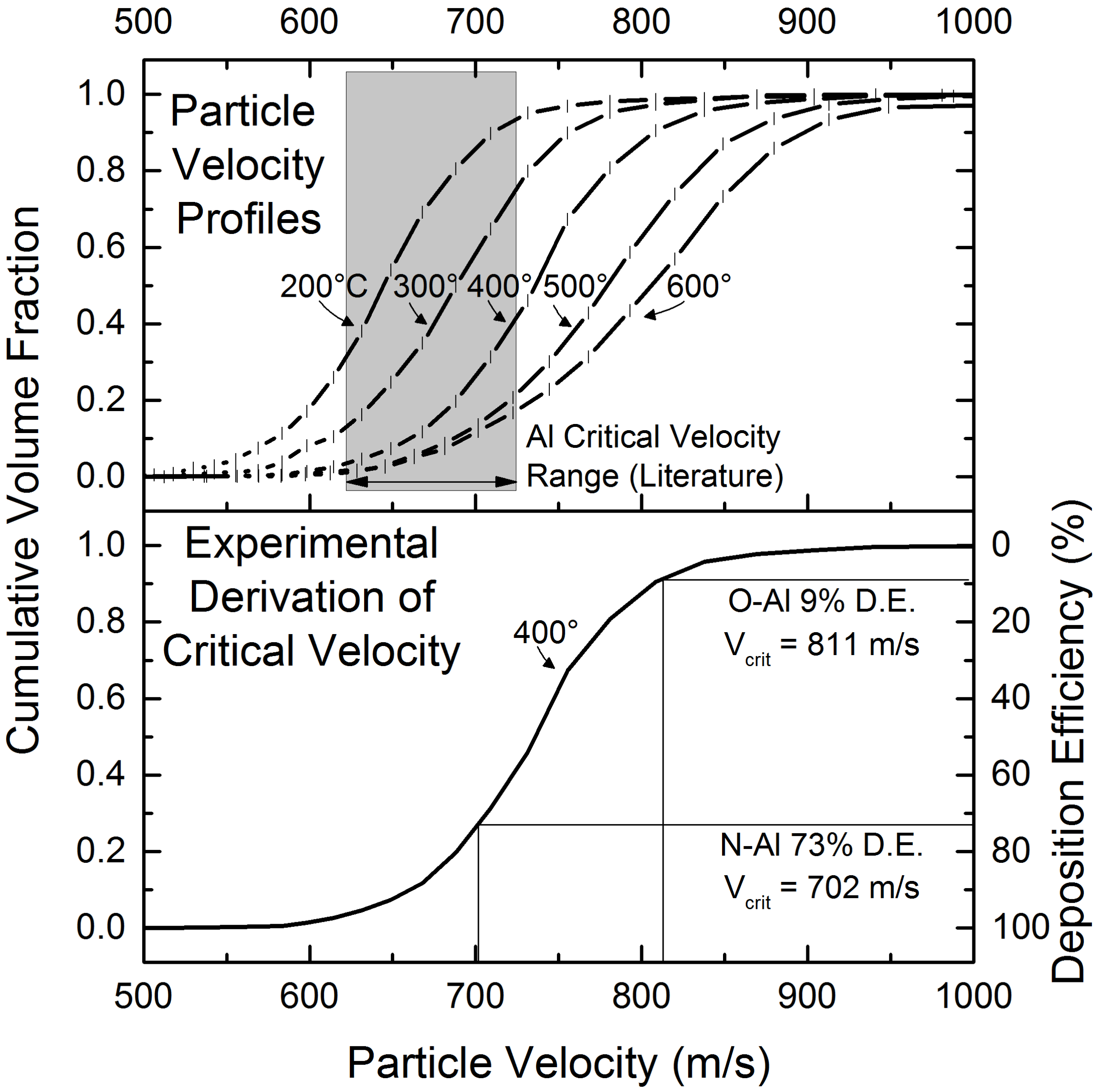

Figure 3.2 – Top: particle velocity profiles for Al powders (O-Al and N-Al) at the tested conditions, with each vertical dash representing a data point; the data points are shown connected by straight lines. Bottom: experimental derivation of critical velocity, where the deposition efficiency is assumed to directly correspond to the fraction of particles exceeding the critical velocity. For the given velocity profile at 400° C, the lower deposition efficiency of powder O-Al compared to N-Al corresponds to a higher critical velocity. This was due to the thicker oxide/hydroxide shell.

Figure 3.1).

The sigmoidal particle velocity profiles showed that as N_2 preheat temperature increased, the velocity increased, as expected (see Figure 3.2). No difference in velocity was measurable between powders O-Al and N-Al. The velocity profiles overlap the range of aluminum critical

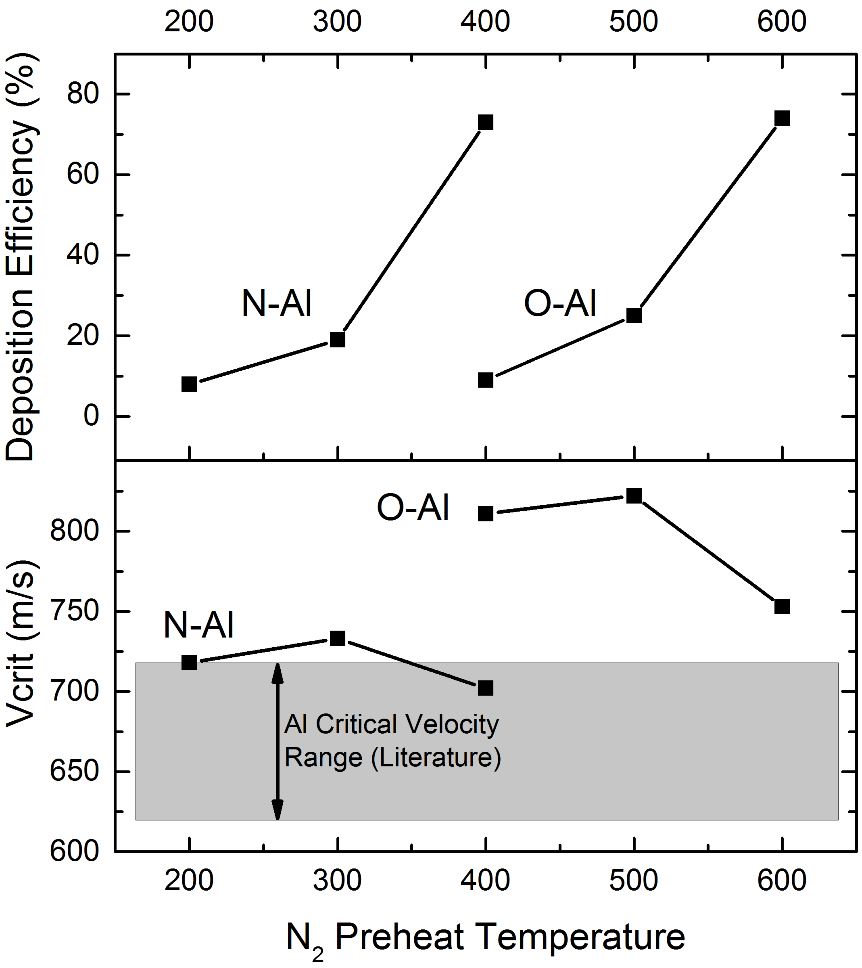

Figure 3.3 – Top: particle velocity profiles for Al powders (O-Al and N-Al) at the tested conditions. Bottom: experimental derivation of critical velocity.

velocities typically (620-720 m/s), both experimentally measured and predicted through simulations [48, 50, 138]. Deposition efficiencies varied between about 10% to 75% (see Figure 3.3). From each sigmoidal particle velocity curve, the critical velocity at each condition was derived from the deposition efficiency on the assumption that any particles travelling faster than the critical velocity would embed, and any going slower would rebound (see Figure 3.2, bottom) [9]. For powder N-Al, the measured critical velocities were within or near the upper range of previously determined criical velocities (see Figure 3.3, bottom). For powder O-Al, at the 400 and 500ºC conditions the critical velocities were above 800 m/s, while at 600ºC it was roughly lower at roughly 750 m/s. The lower critical velocity at 600° may be partly due to higher levels of thermal softening of the powders at this spray condition, considering how close the deposition temperature is to the melting point of pure aluminum (roughly 660°C [139]).

Of practical importance for the purpose of this thesis, the deposition temperature of 400°C was selected in order to obtain the maximum possible deposition efficiency for the metal matrix composites being deposited in subsequent chapters.

3.1.2 Table of materials sprayed

The following samples were used in chapters 4 through 8 of this thesis.

Sample designation	Al in feedstock (wt.%)	Al manufacturer	Al_2O_3 in feedstock (wt.%)	Al_2O_3 morphology (manufacturer)	Deposition parameters
CS0 (Ch. 4-5)	100	Alfa Aesar	0	n/a	SST, 500°C, 0.62 MPa
CS10 (Ch. 4-5)	90	Alfa Aesar	10	Angular (Plasmatec)	SST, 500°C, 0.62 MPa
CS22 (Ch. 4-5)	50	Alfa Aesar	50	Angular (Plasmatec)	SST, 500°C, 0.62 MPa
CS0 (Ch. 6-8)	100	Valimet H-15	0	n/a	PG, 400°C, 3 MPa
ANG10 (Ch. 6-8)	90	Valimet H-15	10	Angular (Plasmatec)	PG, 400°C, 3 MPa
ANG22 (Ch. 6-8)	50	Valimet H-15	50	Angular (Plasmatec)	PG, 400°C, 3 MPa
SPH3 (Ch. 6-8)	90	Valimet H-15	10	Spherical (Tekna)	PG, 400°C, 3 MPa
SPH11 (Ch. 6-8)	50	Valimet H-15	50	Spherical (Tekna)	PG, 400°C, 3 MPa

Table 3.1 – The materials used in this thesis. "SST" refers to the Centerline SST cold spray system and "PG" refers to the Plasma Giken high pressure cold spray system.

3.2 Dry sliding wear tests

Sliding wear tests were performed using a custom built ball-on-flat tribometer (see Figure 3.4). The specimen holder and cantilever arm holding the counterface were enclosed in a bag in which the humidity and temperature were monitored using a thermohygrometer. Dry air was supplied to the bag using compressed air first passed through a filter regulator and then passed through a desiccant dryer. Tests were conducted in dry air (below 1% relative humidity) at room temperature (21-24° C). For blind tests (those not conducted in the *in situ* configuration) the cantilever arm was fitted with either polycrystalline alumina spheres or monocrystalline alumina (sapphire) spheres of 6.35 mm diameter to serve as counterfaces. For tests in the *in situ* configuration, a transparent sapphire hemisphere of 6.35 mm diameter was used as the counterface, which was mounted in a bezel permitting direct observation of the sliding interface through the sapphire [140]. Microscopic observation of the sliding interface was performed using an optical microscope mounted directly above the sapphire hemisphere, equipped with a 10x objective lens and a commercial camcorder. The camera was connected to picture-in-picture box which inserted the cycle number and average friction coefficient into the upper-left hand corner. The composite signal was then recorded using a commercial digital video recorder. All tests were conducted with a sliding speed of 3 mm/s, a track length of 10 mm, and normal load of 1 N (102 gram-force). Normal loading was accomplished by applying deadweight loads to the cantilever arm. Friction forces were measured at a sampling rate of 800 Hz using a piezoelectric sensor mounted underneath the sample stage.

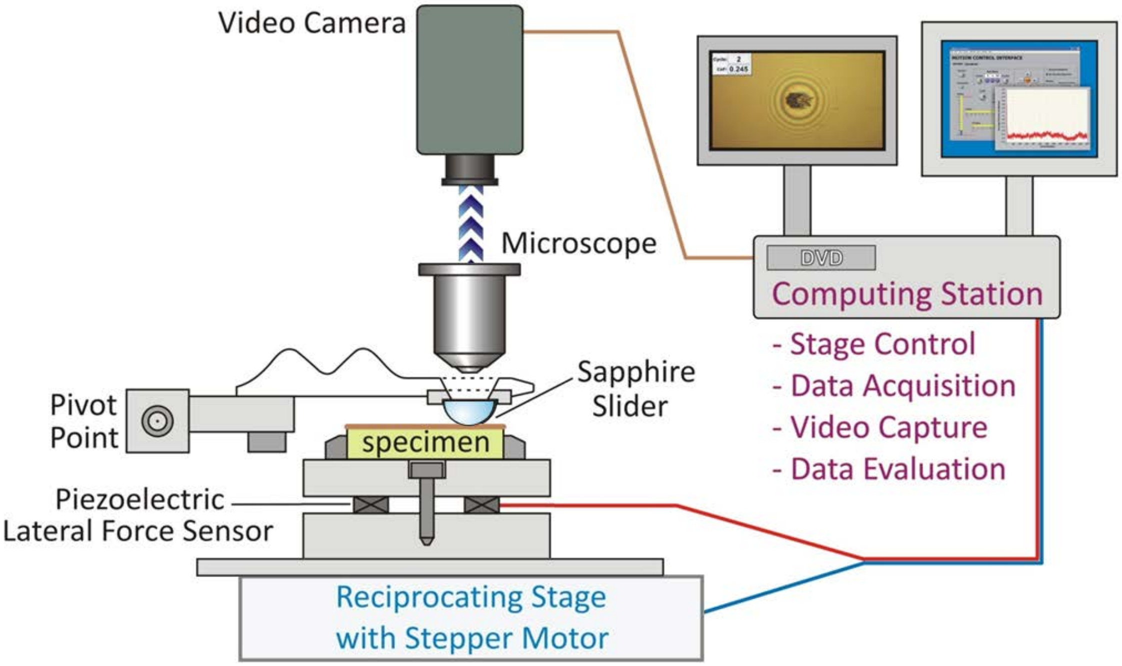

Figure 3.4 – Schematic diagram of the tribometer in the *in situ* setup used for this thesis, courtesy of Holger Strauss [140].

3.3 Characterization

Cross-sections of each coating were prepared for analysis by sectioning using a diamond wafering saw, cold mounting in epoxy, fine grinding using 400, 800, 1200, and 2400 grit sizes, and polishing using 9 µm, 3 µm and 1 µm diamond pastes followed by 0.05 µm colloidal silica. The concentration of Al_2O_3 recovered in each coating was measured by image analysis, during which ten random images of polished cross-sections were taken in a scanning electron microscope (SEM) and analyzed by pixel count to calculate volumetric the Al_2O_3 concentration, which was converted to mass concentration. Prior to wear testing, the coating surfaces were subjected to fine grinding to a root mean square roughness of less than 1 µm and cleaned with ethanol. Microhardness measurements were taken using a Vickers indenter applied at a 200 gf (1.96 N) load with a hold time of 5 seconds, and each hardness value reported here shows the average of at least ten indents taken at random locations on the polished coatings.

Using an SEM, wear track surface features were observed and chemical elemental contrast was revealed by energy dispersive x-ray spectroscopy (EDXS). Surface morphologies of the wear tracks and counterface transfer material were extracted using a Wyko NT8000 optical interferometer. Open source SPM analysis software Gwyddion v2.33 was used to process the data taken from the interferometer. All unresolved data points were interpolated using a Laplace algorithm, after which line profiles 100 µm apart were extracted (see Figure 3.5). Between 80-100 surface profile measurements per wear track were obtained.

Wear rates were calculated in accordance with ASTM Standard G99 [101] by first integrating height profiles across the wear track above and below the original surface height to calculate a net worn cross-sectional area. This was then multiplied by the wear track length to obtain a net volume of material removed from the surface. The worn area was then divided by the total sliding distance and normal force, resulting in units of $mm^3/N/m$.

Sub-surface regions of the worn surfaces were revealed by cross-sectioning. Wear tracks were cut transverse to the sliding direction using a lubricated slow-speed abrasive cutting

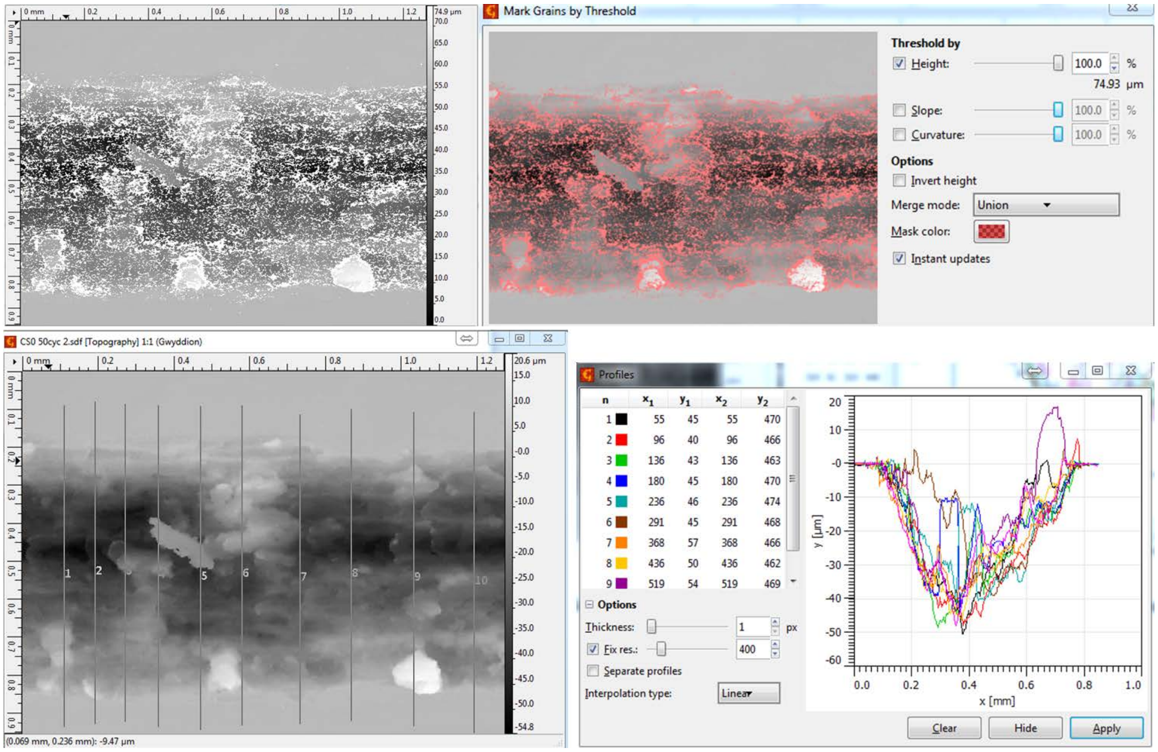

Threshold by

☑ Height: 100.0 %

74.93 µm

☐ Slope: 100.0 %

☐ Curvature: 100.0 %

Options

☐ Invert height

Merge mode: Union

Mask color: ▨

☑ Instant updates

n	x_1	y_1	x_2	y_2
1 ■	55	45	55	470
2 🟥	96	40	96	466
3 🟩	136	43	136	463
4 🟦	180	45	180	470
5 ■	236	46	236	474
6 🟫	291	45	291	468
7 🟧	368	57	368	466
8 🟨	436	50	436	462
9 🟪	519	54	519	469

Options

Thickness: 1 px

☑ Fix res.: 400

☐ Separate profiles

Interpolation type: Linear

Figure 3.5 – Processing a wear track using Gwyddion. Top left: section of a wear track data file from the interferometer with white pixels representing unresolved data points. Top right: the unresolved data points are marked with a pink mask and then calculated using a Laplace interpolation algorithm. Bottom left: after three-point leveling, the individual line profiles are drawn 100 µm apart on the wear track. Bottom right: the overlapping profiles are shown, then are output to a .txt file.

wheel, followed by cold mounting in epoxy and mechanical polishing. Microstructural analysis was carried out in an SEM with a backscattered electron detector to reveal aluminum grains through electron channeling contrast imaging (ECCI).

3.4 Nanoindentation

Nanoindentation was used to measure the mechanical properties of the third body material in the wear track and was performed using a Hysitron Triboindenter. This particular technique was chosen because it permits extremely localized measurement of mechanical properties (as low as a few dozen nanometers), permitting measurements on small quantities of material in comparison with conventional microhardness techniques [141]. The Triboindenter system was equipped with a capacitive transducer, a piezoelectric scanner permitting for "Imaging Mode" scanning probe microscopy (SPM), and an optical micorsope. A diamond indenter of Berkovich geometry was used (see Figure 3.6).

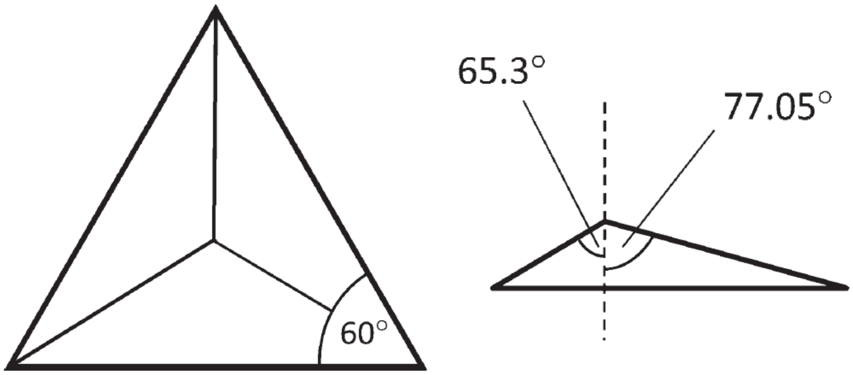

Figure 3.6 – Geometry of a Berkovich tip [141].

The capacitive transducer is the primary component of the machine as it permits the precisely controlled loading and displacement of the indenter tip into the sample, from which hardness and modulus values can be obtained. The transducer consists of three plates (see Figure 3.7) [141, 142]. The top and bottom plates are stationary and each carries an alternating current 180° out of phase with the other, and the middle plate holds the indenter tip and is suspended by springs. The opposite signs of the top and bottom plates create an electric field potential equal to zero in the centerpoint between the plates and varying linearly as a function of distance between the two plates. The center plate assumes the same potential present at its position between the plates, and by measuring its signal, the displacement of the center plate (and hence the indenter) can be measured. When a voltage bias is applied to the AC signal in the bottom plate, this creates an electrostatic force in the center plate that pulls it toward the bottom plate. In this way, load can be applied to the center plate (and hence the indenter) [141, 142]. The force on the tip is calculated based on two parametres: the position of the center plate and the electrostatic force applied by the bottom plate. Since the center plate is suspended by springs of a known spring constant, the force they exert on the plate may be calculated by Hooke's law. If the spring force and the electrostatic force are not perfectly equal, the difference is loading at the indenter tip.

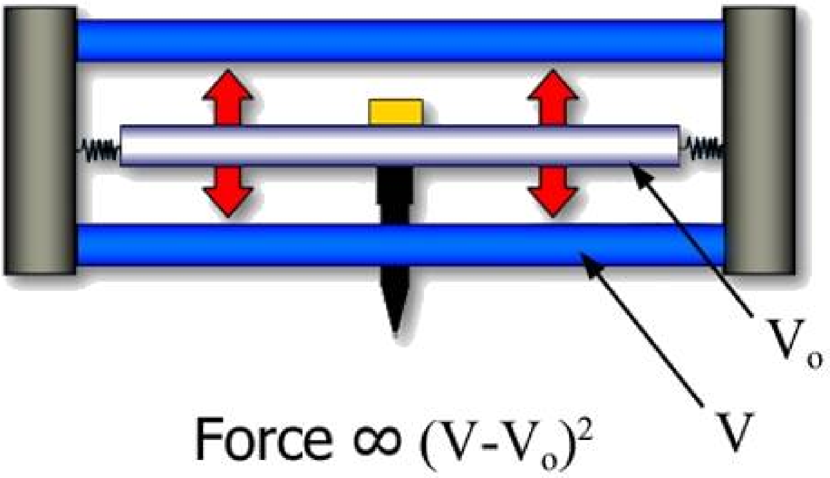

Figure 3.7 – Schematic diagram of a capacitive transducer used for quasi-static indentation in Hysitron systems [142].

Indentation was performed using a linear load function consisting of five seconds of loading time at a constant loading rate (in µN/s), five seconds of time held at maximum load, and five seconds of unloading time at a constant unloading rate. This process results in a characteristic load-displacement curve (see Figure 3.8).

To calculate the hardness from nanoindentation the Oliver and Pharr technique was used, which is described as follows [143]. The tangent of the unloading curve at its maximum slope is measured and used to calculate the stiffness S (see Figure 3.8):

$$S = \frac{dP}{dh} = \frac{2}{\sqrt{\pi}} E_r \sqrt{A} \tag{3.1}$$

where E_r is the reduced modulus of the diamond indenter and the material indented (see Equation 2.6), and A is the projected area of contact of the indentation. The projected area A is related to the contact depth h_c of the indenter according to the indenter area function:

$$A(h_c) = 24.5h_c^2 + C_1h_c^1 + C_2h_c^{1/2} + C_3h_c^{1/4} + ... + C_8h_c^{1/128} \tag{3.2}$$

where 24.5 is the coefficient for a perfect Berkovich indenter and the additional terms

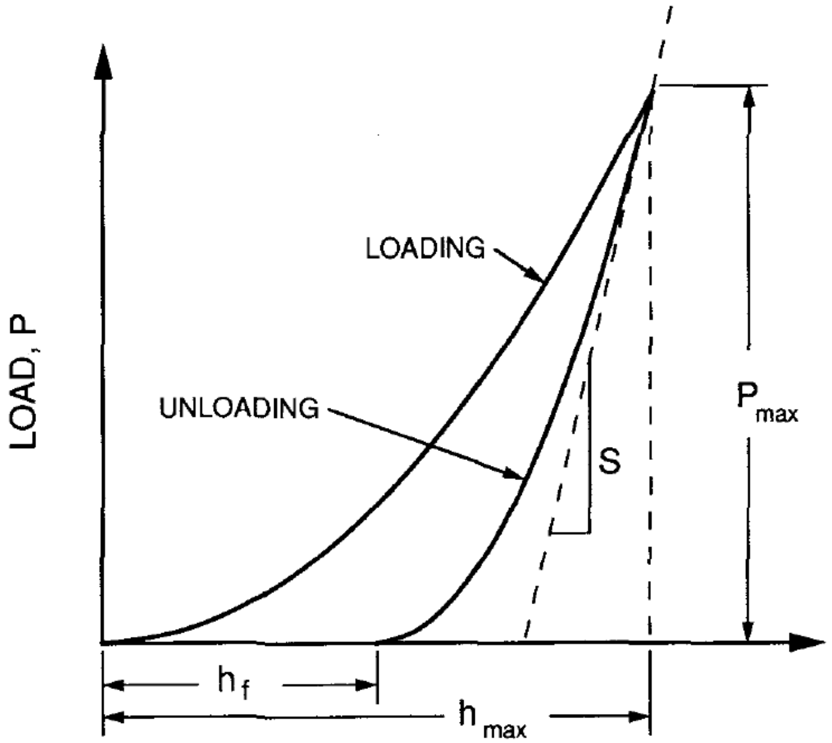

Figure 3.8 – A load-displacement curve from nanoindentation, from which the Oliver and Pharr method can be used to calculate hardness and reduced modulus [143].

account for the defect radius of the tip. The area function is calculated from a series of indents at varying load on fused quartz, which has a known elastic modulus [142]; the indenter tip was periodically checked against fused quartz and the area function is recalibrated as the tip defect radius grows with increasing use. The contact depth h_c is calculated as follows:

$$h_c = h_{max} - 0.75\frac{P_{max}}{S} \tag{3.3}$$

where h_{max} is the maximum indenter depth and P_{max} is the maximum load. Accordingly, hardness is calculated as follows:

$$H = \frac{P_{max}}{A} \tag{3.4}$$

.

3.5 High pressure torsion

Sample preparation was carried out by first performing wire cut electrical discharge machining (EDM) to obtain cylinders of approximately 6 or 12 mm diameter, which were then filed to be within ± 0.1 mm of the target diameter measured using digital calipers. Tubes of scrap aluminum alloy were machined with a lathe to have an inner diameter maching that of the outer diameter of the cylinders, and then the cylinders were put inside using a mallet. Then using a water-cooled wafering saw, disks 0.6 or 0.8 mm thick were cut. By mounting the cylinders inside tubes, the burr that inevitably formed during cutting was on the tubes rather than on the sample material (see Figure 3.9). After cutting, samples were subjected to fine grinding using water-lubricated P2400 grit silicon carbide paper to sample thicknesses of 0.55 to 0.75 mm, after which they were further ground at P3200 and P4000 grit.

Anvils of WC-Co were prepared by machining to the desired dimensions, then polished in a circular or figure-eight motion using P4000 metallographic grinding paper lubricated a 15 µm water-based diamond suspension. At the end of polishing, two final polishing strokes were made in straight lines, one 90° to the other, in order to leave fine scratches on the surface. A stylus line profilometer was used to confirm that the roughness (Ra) was roughly 0.2 µm. Anvils and samples were degreased in an ultrasonic bath, first in heptane and then in ethanol.

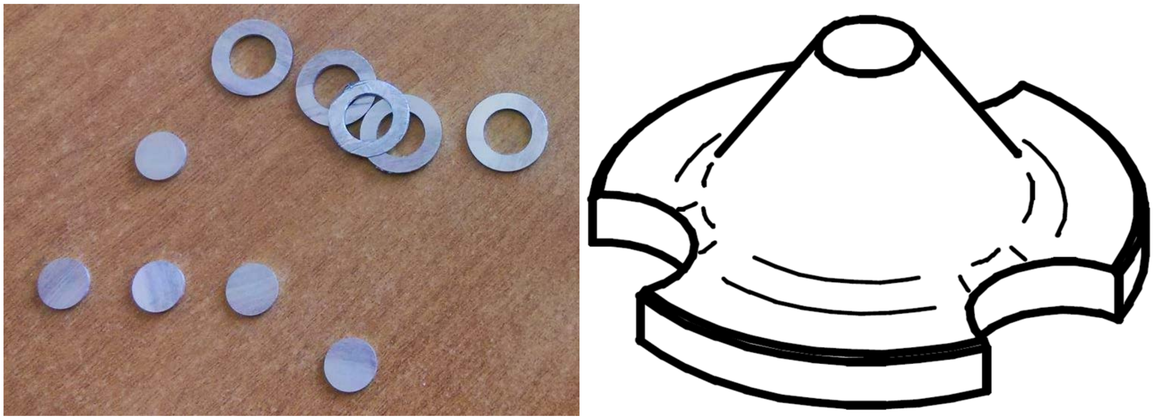

Figure 3.9 – Left: HPT disks of a sample, with their outer rings (photo taken by the author). Right: schematic diagram of a RHEOS anvil of conical geometry (courtesy of Edouard REGIS, LaMCoS, INSA-Lyon).

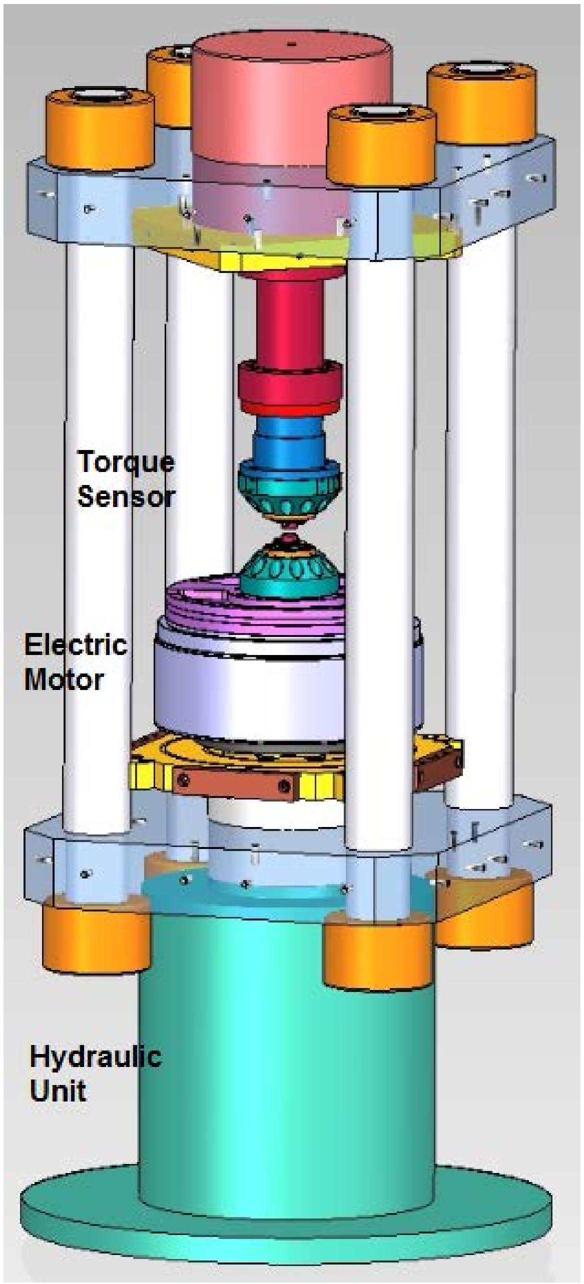

Figure 3.10 – Schematic diagram of RHEOS (courtesy of Edouard REGIS, LaMCoS, INSA-Lyon).

HPT tests were conducted a custom-built test rig named "RHEOS" (RHEOlogy of Solids) at LaMCoS, INSA-Lyon (see Figure 3.10). Normal loading was accomplished using a hydraulic pump and was maintained during testing by a force feedback loop, while rotation was induced using an 8 kW electric motor. The prepared pucks were placed between two WC-Co anvils of 6 or 12 mm diameter, such that tests were conducted in the unconstrained condition [35] (see

Figure 3.11).

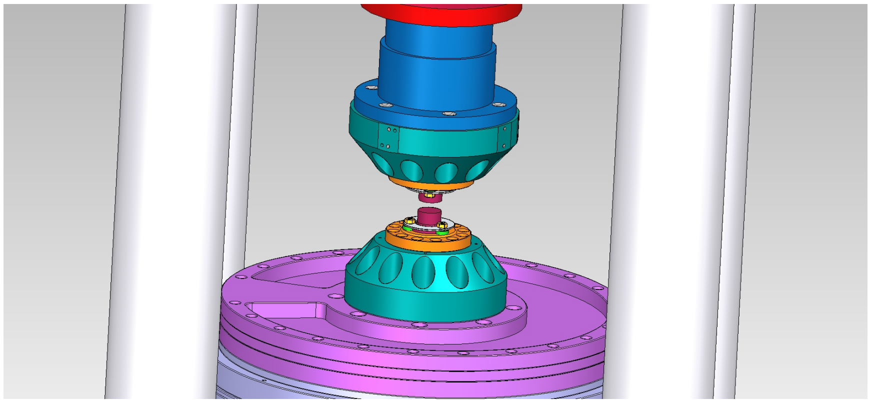

Figure 3.11 – Detail image of anvils, motor, and torque sensor assembly of RHEOS (courtesy of Edouard REGIS, LaMCoS, INSA-Lyon).

After loading to a desired superficial contact pressure, rotation to 180º was carried out at 0.5 or 0.05 RPM. Torque measurement during testing was accomplished using a static torque sensor at an acquisition rate of 50 Hz. Vertical displacement was measured using three inductive sensors, each with an accuracy of 0.01 mm, spaced 120° apart around the axis of rotation. The standard operating procedure (SOP) for RHEOS can be found in Appendix A. The evolution of torque, rotation angle, and sample thickness during HPT were converted into von Mises equivalent stresses and shear strain at the external radius using the Fields and Backofen [113] method:

$$\sigma = \sqrt{3}T\frac{(3+M+N)}{2\pi a^3} \tag{3.5}$$

$$\varepsilon = r\vartheta/\sqrt{3}h \tag{3.6}$$

where ϑ is the rotation angle, T is the measured torque, h is the measured sample thickness, $M = \delta lnT/\delta ln\dot{\vartheta}$is the rotation rate sensitivity of the torque, and $N = \delta lnT/\delta ln\vartheta$ is the rotation sensitivity of the torque. The parameter N was calculated on a local basis for each data point and M was set to zero given that tests were conducted at room temperature [112, 115].

Chapter 4

In situ tribometry of cold sprayed Al-Al_2O_3 coatings

J.M. Shockley, H.W. Strauss, R.R. Chromik, N. Brodusch, R. Gauvin, E. Irissou, J.-G. Legoux

Adapted from a paper of the same title published in *Surface and Coatings Technology* **215** (2013) 350–356.

Abstract

An *in situ* tribometer utilizing a transparent hemispherical counterface was used to conduct sliding wear tests on Al-Al_2O_3 composite coatings deposited by cold spray. Direct observation of the wear interface via the slider allowed for correlation to be identified between the formation of transfer film and friction changes, wear rates, and the evolution of subsurface structures. It was revealed that the presence of hard particles in the Al-Al_2O_3 coating stabilized the transfer film, characterized by less plastic flow and fewer instances of hole formation at the interface. This increase in stability correlated with lower wear rates, stable friction, and the formation of a mechanically mixed layer (MML) in the worn subsurface.

4.1 Introduction

The low density, high thermal conductivity, and inherent corrosion resistance of aluminum and many of its alloys make them attractive as coating materials. However, the tribological performance of these materials is too poor for many applications, unless the alloy is chosen judiciously or the matrix is reinforced using hard secondary phases such as Al_2O_3 or SiC particles [1]. Such aluminum metal matrix composite (Al-MMC) materials have become popular as bulk materials for their enhanced stiffness and wear resistance compared to the unreinforced matrix material [1–3]. For coating applications, Al-MMC materials may be deposited by various techniques and, among them, the cold spray process has been noted for its rapid deposition of coatings with low porosity and high purity [4–8]. The production of so-called "thick" tribological MMC composite coatings by way of cold spray has been investigated in recent years [9–23].

In the mild wear regime, Al-MMC materials typically exhibit sliding wear rates that are several orders of magnitude lower than the unreinforced metal [24–26]. In a study on a cold sprayed Al-Al_2O_3 composite, the decrease in wear rate was found to extend up to five orders of magnitude, with little influence of post-deposition heat treatment [11]. Notably, tribological studies of metallic materials have found that wear rates may not correlate only with bulk strength and hardness, but also with the formation of third bodies such as the mechanically mixed layer (MML) [24, 26, 29]. The action of material mixing and transfer between surfaces is central to the metallic wear process. This has been evidenced by microstructural studies of MMLs, which are often found to be nanostructured and contain material from both of the mechanically contacting faces [29–32]. Furthermore, sudden changes in friction or wear behavior may be attributed to detachment of transfer material during the wear process [32,33]. The presence of hard particles in Al-MMC materials strongly influences the mechanisms of mixing and transfers during sliding, which in turn influence the friction and wear rates [25,34].

Modern understanding of metallic friction and wear comes almost entirely from *ex situ* analysis of worn surfaces. The theories of transfer films and mechanical mixing during sliding wear of metals come from conventional tribometry that excludes direct observation of the sliding interface. While considerable knowledge has been generated by these means, it was suggested by Blau that our understanding of the tribology of metals would greatly benefit from the development of *in situ* methods to observe the sliding interface more directly [33]. In recent years, various techniques of *in situ* tribometry have been developed in which one of the contact partners is a transparent material, permitting direct observation of the sliding interface [140,144]. Past work of *in situ* tribometry includes studies of hard coatings [145–147] and solid lubricant coatings [148–150]. *In situ* methods applied to metallic wear are made somewhat difficult due to the high adhesion of metals, but, nevertheless, any successful implementation of *in situ* methods could address some uncertainty in current understanding due to inferences made from *ex situ* methods. Direct examination of sliding wear in metals would allow for correlating the evolution of transfer film to friction, wear rates, and the evolution of subsurface structures [33]. Also, it would permit study of the evolution of bearing area over time, which dictates the true contact stress [151]. Yet aside from a few *in situ* tribometry studies of metal-doped thin film coatings [146,148] and lubricated contact on steel balls [152] the use of *in situ* techniques on metallic systems remains largely unexplored.

In the present study, a ball-on-flat *in situ* tribometer with a sapphire counterface was used to perform sliding wear tests on cold sprayed Al-Al_2O_3, with weight fractions of the latter ranging from 0 to 22 wt.%. The *in situ* analysis allowed direct observation of the evolution of transfer at the interface, and *ex situ* analysis of wear rates and subsurface structures was performed.

4.2 Experimental

One pure Al and two composite Al-Al_2O_3 coatings 400–600 µm thick were deposited onto mild steel substrates by cold spray. Experimental details such as the choice of cold spray gun, deposition parameters, feedstock powder preparation, powder feed rate, inlet gas temperature, and sample porosity are provided elsewhere [9]. The three coatings contained 0 wt.%, 10.2 ± 1.8 wt.%, and 22.6 ± 2.9 wt.% Al_2O_3, respectively, leading to the designations of CS0, CS10, and CS22 used throughout this work (see Table 4.1). The content of Al_2O_3 in the coatings was determined by image analysis. Ten random images of polished cross-sections were collected for each sample in a scanning electron microscope, then analyzed by pixel count to calculate the Al_2O_3 volume fraction [9]. Porosity was calculated by the same technique and was less than 2% in all samples [9]. Prior to wear testing, the coating surfaces were polished to a root mean square roughness of 600 nm and cleaned with acetone.

Sliding wear tests on the composite coatings were performed in dry air (below 2% relative humidity) at room temperature (21–24° C) using a custom-built reciprocating tribometer [146]. All wear tests were conducted at a sliding speed of 3 mm/s and a track length of 10 mm. Friction forces were measured at a sampling rate of 800 Hz. Monocrystalline and polycrystalline forms of α-Al_2O_3 were used as counterface materials. For *in situ* tribometry tests, 6.35 mm diameter hemispheres made from transparent monocrystalline sapphire were used as counterfaces, which allowed for microscopic observation and video recording of the wear interface [140]. A commercially available camcorder and microscope adapter were employed in combination with a 10× objective lens. *In situ* tests were run to 1000 cycles. For wear testing at intermediate cycles, 6.35 mm diameter balls made from polycrystalline α-Al_2O_3 were used as counterfaces, and these tests were run to 10, 50, 100, and 500 cycles. The 6.35 mm diameter counterfaces were loaded onto the coatings to 1.0 N. In order to calculate the initial contact stress, the elastic moduli of the coatings were predicted to fall between the Reuss and Voigt bounds as a function of alumina content [153]. These were used to calculate a theoretical minimum and maximum range of average Hertzian contact at the beginning of wear testing (see Table 4.1) [73].

After wear testing, cross-sectional profiles of wear tracks were extracted using a Wyko NT8000 optical interferometer. Data points from the wear track above and below the original sample surface height were integrated to calculate a net worn cross-sectional area, then

Sample designation	Al_2O_3 in feedstock powder [9]	Al_2O_3 in deposited coating [9]		Range of initial average Hertzian stress	Mean wear rate by area at 1000 sliding cycles
	wt.%	wt.%	vol.%	MPa	$mm^2\ m^{-1}\ N^{-1}$
CS0	0	0	0	287	6.85×10−4
CS10	10	10.2 ± 1.8	7.0 ± 1.2	297-341	9.90×10−4
CS22	50	22.6 ± 2.9	16.1 ± 1.9	312-399	1.28×10−4

Table 4.1 – Characteristics of tested coatings.

multiplied by the wear track length to obtain a volume of worn material. As mass and volume measurements are a great source of uncertainty in wear rate calculations [154], an excess of 40 cross-sections were extracted per wear track. Sub-surface regions were prepared for study by cutting cross-sections of the wear tracks using a slow-speed abrasive cutting wheel, followed by cold-mounting, mechanical polishing, and argon ion milling. Scanning electron microscopy was carried out using a Hitachi Cold FE SU-8000 equipped with detectors for secondary electrons (SE), backscattered electrons (BSE), and energy dispersive X-ray spectroscopy (EDS). The photodiode BSE detector allowed for individual grains to be revealed by way of the electron channeling contrast imaging (ECCI) technique [155].

4.3 Results

4.3.1 Friction

The friction coefficient is plotted versus cycle number for coatings CS0, CS10, and CS22 in Fig. 4.1. The three friction plots show that each coating exhibited different behaviors. Coating CS0 was found to have the highest overall friction coefficient as well as the largest variations in friction behavior. After an initial spike above 1.1, the friction coefficient fluctuated periodically between roughly 0.5 and 0.9. Coating CS10 exhibited an initial friction spike above 0.95 followed by a short run-in period, after which the friction coefficient remained mostly between 0.5 and 0.6. Friction spiking was periodic in this coating as well, but the spikes were of lower magnitude (between 0.5 and 0.65) and occurred more often than in coating CS0. In contrast, coating CS22 showed a very short run-in period followed by steady state friction coefficient values between 0.55 and 0.7. A shift in steady state friction coefficient from roughly 0.7 to 0.55 occurred between cycle 500 and cycle 600. No periodic friction spiking occurred for coating CS22.

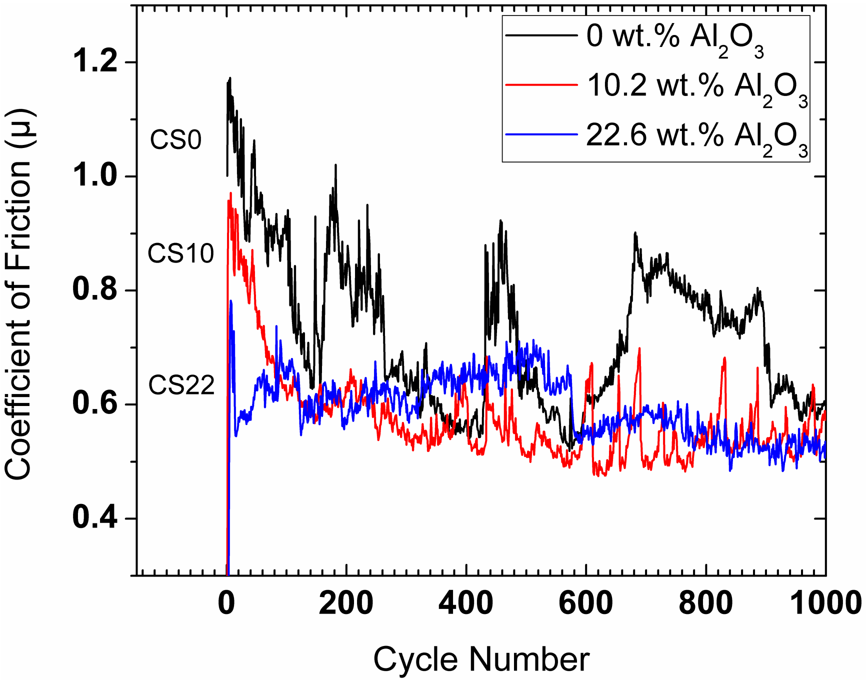

Figure 4.1 – Average friction coefficient versus cycle for the *in situ* tribometry tests on cold sprayed coatings CS0, CS10, and CS22.

4.3.2 Wear

The wear volumes calculated at the end of the 10, 50, 100, 500, and 1000 cycle tests were normalized to the sliding distance and are plotted as a function of cycle number in Fig. 4.2. For all three coatings, wear rates were highest at the beginning of the tests. The wear tracks of coating CS0 had the greatest variation of net cross sectional area, as evidenced by its wider error bars in Fig. 4.2. Wear behavior became more uniform as the concentration of hard particles in the coating increased.

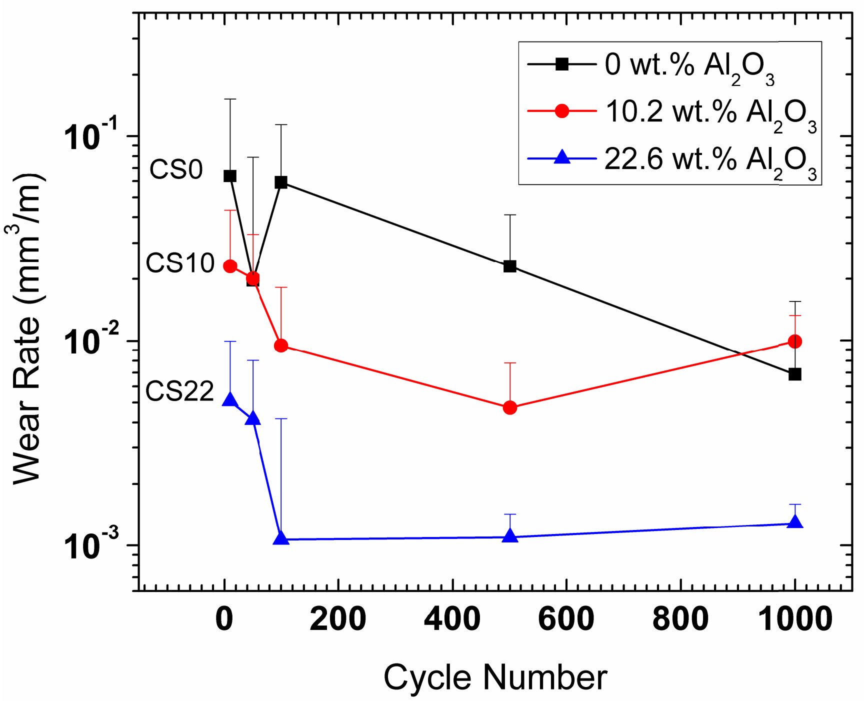

Figure 4.2 – Volumetric wear rate measured at 10, 50, 100, 500, and 1000 cycles. The error bars represent one standard deviation from the mean.

4.3.3 Subsurface microstructure

Electron micrographs of wear track cross sections were used to examine subsurface microstructure of coatings CS0, CS10, and CS22 (see Figs. 4.3, 4.4, and 4.5, respectively), each at 10, 100, and 1000 cycles. In the lower part of the micrographs for CS0 (see Fig. 4.3), microstructural features of the original unworn coating were visible. Grains of the aluminum matrix were resolved with ECCI and found to be equiaxed and generally smaller than 3 µm. The initial cold spray particle boundaries were visible as fine cracks in the matrix (e.g., Fig. 4.3 at 10 and 100 cycles). Dark phases in the unworn microstructure were either porosity in the coating (as in Fig. 4.3) or a combination of porosity and Al_2O_3 phases (as in Figs. 4.4 and 4.5).

In the upper part of the micrographs in Fig. 4.3, the near surface microstructure after wear is revealed for coating CS0. Grain refinement extended below the surface roughly 3 µm at 10 cycles and 10 µm at 100 cycles. After 1000 cycles, the depth of grain refinement

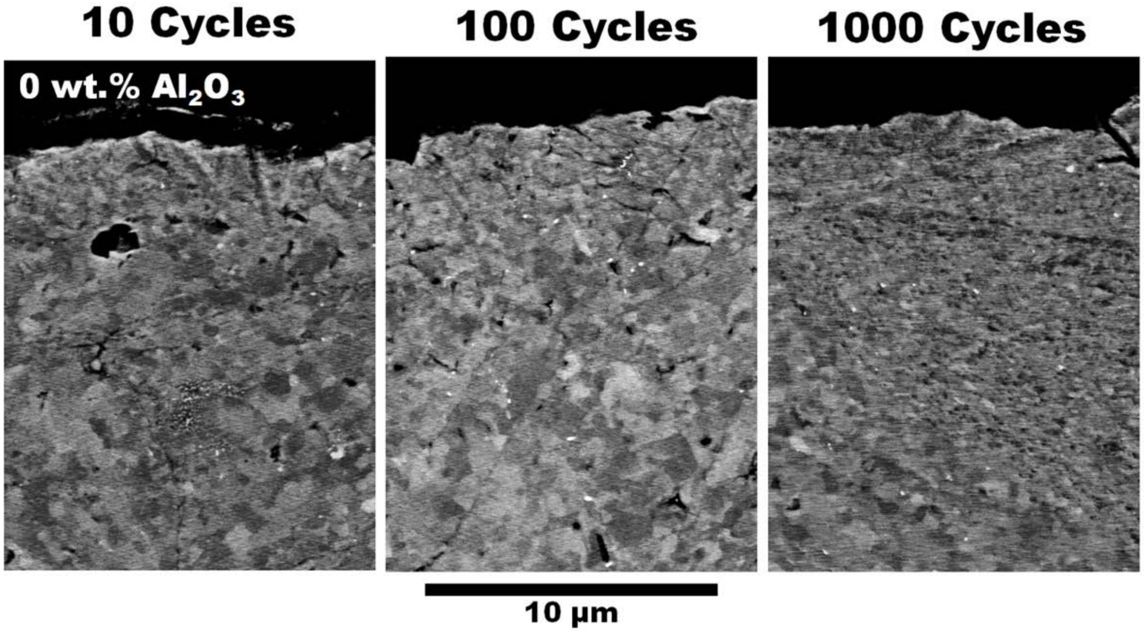

Figure 4.3 – BSE micrographs of the subsurface microstructure of sample CS0 after 10, 100, and 1000 sliding cycles.

remained within this range except in the center of the wear track, where it extended to greater than 20 µm. An increase in porosity was also observed in the regions with the greatest depth of grain refinement.

In coating CS10 after 10 cycles, the subsurface aluminum showed grain refinement to depths of 2–5 µm (see Fig. 4.4). However, at 100 cycles, the MML was evident and consisted of flake-like structures 6–10 µm thick visible across the wear track, many containing small cracks. Some regions of the flakes showed grain refinement, while other regions resembled undeformed aluminum grains. Dark phases within the flakes in Fig. 4 were identified as porosity or as oxygen-rich regions, indicative of Al_2O_3. After 1000 cycles, a similar flake-like MML was visible at the worn surface, but it was less coherent. In Fig. 4.4, only a small patch less than 5 µm in thickness is visible, surrounded by bare aluminum grains on both sides.

The cross-section of coating CS22 showed the formation of MML after the 10 cycles (see Fig. 4.5, white arrows). At the very top of the wear track surface after 10 cycles, some alumina particles roughly 1–3 µm wide are visible, along with unrefined aluminum grains and a patch of MML roughly 2 µm thick formed just above a larger particle of Al_2O_3. By 100

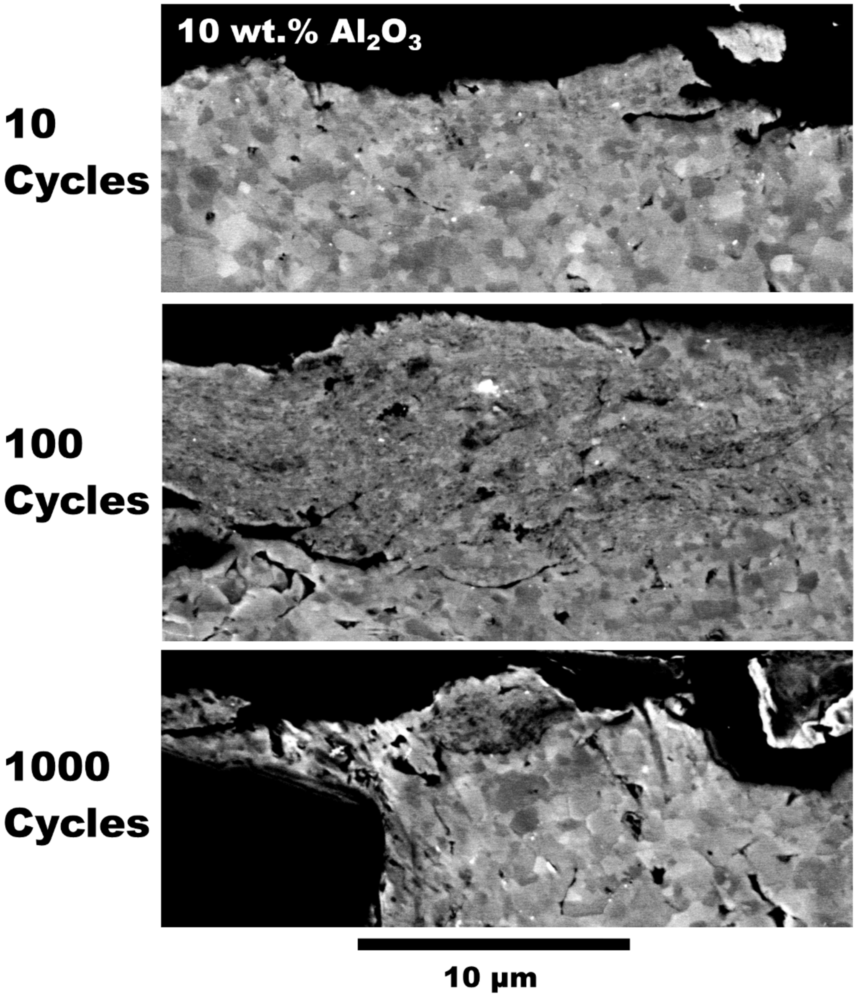

Figure 4.4 – BSE micrographs of the subsurface microstructure of sample CS10 after 10, 100, and 1000 sliding cycles.

cycles the wear track surface was covered in either Al_2O_3 particles or patches of MML 2–3 µm thick, and by 1000 cycles the surface was entirely covered by a MML of the same thickness (see Fig. 4.5, white dashed line). The MML at 1000 cycles showed higher oxygen content than that of 100 cycles as revealed by EDS. The higher oxygen content greatly decreased the contrast between the MML and the background, necessitating the use of SE imaging for the 1000 cycle wear track in Fig. 4.5.

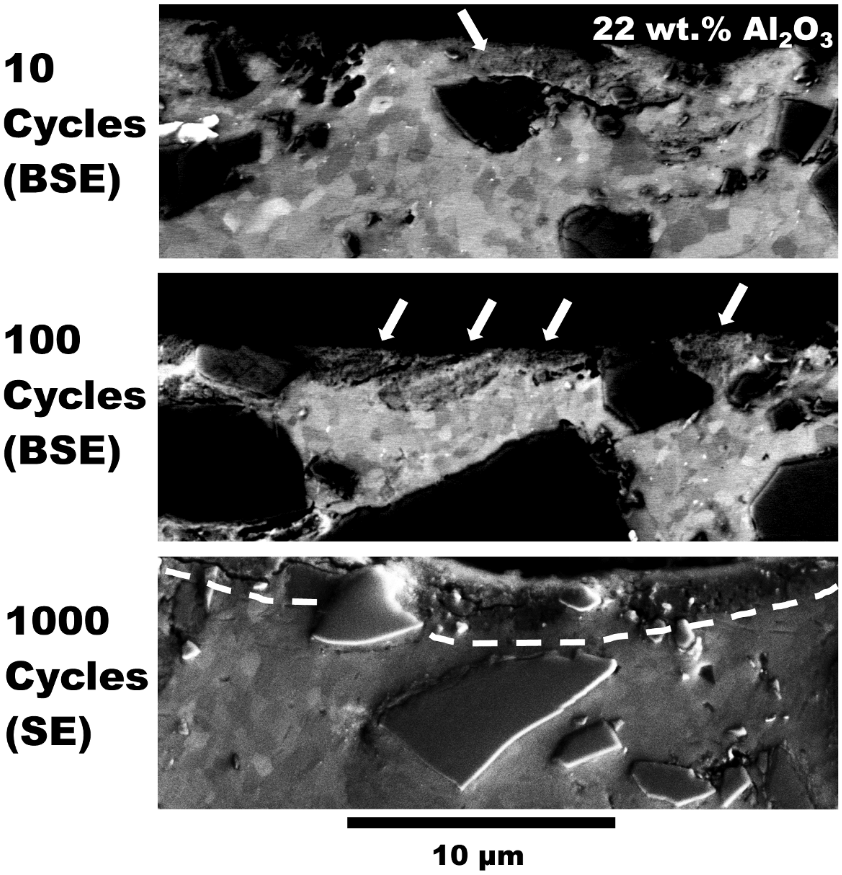

Figure 4.5 – BSE and SE micrographs of the subsurface microstructure of sample CS22 after 10, 100, and 1000 sliding cycles. White arrows show patches of MML at 10 and 100 cycles, while the dotted line shows the border of MML at 1000 cycles on the SE micrograph.

4.3.4 *In situ* micrographs

Optical observation through the sapphire counterface was used to identify changes in transfer film morphology during the tests (see Fig. 4.6). For all three coatings, a transfer film formed on the sapphire counterface within one to two sliding cycles (not shown). Before the formation of transfer film, the coefficient of friction was low, on the order of 0.15. Upon formation of transfer films, plastic flow of the matrix material was evident at the interface and the friction coefficient increased above 0.5 (see Fig. 4.1).

During the initial cycles on CS0, wear debris was plowed on the advancing slide of the slider and was deposited at the end of the wear track upon change of direction. By cycle 10, a transfer film had accumulated in the center of the contact region and remained present after changing direction (see Fig. 4.6a). The transfer film that formed was modified dynamically throughout the test as evidenced by plastic flow of third bodies, formation of holes in the transfer film, and subsequent healing of the holes with the adhesion of new material. The frequency of this activity decreased as the test went on, and this corresponded to a drop in friction coefficient in roughly the first 150 test cycles (see Fig. 4.1). During later testing cycles, hole formation was supplanted by scoring of the transfer film, occurring primarily across its center in the direction of sliding (see Fig. 4.6a, 1000 cycles). Throughout testing, periods of frequent hole forming and scoring activity of the transfer film correlated with friction coefficients in excess of 0.7.

The transfer film of coating CS10 exhibited greater stability than that of CS0. The hole formation for CS10 only occurred after several dozen cycles (see Fig. 4.6b) while for CS0 this process began within 5 sliding cycles. Also, throughout testing, the hole formation activity for CS10 was far less frequent and created smaller patches of holes than for CS0. The transfer film diameter of CS10 increased steadily throughout testing as did CS0, but at each cycle, the diameter for CS10 was smaller than that corresponding to CS0 (compare Figs. 4.6a and 4.6b). Scoring of the center of the transfer film was mostly absent during testing of CS10.

The transfer film for coating CS22 formed in the first 10 cycles and remained intact throughout most of the test (see Fig. 4.6c), which demonstrated greater stability than the transfer films of CS0 and CS10. Little plastic flow of the transfer film was visible even during the first 10 cycles, and the activity of hole formation and scoring across the center of the transfer film observed for CS0 was not present for CS22. However, during latter part of the test, fine dark score marks appeared above and below the transfer film and gradually abraded the original transfer film (see Fig. 4.6c, 999 cycles).

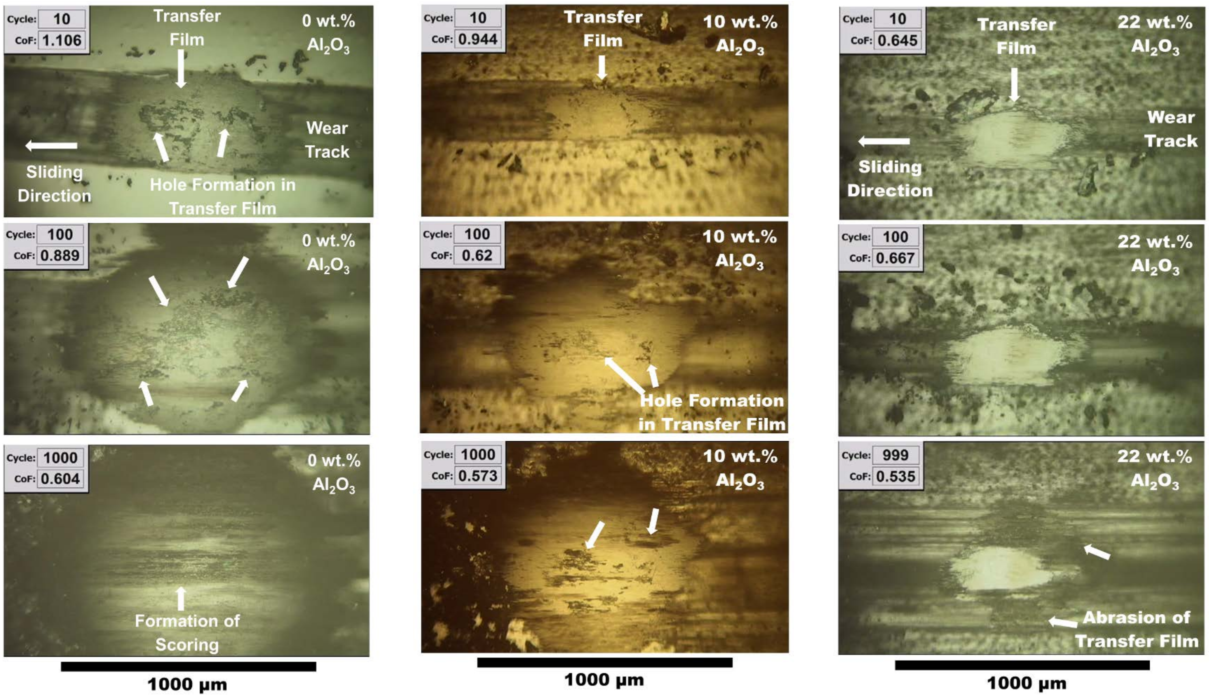

(a) (b) (c)

Figure 4.6 – *In situ* micrographs of coatings (a) CS0, (b) CS10, and (c) CS22 during the wear process. Arrows on the transfer films show (a and b) hole formation and scoring across the center of the transfer film and (c) abrasion at the edges of the transfer film. Plastic flow and hole formation of the transfer film were visible after 10 cycles, followed by a more continuous transfer film by 100 cycles.

4.4 Discussion

In the present study, three cold spray deposited Al-MMC coatings, reinforced with various concentrations of Al_2O_3 particles, were subject to sliding wear testing using an *in situ* tribometer. Friction and wear results showed that the presence of hard particles increased the stability of the friction coefficient and, when present in sufficient volume, lowered the volumetric wear rate by up to 2 orders of magnitude (see Figs. 4.1 and 4.2). These findings are in good agreement with previous studies on Al-MMCs reinforced with hard particles, which found decreases in wear rate between 1 and 3 orders of magnitude in the presently explored range of hard particle volume fraction [1, 11]. A previous study by Spencer et al. on a similar system found that at higher Al_2O_3 volume fractions than those studied in the present work, the decrease in wear rate could extend up to 5 orders of magnitude [11].

To further compare wear measurements in the present study to those in the previous study by Spencer et al. [11], a wear rate at 1000 sliding cycles, in units of $mm^2\ m^{-1}\ N^{-1}$, was calculated from the cross-sectional wear area, sliding distance and normal load (see Table 1). In the same units, the mean wear rates measured by Spencer et al. were roughly $6.6\times10{-}3$ $mm^2\ m^{-1}\ N^{-1}$, $1.3\times10{-}4$ $mm^2\ m^{-1}\ N^{-1}$, and $6.7\times10{-}5$ $mm^2\ m^{-1}\ N^{-1}$ for coatings of 0, 11, and 25 wt.% Al_2O_3, respectively [11]. Comparing the results from the two studies (see Table 1), the wear rates were similar for the composite coatings with similar content of Al_2O_3. While they differ by as much as a factor of 2, the agreement is quite good considering that the starting powders, cold spray systems, spray conditions, wear test parameters, and counterface materials were different. For the pure aluminum coatings, the wear rate of coating CS0 was roughly an order of magnitude lower than that measured for a pure aluminum coating by Spencer et al. This difference is somewhat significant, but may again be attributed to any number of differences between the two studies. Considering that the coatings fabricated by Spencer et al. were made using helium as the propelling gas and those made here used nitrogen, two factors influencing the coatings could be the particle velocity and the heat input to the particles [51]. It would be interesting to conduct a more direct comparison between coatings fabricated with the two methods to determine the cause for differences in wear rates.

Cross sections of wear tracks revealed subsurface changes as a function of hard particle content and sliding cycles. Neither the microstructure nor the compositions of the subsurface layers were exhaustively explored in this work, yet for all three samples, distinct features were observed. For the pure aluminum coating CS0, deformation and mechanical mixing caused near-surface grain refinement. The increase in the depth of this layer visible after 1000 cycles (see Fig. 3) was likely due to the formation of flake-like wear debris, which is typical of metallic wear [25,32,146]. The evolution of subsurface grain refinement to flake-like wear debris was also observed for coating CS10, yet it occurred more quickly, being visible after 100 cycles (see Fig. 4). This corresponded to a faster friction run-in period, more stable friction coefficient, and a faster decrease of wear rate compared to CS0. Yet at cycle 1000, both CS0 and CS10 exhibited similar wear rates. Thus, while the relatively small Al_2O_3 volume fraction of CS10 influenced transfer film, MML, and friction behavior during run-in, its efficacy for influencing long term wear performance seemed to be minimal.

In comparison to CS0 and CS10, the subsurface features of coating CS22 demonstrated evidence of MML formation as early as 10 cycles and it grew laterally to cover the wear surface (see Fig. 5). Fragmentation and size reduction of the reinforcement particles was evident during this process. The aluminum grains in the subsurface remained equiaxed and generally of similar size as in the bulk coating, suggesting that little deformation occurred below the MML. Correspondingly, the wear rates were lower than those of CS0 and CS10, remaining so throughout the test, and the friction coefficient was stabilized. This is in agreement with previous studies, showing that the formation of a thin, stable MML is responsible for the improved sliding wear performance of Al-MMC materials [1, 24, 25].

Observations of transfer films and third bodies by *in situ* tribometry were correlated to the friction, wear, and subsurface microstructure data. For the three coatings tested, the initial formation of transfer film occurred through plastic flow at the interface. For CS0, plastic flow at the interface decreased slowly from the first cycle until about 30 cycles into the test. Throughout the test, hole formation and scoring through the center of the transfer filmwere frequently observed, particularly during times of highermeasured friction. In light of the observed formation of flake-like structures in the middle of the wear track cross section at cycle 1000, it may be presumed that scoring through the center of the transfer filmwas linked to the formation or detachment of debris from the center of the wear track. For CS10, less activity such as plastic flow, hole formation, and scoring of the center of the wear track was observed, and this corresponded with lower wear rates during the early portions of the tests. During the later portion of the tests (last 100 cycles), the CS0 transfer film remained relatively stable and exhibited lower friction values with wear rates nearly identical between CS0 and CS10. For sample CS22, the initial plastic flow of the transfer film stopped within the first 5 cycles, yielding a stable transfer film that remained nearly unchanged after 100 cycles (see Fig. 8). During this same timeframe, the wear rate was observed to decrease by a factor of nearly 10 (see Fig. 2), and the MML was seen to grow from a few patches to a continuous layer (see Fig. 5). After the formation of a continuous MML, the CS22 wear rate remained low. The formation of fine scoring on the outside of the CS22 transfer film occurred primarily near the end of the test (see Fig. 8). The CS22 subsurface observed at this timewasmore heavily oxidized than at previous cycles, suggesting that the fine scoring was the abrasion of transfer film by hardened asperities of the MML. A previous study by Spencer on cold sprayed Al-Al_2O_3 showed that a shift from adhesive to abrasive wear occurred as the hard particle volume fraction increased [11]. This is corroborated in the present study by the observation of MML formation and transfer film abrasion at higher hard particle volume fractions. Meanwhile, coatings CS0 and CS10 showed a considerably more dynamic nature to the transfer film than CS22.

As a consequence of the *in situ* tribometer used for this experiment, the present study differs from more traditional tribological characterization of Al-MMC materials. For instance, many previous studies have used steel counterfaces [1, 11, 24, 26, 27] as opposed to the α-Al-Al_2O_3 used in this study. Consequently, iron has been typically found as a primary component of MML species, which was not the case here. While our experiments use a counterface material not typically found in engineering applications, the contact conditions can be thought of as more representative of sliding wear applications for Al. A metal-on-metal contact was created in all circumstances, with no concerns for iron contributions to the MML. However, for wear testing of bulk Al-MMC materials, pin-on-disk or pin-on-ring testing is often the preferred [1, 24, 34] tribometry method over ball-on-flat [11]. Also, our methods use a sliding velocity several orders of magnitude lower than many previous studies [1, 83], and thus far we have limited our experiments to much shorter sliding distances than most endurance type testing of Al and Al-MMCs. Nevertheless, there was good agreement between the friction, wear, and subsurface features observed by *ex situ* methods in the present study and those of previous tribological studies of Al-MMC systems [11, 34]. And, by the additional information from *in situ* tribometry, the dynamic nature of third bodies in metallic friction and wear for Al and Al-MMCs has been revealed. Connections between modifications to the transfer films observed *in situ*, such as hole formation and scoring, and the development of MMLs have increased our understanding of the third body processes occurring in these coating systems. As Blau predicted in 1981 [33], there is significant information to be gained by applying *in situ* methods to metallic friction that is unavailable by traditional tribometry approaches.

4.5 Conclusions

Three coatings of Al-Al_2O_3 composite deposited by cold spray were tested for dry sliding wear performance by *in situ* tribometry. Friction coefficients were found to become lower and more stable as the Al_2O_3 content in the coating increased, while at the same time wear rates were decreased by up to two orders of magnitude. This was linked to the formation of a mechanically mixed layer (MML) in the wear track surface and subsurface. In turn, this was correlated to an increase in transfer film stability when observed *in situ*, characterized by fewer occurrences of dynamic wear processes, such as plastic flow, hole formation, and scoring across the center of the transfer film. The transfer film observed at high Al_2O_3 content (22 wt.%) was observed to break down over the course of the test due to abrasion from the oxidized MML in the wear track, but still provided contact condition that led to the least wear and most stable friction compared to the 10 wt.% Al_2O_3 coating and the pure Al coating.

Acknowledgements

The authors gratefully acknowledge the financial support from the Canadian Foundation for Innovation project no. 8246 for the cold spray equipment and CFI, Leader's Opportunity Fund, project no. 13029 for the *in situ* tribometer, and the Natural Sciences and Engineering Research Council (NSERC) Discovery Grants Program for the operational funding of this project. J. Michael Shockley acknowledges partial financial support from the McGill

Engineering Doctoral Award (MEDA) program.

Chapter 5

Third body behavior during dry sliding of cold sprayed Al-Al_2O_3 composites: *in situ* tribometry and microanalysis

J.M. Shockley, S. Descartes, E. Irissou, J.-G. Legoux, R.R. Chromik

Adapted from a paper of the same title published in *Tribology Letters* **54** (2014) 191–206.

In the previous chapter, the friction and wear behavior of samples CS0, CS10, and CS22 was correlated with transfer film activity monitored through *in situ* tribometry and with subsurface microstructural changes in the wear track. However, many questions remained unanswered in chapter 4 regarding the structure and mechanical properties of the third body material. In this chapter, a more detailed analysis of the third body behavior and properties for samples CS0 and CS22 was carried out, which permitted description of the tribological circuit and velocity accommodation modes (VAMs) for the two sliding systems.

Abstract

Reciprocating sliding wear experiments were conducted on cold-sprayed pure aluminum and Al–22.6 wt% Al_2O_3 coatings using a custom-built *in situ* tribometer. Using a transparent sapphire counterface for the wear tests, the dynamic behavior of third body material in the contact was optically observed. The presence of Al_2O_3 particles led to greater stability of the transfer films adhering to the sapphire counterface, as well as greater stability of the friction coefficient and lower wear rates. *Ex situ* microanalysis of material in the wear tracks and transfer films suggests that the presence of Al_2O_3 particles promoted strain localization during sliding. This produced more uniform third body microstructures and protected the underlying aluminum matrix from deformation, which slowed the rate of transfer to the counterface.

5.1 Introduction

While aluminum and its alloys are highly valued for their corrosion resistance, low density, and high thermal conductivity, their poor tribological behavior limits their use in many applications. For pure aluminum, the lack of alloying elements is a benefit for corrosion resistance, but a significant detriment to mechanical and tribological properties [139]. A popular compromise for applications requiring both corrosion and wear resistance is aluminum matrix composite (Al-MMC) materials, which utilize secondary phases, commonly based on SiC or Al_2O_3 , to provide mechanical reinforcement of the aluminum matrix [2]. Reinforcing phases may be continuous (long fibers) or discontinuous (particles and short fibers), depending on the application and processing route. Al-MMC materials can have corrosion resistance comparable to un-reinforced pure aluminum but substantially lower wear rates in most wear regimes [1, 9, 27, 34].

Classical processing of discontinuously reinforced Al- MMC materials includes bulk casting, spray casting, sintered powder metallurgy, and thermal spray processing routes [2, 3]. More recently, cold gas dynamic spray, more often known as cold-spray, has been utilized for routine deposition of Al-MMC coatings and bulk materials [9, 11, 156, 157]. The cold-spray process operates by accelerating feedstock powders through a preheated inert gas stream that is passed through a de-Laval-type nozzle. The gas and powders attain supersonic velocities, and upon impact with a substrate, extensive plastic deformation is induced; coating buildup takes place through a combination of mechanical interlocking and metallurgical bonding due to adiabatic shear instabilities [4–6, 8, 48]. Hard phases such as SiC and Al_2O_3 may be incorporated into the coatings by admixing them into the feedstock powders [9, 11]. Coatings deposited using the cold-spray process undergo very little oxidation or chemical reaction compared to conventional thermal spray techniques. Cold-spray of pure aluminum and Al-MMC materials is becoming a primary mode of repair and corrosion protection for magnesium aerospace gearbox components [157, 158]. With the growing popularity of cold-sprayed Al and Al-MMC materials in structural and surface engineering applications, it is of interest that their tribological behavior be well understood and characterized.

In Al-MMC materials, a shift toward lower wear rates with increasing hard particle content has been documented. Microanalysis of worn aluminum and other pure metal surfaces typically reveals evidence of adhesion and extensive plastic deformation, resulting in surface grain refinement and material transfer between surfaces [33,69,70,159,160]. For Al-MMCs prepared by traditional methods, several groups have shown that lower wear rates may be correlated to the formation of mechanically mixed layers with constrained grain refinement [1, 25]. For the case of coldsprayed Al-MMCs, specifically Al-Al_2O_3 , reduction in wear rates have been observed, but connections between this reduction to the nature of the mechanically mixed layer have not been made as clear as for traditional Al-MMCs [11, 161].

For the tribology of most materials, including aluminum and Al-MMCs, “third bodies” at the sliding interface ultimately dictate the tribological behavior [67,151]. Third bodies develop due to deformation-induced physical, chemical, and microstructural changes of material at the sliding interface, and often exhibit distinct properties compared to the unworn first bodies [29, 66]. The phenomena of material transfer, mechanical mixing, and wear debris formation are largely third body material flows, and the magnitude of these flows influences the overall performance of the sliding system in terms of friction and wear [67]. In the large body of literature on the tribology of Al and Al-MMCs, assignment of mechanisms is most often done solely with *ex situ* characterization of worn surfaces, i.e., after the test, which provides only static details from which the behavior of third bodies during the test must be inferred.

The technique of *in situ* tribometry allows for real-time observation of third body behavior through the use of a transparent sliding counterface. This technique has been most frequently used for tribology of thin film coatings such as solid lubricants and diamond-like carbon coatings [146, 148–150, 162], but its use on metallic systems has considerably less precedent. In a short previous work by the authors, coatings of cold-sprayed pure Al and Al-Al_2O_3 were subjected to sliding wear tests using an *in situ* tribometer [161]. This study was largely limited to a discussion of *in situ* tribometry results. In the present work, *in situ* tribometry and *ex situ* methods are combined to develop a more complete understanding in terms of third body flows and velocity accommodation [140]. The observed *in situ* behavior of third bodies, primarily transfer films, are correlated to observations from complementary *ex situ* microanalysis of the worn coatings and transfer film material using focused ion beam (FIB) cross-sectioning. By pairing *in situ* observations with *ex situ* analysis of the structural and chemical contrasts in the third body material, a full understanding of the tribological flows and velocity accommodation modes for the cold-sprayed Al and Al-Al_2O_3 samples will be developed.

5.2 Experimental methods and theory

5.2.1 Cold spray deposition

Feedstock powders for cold spray were prepared by admixing commercially available spherical Al powder (Alfa-Aesar, H = 26 ±2 HV10, dm = 36.2 µm) with varying percentages of Al_2O_3 powder (Plasmatec, H = 2,019 ± 426 HV10, dm = 25.5 µm) [9]. Coatings were deposited onto mild steel substrates using a Centerline SST series P cold spray system, achieving a thickness of 500–600 µm [9]. Other details of coating deposition, including inlet gas temperature, spray velocity, deposition efficiency are provided in an earlier work [9]. The concentration of Al_2O_3 recovered in each coating was determined by image analysis, during which ten random images of polished cross-sections were taken in a scanning electron microscope (SEM) and analyzed by pixel count to calculate the Al_2O_3 content. Previous studies on coldsprayed Al-Al_2O_3 have shown that tribological behavior shifts as a function of Al_2O_3 content toward lower sliding wear rates and more stable friction [11, 161] [8, 23]; the coatings used in this study were chosen to highlight the contrast of this behavior. The coatings selected for the present study contained 0 wt.% and 22.6 ± 2.9 wt.% Al_2O_3 , which were assigned the designations of CS0 and CS22, respectively (see Fig. 5.1). Prior to wear testing, the coating surfaces were polished using water-based 9-, 3-, and 1-µm diamond suspensions, followed by colloidal silica. Surfaces were cleaned in acetone after the final polishing step, and the root mean square roughness of all surfaces was less than 600 nm. Mean aluminum grain sizes in the initial coatings were determined by tracing electron channeling contrast micrographs and found to be 640 ± 370 nm, while initial Al_2O_3 particle sizes were between 2 and 30 µm. Cross-sectioning and electron channeling contrast imaging (ECCI) observation of the polished surfaces showed negligible near-surface microstructural changes due to polishing.

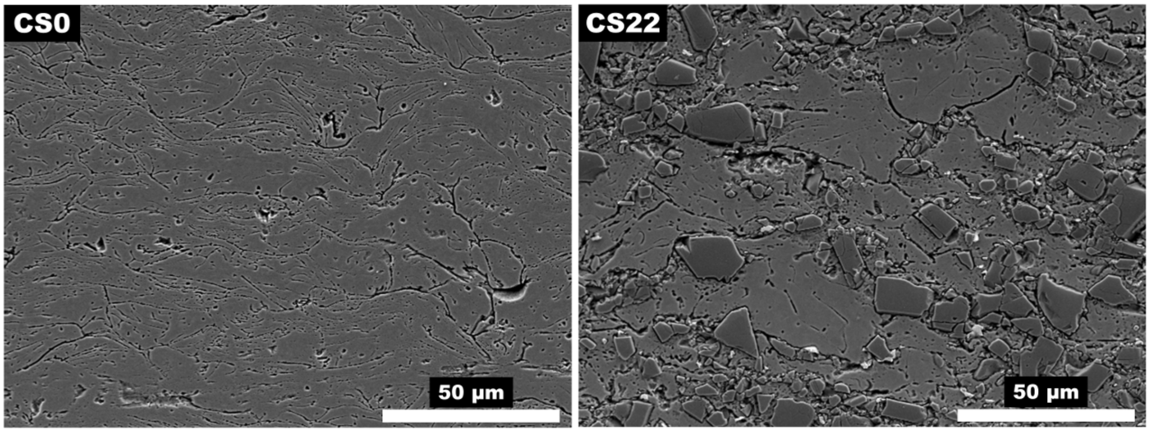

Figure 5.1 – Secondary electron (SE) images of etched unworn microstructures of CS0 and CS22 viewed in cross-section 250 µm below the surface. Particle boundaries are visible in the etched microstructures, as are porosity and strain lines. Al_2O_3 particles in CS22 are embedded near particle boundaries.

5.2.2 Wear test conditions

Sliding wear tests on the polished coatings were performed in dry air (below 2 % relative humidity) at room temperature (21–24° C). All wear tests were conducted at a sliding speed of 3 mm/s, a track length of 10 mm, and normal load of 1 N. Transparent monocrystalline α-Al_2O_3 (sapphire) was used as the counterface material in the form of 6.35-mm diameter hemispheres. In order to calculate the initial contact stress, the elastic moduli of the coatings were predicted to fall between the Reuss and Voigt bounds as a function of alumina content [23]. These were used to calculate a theoretical minimum and maximum range of average Hertzian contact at the beginning of wear testing (see Table 1). Wear tests were run to 500 and 2,000 sliding cycles, corresponding to total sliding distances of 5 and 20 m, respectively.

Sample	Al_2O_3 in feedstock powder [9]	Al_2O_3 in deposited coating [9]		Range of initial average Hertzian stress	Hardness	Wear rate after 500 cycles	Wear rate after 2000 cycles
	wt.%	wt.%	vol.%	MPa	HV_{200}	10^{-2} mm^3 N^{-1} m^{-1}	10^{-2} mm^3 N^{-1} m^{-1}
CS0	0	0	0	287	53.4 ± 1.7	2.815 ± 0.263	0.911 ± 0.113
CS22	50	22.6 ± 2.9	16.1 ± 1.9	312-399	78.9 ± 4.7	0.357 ± 0.097	0.148 ± 0.020

Table 5.1 – Properties, initial average Hertzian stress, and wear rates of the tested coatings.

5.2.3 *In situ* analysis

Friction forces were measured at a sampling rate of 800 Hz using a piezoelectric sensor mounted underneath the sample stage. Microscopic observation of the contact region was carried out *in situ* through the transparent counterface using an optical microscope. The microscope was mounted above the transparent counterface and was equipped with a 10x objective lens and a commercially available camcorder.

5.2.4 *Ex situ* analysis

After wear testing, the wear tracks and counterface transfer material were analyzed *ex situ*. Using a Philips XL-30 scanning electron microscope (SEM), wear track surface features were observed and elemental contrast was revealed by energy dispersive X-ray spectroscopy (EDXS). Surface morphologies of the wear tracks and counterface transfer material were extracted using a Wyko NT8000 non-contact optical profiler. Wear rates were calculated in accordance with ASTM Standard G99 by first integrating height profiles across the wear track above and below the original surface height to calculate a net worn cross-sectional area. This was then multiplied by the wear track length to obtain a net volume of material removed from the surface. A total of 30–40 surface profile measurements per wear track were obtained.

Subsurface regions of the worn surfaces were studied by both conventional metallurgical preparation of cross-sections and by focused ion beam (FIB) cross-sectioning. For the conventional cross-sectioning, wear tracks were cut transverse to the sliding direction using a lubricated slowspeed abrasive cutting wheel, followed by cold mounting in epoxy and mechanical polishing. For FIB cross-sections, a Zeiss NVision 40 dual beam FIB/SEM was used with a gallium ion source. Samples were coated with a layer of gold prior to analysis, and then cross-sections were cut parallel and transverse to the original sliding direction. Carbon was deposited as a shielding material to reduce ion beaminduced artefacts in the cross-sections. For images collected in the FIB/SEM, grain contrast was revealed by ECCI. Quantitative analysis of grain size was carried by tracing each grain and calculating its equivalent circular diameter.

Nanoindentation was performed on mechanically polished surfaces using a Hysitron Triboindenter equipped with a Berkovich diamond indenter with a tip defect radius of approximately 125 nm. Indents were performed using a 5 s linear loading time to a maximum force of 400 μN, 5 s hold time at maximum load, and 5 s linear unloading time. Each hardness value reported was calculated using the Oliver and Pharr method [143] and represents the average of at least 12 indents.

5.2.5 Theory and nomenclature

The material flows in a sliding system may be described using the tribological circuit (see Fig. 5.2a) [67]. The first bodies are contacting and are in relative motion to one another; third bodies form at the sliding interface. The source flow, Qs, represents detachment or transformation of first body material to become the third bodies; the internal flow, Qi, is movement of material across the interface; the ejection flow, Qe, is material ejected from the interface; the recirculation flow, Qr, is ejected material that has been reintroduced to the interface; and the wear flow, Qw, is material permanently removed from the sliding system. When applied to metallic systems, the phenomena of third body formation, mechanical mixing, and wear debris formation [69–71] may be readily assigned theoretical counterparts in the tribological circuit. In the present ball-on-flat sliding system, third bodies are formed in the wear track and as transfer film adhering to the hemispherical counterface (see Fig. 5.2b). Ejection flow occurs as material is deposited at the ends of the wear track or pushed to the sides of the wear track. This material becomes wear flow unless it somehow recirculates into the contact, for instance as the wear track widens.

The surface adaptation to relative motion during dry sliding may be classified according the so-called velocity accommodation modes (VAMs) [72]. This analysis permits description of the locations and mechanisms by which relative motion is manifested at the sliding interface. Classically, the mechanisms of elastic deformation, fracture, shear, and/or rolling may take

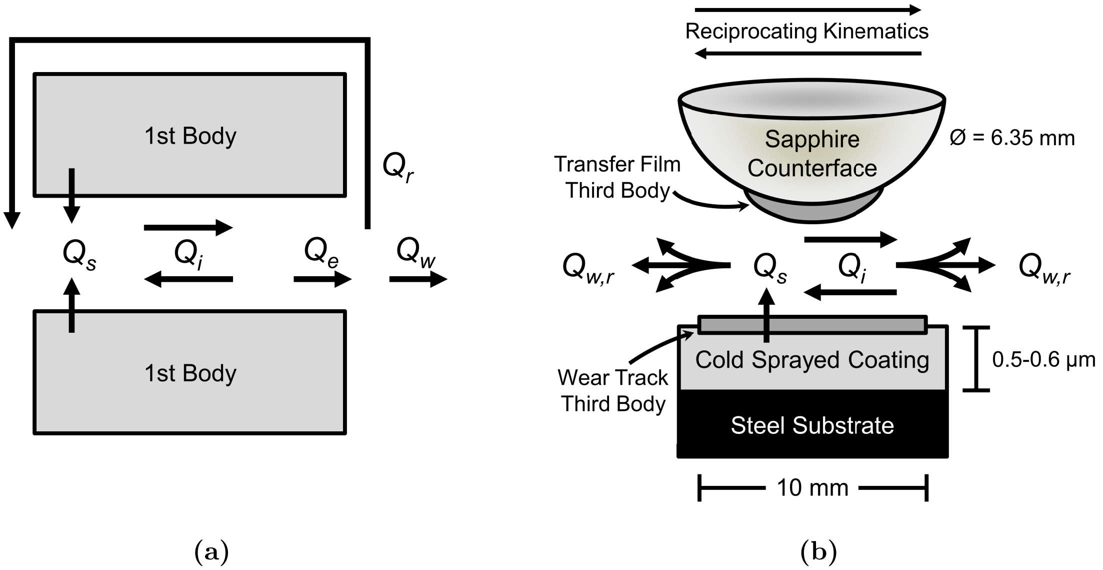

Figure 5.2 – The tribological circuit: (a) theoretical [67] and (b) applied to the current system (not to scale). Wear and recirculation flows in (b) may be ejected longitudinally at the ends of the wear track or laterally, as indicated by the arrows.

place in some combination of the first bodies, third bodies, and the interfaces in between; each combination represents a VAM [72]. A shift in VAM may influence the material flows in the tribological circuit and hence the friction and wear of the sliding system.

5.3 Results and discussion

5.3.1 Friction

The friction coefficient throughout the tests to 2,000 cycles are plotted in Fig. 5.3. Sample CS0 exhibited a friction coefficient that fluctuated between 0.6 and 1.3, with many spikes and temporary shifts to varying plateau values. The CS0 friction coefficient started with an initial spike above 1.0, then gradually decreased over the initial 250 cycles. The friction coefficient of sample CS22 remained generally between 0.5 and 0.7. The friction behavior of sample CS22 was considerably more stable than that of CS0, and as a whole, lower. This behavior is the same as that observed in our previous study on the same coatings slid against sapphire and polycrystalline Al_2O_3 counterfaces [161]. Spencer et al. [11] observed a similar friction stabilization due to Al_2O_3 during dry sliding of Al and Al-Al_2O_3 coatings against steel counterfaces, where the specimens had been cold sprayed using helium as carrier gas on an Inovati Kinetic Metallization (KM) cold spray system [11]. Wang et al. [77] also observed a reduction and stabilization of friction with hard-phase content during dry sliding wear of bulk 6092 aluminum alloy and composites of 6092/15 % Ni_3Al against steel counterfaces, where the friction coefficient was roughly 0.5 for the unreinforced alloy and roughly 0.42 for the Al-MMC material [77].

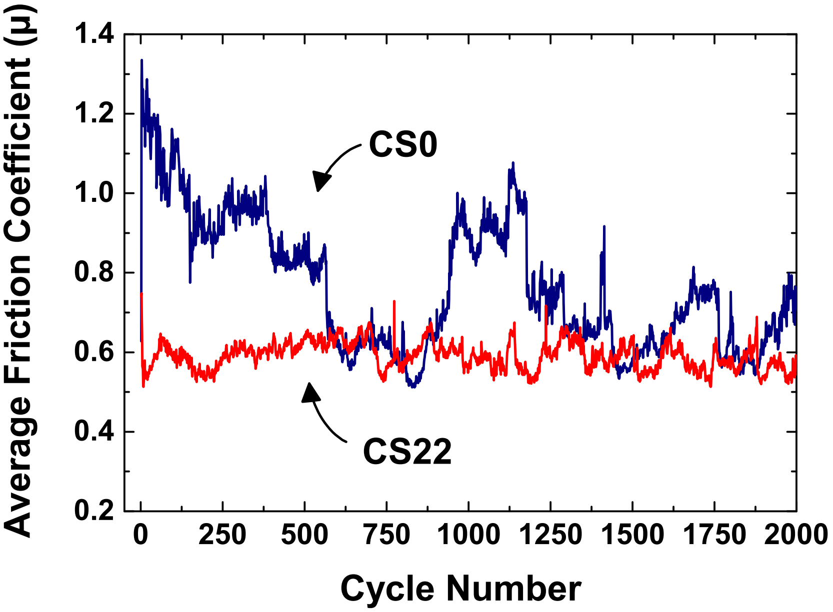

Figure 5.3 – Mean friction coefficient per cycle plotted versus cycle number for tests run to 2,000 cycles.

5.3.2 *In situ* observations of transfer film behavior

5.3.2.1 Transfer film behavior of CS0

During the opening cycles of the CS0 wear tests, extensive plowing was observed. During the first sliding cycle, the initial plowed material adhered to the slider and steadily accumulated to form a prow (see Fig. 5.4). Prow formation behavior, where material accumulates ahead of the slider, was documented in aluminum and other metals in early studies on metallic transfer [70], and was found to be cyclic and largely observed early in the sliding process [31]. This early transfer process is the initial activation of source flow, Qs, and for CS0, it corresponded to the period of highest friction coefficient. For CS0, the prow grew steadily until it reached a length of roughly 215 μm (measured parallel to the sliding direction) and width of 150 μm (see Fig. 5.4, far right), after which it detached from the contact (as ejection flow, Qe) and was left on the wear track. A new prow started to form immediately after, and upon the return pass, the first prow was recirculated back into the contact (Qr). As this process continued, some ejected prow material was left at the ends of the wear track as wear flow (Qw) as were smaller pieces of wear debris.

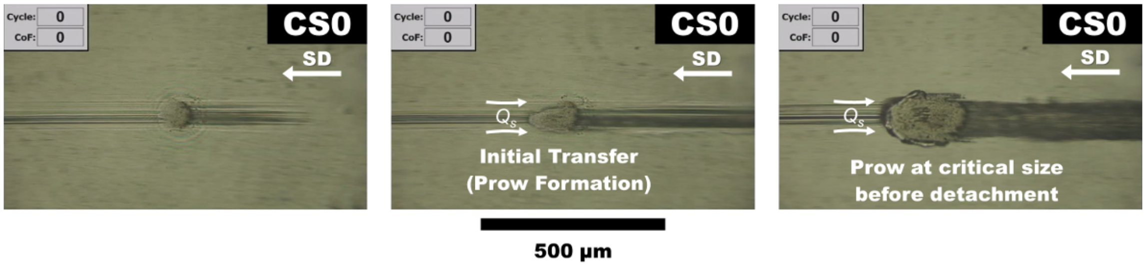

Figure 5.4 – *In situ* micrographs showing the formation of the initial CS0 transfer film during the first sliding cycle. "SD" indicates sliding direction.

After the initial few sliding cycles, the formation and detachment of several prows left permanent transfer film on the slider (see CS0 in Fig. 5.5). Throughout roughly the first 100 cycles, this transfer film was highly unstable. The instability during this period was characterized by observable plastic internal flow (Qi) of the transfer film, and frequent detachment of material from the contact (Qe) leaving holes that were quickly filled in with new material (Qs). The transfer film continued to grow throughout the test, as did the observable width of the wear track, and both eventually became larger than the field of view of the microscope. While visible, the apparent transfer film remained roughly circular and grew in diameter; for instance, it grew from roughly 730 μm at 50 cycles to 1,060 μm at 500 cycles. Later in the test, streaks running parallel to the sliding direction were formed, indicating internal flow of the transfer film (Qi) or material removal (Qe).

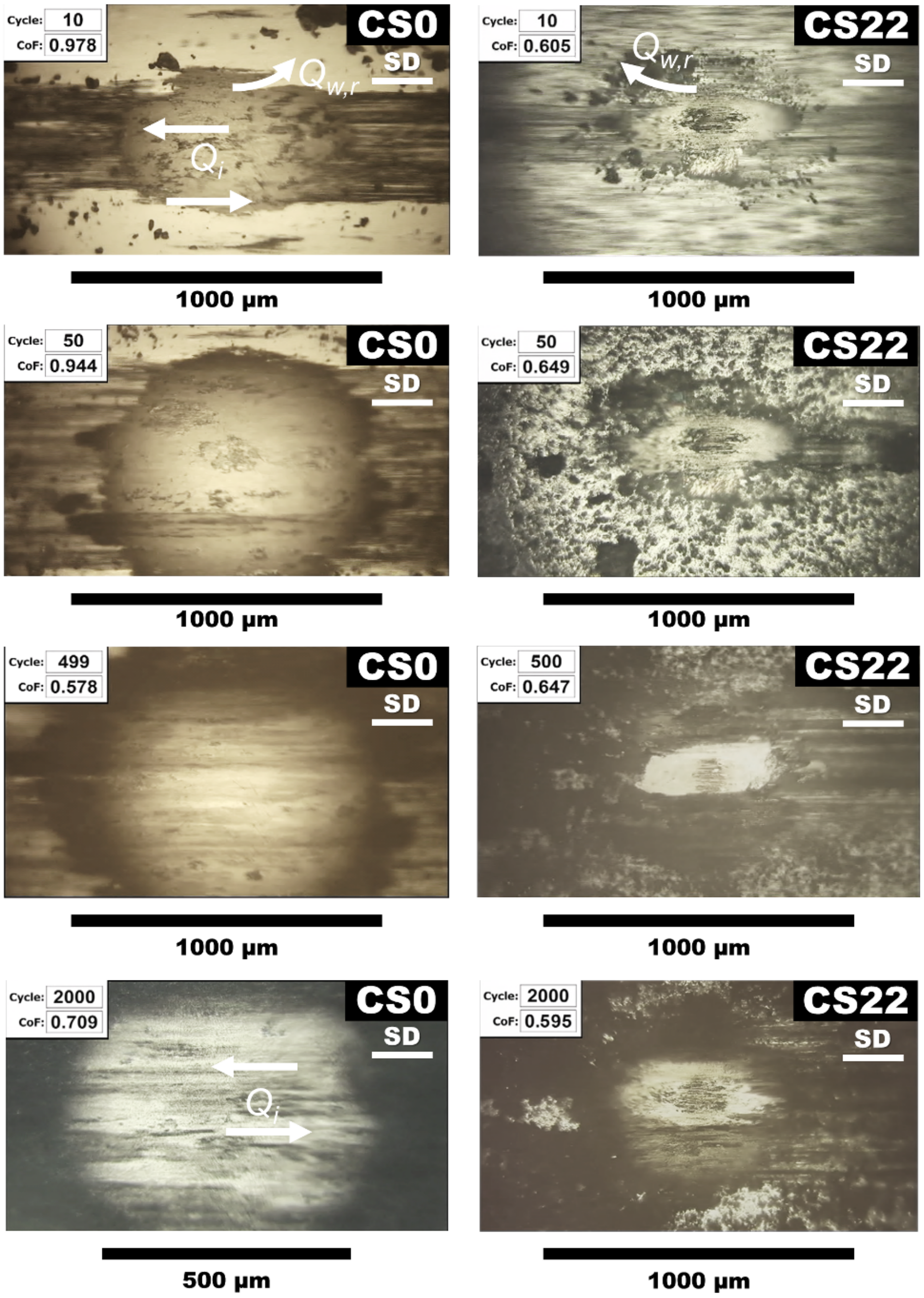

Figure 5.5 – *In situ* micrographs of transfer films from CS0 and CS22 at 10, 50, 500, and 2,000 cycles.

At several points where the COF underwent large shifts from one steady-state value to another, the transfer film showed corresponding detachments of large patches of material (see Fig. 5.6). In both cases a and b, patches of transfer film material appeared to loosen over the course of several cycles prior to detachment (outlined regions in a1 and b1). As each patch of transfer film loosened from the sapphire, a narrow air gap was created between the two, which caused optical interference fringes to form. The fringes were visible *in situ* as rapidly fluctuating rainbow colors, indicating that the gap fluctuated in height while the transfer film passed over the uneven wear track topography. This phenomenon of seeing optical interference fringes during tribology tests is similar to that observed for solid lubricants [163], but does not provide a straightforward method for analysis that could measure the transfer film thickness. However, the appearance of the fringes does provide evidence of gradual detachment between the transfer film and sapphire.

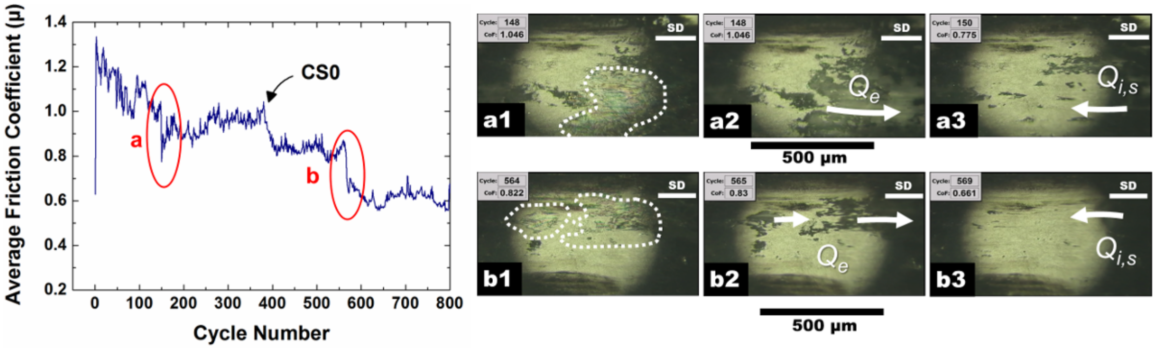

Figure 5.6 – Average friction coefficient versus cycle number (left), *in situ* micrographs of CS0 transfer films in the vicinity of two friction events, a and b (right). Patches of interference fringes are evident just prior to the event (highlighted in a1 and b1), after which point material detached (a2 and b2) and was replaced with newly plowed material (a3 and b3).

After the fringes were visible for about 5 cycles, the loosened material was ejected from the contact (as Qe in a2 and b2), and the hole was quickly filled in with new material as internal (Qi) or source flow (Qs) from the wear track (a3 and b3). Although dynamic friction events occurred throughout testing for CS0 (see Fig. 5.3), many of them did not easily correlate with events easily visible *in situ* such as this. One possible explanation is that as the transfer film grew beyond the microscope's field of view, such events occurred there. A second explanation is that not all of the events resulted from an adhesive failure at the interface of the transfer film and sapphire, with the failure instead occurring cohesively within the transfer film.

5.3.2.2 Transfer film behavior of CS22

The initial CS22 transfer film formed through prow formation similar to that of CS0, and for the initial few cycles, transfer film instability comparable to CS0 was observed as internal flow (Qi). However, after just a few sliding cycles, the observable internal flow essentially ceased and the transfer film remained stable throughout the opening several hundred cycles (see CS22 in Fig. 5.5), taking the form of an oval roughly 600 µm long and 200 µm wide. In this stable state, none of the behaviors observed in the CS0 transfer film, such as obvious internal and ejection flows, were present—and neither were the corresponding jumps in COF. At higher cycle numbers the wear track widened, as did the transfer film, but to a lesser extent than CS0 (see Fig. 5.5 at 500 and 2,000 cycles). The enhanced stability of the CS22 transfer film when observed *in situ* may be interpreted as lower magnitudes, and less frequent activation, of source, internal, and ejection flows.

5.3.3 *Ex situ* observations of third bodies

5.3.3.1 Morphology of CS0 transfer film and wear track

Viewed *ex situ*, the CS0 transfer film after 500 sliding cycles was patchy and mostly consisted of material less than 20 µm thick (see Fig. 5.7a, b). However, near the center was a prominent patch of material roughly 400–500 µm long, 150–200 µm wide, and generally greater than 40 µm thick. At the top of this patch of material was a prow (see 5.7c) of similar length and width as those prows observed *in situ* early in sliding (see Fig. 5.4). This prow reached a maximum thickness of roughly 75 µm. The streaks of material correspond strongly to the scoring marks visible in the transfer film in Fig. 5.5. In the regions of thin transfer material, the underlying sapphire counterface was frequently visible (see 5.7d). Flake-shaped wear debris were visible adhering to the transfer film as well.

The *ex situ* observations in Fig. 5.7 suggest that the *in situ* appearance of the CS0 transfer film, nominally greater than 1 mm in diameter, as in Fig. 5.5, is misleading in terms

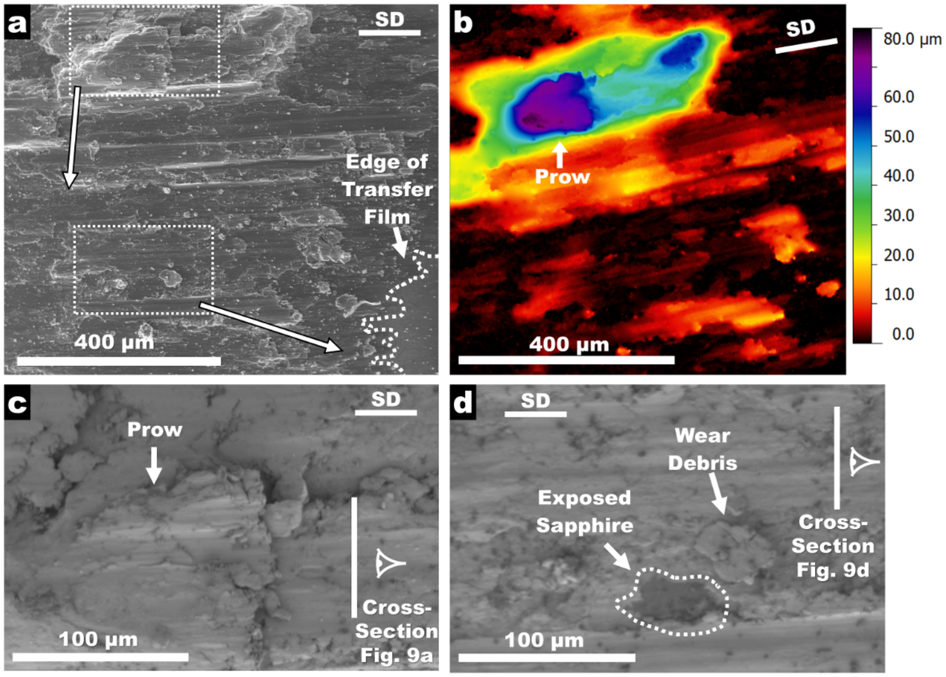

Figure 5.7 – Features of the CS0 transfer film observed *ex situ* after 500 sliding cycles. (a) Overall view of main features, including the location and perspective of FIB crosssections in Fig. 9; (b) flattened height profile of the features in (a); detail images of (c) the highest prow and (d) a region of thin material showing regions selected for cross-sectioning

of the volume of third body material attached to the sapphire. Much of the CS0 transfer film after 500 sliding cycles consisted of very thin, smeared material. This thick region of transfer film may have been the main area of contact, which is supported by the observation of a prow at its leading edge, as it is evidence of source flow that occurred just prior to stopping the test.

Features in the CS0 wear track were characteristic of adhesive wear, similar to that seen in previous dry sliding wear studies of pure bulk [164] and cold-sprayed aluminum [11]. Layered structures of adhesively smeared material were present (see Fig. 5.8a, b). Wear debris was also visible in flake morphologies 5–20 µm in diameter. Some scoring in the direction of sliding was also evident. Wear rates after 500 and 2,000 sliding cycles are reported in Table 1. These wear rate values are of a similar order of magnitude as those measured in previous studies when sliding against balls made of Al_2O_3 [161] and 100Cr6 steel [11] with similar loading conditions as in the present study.

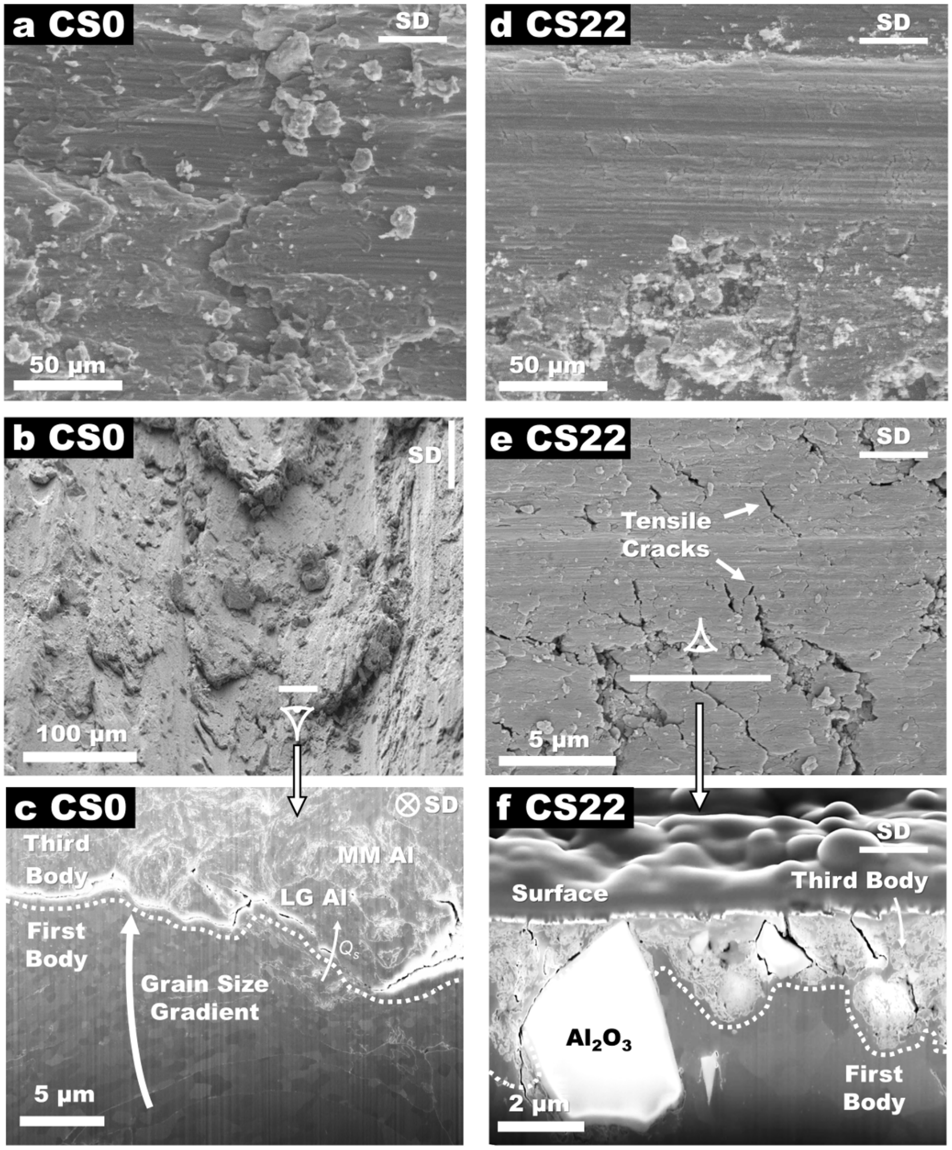

Figure 5.8 – Features and microstructures in the wear tracks of CS0 and CS22 viewed *ex situ*. (a) and (d): top-down views; (b) and (e): locations and perspectives of FIB crosssections in (c) and (f). In image (c), the sliding surface is 3–4 µm above the top of figure

5.3.3.2 Microstructures of CS0 transfer film and wear track

In the CS0 transfer film, the two regions selected for further microstructural observation by FIB cross-sectioning were the top of the thick patch of transfer film (see Fig. 5.7c), which is roughly 45 µm thick, and a region of thinner transfer film 5–10 µm thick (see Fig. 5.7d). Figure 5.9 shows the microstructures cut transverse to the sliding direction in the CS0 transfer film, which have three main features. The first feature is ultrafine aluminum grains, which are present in bands 1–5 μm thick. Given the imaging technique used in this study, it is difficult to quantify the size and morphology of the ultrafine structured grains, but they appear to be below 150 nm. Grain refinement is a consequence of the mechanical mixing processes and severe plastic deformation occurring during sliding [31,165]. Also visible in the microstructures are bands of relatively larger aluminum grain showing grain sizes on the order of 200 nm to 2 μm. These larger grain sizes indicate that these regions have gone through less plastic deformation than the ultrafine grained regions. Finally, thin cracks exist between adjacent patches within the microstructures (see Fig. 5.9a). Cracks between these regions indicate that the transfer film consists of patches of material, some subjected to more mechanical mixing than others, pushed together but not necessarily bonded. The grain refinement visible in material just next to the cracks (see detail images Fig. 5.9b, c) may have originated from contact and deformation between these regions during sliding. Microstructures from the thin regions of CS0 transfer film (see Fig. 5.9d) show similar features as those in the thicker regions. The sapphire is apparent under a region of transfer film 4–5 μm in thickness, similar to the interferometry measurements in Fig. 5.7a. In this region and others observed, the only material observable at the interface with the sapphire was ultrafine grained aluminum.

For comparison, the edge of a piece of adhesively smeared material in the bottom of the CS0 wear track was selected for microstructural analysis, and a FIB cut was performed transverse to the sliding direction (see Fig. 5.8b, c). Third body material is visible sitting on top of first body, separated by a crack. The microstructure of the third body region shows highly refined aluminum grains and cracks existing in the material, which are both evidence of plastic deformation and mechanical mixing as part of the internal flow (Qi) that occurred during the adhesive smearing behavior. In the first body, there is a gradient of grain size. Grain size analysis of a similar region (not pictured) showed that at roughly 500 nm below the separation of third body from first body, grain sizes were roughly 150 ± 63 nm. Grain sizes grew steadily as a function of depth below the surface, until stabilizing at a grain size of

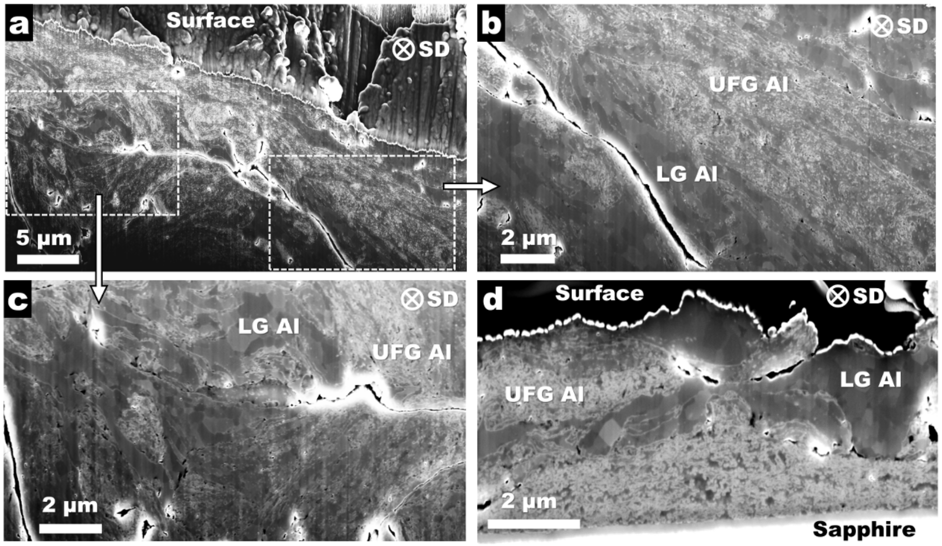

Figure 5.9 – Microstructures from two regions of the CS0 transfer film after 500 sliding cycles. The locations and perspectives are shown in Fig.5.7. (a) Microstructures in the thick region of transfer film, with details highlighted in (b) and (c); (d) microstructures in the thin region of transfer film. Microstructural features of ultrafine grained aluminum (UFG Al), relatively largegrained aluminum (LG Al), and cracks between sections are visible in each micrograph.

400 ± 250 nm roughly 8 µm below the surface. This gradient of grain size demonstrates that plastic strain accumulated deep into the first body, and strain would continue to accumulate until the material would detach and join the source flow (Qs).

5.3.3.3 Morphology of CS22 transfer film and wear track

When viewed *ex situ* after 500 sliding cycles, the CS22 counterface appeared to include one primary patch of transfer film 300–400 µm long, 100–250 µm wide, and the 40 µm thick at maximum (see Fig. 5.10a, b). It was 300–400 µm long and 100–250 µm wide. The length scale of this transfer film is relatively similar to the most prominent patch of the CS0 transfer film in Fig. 5.7, without the large prows and the streaks of transferred material. Furthermore, the transfer film size viewed *ex situ* is strongly comparable to its appearance *in situ*, unlike CS0. The highest point of the transfer film is shown and is relatively flat, with scoring marks parallel to the sliding direction. The lack of a prominent prow as was observed in CS0 suggests that less source flow (Qs) was activated at the time that the test was stopped, and this compares well with the *in situ* observations that less source flow and internal flow was activated for CS22. Fine wear debris, on the length scale of 1–10 µm, was observed adhering to the transfer film (see Fig. 5.10c and d).

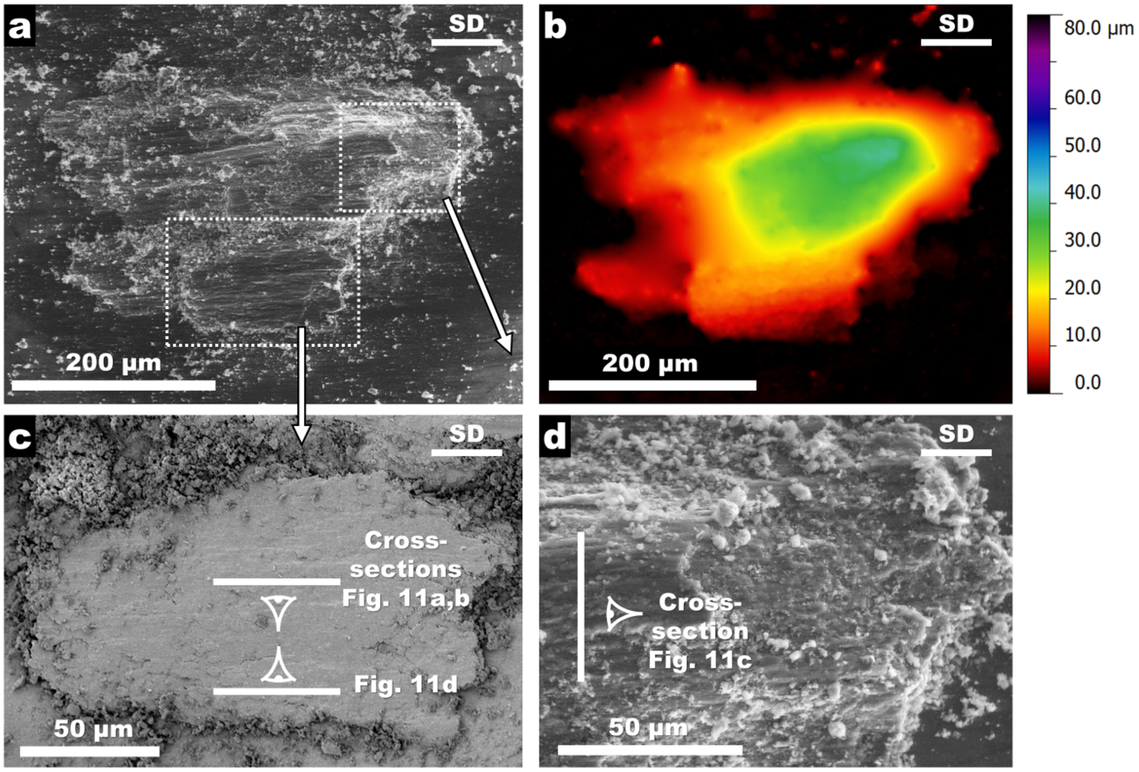

Figure 5.10 – Features of the CS22 transfer film viewed *ex situ* after 500 sliding cycles. (a) Overall view of main features, including the location and perspective of FIB cross-sections in Fig. 10; (b) flattened height profile of the features in (a); (c) and (d) detail images showing regions selected for cross-sectioning.

The CS22 wear tracks showed more uniformity than CS0 when run to similar numbers of cycles (see Fig. 5.8a, d). The wear track shows evidence of the development of a relatively smooth, coherent film, with no Al_2O_3 particles visible in top-down views. Cracking is visible in the wear track and there is extensive scoring of the surface in the direction of sliding, indicative of microplowing. Wear rates after 500 and 2,000 sliding cycles are reported in Table 1; the wear flow rate of CS22 was nearly an order of magnitude less than CS0, again in agreement with wear rates measured in previous studies [11, 161].

5.3.3.4 Microstructures of CS22 transfer film and wear track

Figure 5.10c, d shows the regions selected for microstructural analysis on the CS22 transfer film, with the FIB cross-sections shown in Fig. 5.11. In each case, the transfer film primarily consisted of ultrafine grained aluminum, along with several patches of relatively larger aluminum grains. Also present were fractured particles of Al_2O_3 . Figure 5.11a, b shows an area where there is a layer of ultrafine grain aluminum roughly 10 µm deep, while below that there are larger aluminum grains, pieces of Al_2O_3 1–2 µm in diameter, and a large crack below that. Figure 5.11c shows a cross-section from of thickest region of the CS22 transfer film, where the patch of larger grained aluminum is closer to the sliding surface than in the case of 5.11a. Figure 5.11d shows a cross-section from a thinner region, roughly 7 µm thick, of the transfer film, such that the sapphire was exposed during the cut. A crack runs through the transfer film material near the interface with the sapphire, but some ultrafine grained aluminum is adhering to the sapphire.

Subsurface microstructures in the CS22 wear track were revealed transverse and longitudinal in relation to the sliding direction (see Fig. 5.8f). A clearly distinguishable layer, containing ultrafine grained aluminum and Al_2O_3 particles, is present at the surface of the wear track and is generally 1–3 µm in thickness. In cross-section, some Al_2O_3 particles were clearly evident just under the subsurface layer. These particles were roughly 1–5 µm in diameter, showing considerable size reduction from the initial Al_2O_3 particles in the feedstock and unworn microstructure. The ultrafine grained mechanically mixed layer, with grain sizes that appear to be below 150 nm, is relatively evenly distributed, but it appears thinner in areas surrounding Al_2O_3 particles. In Fig. 5.8f, the cracks observed in the CS22 wear track penetrated this layer, appearing on a length scale similar to the size of wear debris observed in Fig. 5.10 adhering to the transfer film. Below the mechanically mixed layer, the matrix does not exhibit a pronounced grain size gradient like that of CS0. Quantitative grain size analysis of a similar region (not pictured) confirmed grain sizes on the order of 600 nm in the first body microstructure just below the third body. Although previous literature on

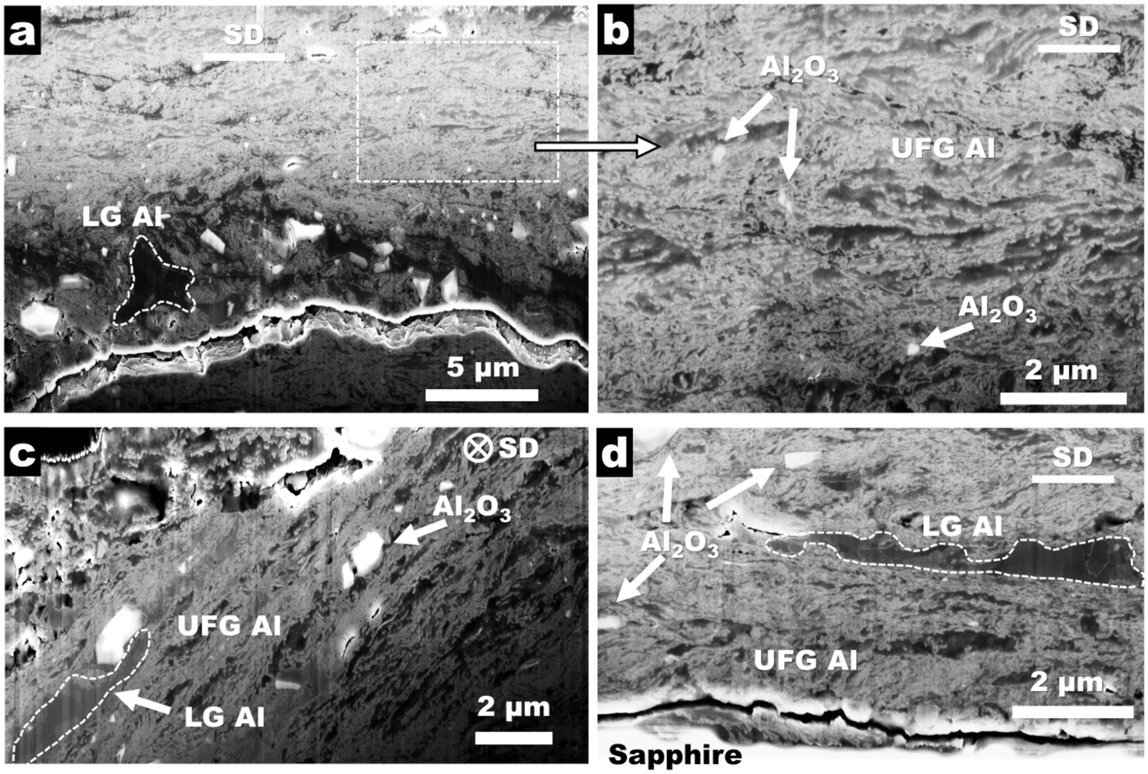

Figure 5.11 – Microstructures from two regions of the CS22 transfer film after 500 sliding cycles. The locations and perspectives are shown in Fig. 10. (a) Longitudinal cross-section, with details in (b) and (c); (d) transverse cross-section from a sloped part of the transfer film. Microstructural features of ultrafine grained aluminum (UFG Al), relatively large-grained aluminum (LG Al) and Al_2O_3 particles are visible. In image (a), the sliding surface is about 2 µm from the top of the figure, in image (c), the surface is visible in the upper-left corner, and in image (d), the surface is about 1 µm from the top of the figure

Al-MMC tribology has shown that grain refinement can penetrate well below the surface, most Al-MMC tribology research has focused on commercial aluminum alloys with much larger grain sizes than those used in this study [81], making even slight grain size gradient more apparent. The lack of grain refinement in the CS22 first body shows that stress and strain levels there were reduced compared to those in the CS0 first body, but they were probably not eliminated.

5.3.4 Mechanical properties and elemental composition of third bodies

In the unworn microstructures, the average hardness measured by nanoindentation of the pure aluminum phases of CS0 and CS22 was 0.85 ± 0.07 GPa, while for the Al_2O_3 particles, it was 21.1 ± 0.96 GPa. The third body regions of CS0 had a hardness of 1.46 ± 0.23 GPa, while the hardness of the CS22 third body was 3.72 ± 0.42 GPa (see Fig. 5.12). Representative load–displacement curves from the nanoindentation tests showed pronounced pop-in behavior during loading for the unworn Al regions, and to a lesser extent on the CS0 third body region. No pop-in behavior was visible for the CS22 third body material, nor for the Al_2O_3 particles. SE images of indents from the tested regions are shown in Fig. 5.13. Several previous studies have shown similar increases in third body hardness for Al-MMC materials compared to the unreinforced matrix material. Venkatamraman and Sundararajan found that for in dry sliding wear of Al-SiC composites against steel, the third body microhardness was roughly six times that of the undeformed material, whereas measurements on third bodies of an unreinforced Al alloy showed considerably less hardening [24]. Another study by Farhat et al. [102] of dry sliding wear of pure bulk aluminum against steel found hardening at the surface layer as high as 1.6 times that of the undeformed bulk. This is similar to the degree of hardening of the CS0 third body compared to the underlying aluminum, which was approximately 1.7 times harder, whereas the CS22 third body was approximately 4.4 times harder than the underlying aluminum.

There are several possible contributions to the higher hardness in the CS22 third bodies. As the wear track material in CS22 was more homogeneous in microstructure and showed finer grain sizes than what was observed for the CS0 (compare Fig. 8e, f), one contribution to the higher hardness could be Hall–Petch strengthening. As the velocity accommodation occurred in a smaller volume of material in CS22 versus CS0, the material in that layer would more highly strained and work hardened. The lack of pop-in behavior in CS22 may be further evidence of this, as the greater dislocation densities and smaller grain sizes would prevent the

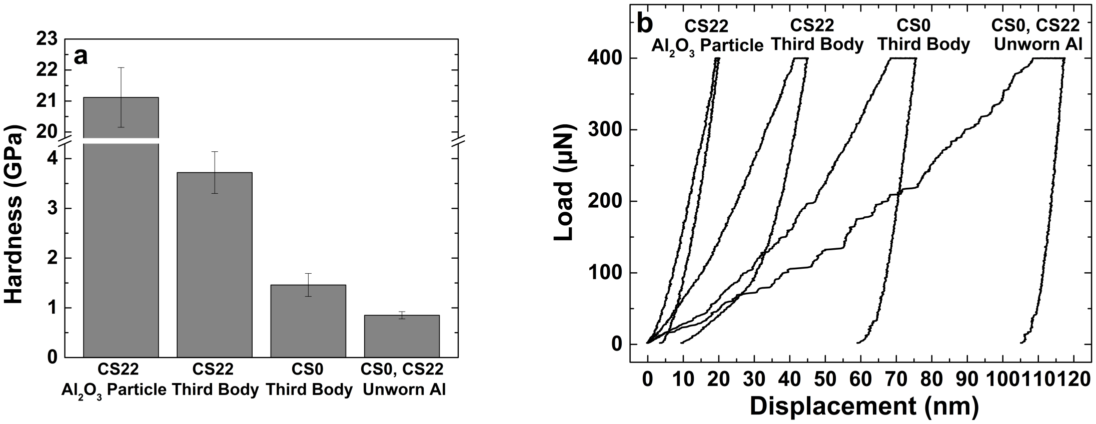

Figure 5.12 – Hardness data from (a) nanoindentation and (b) representative load– displacement curves from CS0 and CS22. Error bars show plus and minus one standard deviation of the mean value.

homogeneous dislocation nucleation events associated with pop-in [166].

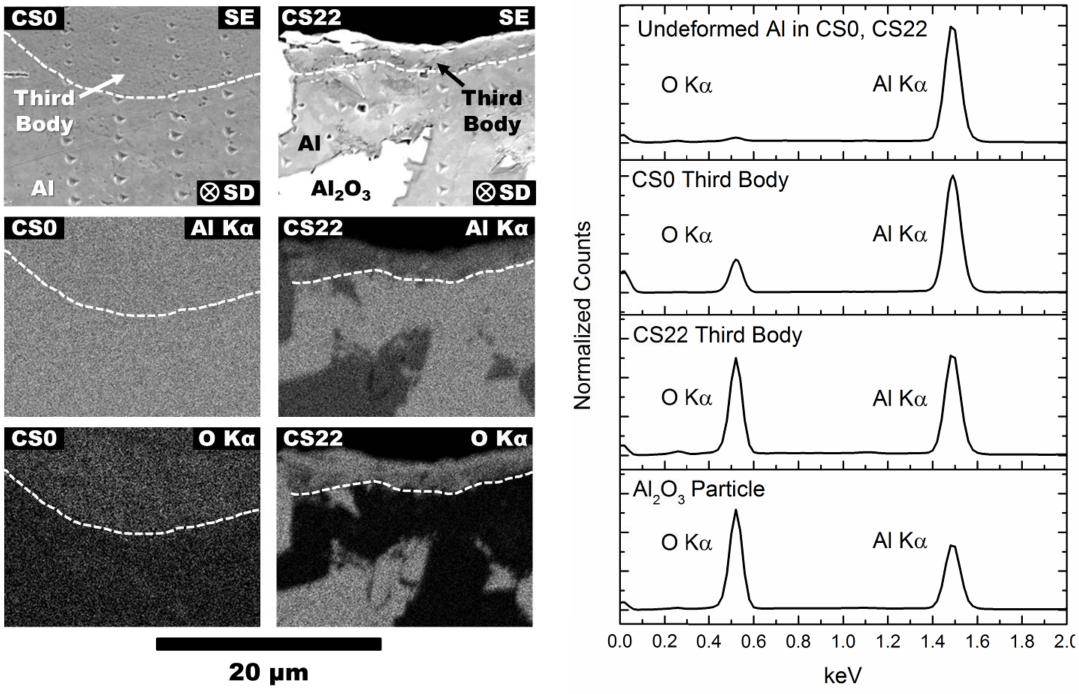

Figure 5.13 – Secondary electron images and EDXS mapping of aluminum and oxygen Ka signals (left) and representative spectra (right) of the polished cross-sections of CS0 and CS22 wear tracks.

Elemental microanalysis of the unworn and third body microstructures revealed increased oxygen in the third body material. EDXS mapping showing the region of interest, oxygen and aluminum Ka peaks, and representative spectra from the regions of interest are shown in Fig. 5.13. While a formal quantitative elemental analysis was not carried out, the relative intensities of Ka peaks of oxygen and aluminum, centered at 0.53 and 1.48 keV, respectively, reveal the different oxygen concentrations of the CS0 and CS22 third body material. In the unworn aluminum, the aluminum peak entirely dominates, while in the pure Al_2O_3 particle, a characteristic ratio is developed with oxygen slightly higher than aluminum. In the CS22 mechanically mixed layer, roughly equal intensities of oxygen and aluminum were measured, while the CS0 third body showed a smaller but significant presence of oxygen. There are several possible explanations for the oxygen content. First, the mechanical mixing exposes clean aluminum surfaces which spontaneously oxidize to form amorphous Al_2O_3 [167]; Kim and Rigney suggested that mechanical mixing induces dissolution of oxygen into the aluminum matrix as a solid solution [159]. As the CS22 third body material has been demonstrated to be highly localized, it is possible that it took up greater concentrations of oxygen. Second, refined Al_2O_3 particles were observed in the CS22 third body material, contributing to the oxygen signal as well.

5.4 The relationship between third body flows and microstructural changes

The opening cycles of transfer film formation for both CS0 and CS22 were nearly identical when observed *in situ*— initial formation and flow of the transfer film occurred because of the low levels of strain. This initial high source flow, Qs, corresponded to the initial friction spikes for both coatings and was quite similar (see Fig. 5.14). After this point, the behavior of CS0 and CS22 third bodies differed greatly.

In CS0, considerable grain refinement occurred due to plastic deformation. Strain penetrated far into the first body and the bulk of the transfer film, as shown through the grain size gradient beneath the third body material (see Fig. 5.8). The source flow (Qs) therefore remained high throughout testing for CS0 (see Fig. 5.14), as new third body material was constantly being generated below the wear track. Some amount of oxygen uptake occurred in the CS0 third bodies as well as new surfaces were exposed to the atmosphere, but it was spread among a relatively large volume of material. The higher internal (Qi) and ejection (Qe) flows prevented formation of a uniform layer, as material was removed from the contact very frequently. Thus, the third body consisted of a mix of material subjected to differing degrees of grain refinement and work hardening.

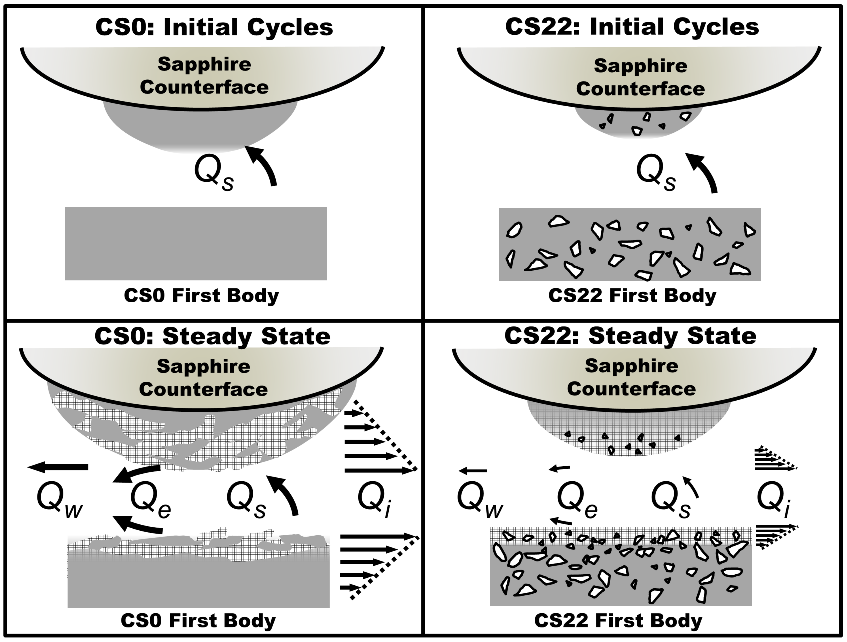

Figure 5.14 – Schematic diagram of tribological flows and third body microstructures for CS0 and CS22 during and after running-in. The CS0 source flow (Qs) remains high throughout the test, as do the ejection (Qe), wear (Qw), and internal (Qi) flows. This was related to the evolution of third body microstructures, where UFG material (block pattern) was intermixed with larger grained aluminum (gray). Velocity accommodation occurred throughout the transfer film and deep into the wear track. The CS22 source flow is high during initial transfer film formation, but decreases after running-in. The lower flows were associated with the formation of uniform UFG microstructures in the third bodies due to the presence of Al_2O_3 particles.

The high internal and ejection flows visible in the CS0 transfer film are partly due to structural instability. The causes of this instability could be among the following. First, the thicker the transfer film, the greater the mechanical moment induced from the friction force.

Second, the more material that accumulates as part of the transfer film, the greater chance that defects or incomplete bonding will provide a location for failure. And finally, should the contact pressure on the prow of transfer film be lost due to ejection flow of third body material, the hydrostatic pressure preventing crack propagation would be lost. Thus, the catastrophic detachment of transfer film observed in Fig. 5.3 should not be surprising in this scenario, and such an internal flow could originate at the sapphire/ transfer film interface or from preexisting cracks in the transfer film. Velocity accommodation in the form of shear occurred throughout the third body and 8–10 µm deep into the coating first body.

In CS22, during and after initial transfer film formation, grain refinement occurred due to strain localization in the vicinity of the Al_2O_3 particles. This led to stable, more highly refined microstructures in the transfer film and wear track. Strain localization then prevented deformation in the underlying microstructure and decreased the source flows considerably (see Fig. 5.14). As the mechanically mixed layers in CS22 became uniform and hardened, transfer was less likely to occur for several reasons. First, higher hardness led to a greater resistance to conformal adhesion. Second, fewer instances of microwelding, and hence adhesion, could occur because of passivation through uniform and high levels of oxygen. The layered microstructures in the CS22 transfer film indicate that either bands of mechanically mixed material were transferred directly to the counterface, but this seems unlikely due to their demonstrated stability. A more likely scenario is that after a piece of third body material detaches from the wear track as part of the wear flow, the underlying first body material is exposed and readily transferred to the counterface. Then, the same deformation process could occur there as in the wear track. The resulting internal and ejection flows were very low compared to CS0, and correspondingly the wear flow was lower by roughly an order of magnitude. The VAM are three in this scenario: shear in the third body, which is constrained to a thin layer, tensile cracking in the wear track third body, and elastic deformation of the third body and first body material. The presence of the tensile cracks permits elastic deformation through flexing of the third body material [72].

The mechanisms for the contrasting tribological behaviors of CS0 and CS22 could be through their differences in mechanical properties, adhesion, or both. In terms of adhesion, clean sapphire has a layer of surface oxygen atoms, and plastic deformation by the harder sapphire asperities would contribute to intimate contact at the sapphire/ transfer film interface [168]. The high adhesion of clean aluminum surfaces to sapphire can be related to the free energy of formation of aluminum oxide [169, 170], and bonding at this interface was found to be mixed ionic covalent by molecular dynamics simulations [171]. Thus, the formation of transfer film, particularly in early stages of sliding, can be partly attributed to adhesion at the sapphire-aluminum interface.

However, interfacial adhesion alone does not explain the instability of the CS0 transfer film versus the relative stability of CS22. As no Al_2O_3 particles have been observed directly at the sapphire/transfer film interface, it is questionable whether they play any role in enhancing adhesion at this interface. The relatively stability of the CS22 transfer film is more likely due to the enhanced mechanical properties of the CS22 third body material, which is driven by the presence of Al_2O_3 particles. Furthermore, the weaker third bodies of CS0 permit fracture and subsequent exposure of clean aluminum surfaces through source flow (Qs), leading to higher adhesion and friction at the sliding interface for CS0 than for CS22.

As the microstructural evolution of third body material is induced through deformation, some understanding of the microstructural changes occurring may be drawn from the literature on severe plastic deformation (SPD) processes. Various SPD processes, such as high-pressure torsion (HPT) and equal channel angular processing (ECAP), are employed to induce high shear strains into materials at low temperatures to create very fine grain structures [172]. Accumulated strains in excess of 10 may be readily induced using these methods, progressively forcing grains to subdivide at finer and finer length scales through the formation of high-angle grain boundaries [173]. Eventually, the high-angle grain boundary spacing converges with the subgrain size and the process saturates at grain/subgrain sizes on the order of 100–200 nm [80, 173]. SPD processes operate at high degrees of hydrostatic pressure and shear stress, and hence, they bear similar conditions to tribological contacts [80, 112]. Frequently, the crystallite sizes observed in third body microstructures are considerably smaller than what typically arises from SPD processes on Al and its alloys [173]. Mahato attributed this to the higher strain rates in sliding wear compared to SPD processing [80].

For both CS0 and CS22, third body microstructures showed ultrafine grain regions, with grain sizes appearing to be below 150 nm (see Figs. 5.9, 5.11). Yet the finest grained regions within the CS0 third bodies were mixed very closely with less highly deformed grains; this was particularly clear in Fig. 5.9 where the gradient of grain sizes and turbulent microstructures demonstrate the disorder of this process. The contrasting uniformity in the CS22 third body microstructures arises from the higher strain gradients and shear localization of the Al matrix around the Al_2O_3 particles. A study by Apps et al. [173] compared the SPD-processed microstructures of a single-phase Al alloy and an alloy containing micron-scale hard $Al_{13}Fe_4$ particles, finding that grain refinement occurred much more rapidly in the particle-containing alloy. Similar findings in an SPD-processed Al–Si alloy were attributed to enhanced dislocation formation around Si particles [174, 175]. Geometrically necessary dislocations, which form due the strain gradient surrounding the harder Si particles, cause a higher local rate of dislocation formation and hence accelerate the grain refinement process [174, 176]. Such models have been incorporated into tribological studies as well, as several studies in aluminum tribology have demonstrated smaller grains in the vicinity of stiff reinforcement phases [79, 80, 165]. Fragmentation of hard particles is commonly observed in SPD and tribology studies alike [1, 27, 76, 80, 174], further contributing to a higher strain gradient.

5.5 Conclusions

Dry sliding tribology experiments showed that dry sliding friction of sapphire against cold-sprayed Al—22 wt% Al_2O_3 (sample CS22) was generally lower and more stable than the cold-sprayed pure aluminum (sample CS0). *In situ* tribometry revealed strong contrasts between the two samples in terms of the behavior of the third body material adhering to the sapphire counterface. The CS0 transfer films exhibited instability marked by visible plastic flow, debris detachment, and subsequent plowing of new material, and some of these events corresponded with shifts in the friction coefficient. The CS22 transfer films remained stable throughout testing, correlating with the more steady friction behavior. This behavior remained true after 500 and 2,000 sliding cycles.

Subsequent *ex situ* analysis after 500 sliding cycles revealed further contrasts between CS0 and CS22 in terms of third body morphology, flow, and microstructure. The wear track and transfer film of CS0 showed evidence of bulk flow of third body material. The near-surface microstructures of CS0 were highly inhomogeneous and revealed that plastic deformation extended into the first body microstructures. The CS22 wear track and transfer film were comparatively more homogeneous, with the microstructures being largely constrained to a thin surface layer and consisting of ultrafine grained aluminum and fragmented Al_2O_3 particles. Nanoindentation revealed that the CS22 third body was considerably harder than that of CS0. The volumetric wear rate of CS22 was lower by roughly an order of magnitude compared to CS0 after 500 and 2,000 sliding cycles. Many of the *ex situ* observations are similar to previous dry sliding wear investigations of Al and Al-MMC materials, both cold sprayed and prepared by other processing routes.

The use of *in situ* and *ex situ* techniques in this study proved particularly powerful as the combination of the two permitted a more complete analysis of the tribological circuit for CS0 and CS22. This revealed that the strain localization caused by the presence of Al_2O_3 particles forced the internal flows (Qi) to be constrained to a thin layer. This promoted greater work hardening and oxidation of the CS22 third body, preventing deformation deeper in the first body. By constraining velocity accommodation to the third body material, the CS22 source flow (Qs) was greatly reduced, which slowed the rate of transfer to the counterface. With no strain localization, the source flow remained activated for CS0 throughout testing.

Acknowledgments

The authors gratefully acknowledge the financial support from the Canadian Foundation for Innovation (CFI) project No. 8246 for the cold-spray equipment, the CFI Leader's Opportunity Fund project No. 13029 for the *in situ* tribometer and nanoindentation equipment, and the Natural Sciences and Engineering Research Council (NSERC) Discovery Grants Program for the operational funding of this project. JMS acknowledges partial financial support from the McGill Engineering Doctoral Award (MEDA) program. Thanks are also due to the CLYM (Center Lyonnais de Microscopie, http://clym.insa-lyon.fr) for the access to the FIB/SEM (Zeiss NVision 40) and to N. Blanchard, A. Descamps-Mandine, Th. Douillard, and B. Van De Moortèle for the technical help. CLYM is supported by CNRS, le Grand Lyon, and le Conseil Régional Rhône-Alpes (France)

Chapter 6

The influence of Al_2O_3 particle morphology on the cold spray coating formation and dry sliding wear behavior of Al-Al_2O_3

J. M. Shockley, S. Descartes, P. Vo, E. Irissou, R.R. Chromik

Adapted from a paper of the same title published in *Surface and Coatings Technology* (2015), DOI 10.1016/j.surfcoat.2015.01.057. In the previous two chapters, the dry sliding wear behavior of Al and Al-Al_2O_3 samples, containing angular Al_2O_3 and consolidated with low pressure cold spray, was analyzed. Part of the analysis revealed that the formation of third body material occurred in the immediate vicinity of the Al_2O_3 particles, and this raised a question of how the Al_2O_3 particle morphology would influence the dry sliding wear behavior. A similar question could be posed regarding the influence of Al_2O_3 particle morphology on the coating formation during cold spray, described in terms of deposition efficiency and the relative recovery of Al_2O_3 into the coating. Thus, in this chapter, Al and Al-Al_2O_3 coatings were deposited using high pressure cold spray, using angular and spherical morphologies. The deposited coatings were subjected to dry sliding wear and analyzed in terms of the friction, wear, and third body behavior and properties.

Abstract

Five Al-Al_2O_3 coatings were deposited by gas dynamic cold spray, using feedstocks containing 0, 10, and 50 wt.% of Al_2O_3 particles admixed into commercially pure Al powders. Two feedstocks were made using Al_2O_3 powders with an angular, blocky Al_2O_3 morphology, two feedstocks used Al_2O_3 powders with a spherical morphology, and the fifth consisted of 100% Al. The influence of Al_2O_3 concentration and morphology in the feedstock powders on the cold spray coating formation was measured in terms of Al_2O_3 recovery in the coatings, deposition efficiency, and microstructural analysis. The Al-Al_2O_3 coatings were then subjected to dry sliding wear experiments from which the friction, wear, and microevolution of third body structures in the wear track and transfer film were observed. The spherical Al_2O_3 morphology was associated with improved tribological behavior compared to the angular morphology when comparing similar coating concentrations of Al_2O_3.

6.1 Introduction

Aluminum matrix composite (Al-MMC) materials with hard reinforcements are valued for their corrosion resistance, low density, and improved wear resistance over the unreinforced alloy materials [2]. Depending on the processing route and application, the reinforcement phase may consist of long fibers, short fibers, or particulates, and are often based on SiC or Al_2O_3, among other materials [1]. Particulate-reinforced Al-MMC materials may be produced through bulk processing or applied as coatings, and have been found to have substantially lower wear rates compared to the un-reinforced matrix alloy in most wear regimes [1, 9, 27, 34, 177].

Although thermal spray routes are the most conventional choice for depositing Al-MMC coatings, a more recent alternative is the cold gas dynamic spray technique, more often known as cold spray [9, 11, 156, 157]. The cold spray process operates by accelerating feedstock powders through a preheated inert gas stream that is passed through a de Laval-type nozzle. The gas and powders attain supersonic velocities, and upon impact with a substrate, extensive plastic deformation is induced and metallurgical bonding takes place by way of an adiabatic shear instability [4–6, 8, 48]. In-flight chemical reactions and substrate heating during cold spray are minimal compared to conventional thermal spray processes because of the lower gas temperatures. Furthermore, the high velocities during deposition lead to a very high density in the cold sprayed deposits [48]. Cold spray of pure aluminum and Al-MMC materials has become a mode of repair and corrosion protection for magnesium aerospace gearbox components, among other applications [157, 158].

To produce Al-MMC coatings by cold spray, reinforcement particles are admixed into the feedstock powder, and during deposition some particles are recovered into the final coating. Hard reinforcement particles do not participate in the adiabatic shear instability process, so the particles must embed themselves in the coating during formation and the recovery of hard particles may be less than in the initial feedstock [9, 11]. The commonly available Al_2O_3 powders are fused and crushed, which are dense with no internal porosity and have blocky, angular morphologies. One means of modifying the Al_2O_3 particle morphology is by post-treating angular Al_2O_3 by way of a plasma spheroidization process. Previous studies by the authors explored the dry sliding wear behavior and wear mechanisms of cold sprayed pure Al and Al-Al_2O_3 composite coatings using the angular morphology [161, 177]. In these studies, the role of angular Al_2O_3 particles in the tribological processes was explained through the use of *in situ* tribometry and microanalysis of the "third bodies," which are the mechanically modified structures formed at the sliding interface [66]. However, given the commercial availability of both angular and spherical Al_2O_3 particle morphologies, understanding the influence of Al_2O_3 morphology in the cold spray deposition process and tribological behaviors of cold sprayed Al-Al_2O_3 is of potential significance to the coatings industry.

In the present study, the influence of Al_2O_3 particle morphology on the cold spray deposition and subsequent dry sliding wear behavior of Al-Al_2O_3 coatings is explored. Two Al_2O_3 powders, one angular and one spherical, were admixed into commercially pure Al powder at varying concentrations and the powder mixtures were cold sprayed at simliar deposition conditions. Analysis of deposition efficiency was conducted through *in situ* monitoring of powder flow rates, and Al_2O_3 recovery in the coating was analyzed through microstructural analysis. Then dry sliding wear tests were conducted against a sapphire counterface, by which the evolution of wear rate, frictional forces, and the subsurface microstructure were studied. Through the study of cold spray deposition behavior, coating microstructure, and dry sliding wear behavior, a discussion of the implications of Al_2O_3 morphology will be developed.

6.2 Experimental methods

6.2.1 Cold spray deposition and coating characterization

Four batches of feedstock powder were prepared by admixing commercially available spherical Al powder (Valimet H-15, d_{50}= 22.6 µm) with 10 and 50 wt.% of either angular morphology Al_2O_3 powder (Plasmatec, d_{50}= 25.5 µm) or a plasma spheroidized spherical morphology Al_2O_3 powder (Tekna, d_{50} = 24.3 µm) (see Figure 6.1). Coatings were deposited onto aluminum alloy AA6061 substrates using a Plasma Giken PCS-800 cold spray system, achieving a thickness of 4-5 mm. A nitrogen carrier gas was used at a 400° chamber temperature and 3 MPa chamber pressure. The 76.2 mm wide substrates were kept stationary and the gun nozzle moved at a 200 mm/s traverse speed with a 1 mm step size. Powder consumption was monitored *in situ* using digital scales upon which the powder hopper was mounted. Deposition efficiency was calculated by dividing the total mass of the deposited coating by the mass of powder sprayed.

Cross-sections of each coating were prepared for analysis by sectioning using a diamond wafering saw, cold mounting in epoxy, fine grinding using 400, 800, 1200, and 2400 grit sizes, and polishing using 9 µm, 3 µm and 1 µm diamond pastes followed by 0.05 µm colloidal silica. The concentration of Al_2O_3 recovered in each coating was measured by image analysis, during which ten random backscattered electron (BSE) images of polished cross-sections at 700x magnification were taken in a scanning electron microscope (SEM) and analyzed by pixel count to calculate volumetric the Al_2O_3 concentration, which was converted to mass concentration. Prior to wear testing, the coating surfaces were subjected to fine grinding and cleaned with ethanol. The root mean square roughness value fell between 0.4 and 0.8 µm for all samples after preparation. Microhardness measurements were taken using a Vickers indenter applied at a 200 gf (1.96 N) load with a hold time of 5 seconds, and each hardness value reported here shows the average of at least ten indents taken at random locations on the polished coatings.

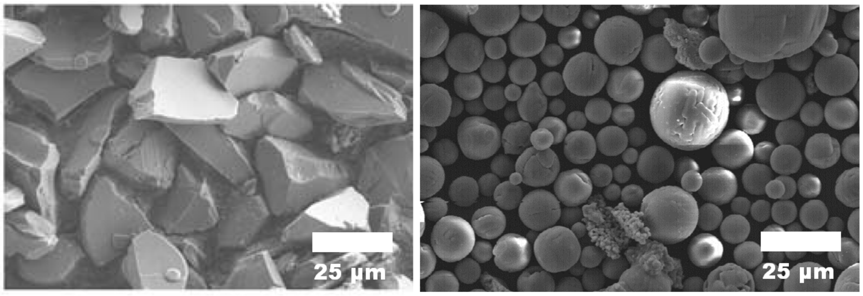

Figure 6.1 – Feedstock Al_2O_3 powders before admixing. Left: angular Al_2O_3(from [9]). Right: spherical Al_2O_3.

6.2.2 Sliding wear test conditions

Sliding wear tests on the prepared coatings were performed in dry air (below 1% relative humidity) at room temperature (21-24° C). All tests were conducted with a sliding speed of 3 mm/s, a track length of 10 mm, and normal load of 1 N. Friction forces were measured at a sampling rate of 800 Hz using a piezoelectric sensor mounted underneath the sample stage. Monocrystalline α-Al_2O_3(sapphire) spheres (or hemispheres for *in situ* tests) of 6.35 mm diameter were used as the counterface material. Wear tests were run to 50, 500 and 2000 sliding cycles, corresponding to total sliding distances of 0.5, 5, and 20 m, respectively. Three repeats were used for the 50 and 500 cycle condition, while two repeats were used for the 2000 cycle condition. One 500-cycle test per coating was performed in the *in situ* configuration, in which microscopic observation of the contact region was carried out through the transparent hemispherical counterface using an optical microscope [140, 161, 177]. For this purpose, the microscope was mounted above the counterface and was equipped with a 10x objective lens and a commercially available camcorder. The use of the *in situ* configuration was not found to influence the friction or wear rate behavior compared to the conventional configuration.

6.2.3 Analysis of wear tracks

Using an SEM, wear track surface features were observed and elemental contrast was revealed by energy dispersive x-ray spectroscopy (EDXS). Surface morphologies of the wear tracks and counterface transfer material were extracted using a Wyko NT8000 optical interferometer. Wear rates were calculated in accordance with ASTM Standard G99 by first integrating height profiles across the wear track above and below the original surface height to calculate a net worn cross-sectional area. This was then multiplied by the wear track length to obtain a net volume of material removed from the surface. Between 80-100 surface profile measurements per wear track were obtained.

Sub-surface regions of the worn surfaces were revealed by cross-sectioning. Wear tracks were cut transverse to the sliding direction using a lubricated slow-speed abrasive cutting wheel, followed by cold mounting in epoxy and mechanical polishing. Microstructural analysis was carried out in an SEM with a backscattered electron detector to reveal aluminum grains through electron channeling contrast imaging (ECCI).

Nanoindentation was performed on wear track cross-sections and directly on wear track surfaces using a Hysitron Triboindenter equipped with a Berkovich diamond indenter with a tip defect radius of approximately 125 nm. Indents were performed using a 5 second loading time to a maximum force of either 400 or 2000 µN, a 5 second hold time at maximum load, and a 5 second unloading time. To precisely control the location of the indents, the Berkovich indenter was used to collect *in situ* scanning probe microscopy (SPM) images that were matched to previously acquired electron micrographs of the areas of interest. Each hardness value reported was calculated using the Oliver and Pharr method [143], and represents the average of at least 8 indents.

6.3 Coating formation

The recovery of Al_2O_3 varied according to the feedstock content and Al_2O_3 particle morphology (see Table 1 and Figure 6.2). The angular Al_2O_3 recovery was similar to that measured in previous studies, in spite of the use of different cold spray guns and deposition velocities [9,11]. The amount of recovery of spherical Al_2O_3 was considerably lower than the amount of recovery of angular Al_2O_3. The deposition efficiency (DE) of the 10 wt.% Al_2O_3 feedstock powder was unchanged from that of the pure Al powder for the angular Al_2O_3 morphology and slightly higher for the spherical morphology. The DE of both 50 wt.% Al_2O_3 feedstock powders was significantly lower for both morphologies (see Figure 6.2).

Sample Designation	Al_2O_3Particle Morphology	Al_2O_3 in Feedstock Powder (wt.%)
CS0	n/a	0
ANG10	Angular	10
ANG22	Angular	50
SPH3	Spherical	10
SPH11	Spherical	50

Table 6.1 – Sample designations and Al_2O_3 content in the feedstock powder. Sample designations refer to the morphology and amount of Al_2O_3 recovered in the coating (see Figure 2).

In cold spray of pure metals, coating formation has been attributed to plastic deformation at the interface of the impacting particle, which leads to "jetting" of the interfacial material and metallurgical bonding by way of adiabatic shear instabilities [4–6, 8, 48]. Thus a hard elastic secondary phase, in this case Al_2O_3, is not believed to participate in this aspect of the coating process due to its lack of plasticity in this temperature range. When hard ceramics

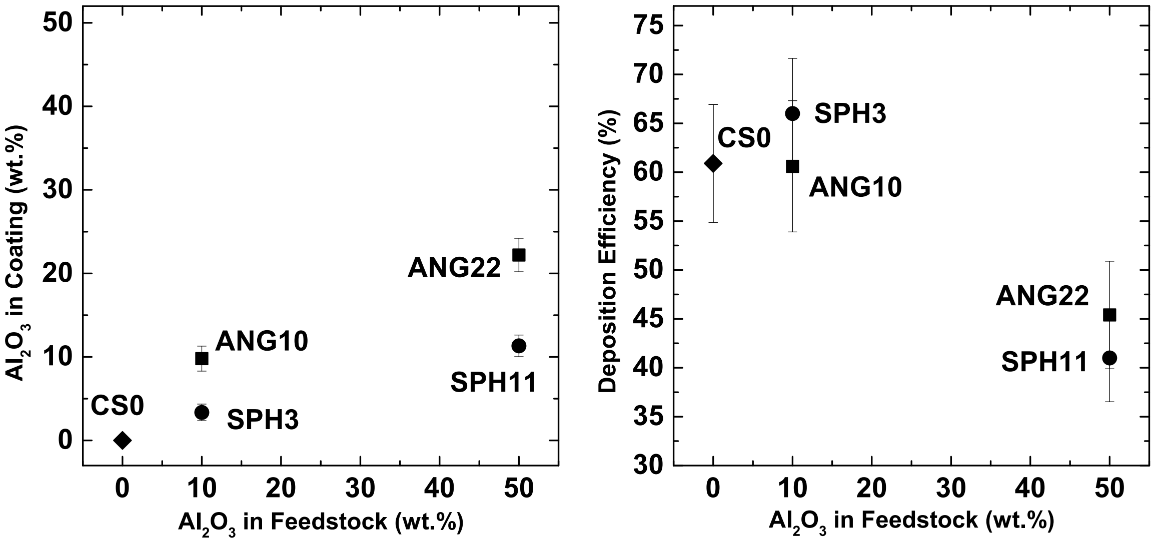

Figure 6.2 – Recovery of Al_2O_3 (left) and deposition efficiency (right) of the sprayed coatings.

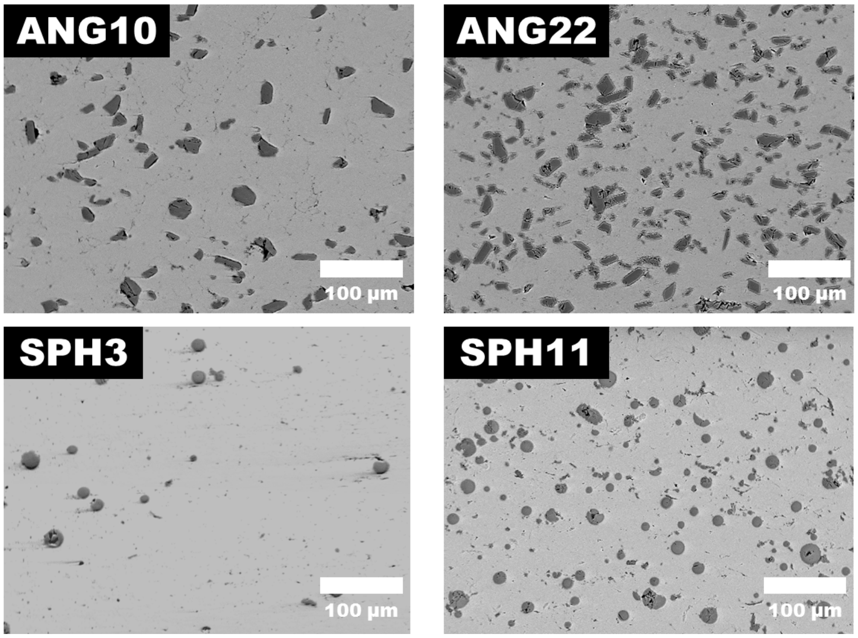

Figure 6.3 – Cross-sections of the as-sprayed microstructures viewed roughly 1 mm below the top surface of the deposits.

are cold sprayed alone, they behave erosively and no coating is formed [9,178]. When admixed into Al powder, they can be recovered in the coating, but generally the coating contains a lower hard particle content than the feedstock powder [9]. The results presented in Figure 6.2 showed lower Al_2O_3 concentration than their feedstock powders, with the exception of ANG10, which had roughly the same amount. This Al_2O_3 recovery behavior is consistent

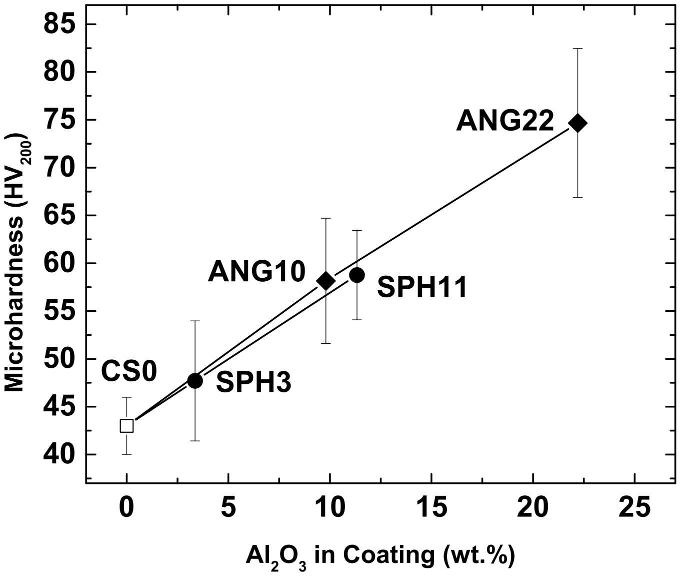

Figure 6.4 – Microhardness measurements of the tested coatings.

with that observed in previous studies [9,11]. The change of deposition efficiency as a function of feedstock Al_2O_3 has also been previously observed, where at lower Al_2O_3 contents it can be beneficial to the DE, but beyond a certain point is detrimental [9,16]. The initial benefit to DE may be attributed to peening and cleaning of the surface by the hard particles, but at higher concentrations, the DE is lowered through erosive behavior and a lack of bonding between Al_2O_3 particles.

The lower recovery of spherical Al_2O_3 compared to the angular morphology can be partly explained by modelling and experimental work by Getu et al. [179] on the embedding behavior of hard spherical and angular particles in ductile substrates. In both cases, the elastic rebound forces during impact could be sufficient to prevent embedding unless certain criteria were met. For angular particles, the directions of the normal and tangential components of elastic rebound forces remain constant due to the flat sides and sharp corners, and so long as the static friction forces between particle and substrate materials were sufficiently high, the particle will imbed [179]. For spherical particles, the constant curvature of the particle boundary leads to higher elastic rebound forces normal to the impact direction, and to embed the sphere must impact to a depth greater than its radius and be enveloped by material. Furthermore, spherical particles were not predicted to embed at all at impact angles perfectly normal to the substrate, as the elastic rebound forces were always higher than the friction forces retaining it [179]. Although this study does not consider the multi-particle impact scenario of cold spray, nor does it consider possible velocity differences between the angular and spherical particles, nonetheless the more stringent criteria for embedding spherical particles may be the cause for the lower spherical Al_2O_3 recovery seen here.

Microstructural examination revealed that the angular and spherical Al_2O_3 morphologies were retained after the cold spray process, although evidently some particle fracture occurred during deposition (see Figure 6.3). The porosity was below 2% for each coating. Microhardness measurements showed a linear relationship as a function of coating Al_2O_3 content, regardless of particle morphology (see Figure 6.4). Grain sizes in the aluminum matrix for all coatings showed a variation between roughly 200 nm and 5 µm; the arithmetic mean of several hundred grains on sample CS0 was 1.0 ± 0.8 µm (see Figure 6.5).

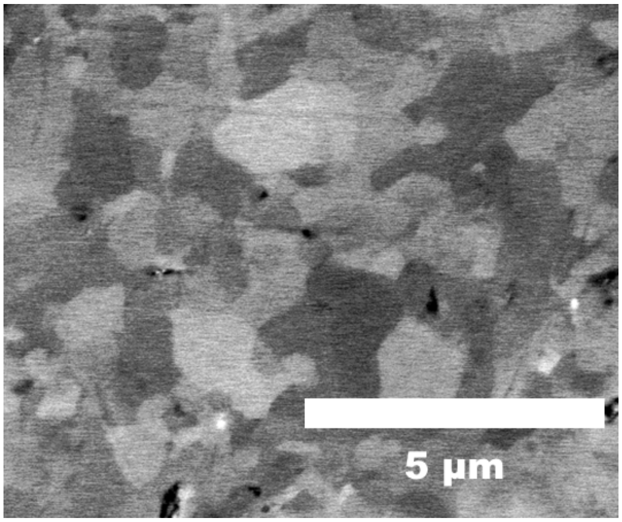

Figure 6.5 – Representative ECCI micrograph of typical as-sprayed grain sizes in the aluminum matrix for all samples prior to sliding wear testing.

6.4 Dry sliding wear tests

6.4.1 Friction and transfer film behavior

The friction behavior during sliding wear tests was strongly influenced by the presence, concentration, and morphology of Al_2O_3 (see Figure 6.6). Sample CS0 exhibited a randomly fluctuating friction coefficient, varying between 0.45 and 1.2. Samples ANG10 and SPH3 showed less fluctuation behavior than CS0, while samples ANG22 and SPH11 showed the least fluctuation after an initial run-in period. Average friction data from all tests in the ranges of 0-50 cycles, 200-500 cycles, and 1000-2000 cycles were compiled as histograms (see Figure 6.7). Friction fluctuation corresponds to wide peaks, and in many cases peaks appear to be composed of multiple smaller peaks. As friction stabilizes, the peaks become narrower; this effect was clearly visible for samples ANG22 and SPH11 after 500 and 2000 cycles. Although the pattern for the friction spikes was semi-stochastic, the general friction behavior of samples as revealed through the histograms in Figure 6.7 was generally reproducible from test to test.

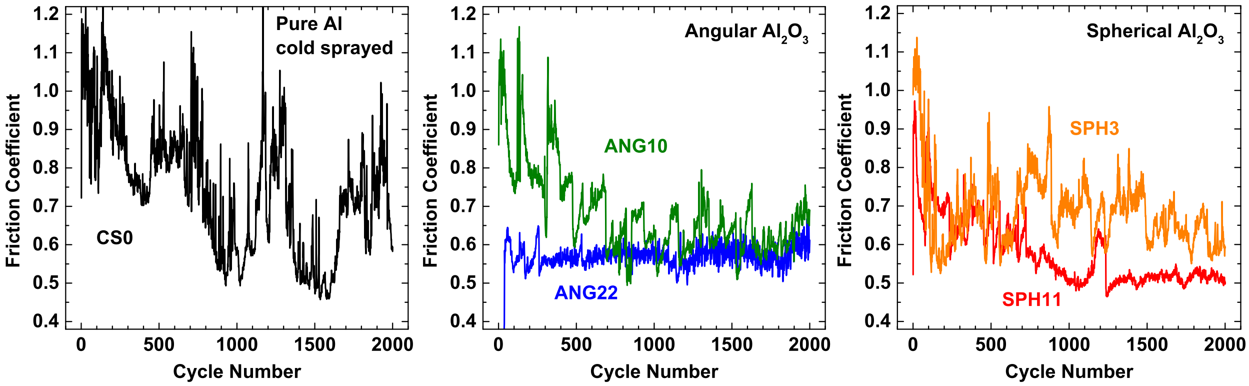

Figure 6.6 – Representative plots of average friction coefficient plotted versus cycle number: pure cold sprayed Al (left), angular Al_2O_3 samples (middle), and spherical Al_2O_3 samples (right).

Behavior of third body material, monitored through *in situ* tribometry, also varied according to Al_2O_3 concentration and morphology (see Figure 6.8) [140, 161, 177]. Samples SPH3 and ANG10 showed similar behavior, where the transfer films were highly active; plowing and material transfer were clearly visible, as were plastic flow and material detachment. The

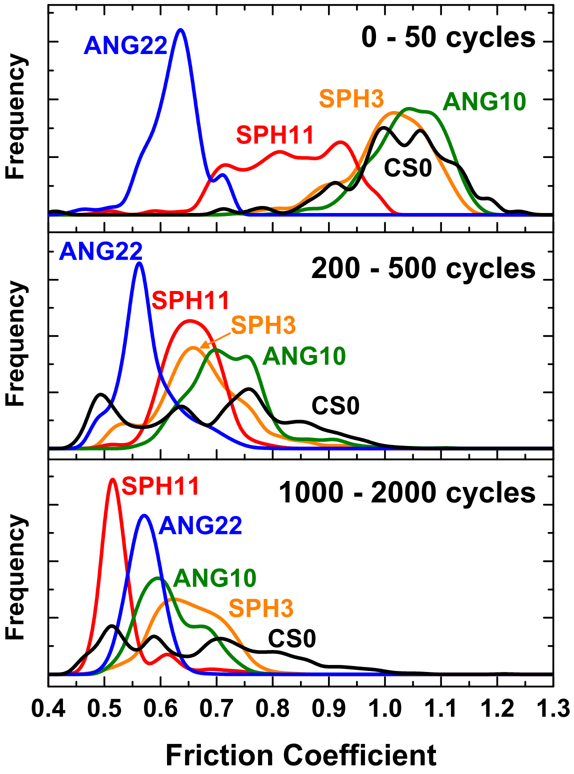

Figure 6.7 – Friction plotted as frequency distributions; a spline fit was used plot the binned data.

holes left by material detachment were soon filled in by new transfer material. In some cases friction events could be directly correlated to events in the transfer film, while in other cases no change in the tranfser film was visible. After 100 sliding cycles, samples SPH3 and ANG10 show large transfer films that take up most of the roughly 2 mm field of view (see Figure 6.8). The transfer films continued growing after this point and, by 500 sliding cycles, became larger than the field of view. Viewed *ex situ*, the SPH3 and ANG10 transfer film morphologies exhibited a maximum thicknesses of 90 - 100 µm at the prows, the leading edge of material transfer [70, 177]. In contrast to SPH3 and ANG10, *in situ* observations of samples SPH11 and ANG22 showed less transfer film activity after the initial transfer film formation. Activity such as hole formation and plastic flow was less obvious, if at all. The apparent area of transfer film of SPH11 remained relatively constant after the first 100 cycles, and by 500 cycles a central region opened where movement was visible, as evidenced through the *in situ* observations as well as the transfer film morphology. For ANG22, the center of the transfer film remained stable and present after 500 sliding cycles. For both SPH11 and ANG22, the thickness of transfer film viewed *ex situ* adhering to the sapphire did not exceed roughly 25 µm.

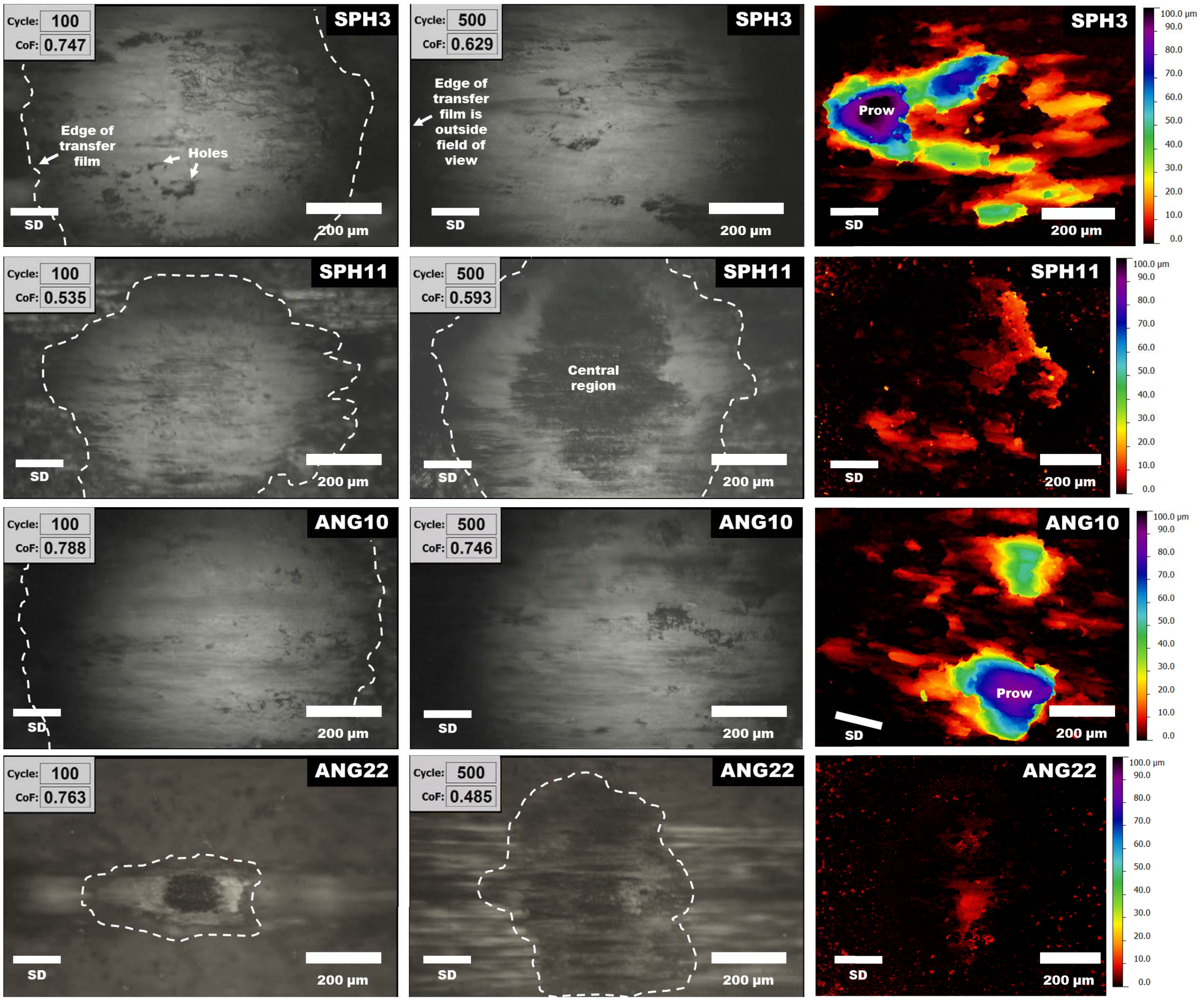

Figure 6.8 – Left and middle: Transfer films observed *in situ* at 100 and 500 sliding cycles. Transfer film borders are marked where visible. Right: morphologies of transfer films adhering to the counterface after 500 cycles. "SD" indicates sliding direction.

6.4.2 Wear track surface analysis

Surface analysis of wear tracks in an SEM revealed differences in the morphologies of third body material, which varied as a function of Al_2O_3 particle content, morphology, and sliding cycles (see Figure 6.9, left). After 50 cycles, samples SPH3, SPH11, and ANG10 showed some evidence of adhesive wear. This is characterized by smearing behavior, which results in tongue-shaped, layered structures on the surface of the wear track, and is commonly observed in aluminum tribology [11, 164, 177]. Sample ANG22, in contrast, showed the development of a coherent and smooth tribofilm after 50 cycles. Some regions of the SPH11 wear track also showed early stages of this development after 50 cycles, as evidenced by the smoother band of material in the center compared to the smeared material around it.

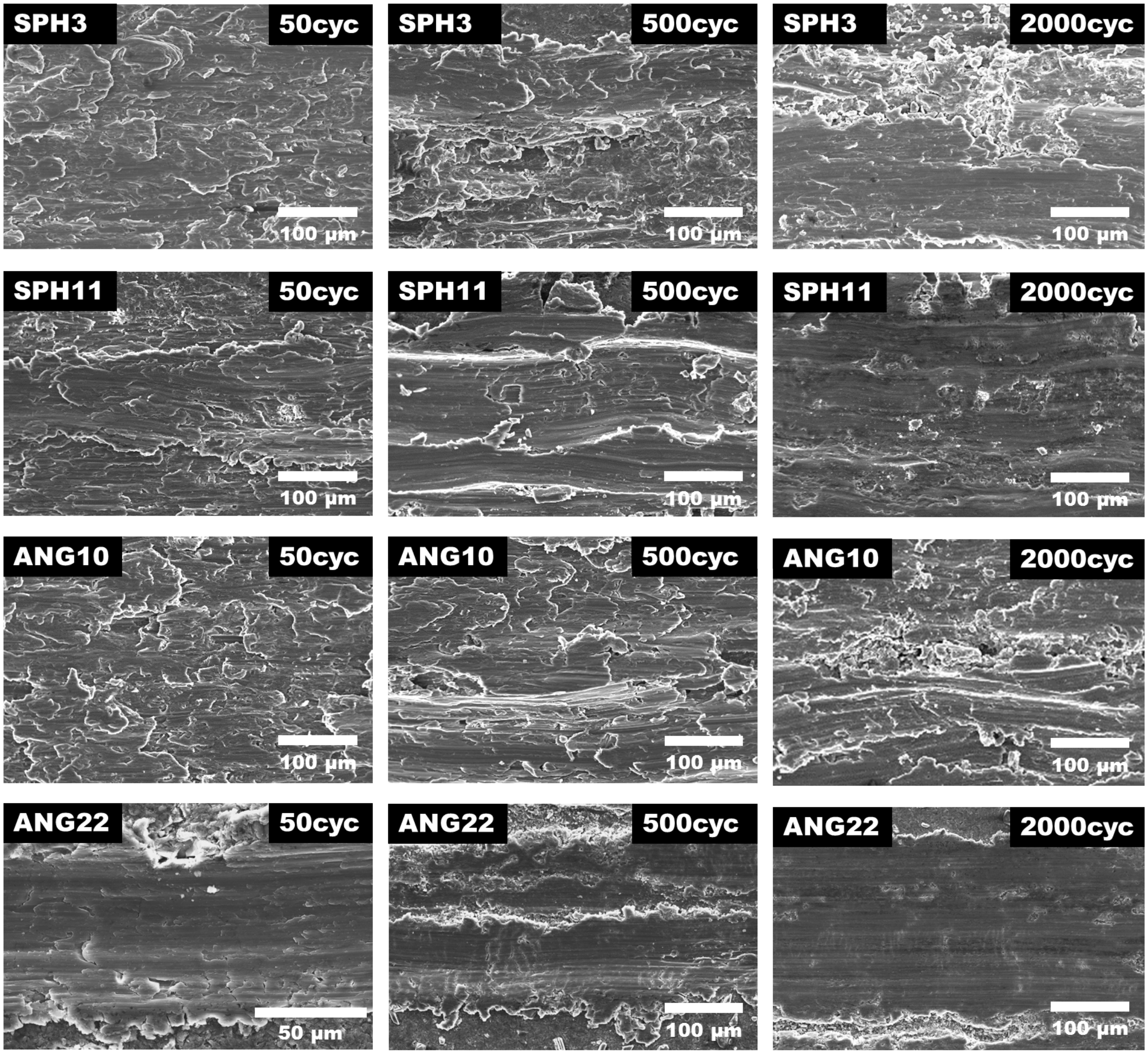

Figure 6.9 – Surface features of the wear tracks after 50, 500, and 2000 sliding cycles. Sliding direction is horizontal.

After 500 and 2000 cycles, surface analysis revealed a mix of adhesive wear and the development of third bodies (see Figure 6.9, middle and right). Sample SPH3 showed the beginning of tribofilm develoment after 500 cycles, and by 2000 cycles distinct patches of smooth tribofilm were present in the wear track, surrounded by regions of adhesive smearing and wear debris. SPH11 showed uniform coverage of a third body film after 500 cycles, present as half-cylinder regions about 100 µm wide, while after 2000 cycles these regions had flattened into a single coherent, smooth film. ANG10 showed continued evidence of adhesive wear after after 500 and 2000 cycles, although tribofilm patches were visible in the wear track as well. Finally, ANG22 showed smooth, coherent tribofilms throughout testing, in keeping with previous studies [11, 177].

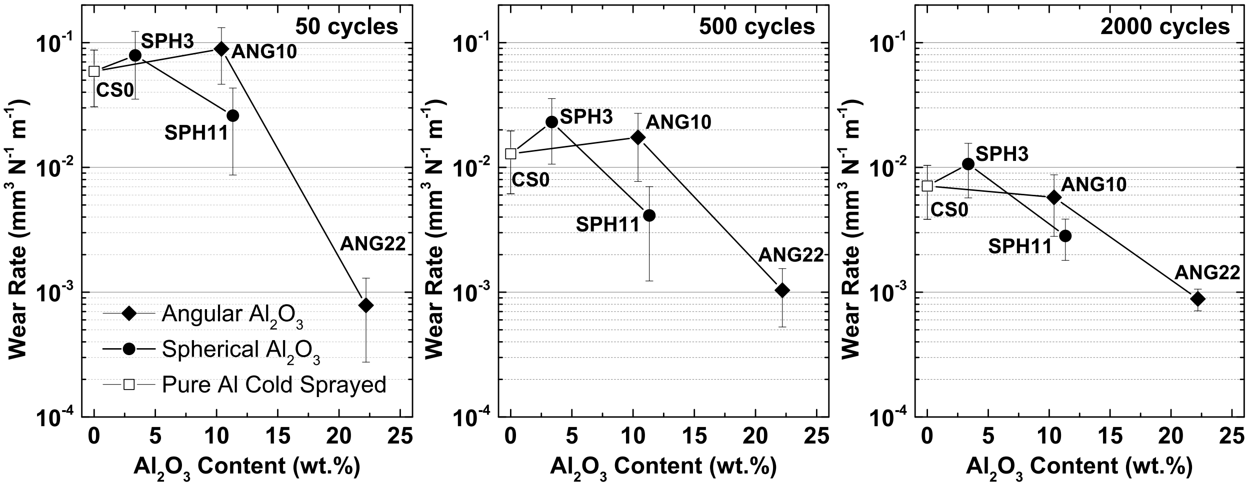

Figure 6.10 – Volumetric wear rate plotted versus cycle number. The error bars show plus and minus one standard deviation.

Wear rates were dependent on Al_2O_3 concentration and morphology (see Figure 6.10). For all samples except ANG22, wear rates were highest at 50 cycles and lower at 500 and 2000 cycles. CS0, SPH3 and ANG10 had comparable wear rates, although the wear rate of SPH3 was slightly higher than that of CS0. Sample SPH11 consistently showed a lower wear rate than ANG10, in spite of similar Al_2O_3 concentrations. This effect was most prominent at 50 and 500 cycles, where the mean wear rate of SPH11 was roughly one third of that measured for ANG10, while after 2000 cycles it was roughly one half.

6.4.3 Wear track microstructural analysis and mechanical properties

Transverse cross-sections of a wear track of SPH3 after 500 sliding cycles revealed a mix of smooth and rough sections as was visible through surface analysis in Figure 6.9. In a smooth section shown in Figures 6.11(a) and 6.11(b), a coherent layer of ultrafine-grained Al (UFG Al) is present 3-10 µm thick. Underneath the UFG Al layer is coarse-grained aluminum (CG Al) appearing similar to that observed in the as-sprayed microstructure (see Figure 6.5). Similar to SPH11, the UFG Al runs up the side and partially envelops the spherical Al_2O_3 particle. In the rough region shown in Figure 6.11(c), an extruding region of material largely consisting of UFG Al is visible, with cracks visible between various sections.

Cross-sections of the near-surface material in ANG10 after 500 sliding cycles revealed deformed, ultrafine-grained material in a region 10 - 20 µm thick on top of the underlying coating which appears to be very little changed from the as-sprayed microstructure (see Figure 6.12). The deformed region consists of a mixture of ultrafine grained aluminum (UFG Al) and Al_2O_3 particles, some of which have been fragmented during the cold spray process or during sliding. Cracks are visible between layers of UFG Al and at the interface with the underlying large-grained aluminum (CG Al), and these cracks often run to the corners of Al_2O_3 particles. The underlying CG Al microstructure shows grain refinement in roughly the top 5 µm.

Wear track microstructures from sample SPH11 after 500 sliding cycles (Figure 6.13) show the formation of a coherent, fine-grained layer across the entire wear track surface. Generally, this layer is roughly 5-10 µm thick, consisting of a UFG Al enveloping and partially spread along the top of Al_2O_3 particles. Below this layer is CG Al. Compared to the thick region of fine grained material of ANG10, few cracks are visible in sample SPH11, nor are any visible at the interface with the underlying first body. In the UFG layer, regions of dark contrast closer to the sliding surface contained elevated levels of oxygen.

Wear track microstructures of CS0 and ANG22 (not pictured) were examined in a previous study on cold sprayed Al-Al_2O_3 [177]. In that study it was observed that for CS0, layers of material 10-20 µm thick, exhibiting a mix of UFG and CG Al material were smeared on top of the underlying material in a similar fashion as ANG10 in Figure 6.12, and grain refinement was visible penetrating 5-10 µm deep into the underlying microstructure. For ANG22 (not pictured), a coherent UFG Al layer 2-5 µm deep with occasional fragments of Al_2O_3 was observed on top of a microstructure that appeared unchanged from the as-deposited state.

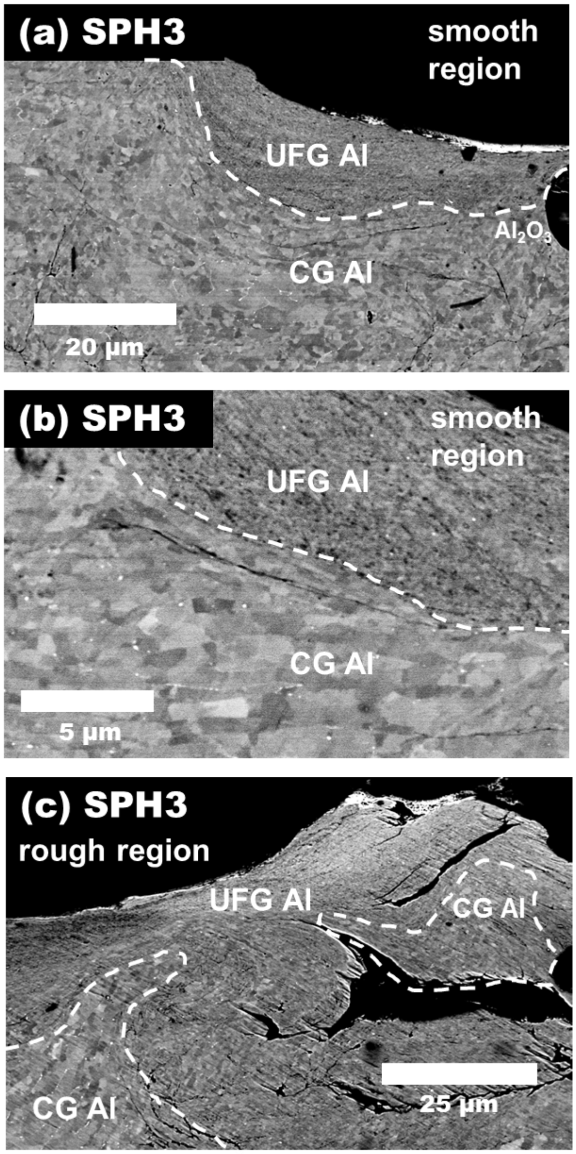

Figure 6.11 – Cross-sections of the near-surface microstructures after 500 sliding cycles for sample SPH3.

Nanoindentation on the UFG Al regions of the SPH3, ANG10, SPH11, and ANG22 wear

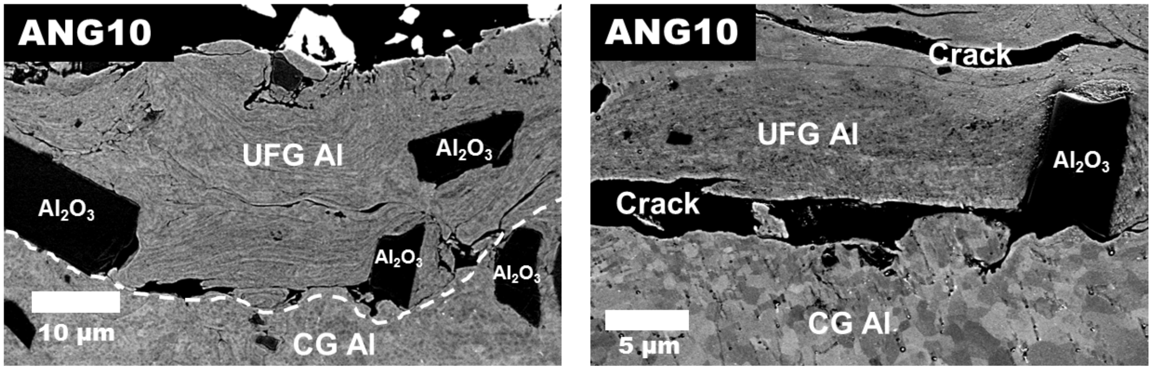

Figure 6.12 – Cross-sections of the near-surface microstructures after 500 sliding cycles for sample ANG10.

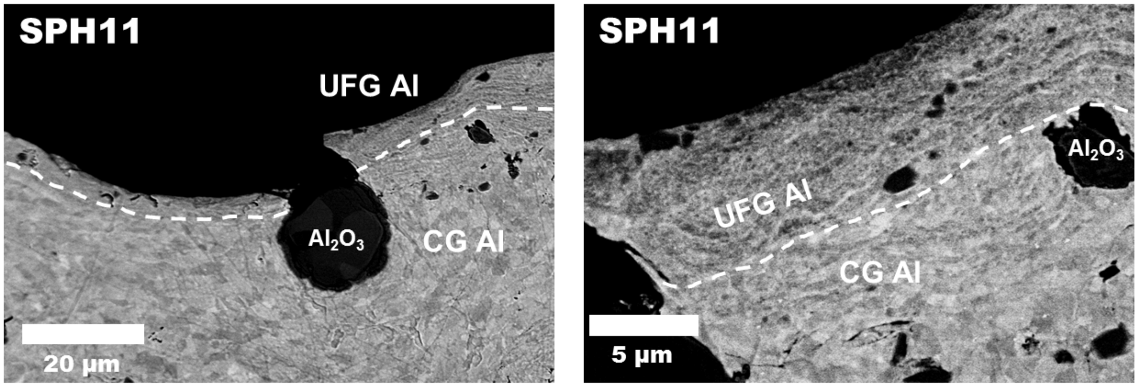

Figure 6.13 – Cross-sections of the near-surface microstructures after 500 sliding cycles for sample SPH11.

tracks after 500 sliding cycles were found to be of elevated hardness compared to the CG Al regions (see Figure 6.14). For SPH11 and ANG22, the average hardness was roughly 3.8 GPa, which is very close to ANG22 wear track measurements in a previous work [177]. For both SPH3 and ANG10, the average hardness was around 2 GPa. This is slightly higher than previous measurements on CS0 which were on average around 1.5 GPa [177]. In all cases the UFG regions were harder than the underlying CG Al which had an average hardness of roughly 1 GPa, which is similar to that observed previously [177] and is the same as the hardness of the as-sprayed aluminum matrix prior to any wear testing.

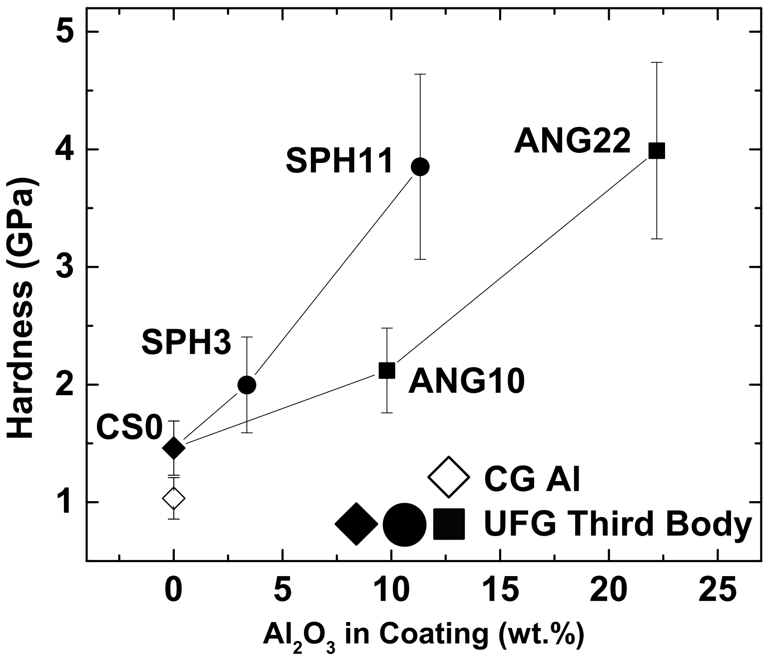

Figure 6.14 – Hardness of CG Al and UFG material (from Figures 6.12, 6.13, and 6.11) in the tested samples. Data for CS0 UFG Al was taken from a previous study by the authors [177].

6.5 Connections between Al_2O_3 particle morphology and the observed tribological behavior

For the tested Al-Al_2O_3 materials, contrasts were revealed in the friction, wear rates, transfer film behavior, and sub-surface microstructural changes that occurred during dry sliding. As tribological behavior is ultimately dictated by the behavior of third bodies at the sliding interface, it is clear through these results that both the morphology and the concentration of Al_2O_3 particles help drive the material transformations that create an "efficient" third body layer that lowers friction and wear.

Samples CS0, ANG10, and SPH3 exhibited the highest wear rates and the most unstable friction coefficients. Correspondingly, the third body behavior was very similar between ANG10 and SPH3. When viewed *in situ*, the third bodies were highly dynamic and exhibited frequent detachment of material; and when viewed *ex situ*, thick prow-shaped regions on the order of 100 µm thick were observed (see Figure 6.8). These so-called Antler prows are associated with the active transfer of material from one surface to another, and it can lead to generation of new third body material [70,177]. In the SPH3 and ANG10 wear tracks, surface analysis revealed evidence of adhesive wear, characterized by extensive plastic deformation causing a smearing effect. For ANG10, microstructural analysis showed that the adhesive wear led to thick third body layers settling in the bottom of the wear track, consisting of UFG Al and Al_2O_3 particles. For SPH3, the smooth regions of UFG Al show the beginning of a coherent third body layer forming, but the rough regions show that the process of wear debris formation was still very active. In spite of the different morphologies between the ANG10 and SPH3 third bodies, they were of comparable similar hardness values (Figure 6.14). The behavior of ANG10 and SPH3 in terms of friction, wear, and third body behavior is similar to that observed for CS0 in a previous study [177], indicating that the contents of 3 wt.% spherical Al_2O_3 and 10 wt.% angular Al_2O_3 were insufficient to greatly modify the tribological behavior in dry sliding.

Samples SPH11 and ANG22 exhibited the lowest wear rates and the most stable friction coefficients. The third body behavior viewed *in situ* for both samples was far less active than for the SPH3 and ANG10, and *ex situ* analysis revealed thin transfer films adhering to the counterfaces without any visible Antler prows. Surface analysis of SPH11 and ANG22 revealed wear tracks that were relatively smooth, and in cross-sections SPH11 revealed the formation of smooth, coherent third body layers 5-10 µm thick of UFG Al that partially enveloped the spherical Al_2O_3 particles. The microstructures of SPH11 are quite comparable to those observed in ANG22 [177], where a consistent, coherent third body layer consisting of UFG Al and fragments of Al_2O_3 was formed. Furthermore, the SPH11 and ANG22 third body layers were of very similar hardness values. Although the wear rates were lower for ANG22 than for SPH11, and the friction coefficient of SPH11 was more unstable than that of ANG22 at early sliding cycles, the tribological processes were nonetheless similar between the two samples after the initial running-in period, which was longer for SPH11 than ANG22.

Therefore to achieve lower wear rates and friction, the most effective third body for this system consisted of a single coherent layer of UFG Al that is between 2 and 10 µm thick, is relatively free of cracks, and has a hardness of roughly 3.8 GPa. Third body layers of these criteria formed only for samples SPH11 and ANG22. The formation of this layer was linked to a coupling of sufficiently high concentration of Al_2O_3 particles and of the particle morphology. As aluminum is transferred and smeared across Al_2O_3 particles, strain localization and high strain gradients in the vicinity of the hard particles results in enhanced dislocation formation and grain refinement. This effect of localized grain refinement in the vicinity of hard particles has been observed in severe plastic deformation (SPD) process such as high pressure torsion [173–175]. The increase in hardness is linked to the extreme amount of grain refinement and work hardening in this layer, as well as tribo-oxidation. Kim et al. studied the oxygen contained in wear debris formed after dry sliding on pure aluminum and found that it could be present as a metastable oxygen solid solution, formed through the extreme plastic deformation processes occurring at the sliding interface [159]. Although a quantitative analysis of oxygen content in the mechanically mixed material was not carried out in this study, a previous study by the authors on the third body material of a similar material system found significant oxygen content, yet it was lower than that of stoichiometric Al_2O_3 [177].

SPH11 and ANG10 had comparable Al_2O_3 contents and microhardness values; yet at this concentration of Al_2O_3, the most effective third body layer formed only in the case of the spherical Al_2O_3 morphology. Reinforcement particle morphology in Al-MMC materials has been previously shown to strongly influence tribological behavior. Tribological studies on Al-Si alloys, which are considered *in situ* Al-MMC materials and are frequently used in tribological applications, have found that the sphericity of the Si phase can have a strong effect on wear rates. Elmadagli et al. found that in Al-Si alloys, heat treatments could cause the as-cast acicular Si morphology to spheroidize [82]. This spheroidization step was attributed to a reduction of wear rates by roughly 30%. Yang et al. measured similar reductions in wear rates after adding alloy elements promoting Si spheroidization, and partly attributed this to the observation that cracks in angular Si particles could propagate into the third body layer and lead to detachment of wear debris [180]. Such third body instability would lead to greater wear debris generation, and this is likely the case in the present study as well.

Further study of literature on the deformation behavior of Al-MMCs offers a partial explanation for the influence of particle morphology. When Al-MMC materials are deformed, whether in tension, compression, or shear, the plastic flow of the matrix is constrained in the vicinity of stiff reinforcement particles [133]. The resulting stress concentration induces strengthening to the composites compared to the unreinforced matrix material [181], and the microstructural changes responsible for this strengthening have been observed in tensile loading [135] and in tribological scenarios [165]. However, reinforcement morphology strongly influences the constrained plastic strain fields in the matrix, with severe stress concentration in the regions close to sharp corners of angular particles [133]. Although angular reinforcements can result in higher strength in tensile loading compared to spherical, they also lead to reduced ductility due to enhanced particle fracture and matrix damage accumulation at stress concentration sites [135]. It follows that in a tribological scenario like the present study, it is possible that the reduced ductility and damage accumulation at the sharp corners of angular particles act to allow material detachment during sliding, more readily generating wear debris and clearing away regions of MML. This would be closely linked to spikes in the friction coefficient and activity in the transfer film, which were associated with higher overall wear rates.

Therefore for this sliding system, two competing processes occured in the vicinity of hard particles: third body formation through strain localization and oxidation, and third body disturbance/removal contributing to the detachment of wear debris. For sample SPH3, some smooth patches of third bodies formed in the wear track, but the amount of Al_2O_3 was insufficient to prevent its disturbance and removal as wear debris. For ANG10 and SPH11, with similar concentrations of particles, the sharp corners of the angular Al_2O_3 in ANG10 promoted crack formation and detachment. The stability of the third body layer for SPH11 allowed it to contribute to work hardening and oxidation, leading to its elevated hardness. ANG22 had such high quantities of angular Al_2O_3 that the third body formation process dominated over the detachment process, leading to the elevated hardness and stability of the third body layer similar to that of SPH11, but at a lower wear rate.

6.6 Conclusions

The present study has explored the influence of Al_2O_3 morphology on the deposition behavior and dry sliding wear behavior of cold sprayed Al-Al_2O_3 using admixed feedstock powders. During cold spray deposition, significantly less spherical Al_2O_3 compared to angular Al_2O_3 was recovered at similar feedstock concentrations. Coating microhardness was found to depend only on the concentration of Al_2O_3 in the coating and not on the particle morphology.

In dry sliding wear tests, coatings with 3 wt.% spherical (SPH3) and 10 wt.% angular (ANG10) Al_2O_3 were found to have similar wear rates as unreinforced cold sprayed pure Al and similarly high, unstable friction coefficients. Coatings of 11 wt.% spherical (SPH11) and 22 wt.% Al_2O_3 (ANG22) were found to have lower wear rates and lower, more stable friction coefficients compared to the coatings of lower Al_2O_3 content. Tribological mechanisms were observed through *in situ* tribometry and *ex situ* analysis of worn material. Samples exhibiting high wear rates and high friction were found to have high levels of material flow at the sliding interface, and this resulted in disordered, inhomogeneous microstructures in the third body material in the wear track. Samples exhibiting low wear rates and low friction were found to have stable third body material present in a thin, hardened, coherent layer of fine-grained material that was highly oxidized. The “critical” concentration of Al_2O_3 required to form this layer was strongly dependent on the morphology of the Al_2O_3 particles, with less spherical Al_2O_3 being needed compared to angular.

Acknowledgments

The authors gratefully acknowledge the financial support from the Canadian Foundation for Innovation (CFI) project No. 8246 for the cold spray equipment, the CFI Leader's Opportunity Fund project No. 13029 for the *in situ* tribometer and nanoindentation equipment, and the Natural Sciences and Engineering Research Council (NSERC) Discovery Grants Program for the operational funding of this project. Thanks are also due to Tekna Inc. of Sherbrooke, QC for providing the spherical Al_2O_3 powders. JMS acknowledges partial financial support from the Rio Tinto Alcan Graduate Fellowships program.

Chapter 7

Significance of Al_2O_3 particle morphology in the microstructure evolution of cold-sprayed Al-Al_2O_3 during unconstrained high-pressure torsion

J. M. Shockley, S. Descartes, R.R. Chromik

This chapter is a manuscript, intended for publication. The previous chapter revealed that the Al_2O_3 particle morphology, whether spherical or angular, led to significant differences in the cold spray consolidation and dry sliding wear behavior of Al-Al_2O_3 coatings. Analysis of the third bodies formed during the wear process revealed that even for samples of similar Al_2O_3 concentration but different Al_2O_3 morphology, such as ANG10 and SPH11, the structure and properties of the third body material were quite distinct. This correlated with differences in friction and wear behavior. In this chapter, in an attempt to study the deformation behavior of the Al matrix in the vicinity of Al_2O_3 particles, high pressure torsion (HPT) was used to induce severe plastic deformation on samples ANG10 and SPH11. The HPT tests were followed by cross-sectioning and electron microscopy to study the microstructural changes induced during the deformation process, and this was correlated with finite element modeling to study the stresses in the aluminum matrix around Al_2O_3 particles. Parallels were drawn between the behavior during HPT and during the dry sliding wear process.

Abstract

Unconstrained high pressure torsion (HPT) tests were performed on two cold-sprayed Al-Al_2O_3 composites, one with spherical Al_2O_3 particles and the other with angular. Derivation of stress-strain curves during HPT revealed higher von Mises stress in the spherical sample compared to the angular samples, which is the opposite behavior of that observed in tension. Microstructural analysis revealed extensive crack formation in the angular sample, and finite element modelling revealed a greater likelihood of crack formation in the vicinity of angular particles.

7.1 Body of work

Composite cold sprayed coatings of pure Al with Al_2O_3 particles have attracted interest due to their improved tribological behavior compared to un-reinforced cold sprayed pure Al, while maintaining corrosion protection for the underlying substrate [11]. A recent study by the authors [182] (Chapter 6) found that the coating formation process and dry sliding wear behavior of cold sprayed Al-Al_2O_3 was strongly influenced by whether angular or spherical Al_2O_3 particles were used. At similar concentrations of Al_2O_3, the composites containing spherical Al_2O_3 exhibited substantially lower wear rates and more stable friction behavior than those containing angular Al_2O_3. During wear of metallic materials, the near-surface layers in mechanical contact undergo structural changes; this is in response to the tribological stresses, namely shear and compressive stresses, which may reach instantaneous pressures on the order of several GPa [36,67]. Due the impossibility of making precise observations of the conditions inside tribological contacts, it has been considered that high pressure torsion (HPT) may be utilized to study the mechanisms occurring during tribological deformation [36,112,183]. Furthermore, shear induced stress-strain curves can be obtained from the torque and height values measured during rotation [110,112]. When stress-strain curves are derived in tension for aluminum matrix composite materials, experiments and modelling have found that stress concentrations at the corners of angular particles leads to earlier yielding of the matrix compared to spherical particles (e.g., [133,135,136]). The associated work hardening at lower composite strain leads to higher tensile strengths, but lower tensile ductility [135]. The extent to which these mechanisms may be active in shear, however, appear to be unexplored in literature. Thus in the present study, cold sprayed Al-Al_2O_3 was subjected to HPT, and the influence of Al_2O_3 morphology on the deformation behavior will be discussed.

Cold spray was conducted using feedstock prepared by admixing spherical Al powder either with angular morphology or with a plasma spheroidized Al_2O_3 powder. A Plasma Giken PCS-800 cold spray system was used, achieving a deposit thickness of 4-5 mm. Details on the cold spray methodology can be found in another publication by the authors [182]. The deposits were cut into cylinders of 6.0 ± 0.1 mm diameter using wire-cut electrical discharge machining (EDM), then sectioned into disks and polished to 0.4 ± 0.03 mm in thickness. Torsion tests were conducted a custom-built HPT test rig. The disks were placed between two WC-Co anvils of 6 mm diameter, such that HPT was conducted in the unconstrained condition [35] (see Figure 7.1, inset). After loading to a pressure of 0.5 or 1.0 GPa, rotation to 180° was carried out at 0.5 RPM. Torque measurement was accomplished using a static torque sensor and vertical displacement, to monitor the change in sample thickness, was measured using inductive sensors. The evolution of torque, rotation angle, and sample thickness during HPT were used to calculate von Mises equivalent stress and shear strain at the external radius using the Fields and Backofen [113] method:

$$\sigma = \sqrt{3}T\frac{(3+M+N)}{2\pi a^3} \tag{7.1}$$

$$\varepsilon = r\vartheta/\sqrt{3}h \tag{7.2}$$

where ϑ is the rotation angle, T is the measured torque, h is the sample thickness, $M = \delta lnT/\delta ln\dot{\vartheta}$is the rotation rate sensitivity of the torque, and $N = \delta lnT/\delta ln\vartheta$ is the rotation sensitivity of the torque. The parameter N was calculated on a local basis for each data point and M was set to zero given that tests were conducted at room temperature [115]. This methodology was adapted to HPT on the assumption that adherence between the anvils and slider is perfect; this was confirmed by checking that the scratches on the original anvil surface were imprinted on the sample surfaces post-HPT [112].

Sample Designation	Al_2O_3Particle Morphology	Al_2O_3 in Feedstock Powder (wt.%)	Al_2O_3Recovered in Coating (wt.%)	Deposition Efficiency (wt.%)	Hardness (HV_{200})
ANG10	Angular	10	9.8 ± 1.5	60.6 ± 6.7	58.2 ± 6.6
SPH11	Spherical	50	11.3 ± 1.3	41.0 ± 4.5	58.8 ± 4.7

Table 7.1 – Sample designations and Al_2O_3 content in the feedstock powder. Sample designations refer to the morphology and amount of Al_2O_3 recovered in the coating (see Figure 2).

The stress-strain curves during HPT showed that after strain of about 10, the von Mises stress reached relatively steady plateau values for each sample and pressure (see Figure 7.1). The total degree of strain was higher for tests at 1.0 GPa than 0.5 GPa due to the greater amount of material squeezed out of the contact, and hence greater sample thickness change, at higher pressure. The variability of shear stress in HPT due to the applied pressure can be partly attributed to interactions at the interface of the anvil and the sample, which may have greater contact area and less slippage at high pressures [110, 184]. Of particular note in Figure 7.1 is that at both 0.5 and 1.0 GPa conditions, the average von Mises stress of SPH11 was 8-10 % higher than ANG10. The higher shear stress of SPH11 is responsible for the higher overall strain of ANG10 at 0.5 and 1.0 GPa, as its lower resistance to plastic flow led to more extrusion. Notably, the observation that higher stress levels were associated with the presence of spherical particles, rather than angular, runs contrary to the greater body of experimental and numerical studies on metal matrix composites [133–136].

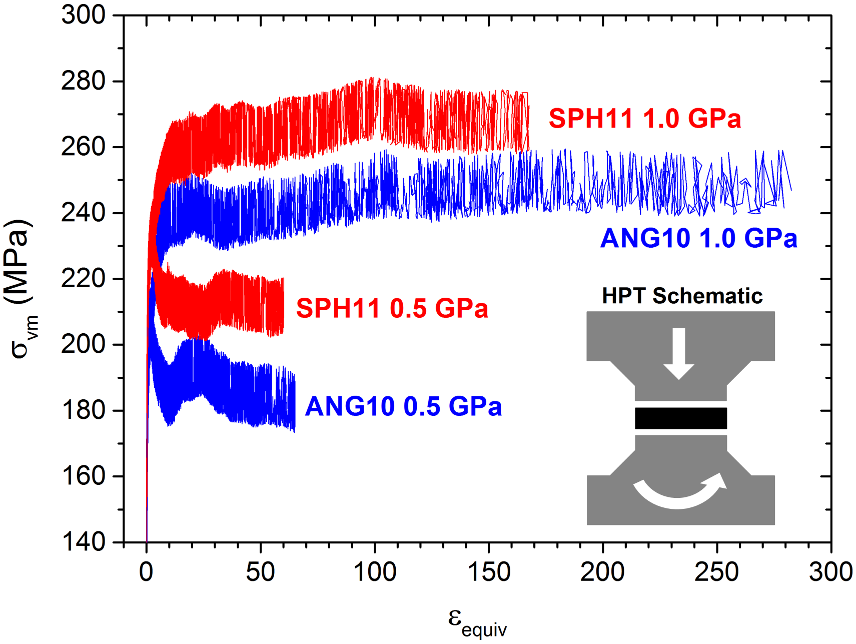

Figure 7.1 – Plots of von Mises stress vs. equivalent strain for the Al-Al_2O_3 composites with spherical (red) and angular (blue) reinforcements at 0.5 and 1.0 GPa.

Cross-sectional microstructural observations of the post-HPT processed SPH11 and ANG10 specimens were carried out by sectioning across the disk diameters, followed by metallographic polishing and surface cleaning using an argon ion mill. Scanning electron microscopy of relatively isolated angular and spherical particles reveal grain refinement and plastic flow in the matrix around them (see Figure 7.2). For both angular and spherical particles, a contoured "pocket" of grains 0.5-2 μm in diameter exists to the left and right of the particle, similar to the grain sizes measured before HPT. Grains running along the edge of this region are finer, and in some cases, stretched in the direction of the contours. For the angular particle, microcracks are observed running in the contour direction, while very few of such cracks are observed for the spherical particle. These microstructural features were observed for tests at 1.0 GPa as well as 0.5 GPa.

The existence of microcracks in the post-HPT microstructure could be driven by several factors. The adiabatic shear instabilities that cause interfacial bonding during cold spray only form on portions of the particles during impact [48]. This may leave some fraction of particle interfaces unbonded, which could be manifested as cracks in the microstructure. Furthermore, during cold spray, low deposition efficiencies can create an erosive and/or peening effect on the deposited coating, leading it to densify [48]. The lower deposition efficiency of SPH11 compared to ANG10 could conceivably result in an increase in interface bonding and thus fewer particle boundary defects that could form cracks (see Table 7.1). However, no significant contrasts in porosity or microcrack presence were readily observed in the SPH11 and ANG10 microstructures pre-HPT.

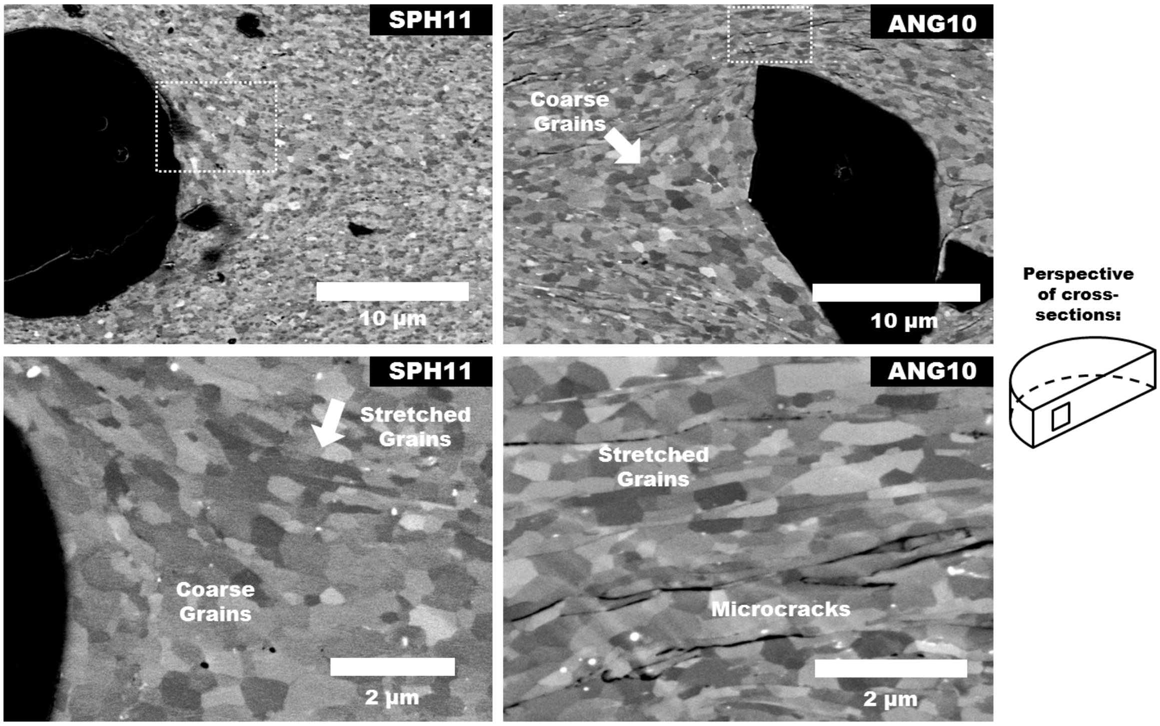

Figure 7.2 – Representative ECCI images of relatively isolated spherical (left) and angular (right) particles after HPT at 1.0 GPa. The detail image of cracks (bottom right) is the area just above the top corner of angular particle (top right). The region observed is roughly halfway between the center of the HPT puck and the edge; the normal loading is vertical and the shear strain direction is perpendicular to the image plane.

An additional factor for the formation of microcracks is due to the disruption to plastic flow at the sharp corners of the angular particles. One criterion for damage accumulation in ductile solids is the triaxiality factor, η:

$$\eta = \sigma_{hs}/\sigma_{vm} \tag{7.3}$$

where σ_{hs} is the hydrostatic stress and σ_{vm} is the von Mises stress [128]. Plastic strain to failure in positive triaxiality regimes, such as ordinary tensile testing, has shown to be reduced as the triaxiality factor is increased. In a state of negative triaxiality, where the hydrostatic stress is compressive, the damage mechanisms such as void and microcrack formation can be strongly suppressed [130,131]. To study the influence of particle morphology on the stress and strain fields in the aluminum matrix during compression, commercial finite element analysis software (ABAQUS 6.11) was used to produce a 2D plane strain unit cell model of a single isolated Al_2O_3 particle embedded in a matrix of elastic-plastic aluminum. A compressive strain of ˜2% was induced on the top surface, while the bottom surface was fixed in the vertical direction. The left and right edges of the cell were rigid vertical members permitted to expand horizontally.

The equivalent plastic strain (PEEQ) fields in the aluminum matrix reveal load bearing by the hard particle, leading to a region of zero strain perpendicular to the loading direction (see Figure 7.3). These regions were larger for the angular particle and correspond well with the microstructures in Figure 7.2. Also, the region of maximum strain in the matrix occurred at the 45º edges of the particles, which was smaller for the angular particle. Thus, concentrated strain occurred at the sharp corner; this effect has been observed in tensile studies as well and is characteristic of the deformation patterns around angular particles [134,135]. Also, the region of higher strain runs along the edge of the region of lower strain for the angular particle, which is not the case for the spherical.

The fields of local stress triaxiality reveal that in areas of the matrix far from the particles, the triaxiality factor is between -0.30 and -0.35 (see Figure 7.4). The triaxiality factor was more negative on the top and bottom of the particle, reaching a maximum magnitude of about -0.55. Near the particle sides, the magnitude of triaxiality was reduced to roughly -0.2

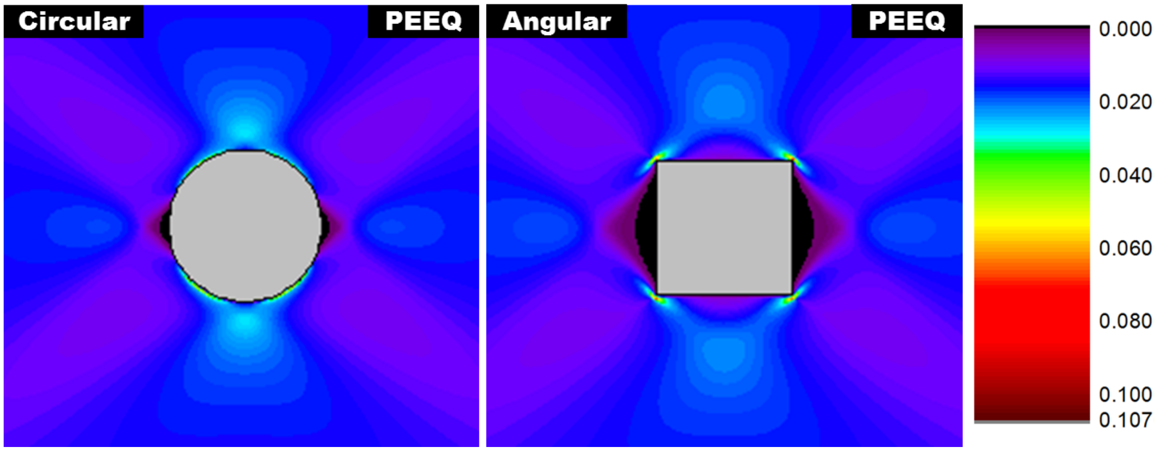

Figure 7.3 – Contour plots of the unique nodal outputs of the plastic equivalent strain (PEEQ) for the aluminum matrix surrounding a circular (left) and angular (right) Al_2O_3 particle.

in contours running along the outside of the region of low strain observed in Figure 3, and in some areas it was zero. Notably, the regions of near-zero triaxiality were directly at the sharp corners for the angular particle, where the magnitude of strain was also high; for the circular particle, the near-zero triaxiality region was close to the particle and did not correspond to an area of high strain. The negative triaxiality value of η = -0.33 has been proposed as a critical value for damage accumulation; when more negative the solid is protected from microcrack or void formation, while at higher values damage accumulation by microcracking and/or void formation may be observed [131]. The microcracking observed around the region of coarse grains of the angular particle in Figure 7.2 corresponds to the regions observed in Figure 7.4.

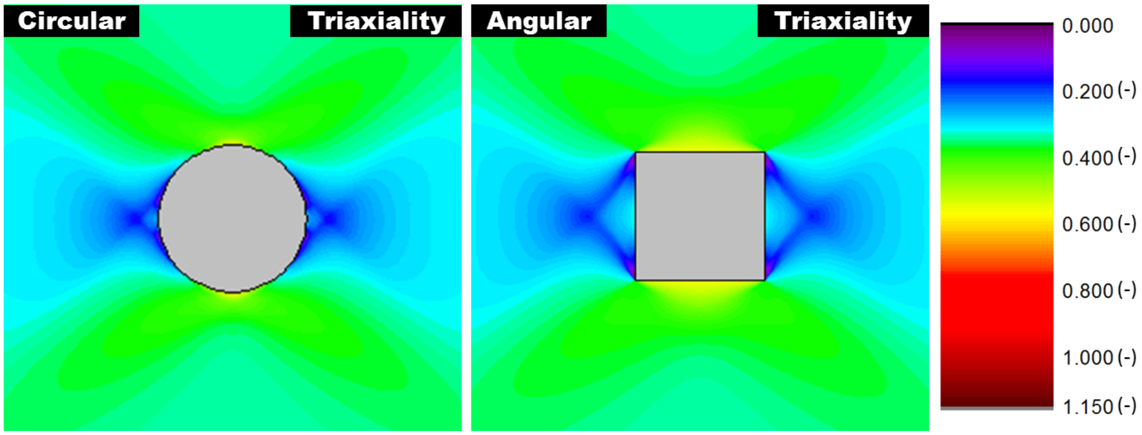

Figure 7.4 – Contour plots of the unique nodal outputs of the triaxiality factor for the aluminum matrix surrounding a circular (left) and angular (right) Al_2O_3 particle.

Correlating the observed microstructural features to the model requires some assumptions. The model presented here is simple; no crack formation criteria were used, nor were other factors such as polycrystallinity. Furthermore, no shear is induced in the presented model. Nonetheless, much was gained from studying the static stress distribution, as the normal load is constantly maintained throughout HPT. Given the potential for microcrack formation due to the stress and strain distribution, the two potential factors contributing to microcrack observation in the post-HPT microstructure could be synergistic. Since there is a larger area of damage-causing triaxiality fields for the angular particles, then during shear a greater volume of material would pass through it. If more incompletely bonded interfaces were present in the angular microstructure before HPT than the spherical microstructure, then these could become opened and extended by the triaxiality fields as well. And given the strong correlation between the regions of coarse grains in the microstructures and low-strain regions observed in the plastic equivalent strain distribution, there could be greater load bearing of the normal load by the angular particles, resulting in less material moving to accommodate plastic shear flow during the shear process. Thus the lower von Mises stress observed during the HPT process for the angular particles would be a combination of the crack formation mechanisms and the greater quantity of material exhibiting “zero” strain due to load bearing.

Crack formation at sharp corners, which contributed to the lower von Mises stress in HPT, would also facilitate wear debris particle formation and material transfer during sliding. This would contribute to a higher wear rate and unstable friction coefficient. By revealing the deformation behavior during HPT, this study reveals key mechanisms that could influence the tribological behavior ANG10 and SPH11.

7.2 Acknowledgements

The authors gratefully acknowledge the financial support from the Canadian Foundation for Innovation (CFI) project No. 8246 for the cold spray equipment and the Natural Sciences and Engineering Research Council (NSERC) Discovery Grants Program for the operational funding of this project. JMS acknowledges partial financial support from the Programme Avenir Lyon St-Etienne doctoral mobility fellowship. The authors also acknowledge the partial financial support from “Région Rhône-Alpes” (within the context SRESR 2007-2010) via MaCoDev (”Matériaux et Conception pour un Développement durable”) research cluster grant n° 08 013 865 01. Thanks are also due to Lionel Lafarge and Edouard Régis for their technical help.

Chapter 8

High pressure torsion of cold-sprayed $Al\text{-}Al_2O_3$ composites in the unconstrained condition

J. M. Shockley, S. Descartes, R.R. Chromik

This chapter is a manuscript, intended for publication. In the previous chapter, high pressure torsion (HPT) was carried out on two cold sprayed Al-Al_2O_3 samples, ANG10 and SPH11, containing similar Al_2O_3 concentrations but different Al_2O_3 morphologies. In this chapter, this study was expanded to include samples CS0 and ANG22. The finite element modeling was expanded to include shear in addition to compression.

8.1 Introduction

Aluminum matrix composite (Al-MMC) materials with hard reinforcements such as SiC or Al_2O_3 are valued for their corrosion resistance, low density, and higher hardness over the unreinforced alloy materials [2]. They are further noted for having lower wear rates and more stable frictional forces during dry sliding wear compared to their unreinforced matrix alloys [1,27,177]. The cold spray process is a somewhat new addition to the methods by which

Al-MMC materials may be consolidated, but has generated interest due its low temperature relative to conventional thermal spray, which lessens the chance of phase changes or chemical reactions in the feedstock or substrate materials [9, 11, 185]. Cold sprayed Al-Al_2O_3 is a coating system of particular interest as a repair material for aerospace components, and recent publications by the authors have explored the mechanisms leading to the shift in tribological behavior due to the presence of Al_2O_3 particles [161, 177, 182]. Ultimately, the macro-tribological behaviors of friction and wear are determined by the "third bodies" occuring within the region a dozen or so microns away from the sliding interface [66, 67]. During wear of metallic materials, these near-surface layers undergo significant structural changes; this is in response to the tribological stresses, namely shear and compressive stresses, which may reach instananeous pressures on the order of several GPa [36, 67].

As it is impossible to make precise observations of the conditions inside mechanical contacts, it has been considered that high pressure torsion (HPT) may be utilized to study the mechanisms occuring during tribological deformation [36]. HPT is prominent among the various severe plastic deformation (SPD) techniques which are used to induce grain refinement and strengthening in metallic materials through extensive cold working. During HPT a disk of material is placed in a gap between two anvils, which are then loaded to a chosen superficial contact pressure, typically on the order of 0.5 - 6 GPa [35]. Then one anvil is rotated to induce torsional straining while the contact load is maintained constant. The most common anvil geometry is the constrained or quasi-constrained condition, where the outward flow of material is prevented to the greatest degree possible [35]. Although the constrained condition helps maintain the original disk dimensions, the friction arising from contact among the constraining member(s) would conflate any torque measurement of the material shear stress. Alternatively the unconstrained condition, reminiscent of the original Bridgman experiments [106], permits outward material flow. This makes the unconstrained condition impractical for true materials processing, but the measured torque can be used in the derivation of stress-strain behaviors of the material under compression and shear strain conditions [110].

In spite of the interest and research in Al-MMC materials in tribological scenarios, there is limited discussion of deformation behavior and microstructural evolution of Al-MMC materials in shear. When stress-strain curves are derived in tension for Al-MMC materials, experiments and modelling have found that stress concentrations at the corners of angular particles leads to earlier yielding of the matrix compared to spherical particles (e.g., [133–136]). The associated work hardening at lower composite strain leads to higher tensile strengths, but lower tensile ductility [135]. The extent to which these mechanisms may be active in HPT, however, appear to be unexplored in the literature. In one early SPD study of AA6061-10% Al_2O_3 composites found evidence of grain refinement and hardening after HPT and Equal Channel Angular Processing (ECAP) [123]. However, no stress-strain curve derivation was conducted, nor was any discussion of particle morphology incorporated.

In the present study HPT in the unconstrained condition was used to study the deformation behavior under compression and shear strain conditions for cold sprayed Al and Al-Al_2O_3 composites. After HPT tests at 0.5 and 1.0 GPa contact pressures, cross-sectioning and microstructural analysis was carried out to observe the local flow behaviors of the matrix material around Al_2O_3 particles. By observing the patterns of grain refinement and damage accumulation in the matrix material, a full discussion of the behavior in compression and shear and its link to the tribological behavior of the same materials will be developed.

8.2 Methodology

8.2.1 Experimental

Cold spray was conducted using feedstock prepared by admixing commercially available spherical Al powder (Valimet H-15, d_{50}= 22.6 µm) either with angular morphology Al_2O_3 powder (Plasmatec, d_{50}= 25.5 µm) or with a plasma spheroidized spherical morphology Al_2O_3

powder (Tekna, d_{50} = 24.3 µm). Coatings were deposited onto aluminum alloy AA6061 substrates using a Plasma Giken PCS-800 cold spray system, achieving a thickness of 4-5 mm. Additional details on the cold spray methodology used here can be found in another publication by the authors [182].

Sample Designation	Al_2O_3 Particle Morphology	Al_2O_3 in Feedstock Powder (wt.%)	Al_2O_3 Recovered in Coating (wt.%)	Deposition Efficiency (wt.%)	Hardness (HV_{200})
CS0	n/a	0	0	60.9 ± 6.0	43.0 ± 3.0
ANG10	Angular	10	9.8 ± 1.5	60.6 ± 6.7	58.2 ± 6.6
ANG22	Angular	50	22.2 ± 2.0	45.4 ± 5.5	74.7 ± 7.8
SPH11	Spherical	50	11.3 ± 1.3	41.0 ± 4.5	58.8 ± 4.7

Table 8.1 – Sample designations and Al_2O_3 content in the feedstock powder. Sample designations refer to the morphology and amount of Al_2O_3 recovered in the coating (see Figure 2).

The deposits of Al-Al_2O_3 were cut into cylinders of 6.0 ± 0.1 mm diameter using wire-cut electrical discharge machining (EDM). A water lubricated wafering blade was used to section the cylinders roughly 0.6 mm in thickness which were then thinned using 2400- and 4000-grit SiC grinding paper to approximately 0.40 mm. Each sample was confirmed to be of uniform thickness within 0.03 mm using digital calipers. Prior to testing, the samples were cleaned in an ultrasonic bath using heptane and ethanol. Torsion tests were conducted a custom-built HPT test rig [186]. Normal loading was accomplished using a hydraulic pump and was maintained during testing by a force feedback loop, while rotation was induced using an 8 kW electric motor. The prepared pucks were placed between two degreased WC-Co anvils of 6 mm diameter with a surface roughness (Ra) of 0.2 µm. The anvil geometry was such that tests were conducted in the unconstrained condition [35]. After loading to a superficial contact pressure of 0.5 or 1.0 GPa, rotation to 180^{o} was carried out at 0.5 RPM. Torque measurement during testing was accomplished using a static torque sensor at an acquisition rate of 50 Hz. Vertical displacement was measured using three inductive sensors, each with an accuracy of 0.01 µm, spaced 120° apart around the axis of rotation. The evolution of torque, rotation angle, and sample thickness during HPT were converted into von Mises equivalent stresses and shear strain at the external radius using the Fields and Backofen [113] method:

$$\sigma = \sqrt{3}T\frac{(3+M+N)}{2\pi r^3} \tag{8.1}$$

$$\varepsilon = r\vartheta/\sqrt{3}h \tag{8.2}$$

where ϑ is the rotation angle, T is the measured torque, h is the sample thickness, $M = \delta lnT/\delta ln\dot{\vartheta}$is the rotation rate sensitivity of the torque, and $N = \delta lnT/\delta ln\vartheta$ is the rotation sensitivity of the torque. The parameter N was calculated on a local basis for each data point and M was set to zero as tests were conducted at room temperature [115]. Surface analysis of the samples after HPT confirmed that the

Microstructural analysis was carried out by first cross-sectioning across the center of sample pucks post-HPT using a lubricated slow-speed abrasive cutting wire, followed by cold mounting in epoxy and mechanical polishing. This was followed by an argon ion milling step to remove any remaining deformed material from the polishing process and adhering polishing media. Microstructural analysis was carried out in an SEM with a backscattered electron detector to reveal aluminum grains through electron channeling contrast imaging (ECCI).

8.2.2 Finite element modeling

To study the influence of particle morphology on the stress and strain fields in the aluminum matrix during compression and shear, commercial finite element analysis software (ABAQUS 6.11) was used to produce a micromechanical model of a unit cell in 2D plane strain of a single isolated elastic Al_2O_3 particle embedded in a matrix of isotropic aluminum. To study the effect of compression only, a compressive strain of ˜2% was induced on the top surface, while the bottom surface was fixed in the vertical direction. The left and right sides of the cell were rigid members permitted to expand horizontally. To study the effect of

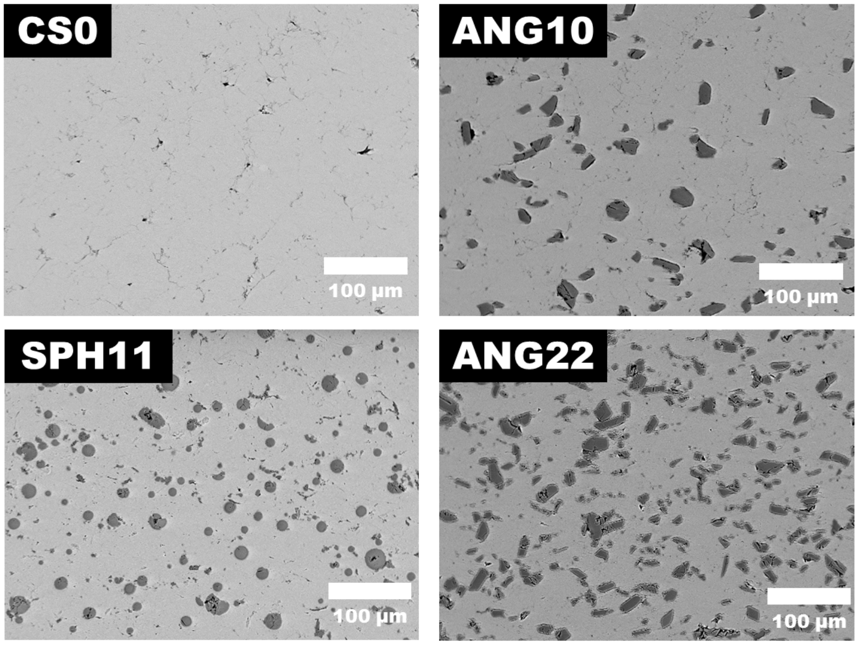

Figure 8.1 – Cross-sections of the initial microstructures viewed roughly 1 mm below the top surface of the deposits.

compression in combination with shear, after the compression step a shear strain of ˜2% was imposed on the top surface while the bottom remained fixed.

8.3 Experimental results

8.3.1 Behavior during HPT

Surface analysis was conducted on samples post-HPT, and for each sample three distinct regions were visible (see Figure 8.2). A large adhesion zone was visible for each sample, where the roughened surfaces of the of the anvils were imprinted. The anvil imprints were visible for large areas of the sample. The next region was a flow zone roughly 100 µm wide was visible, leading to the edge of the sample. Finally, extruded material was visible in a layered morphology.

The torque, height, and stress-strain evolution during HPT at 1.0 and 0.5 GPa are shown in Figure 8.3 and 8.4, respectively. At 1.0 GPa, for all samples the torque steadily increased during the first 60° of rotation, during which period the steepest change in sample thickness

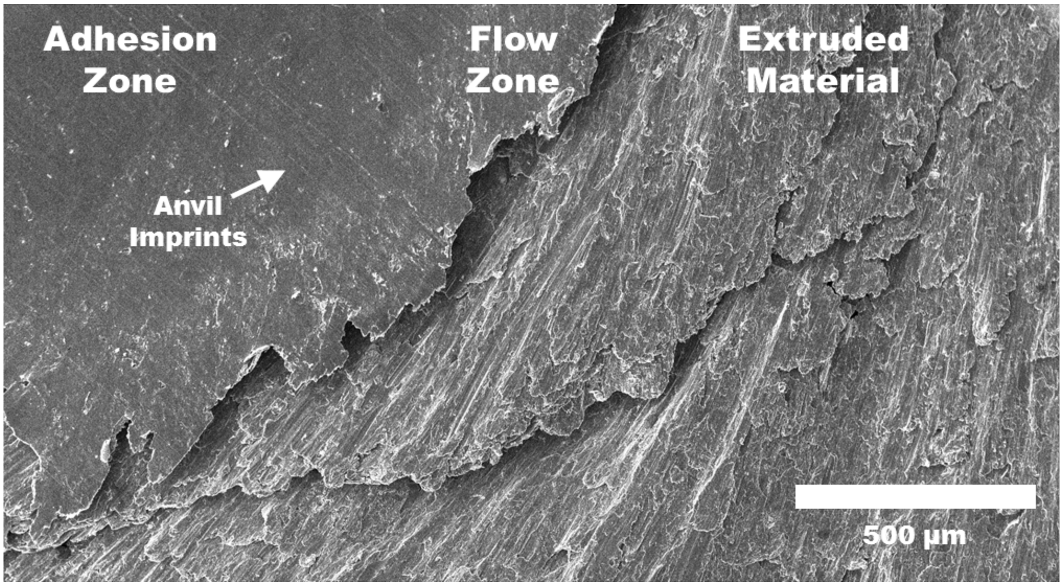

Figure 8.2 – Surface analysis of the edge of a sample after HPT.

occurred. After roughly 60° of rotation, the torque values reached a relatively stable plateau, with sample SPH10 exhibiting the heighest torque followed by ANG10, ANG22, and CS0. When these measurements were converted into stress-strain relations, plateaus were visible for samples SPH11, ANG10, and ANG22 with SPH11 once again taking the highest value. The stress for CS0 decreased slightly between strain values of 20 and 70.

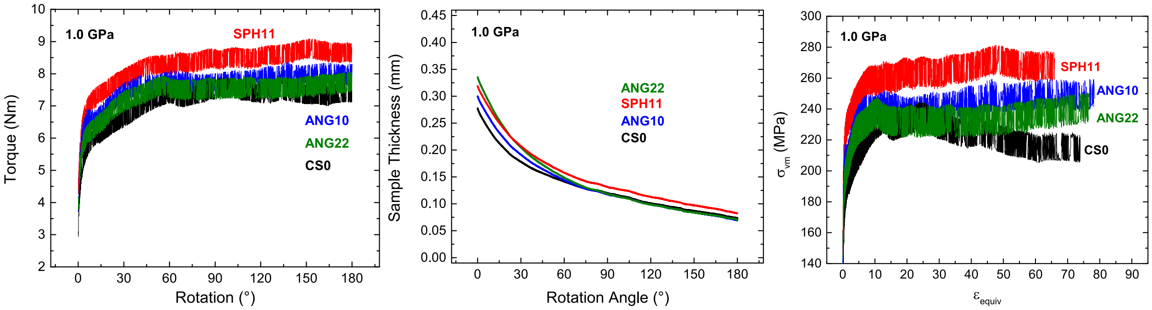

Figure 8.3 – Plots of torque vs. rotation angle (left), sample thickness vs. rotation angle (middle), and von Mises flow stress vs. equivalent strain (right) for samples CS0 (black), ANG10, (blue), and SPH11 (red) at 1.0 GPa.

At 0.5 GPa, sample CS0 displayed similar torque and height evolution as at 1.0 GPa, with the torque reaching a plateau value after roughly 45° of rotation. For samples ANG22, SPH11, and ANG10 the torque values reached an initial peak between rotation angles of 15°

and 30° after which point the torque values declined and stabilized to a plateau value. The decline for ANG22 was by roughly 20%, while for samples SPH11 and ANG10 it was roughly 10%, and only until rotation values of roughly 60°. Stress-strain curves of SPH11 and ANG10 at 0.5 GPa revealed a peak at strain values of roughly 3, after which it declined until a strain of roughly 7; beyond this point it was relatively stable. A sharp peak in flow stress was not observed for sample CS0, although there is a gradual decline between its peak stress at a strain of 7 until it settled between strains of 20 and 35.

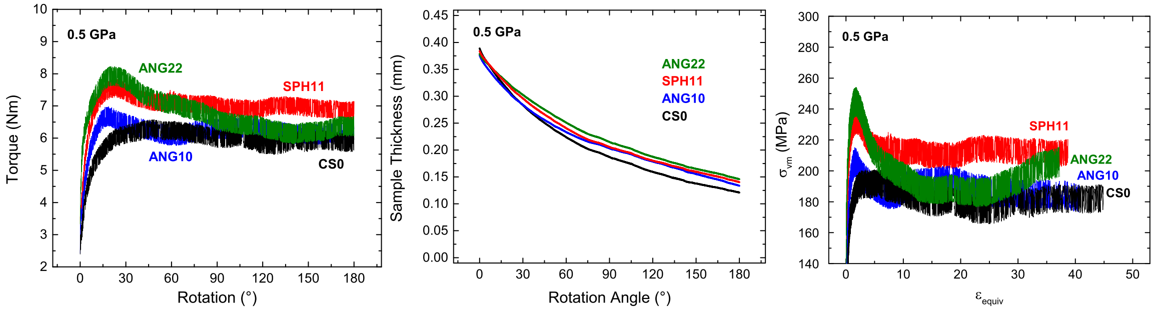

Figure 8.4 – Plots of torque vs. rotation angle (left), sample thickness vs. rotation angle (middle), and von Mises flow stress vs. equivalent strain (right) for samples CS0 (black), ANG10, (blue), and SPH11 (red) at 0.5 GPa.

8.3.2 Microstructural analysis

In the cross-sectioned microstructure of CS0, aluminum grains ranging from 0.1 to 1.0 µm were found throughout the matrix, with microcracks perpendicular to the loading direction visible throughout the microstructure (see Figure 8.5). For relatively isolated angular and spherical particles in ANG10 and SPH, respectively, plastic flow of the matrix is visible around the particles. For both angular and spherical particles, a contoured “pocket” of grains 0.5-2 µm in diameter exists to the left and right of the particle, while grains running along the edge of this region are finer, and in some cases, elongated in the direction of the contours. For ANG10, microcracks are observed running in the contour direction, while very few such cracks are observed for the spherical particles. For ANG22, there are contoured regions of larger grains as well, but no cracks are visible. These microstructural features were observed for tests at 1.0 GPa as well as 0.5 GPa.

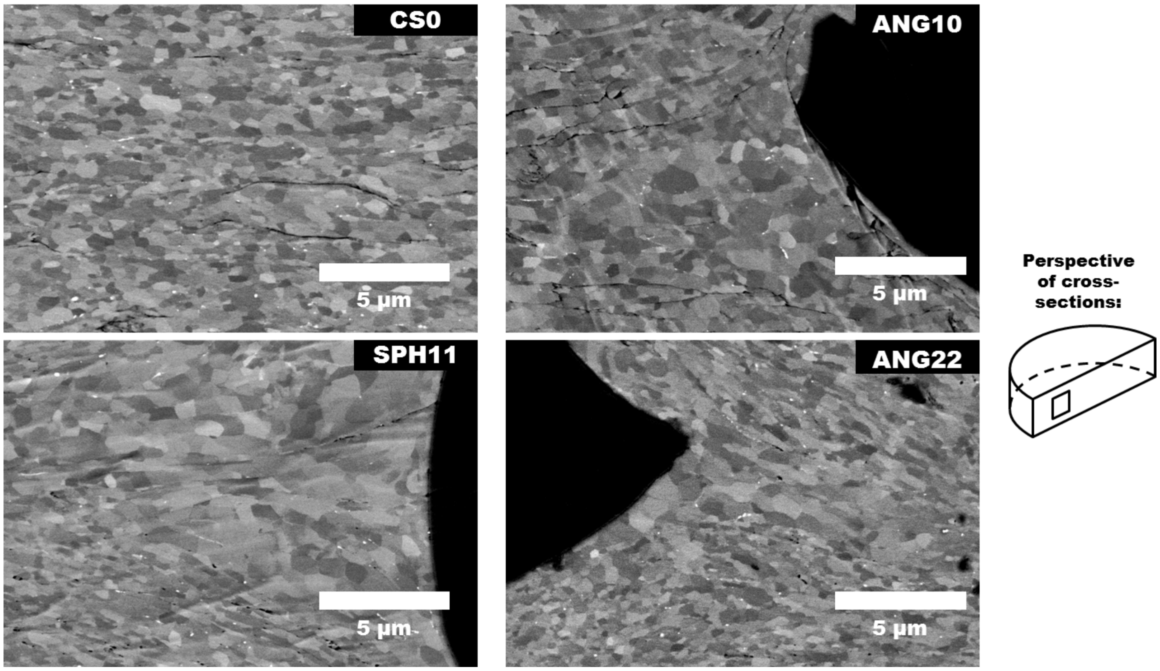

Figure 8.5 – Representative microstructural images of CS0, ANG10, SPH11, and ANG22. For each composite, the edge of an Al_2O_3 particle is visible (in black) and the region of the aluminum matrix in the vicinity is shown.

8.4 Modeling results

An additional factor for the formation of microcracks during HPT is due to the disruption to plastic flow at the sharp corners of the angular particles. One criterion for damage accumulation in ductile solids is the triaxiality factor, η:

$$\eta = \sigma_{hs}/\sigma_{vm} \tag{8.3}$$

where σ_{hs} is the hydrostatic stress and σ_{vm} is the von Mises stress [128]. The stress triaxiality factor is often incorporated into damage criteria in finite element modelling [129]. Plastic strain to failure in positive triaxiality regimes, such as ordinary tensile testing, has shown to be reduced as the triaxiality factor is increased. In a state of negative triaxiality, where the hydrostatic stress is compressive, the damage mechanisms such as void and microcrack formation can be suppressed [130, 131].

The equivalent plastic strain (PEEQ) fields in the aluminum matrix after compression were affected by particle morphology (see Figure 8.6). As shown previously [187], during the compression step, load bearing by the hard particle leads to a region of zero strain in the region perpendicular to the loading direction, and these regions were larger for the angular particle. This corresponds well with the microstructures in Figure 8.5, where the region of coarser, equiaxed grains was larger for the case of the angular particle. Also, the region of maximum strain occurred along the 45º region of the particles, which was much larger for the spherical than the angular. This led to strain localized at the sharp corner; this effect has been observed in tensile studies as well and is characteristic of angular particles [134, 135]. Furthermore, the region of higher strain runs along the edge of the region of lower strain for the angular particle, which is not the case for the spherical. With shear factored in, the plastic strain fields became more complex. For both the angular and spherical particles, there is a region of low strain near the top and bottom of the particles, while plastic flow is concentrated on the sides. As in the compression-only case, the region of low strain is larger for the angular particle than for the spherical.

The stress triaxiality factors were also affected by particle morphology (see 8.7). As shown previously [187], during the compression step, the stress triaxiality throughout the modelled results is entirely negative, but it is closest to zero in a region on the left and right sides of the particles, just like the low-strain regions in Figure 8.6. This corresponds with the contour lines visible in Figure 8.5 and specifically the cracks around the particles in ANG10. When shear was applied, the stress triaxiality was much more uniform and in the range of -0.4 to -0.6 in most parts of the matrix, but there are contoured regions around which the triaxiality is in the range of roughly -0.3. For the angular particle, these regions were visible extending

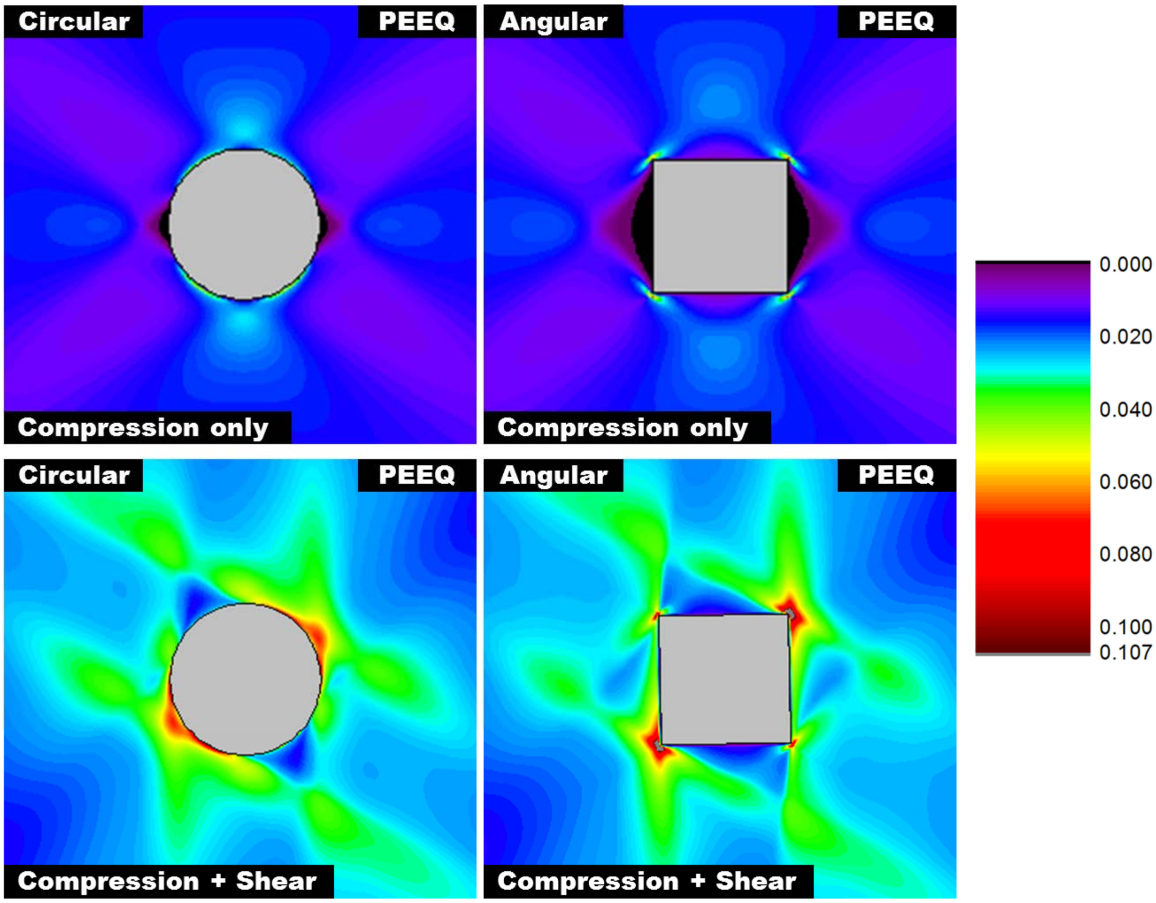

Figure 8.6 – Contour plots of the unique nodal outputs of the plastic equivalent strain (PEEQ) for the aluminum matrix surrounding a circular (left) and angular (right) Al_2O_3 particle.

far into the matrix, whereas they remained close to the spherical particle.

To explore the effect of the orientation of the angular particle, the angular particle was tested at 20° and 45° relative to the direction of shear in addition to the 0° shown in Figures 8.6 and 8.7. At each angle of rotation, a low strain region was visible on either side of the particle while the highest degree of strain was concentrated at the corners 8.8. In the corresponding regions of triaxiality, the levels of triaxiality closest to zero were in the vicinity

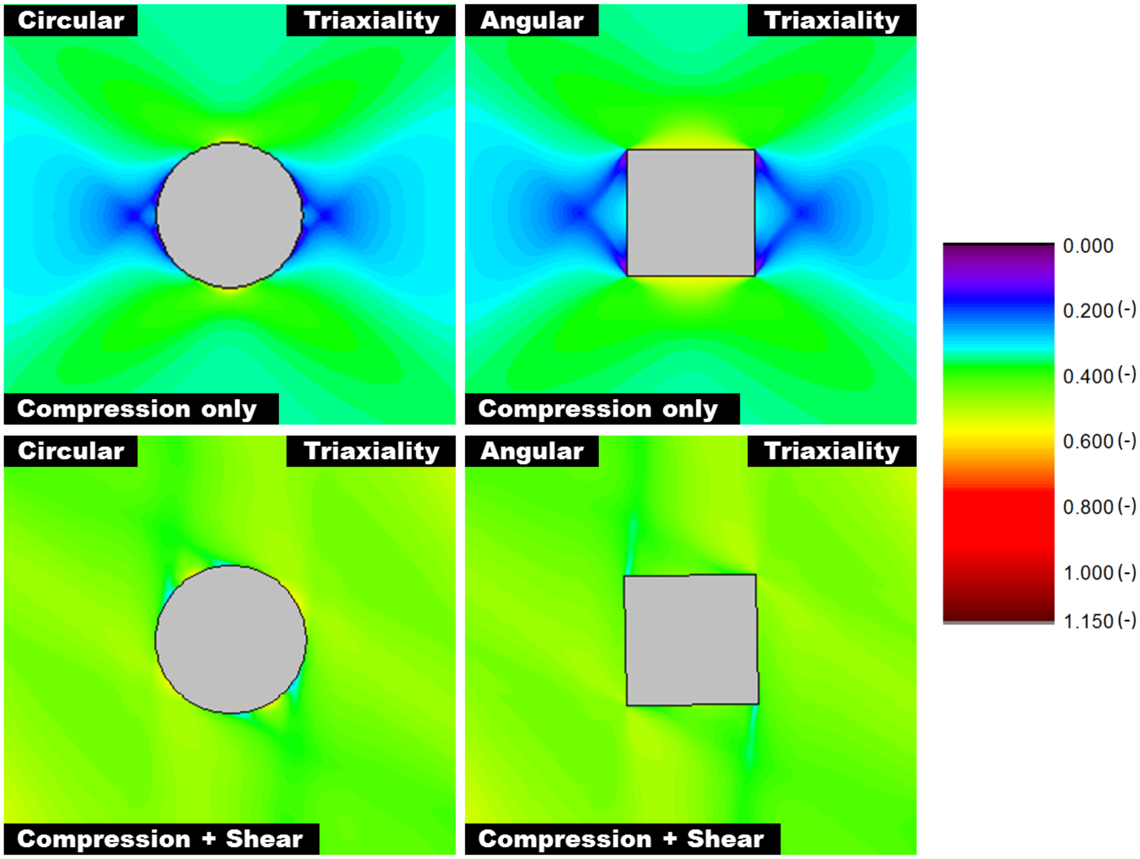

Figure 8.7 – Contour plots of the unique nodal outputs of the triaxiality factor for the aluminum matrix surrounding a circular (left) and angular (right) Al_2O_3 particle.

of the corners, and ran along the zero-strain region.

8.5 Discussion

The experimental and modelling results have shown complex relationships between the torque and height evolution of the tested samples, the stress-strain behavior calculated thereof, the microstructural features observed after the HPT process, and the calculated fields of stress and strain in the vicinity of a single Al_2O_3 particle for a simple unit cell model. The stress-strain curves at 1.0 GPa revealed similar magnitudes of saturation stress values for samples CS0, ANG10, and ANG22, while for SPH11 it was significantly higher. Microstructural analysis revealed fine equiaxed aluminum grains throughout the observed microstructures except in the vicinity of Al_2O_3 particles, where inhomogeneous microstructures were present in contours

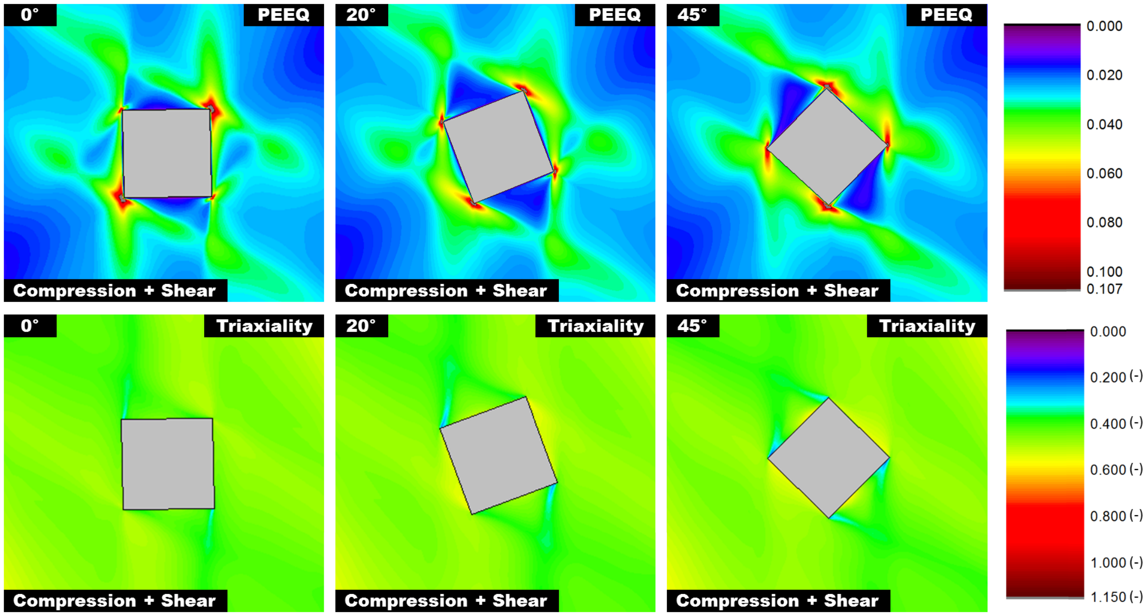

Figure 8.8 – Contour plots of plastic equivalent strain (PEEQ, top) and stress triaxiality factor (bottom) for the aluminum matrix surrounding an angular Al_2O_3 particle set at rotation angles of 0°, 20°, and 45° relative to the shear direction.

around the Al_2O_3 particles. Furthermore, for CS0 and ANG10, cracks were visible throughout the microstructures, whereas for ANG22 and SPH11, few if any cracks were observed in the microstructures.

Two main factors could be contributing to the presence of cracks in the post-HPT microstructures. The first is the presence of unbonded particle boundaries. The proposed bonding mechanism in cold spray is adiabatic shear instabilities during particle impact, which form on only portions of the particles during impact [48]. This may leave some fraction of particle interfaces unbonded, which could be manifested as cracks in the microstructure. Furthermore, during cold spray, low deposition efficiencies can create an erosive and/or peening effect on the deposited coating, leading it to densify [9]. The lower deposition efficiency of SPH11 and ANG22 compared to ANG10 and CS0 could conceivably result in an increase in interfacial bonding, and thus cracks would not be observed post-HPT (see Table 8.1). However, the similar microhardness levels of SPH11 and ANG10 call this effect into question, as the existence of poorly-bonded cold spray particle interfaces should affect the microhardness [188]. Furthermore, examinations of the as-sprayed microstructures revealed that particle boundaries were equally visible among all the samples. Nonetheless, the cracks visible in CS0 make it clear that they are due to the cold spray process itself. This raises the question of whether the HPT process itself could have induced bonding in the microstructure for samples SPH11 and ANG22 and not in ANG10.

The second factor affecting the cracks in the post-HPT microstructures is the stress and strain field distribution of the aluminum matrix as affected by the particle morphology and configuration. The modelling work has helped reveal that in cases of pure compression, as previously reported [187], as well as in a state of compression and shear, the sharp corners of angular particles can create regions of the matrix in a state of stress triaxiality in which damage accumulation is favorable. Consistently, these regions occur at the boundary between regions of low and high strain. The correlation is strong between the modelling results and the microstructural features of cracks (when present) and elongated grains at these boundaries, particularly in the pure compression state. This is because the perspective of the cross-sections in Figure 8.5 is such that the direction of shear is perpendicular to the visible plane, so it is more strongly comparable to the modelling of pure compression rather than compression and shear. If any preexisting defects in the microstructure such as incomplete particle bonding were to pass through these regions of damage accumulation, they could become deformed and possibly enlarged.

All of these factors for microcrack formulation do not entirely explain the lower shear stress in the case of ANG22 compared to SPH11, given that neither showed evidence of crack formation post-HPT. It must be noted that the modelling results shown here are highly simplified; they only consider the region surrounding one isolated Al_2O_3 particle. The interaction of stress fields of multiple nearby particles was not considered, and any such interaction would be influenced by particle morphology and spacing [129, 189]. In spite of this limitation, the modelling work shows that the load bearing capacity of an angular particle during compression can extend far into the matrix. If large portions of the aluminum matrix were shielded from strain due to load bearing, then the smaller quantity of material accommodating the strain could translate into a lower measured stress.

Also, the derivation of the stress-strain curves in Figures 8.3 and 8.4 was subject to an important assumption. First, the Fields and Backofen relations require that all of the measured torque derive from deformation of the sample; any slippage could contribute to error [112, 113]. The contact area during unconstrained HPT can be estimated by the ratio of the contact pressure to the hardness of the material ; any value less than unity represents less than full contact [110]. At a pressure of 0.5 GPa, the contact area is estimated as incomplete for samples ANG10, ANG22, and SPH11, while for all other scenarios it is complete contact (see Table 8.2). Although the anvil imprints were evenly visible on the entire sample surface up to the flow zone, as in Figure 8.2, it is possible that the contact was less than 100% at any given time. The values in Table 8.2 help explain the drop in torque and shear stress visible in Figure 8.4. For samples ANG10, ANG22, and SPH11, the initial peak and decline is likely evidence of the onset of sliding at the interface due to the incomplete contact. The magnitude of the decline was the largest for ANG22, which had the lowest ratio of P/H, while the declines were similar in magnitude for ANG10 and SPH11. There was no decline for CS0, which had a P/H ratio above unity.

	H (MPa)	P/H at 0.5 GPa	P/H at 1.0 GPa
CS0	422	1.19	2.37
ANG10	570	0.88	1.75
ANG22	732	0.68	1.37
SPH11	577	0.87	1.73

Table 8.2 – The ratio of the superficial pressure to the hardness (P/H) for the four samples, an indication of contact area.

The materials in this study were subjected to dry sliding wear in a previous study by the authors [182], and several parallels to HPT can be made. The wear rate of ANG10 was found to be similar to that of CS0, and the wear rate of SPH11 was significantly lower. The lowest wear rate, however, was that of ANG22. It is notable that in CS0 and ANG10, which both showed extensive cracking post-HPT, also exhibited the highest wear rates.

8.6 Conclusions

The present study has applied unconstrained HPT testing to four samples of cold sprayed Al - Al_2O_3 prepared with varying concentrations and morphology of Al_2O_3. The data collected during the HPT revealed that sample SPH11 exhibited the highest shear stress, while samples ANG10, ANG22, and CS0 showed comparable levels. Microstructural analysis revealed that the particle morphology strongly influenced the degree to which grain refinement and plastic flow occurred in the matrix. A unit cell finite element model was developed to study the local stress and strain fields in the matrix in the vicinity of the hard particles, and particle morphology was shown to influence the degree to which strain and damage accumulation would occur during compressive loading and compressive/shear loading.

8.7 Acknowledgements

The authors gratefully acknowledge the financial support from the Canadian Foundation for Innovation (CFI) project No. 8246 for the cold spray equipment and the Natural Sciences and Engineering Research Council (NSERC) Discovery Grants Program for the operational funding of this project. JMS acknowledges partial financial support from the Programme Avenir Lyon St-Etienne Doctoral Mobility Fellowship. The authors also acknowledge the partial financial support from “Région Rhône-Alpes” (within the context SRESR 2007-2010) via MaCoDev (”Matériaux et Conception pour un Développement durable”) research cluster grant n° 08 013 865 01. Thanks are also due to Edouard Regis, Lionel Lafarge, and Claude Godeau of LaMCoS, INSA-Lyon, France and Christophe Desrayaud of École nationale supérieure des mines, Saint-Étienne, France.

Chapter 9

Concluding Remarks

9.1 Summary and conclusions

Dry sliding tribology experiments showed that the friction and wear behavior of cold sprayed Al and Al-Al_2O_3 composites against α-alumina, whether in the form of polycrystalline alumina or monocrystalline sapphire, was dependent on the content and morphology (angular or spherical) of Al_2O_3 particles in the composites. When comparing the sliding wear behavior of samples ANG22 (Al- 22 wt.% angular Al_2O_3) to CS0 (pure Al), the friction was generally lower and more stable for ANG22 and the wear rate was lower. *In situ* tribometry revealed contrasts between the two samples in terms of the behavior of the third body flows. When viewed *in situ*, the CS0 exhibited instability marked by visible plastic flow, debris detachment, and subsequent plowing of new material, and some of these events corresponded with shifts in the friction coefficient. On the contrary the ANG22 behavior remained stable throughout testing, correlating with more steady friction behavior. The tribological behavior of ANG22 was very similar to that of CS22 (Al- 22 wt.% angular Al_2O_3), even though the former was prepared through high pressure cold spray and the latter was through low pressure cold spray. The microstuctures of the two coatings were also similar, including the relative recovery of Al_2O_3 into the coating compared to the initial feedstock Al_2O_3 concentration.

The same tribological behavior was also observed for both the high and low pressure cold spray deposited CS0 coatings.

Subsequent *ex situ* analysis revealed contrasts in terms of third body morphology, flow, and microstructure. The wear track and transfer film of CS0 showed evidence of bulk flow of third body material. The near-surface microstructures of CS0 were highly inhomogeneous, consisting of a mix of coarse and ultrafine grained material, and revealed that plastic deformation extended into the first body microstructures, on the order of 15-20 µm deep. The ANG22 wear track and transfer film were comparatively more homogeneous, with the microstructures being largely constrained to a thin surface layer of ultrafine grained material 2-5 µm thick with small fragments of Al_2O_3 particles visible throughout. Nanoindentation revealed that the ANG22 third body in the wear track was harder than the CS0 third body, at roughly 3.8 and 1.0 GPa, respectively. Qualitative analysis of oxygen content revealed that the CS0 and ANG22 third body layers both contained elevated oxygen contents, but that the amount of oxygen was much higher for ANG22 than for CS0. However, the intensity of the oxygen $K\alpha$ signal of the ANG22 third body was not as high as for a nearby particle of Al_2O_3, implying that a full transformation into stoichiometric Al_2O_3 was not achieved.

The use of *in situ* and *ex situ* techniques in this thesis proved particularly powerful as the combination of the two permitted a thorough analysis of the tribological behavior for CS0 and ANG22. The paired techniques permitted the description of the tribological circuit and velocity accomodation modes. It was revealed that the strain localization caused by the presence of Al_2O_3 particles promoted greater work hardening in a thin layer closer to the near-surface, meaning deformation was prevented deeper in the first body. So, at the beginning of the contact life, the source flow (Qs) was activated from a small volume of the first body, leading to a small volume of third body for ANG22. This caused the internal flows (Qi) to be constrained to a thin layer. The combination of work hardening and oxidation of this layer resulted in the high hardness of the ANG22 third body compared to CS0, which had no such localization effects. By constraining velocity accommodation to the third body material, the ANG22 source flow (Qs) remained low during the contact life, which slowed the rate of transfer to the counterface. The CS0 source flow remained active throughout testing.

Sample ANG10 behaved similarly to CS10 during dry sliding wear, and similar microstructures and relative Al_2O_3 recovery were obtained, even though they were deposited using high and low pressure cold spray, respectively. Sample SPH3 behaved similarly to ANG10 and CS0 in terms of friction, wear, and third body behavior observed *in situ*, while SPH11 behaved more similarly to ANG22 than to ANG10. Furthermore, the *ex situ* observations of the SPH11 transfer film and wear track morphology were more similar to ANG22 as well, as were hardness measurements in the wear track showing nearly identical hardness values (˜3.8 GPa). The contrasts in dry sliding wear behavior between ANG10 and SPH11, of similar Al_2O_3 content but differing Al_2O_3 morphology, imply that the stress concentration at the sharp corners of the Al_2O_3 samples encourages the detachment of material to form wear debris. This hypothesis motivated additional studies to understand the behavior of the tested materials under severe plastic deformation in straining, and this was accomplished using high pressure torsion (HPT).

HPT testing induced shear straining in the samples under uniaxial compressive loading. For samples ANG10 and SPH11, microstructural analysis revealed the formation of larger-grained regions and microcracks in the vicinity of angular Al_2O_3 particles, while no cracks were visible around spherical Al_2O_3 particles. Also, the von Mises stress was 8-10% higher for the SPH11 compared to ANG10, in spite of similar initial microhardness values. The use of finite element analysis to model the stresses and strain during compression revealed that the large-grained regions due to load bearing by the hard particles, and that the stress and strain contours were warped by the sharp corners and straight edges of the angular particle compared to the smooth curve of the spherical particle. Furthermore, compressive modelling revealed that the cracks formed for ANG10 were in regions where the triaxiality factor was less negative, indicative of less hydrostatic compression relative to the local von Mises stress. This region of damage accumulation was also in an area where strain was high. Modeling around the spherical particle revealed that although a similar region of damage-promoting triaxiality values was present, it was much smaller and in an area of lower strain. The lower degree of crack formation was likely due to a combination of this local stress/strain behavior and of the lower deposition efficiency of the SPH11 sample compared to ANG10, the erosive/peening effect of which may have closed the original particle boundaries that may have acted as crack promotion sites.

Yet, HPT testing and microanalysis of sample CS0 revealed that extensive microcracking was visible throughout the deformed CS0 sample, lending credence to the belief that the cold spray process, leaving particle boundaries incompletely bonded, was the primary driver of the formation of microcracks. Furthermore, HPT testing of ANG22 revealed no crack formation in spite of having many angular particles which could serve as damage accumulation sites as in ANG10 – and the lower deposition efficiency of ANG22 served to compact/erode the particle boundaries, similar to SPH11. Yet ANG10 had relatively isolated particles compared to ANG22, where the stress and strain fields in the matrix were more likely to intersect with one another and with Al_2O_3 particles. Thus drawing direct parallels between the HPT testing and tribological behavior of ANG22 was more challenging.

Thus although the HPT testing in this thesis raised more questions than it necessarily answered, particularly in regard to sample ANG22, the approach of using HPT testing to understand tribological behavior proved to be powerful. The tribological contact consists of a combination of compressive stresses and shear strain, which carries parallels to the stress and strain conditions between HPT anvils. Furthermore, the behavior of the tribological contact was determiend by the rate of source flow (Qs), which is a deformation-induced process, and so HPT could be useful to understand the plastic flow of the near surface layer at the beginning of the contact life. Given the similar distribution and Al_2O_3 content of ANG10 and SPH11, they had very different tribological behaviors in terms of friction, wear, and third body behavior; in parallel, during HPT, they had equally contrasting behavior in terms of the von Mises stress state and the formation of microcracks in the aluminum matrix. The HPT work here reveals that the sharp corners in ANG10 can indeed act as damage accumulation sites; whether or not they are the direct cause of crack formation, or simply a place where preexisting cracks can accumulate, is a subject for future studies. Given the novelty of this research, much remains to be learned regarding the parallels between HPT and dry sliding wear, but the work of this thesis demonstrates that it may prove to be fruitful.

9.2 Suggestions for future work

The present work has raised a wealth of questions that should be analyzed in future studies. The first is in discerning the role of oxidation in the third body behavior of the sliding systems analyzed. The extreme hardness of the ANG22/SPH11 wear tracks cannot be explained through work hardening and grain refinement alone. Detailed microstructural studies and characterization should be carried out to elucidate precisely where the oxygen reports and its chemical state, and particularly in order to understand whether Al_2O_3 directly contributes to the oxygen content. This would best be accomplished by TEM studies from foils cut from the wear track using FIB techniques. To further study the role of oxygen in the present sliding system, studies could be performed in oxygen-free environments such as an inert atmosphere and/or vacuum. Other studies could incorporate water vapor to study hydroxide formation in addition to oxidation. Additionally, because the corrosion resistance of this materials system is of interest, tribocorrosion studies could be carried out to understand how the sliding wear behavior is influenced by corrosive environmental factors such as salt spray.

This study has also raised questions on the cold spray behavior of admixed powders, in which one is a hard ceramic phase. A large diversity of other Al_2O_3 powders exist, including different size distributions far removed from those studied here. One example of this is nanoscale powders that naturally flocculate together due to van der Waals forces. The recovery of Al_2O_3 relative to its initial feedstock concentration should be explored for a range of powder sizes and morphologies to reveal the process-structure relationships that exist for the Al-Al_2O_3 system.

Finally, the HPT experiments raise a number of questions that should be subjects for future research. In order to better understand the role of Al_2O_3 particle morphology in the microstructural evolution during HPT, Al-MMC composites should be produced through a conventional sintering or casting technique rather than cold spray. Performing HPT on these samples will eliminate the peening effects and layered structures that were present in the cold sprayed samples of this thesis, and this way only the hard particle size/morphology/concentration will be the significant factors. Also, the aluminum matrix of each sample in this thesis was heavily work hardened and had small grain sizes due to the cold spray process. Performing HPT (and dry sliding wear) experiments on annealed cold sprayed samples could reveal further details into the deformation behavior in the vicinity of hard particles. However, given the porosity and incomplete bonding of cold sprayed materials, annealing should be carried out under an inert atmosphere to prevent any additional oxidation to take place at these regions. Additional finite element modelling work should also be carried out with realistic Al_2O_3 morphologies and concentrations, using image-based adaptive meshing software such as OOF2 (Finite Element Analysis of Microstructures, available from the National Institute of Standards and Technology [NIST]).

9.3 Original contributions to knowledge

1. The use of *in situ* tribometry carries very little precedent in the context of dry sliding wear of metals as its usual application is for studying thin film coatings and/or solid lubricants. Nonetheless, this technique was found to reveal mechanistic details (described in terms of third bodies) of the phenomena leading to the friction and wear behavior observed for the Al-Al_2O_3 coating systems observed here.

2. The use of the tribological circuit and velocity accommodation modes to describe the observed tribological behavior in cold sprayed Al and Al-Al_2O_3 was performed for the

first time.

3. The use of friction histograms, which is rarely if ever used in tribology research, provided a method of comparing overlapping friction plots which are otherwise be hard to compare.

4. The lower recovery of spherical Al_2O_3 compared to angular Al_2O_3 during cold spray of Al-Al_2O_3 is a phenomenon that has not yet been discussed during cold spray of Al-MMC materials, yet could have practical and financial significance for industrial cold spray facilities.

5. The contrasting friction and wear rate of ANG10 and SPH11 is part of a larger discussion on the influence of hard particle morphology on the tribological behavior of Al-MMC materials. For the first time, this was extended to cold sprayed materials and discussed in the context of the cold spray process.

6. For the first time, cold sprayed Al-Al_2O_3 samples were subjected to HPT and this was used as a comparative method to study deformation mechanisms in materials of a known tribological behavior. The use of HPT on Al-Al_2O_3 composites with spherical and angular morphology is part of a growing research domain where extreme plastic deformation techniques can be used to study mechanisms that can be linked to tribological behavior.

Bibliography

[1] R.L. Deuis, C. Subramanian, and J.M. Yellup. Dry Sliding Wear of Aluminium Composites - A Review. *Composites Science and Technology*, 57:415–435, 1997.

[2] T.W. Clyne and P.J. Withers. *An Introduction to Metal Matrix Composites*, chapter Fabrication Processes, pages 318–360. Cambridge University Press, Cambridge, 1993.

[3] Alexander Evans, Christopher San Marchi, and Andreas Mortensen. *Metal Matrix Composites*, chapter Metal Matrix Composites. Kluwer Academic Publishers, Dordrecht, 2003.

[4] Eric Irissou, Jean-Gabriel Legoux, Anatoly Ryabinin, Bertrand Jodoin, and Christian Moreau. Review on Cold Spray Process and Technology: Part I-Intellectual Property. *Journal of Thermal Spray Technology*, 17(4):495–516, 2008.

[5] A. Papyrin, V. Kosarev, K.V. Klinkov, A. Alkhimov, and V.M. Fomin. *Cold Spray Technology*. Elsevier, Oxford, 2006.

[6] V.K. Champagne. *The Cold Spray Materials Deposition Process: Fundamentals and Applications*. Woodhead Publishing Limited, Cambridge, 2007.

[7] R.G. Maev and V. Leshchinsky. *Introduction to Low Pressure Gas Dynamic Spray: Physics and Technology*. Wiley-VCH Verlag GmbH, Weinheim, 2008.

[8] F. Gartner, T. Stoltenhoff, T. Schmidt, and H. Kreye. The cold spray process and its potential for industrial applications. *Journal of Thermal Spray Technology*, 15(2):223–232, 2006.

[9] Eric Irissou, Jean-Gabriel Legoux, Bernard Arsenault, and Christian Moreau. Investigation of Al-Al_2O_3 Cold Spray Coating Formation and Properties. *Journal of Thermal Spray Technology*, 16(5-6):661–668, 2007.

[10] J.M. Miguel, J.M. Guilemany, and S. Dosta. Effect of the spraying process on the microstructure and tribological properties of bronze-alumina composite coatings. *Surface & Coatings Technology*, 205:2187–2190, 2010.

[11] K. Spencer, D.M. Fabijanic, and M.-X. Zhang. The use of Al-Al_2O_3 cold spray coatings to improve the surface properties of magnesium alloys. *Surface & Coatings Technology*, 204:336–344, 2009.

[12] H. Koivuluoto and P. Vuoristo. Structural analysis of cold-sprayed nickel-based metallic and metallic-ceramic coatings. *Journal of Thermal Spray*, 19(5):975, 2010.

[13] H. K. Kang and S. B. Kang. Tungsten/copper composite deposits produced by a cold spray. *Scripta Materialia*, 49(12):1169–1174, 2003. Cited By (since 1996): 38 Export Date: 13 February 2012 Source: Scopus.

[14] S. V. Klinkov, V. F. Kosarev, A. A. Sova, and I. Smurov. Deposition of multicomponent coatings by cold spray. *Surface and Coatings Technology*, 202(24):5858–5862, 2008. Cited By (since 1996): 7 Export Date: 13 February 2012 Source: Scopus.

[15] S. Shin, Y. Xiong, Y. Ji, H.J. Kim, and C. Lee. The influence of process parameters on deposition characteristics of a soft/hard composite coating in kinetic spray process. *Applied Surface Science*, 254(8):2269, 2008.

[16] Qiang Wang, Kevin Spencer, Nick Birbilis, and Ming-Xing Zhang. The influence of ceramic particles on bond strength of cold spray composite coatings on AZ91 alloy substrate. *Surface and Coatings Technology*, 205(1):50 – 56, 2010.

[17] Ha Lee, Young Yu, Young Lee, Young Hong, and Kyung Ko. Cold spray of SiC and Al-Al_2O_3 with soft metal incorporation: A technical contribution. *Journal of Thermal Spray Technology*, 13(2):184–189, 2004.

[18] S.R. Bakshi, D. Wang, T. Price, D. Zhang, A.K. Keshri, Y. Chen, D.G. McCartney, P.H. Shipway, and A. Agarwal. Microstructure and wear properties of aluminum/aluminum-silicon composite coatings prepared by cold spraying. *Surface and Coatings Technology*, 204(4):503, 2009.

[19] S.R. Bakshi, V. Singh, K. Balani, D.G. McCartney, S. Seal, and A. Agarwal. Carbon nanotube reinforced aluminum composite coating via cold spraying. *Surface and Coatings Technology*, 202(21):5162, 2008.

[20] W.Y. Li, C. Zhang, H. Liao, J. Li, and C. Coddet. Characterizations of cold-sprayed nickel-alumina composite coating with relatively large nickel-coated alumina powder. *Surface and Coatings*, 202(19):4855, 2008.

[21] W.Y. Li, G. Zhang, C. Zhang, O. Elkedim, H. Liao, and C. Coddet. Effect of ball milling of feedstock powder on microstructure and properties of TiN particle-reinforced Al alloy-based composites fabricated by cold spraying. *Journal of Thermal Spray Technology*, 17(3):316, 2008.

[22] K. Spencer, D. M. Fabijanic, and M. X. Zhang. The influence of Al_2O_3 reinforcement on the properties of stainless steel cold spray coatings. *Surface and Coatings Technology*, 206(14):3275–3282, 2012.

[23] K. Spencer, D.M. Fabijanic, and M.X. Zhang. The use of kinetic metallization to form intermetallic reinforced composite coatings by post-spray heat treatment. *Surface and Coatings Technology*, 203(20-21):2019, 2009.

[24] B. Venkataraman and G. Sundararajan. Correlation between the characteristics of the mechanically mixed layer and wear behaviour of aluminium, Al-7075 alloy and Al-MMCs. *Wear*, 245:22–38, 2000.

[25] B. Venkataraman and G. Sundararajan. The sliding wear behaviour of Al-SiC particulate composites - II. The characterization of subsurface deformation and correlation with wear behaviour. *Acta Materialia*, 44(2):451–460, 1996.

[26] M.R. Rosenberger, C.E. Schvezov, and E. Forlerer. Wear of different aluminum matrix composites under conditions that generate a mechanically mixed layer. *Wear*, 259(1-6):590, 2005.

[27] A.T. Alpas and J. Zhang. Effect of microstructure (particulate size and volume fraction) and counterface material on the sliding wear resistance of particulate-reinforced aluminum matrix composites. *Metallurgical and Materials Transactions A*, 25A:969–983, 1994.

[28] A. Alpas and J. Zhang. Effect of SiC particulate reinforcement on the dry sliding wear of aluminium silicon alloys (A356). *Wear*, 155:83–104, 1992.

[29] Maurice Godet. Third-bodies in tribology. *Wear*, 136(1):29–45, 1990.

[30] P. Heilmann, J. Don, T.C. Sun, D.A. Rigney, and W.A. Glaeser. Sliding wear and transfer. *Wear*, 91(2):171, 1983.

[31] D.A. Rigney, L.H. Chen, M.G.S. Naylor, and A.R. Rosenfield. Wear processes in sliding systems. *Wear*, 100:195–219, 1984.

[32] D.A. Rigney. Comments on the sliding wear of metals. *Tribology International*, 30(5):361, 1997.

[33] Peter J. Blau. Mechanisms for transitional friction and wear behavior of sliding metals. *Wear*, 72:55–66, 1981.

[34] B. Venkataraman and G. Sundararajan. The sliding wear behaviour of Al-SiC particulate composites - I. Macrobehaviour. *Acta Materialia*, 44(2):451–460, 1996.

[35] Alexander P. Zhilyaeva and Terence G. Langdon. Using high-pressure torsion for metal processing: Fundamentals and applications. *Progress in Materials Science*, 53(6):893–979, 2008.

[36] S. Descartes, M. Busquet, and Y. Berthier. An attempt to produce ex situ TTS to understand their mechanical formation conditions - The case of an ultra high purity iron. *Wear*, 27:1833–1841, 2011.

[37] F. Ren, S.N. Arshad, P. Bellon, R.S. Averback, M. Pouryazdan, and H. Hahn. Sliding wear-induced chemical nanolayering in Cu-Ag, and its implications for high wear resistance. *Acta Materialia*, 72:148–158, 2014.

[38] K.K. Chawla. *Structure and Properties of Composites*, volume 13, chapter Metal Matrix Composites, pages 122–179. VCH, 1991.

[39] H. Herman and S. Sampath. *Metallurgical and Ceramic Protective Coatings*, chapter Thermal Spray Coatings, pages 261–289. Chapman and Hall, London, 1996.

[40] Alexander Evans, Christopher San Marchi, and Andreas Mortensen. *Metal Matrix Composites*, chapter MMC Companies in Alphabetical Order, pages 79–374. Kluwer Academic Publishers, Dordrecht, 2003.

[41] T.W. Clyne and P.J. Withers. *An Introduction to Metal Matrix Composites*, chapter Applications, pages 454–471. Cambridge University Press, Cambridge, 1993.

[42] S.E. Saliebekov. *Metal Matrix Composites*, chapter Basic components used in the production of metal composites, pages 51–60. Champman & Hall, London, 1995.

[43] D. Lloyd. *Encyclopedia of Materials: Science and Technology*, chapter Metal Matrix Composites with Roughly Equiaxed Reinforcements: Microstructure and Mechanical Behavior, pages 5455–5461. Elsevier, Oxford, 2001.

[44] T.W. Clyne and P.J. Withers. *An Introduction to Metal Matrix Composites*, chapter General Introduction, pages 1–10. Cambridge University Press, Cambridge, 1993.

[45] W.D. Callister. *Materials Science and Engineering: An Introduction*, chapter Composites, pages 527–566. John Wiley and Sons, Inc., 2003.

[46] T.W. Clyne and P.J. Withers. *An Introduction to Metal Matrix Composites*, chapter Basic Composite Mechanics, pages 12–41. Cambridge University Press, Cambridge, 1993.

[47] J.C. Halpin and J.L. Kardos. The halpin-tsai equations: A review. *Polymer Science and Engineering*, 16:344–352, 2004.

[48] Hamid Assadi, Frank Gärtner, Thorsten Stoltenhoff, and Heinrich Kreye. Bonding mechanism in cold gas spraying. *Acta Materialia*, 51:4379–4394, 2003.

[49] B. Bhushan. *Principles and Applications of Tribology*, chapter Types of Wear Mechanisms, pages 480–534. John Wiley and Sons, Inc., New York, 1999.

[50] Tobias Schmidt, Frank Gartner, Hamid Assadi, and Heinrich Kreye. Development of a generalized parameter window for cold spray deposition. *Acta Materialia*, 54:729–742, 2006.

[51] D. Goldbaum, J. Shockley, R. Chromik, A. Rezaeian, S. Yue, J.-G. Legoux, and E. Irissou. The effect of the deposition conditions on adhesion strength of Ti and Ti6Al4V cold spray splats. *Journal of Thermal Spray Technology*, 21(2):288, 2012.

[52] R.R. Chromik, D. Goldbaum, J.M. Shockley, S. Yue, E. Irissou, J.-G. Legoux, and N.X. Randall. Modified ball bond shear test for determination of adhesion strength of cold spray splats. *Surface and Coatings Technology*, 205:1409–1414, 2010.

[53] Hirotaka Fukanuma, Naoyuki Ohno, Bo Sun, and Renzhong Huang. In-flight particle velocity measurements with DPV-2000 in cold spray. *Surface and Coatings Technology*, 201:1935–1941, 2006.

[54] E. Irissou and B. Arsenault. Corrosion study of cold sprayed aluminum coatings onto Al 7075 alloy substrates. In *Global Coating Solutions: Proceedings of the 2007 International Thermal Spray Conference*, 2007.

[55] Maria Parco, Lidong Zhao, Jochen Zwick, Kirsten Bobzin, and Erich Lugscheider. Investigation of HVOF spraying on magnesium alloys. *Surface and Coatings Technology*, 201:3269–3274, 2006.

[56] A. Pardo, M.C. Merino, M. Mohedano, P. Casajús, A.E. Coy, and R. Arrabal. Corrosion behaviour of Mg/Al alloys with composite coatings. *Surface and Coatings Technology*, 203:1252–1263, 2009.

[57] K. Spencer and M.-X. Zhang. The emergence of cold spray as a tool for surface modification. *Key Engineering Materials*, 384:61–74, 2008.

[58] A. Sova, V.F. Kosarev, A. Papyrin, and I. Smurov. Effect of ceramic particle velocity on cold spray deposition of metal-ceramic coatings. *Journal of Thermal Spray Technology*, 20:285–291, 2011.

[59] B. Bhushan. *Principles and Applications of Tribology*, chapter Definition and History of Tribology, pages 1–8. John Wiley and Sons, Inc., New York, 1999.

[60] B. Bhushan. *Principles and Applications of Tribology*, chapter Friction, pages 344–430. John Wiley and Sons, Inc., New York, 1999.

[61] Tadeusz Burakowski and Tadeusz Wierzchon. *Surface Engineering of Metals: Principles, Equipment, Technologies*, chapter The Solid Surface, pages 29–40. CRC Press, Boca Raton, 1999.

[62] E. Rabinowicz. *Friction and Wear of Materials*. Wiley, 1965.

[63] B. Bhushan. *Principles and Applications of Tribology*, chapter Adhesion, pages 294–392. John Wiley and Sons, Inc., New York, 1999.

[64] K. Holmberg and A. Matthews. *Coatings Tribology: Properties, Mechanisms, Techniques, and Applications in Surface Engineering*, chapter Tribology of Coatings, pages 41–175. Elsevier, Amsterdam, 2009.

[65] N. Fillot, I. Iordanoff, and Y. Berthier. Wear modeling and the third body concept. *Wear*, 262:949–957, 2007.

[66] Maurice Godet. The third-body approach: a mechanical view of wear. *Wear*, 100:437–452, 1984.

[67] Y. Berthier. *Wear - Materials, Mechanisms and Practice*, chapter 7: Third-Body Reality - Consequences and Use of the Third-Body Concept to Solve Friction and Wear Problems, pages 291–316. John Wiley and Sons, Ltd., 2005.

[68] A.R. Lansdown. *Molybdenum Disulphide Lubrication*, chapter Transfer in Lubrication, pages 107–120. Elsevier, Amsterdam, 1999.

[69] M. Cocks. Interaction of sliding metal surfaces. *Journal of Applied Physics*, 33(7):2152–2161, 1962.

[70] Morton Antler. Processes of Metal Transfer and Wear. *Wear*, 7:181–203, 1964.

[71] D.A. Rigney. Transfer, mixing, and associated chemical and mechanical processes during the sliding of ductile materials. *Wear*, 245(1):1–9, 2000.

[72] Y. Berthier, M. Godet, and M. Brendle. Velocity Accommodation in Friction. *Tribology Trans*, 32:490–496, 1989.

[73] K.L. Johnson. *Contact Mechanics*. Cambridge University Press, Cambridge, 1985.

[74] A. Sato and R. Mehrabian. Aluminum matrix composites: Fabrication and properties. *Metallurgical Transactions B*, 7B:443–451, 1976.

[75] Kishore K. Anand and Kishore. On the wear of aluminium-corundum composites. *Wear*, 85(2):163–169, 1983.

[76] A.P. Sannino and H.J. Rack. Dry sliding wear of discontinuously reinforced aluminum composites: review and discussion. *Wear*, 189:1–19, 1995.

[77] Y. Wang, W.M. Rainforth, H. Jones, and M. Lieblich. Dry wear behaviour and its relation to microstructure of novel 6092 aluminium alloy-Ni_3Al powder metallurgy composite. *Wear*, 251:1421–1432, 2001.

[78] S.V. Prasad and R. Asthana. Aluminum metal - matrix composites for automotive applications:tribological considerations. *Tribology Letters*, 17(3):445–453, 2004.

[79] C. Perrin and W.M. Rainforth. The effect of alumina fibre reinforcement on the wear of an Al-4.3 *Wear*, 181-183:312–324, 1995.

[80] Anirban Mahato, Nisha Verma, Vikram Jayaram, and S.K. Biswas. Severe wear of a near eutectic aluminium-silicon alloy. *Acta Materialia*, 59:6069–6082, 2011.

[81] J. Li, M. Elmadagli, V.Y. Gertsman, and A.T. Alpas. FIB and TEM characterization of subsurfaces of an Al-Si alloy (A390) subjected to sliding wear. *Materials Science & Engineering, A*, 421:317–327, 2006.

[82] M. Elmadagli, T. Perry, and A.T. Alpas. A parametric study of the relationship between microstructure and wear resistance of Al-Si alloys. *Wear*, 262:79–92, 2007.

[83] S. Wilson and A.T. Alpas. Wear mechanism maps for metal matrix composites. *Wear*, 212(1):41, 1997.

[84] S.R. BS.R. Bakshi. Wang, T. Price, D. Zhang, A.K. Keshri, Y. Chen, D.G. MD.G. McCartney.H. Shipway, and A. Agarwal. Microstructure and wear properties of aluminum/aluminum-silicon composite coatings prepared by cold spraying. *Surface and Coatings Technology*, 204(4):503, 2009.

[85] F. M. Hosking, F. F. Portillo, R. Wunderlin, and R. Mehrabian. Composites of aluminium alloys: Fabrication and wear behaviour. *Journal of Materials Science*, 17:477–498, 1982.

[86] S. Chung and B.H. Hwang. A microstructural study of the wear behaviour of SiCp/Al composites. *Tribology International*, 24:307–314, 1994.

[87] A.P. Sannino and H.J. Rack. Tribological investigation of 2009 Al-20vol.part i: Composite performance. *Wear*, 197:151–159, 1996.

[88] S. Skolianos and T.Z. Kattamis. Tribological properties of sicp-reinforced Al-4.5alloy composites. *Materials Science and Engineering A*, 163:107–113, 1993.

[89] M Roy, B. Venkataraman, V.V. Bhanuprasad, Y.R. Mahajan, and G. Sundararajan. The effect of particulate reinforcement on the sliding wear behavior of aluminum matrix composites. *Metallurgical Transactions A*, 23A:2833–2847, 1992.

[90] J. Jiang, F.H. Stott, and M.M. Stack. A mathematical model for sliding wear of metals at elevated temperatures. *Wear*, 181-183:20–31, 1995.

[91] S.L. Rice, H. Nowotny, and S.F. Wayne. Characteristics of metallic subsurface zones in sliding and impact wear. *Wear*, 74:131–142, 1981-1982.

[92] Y. Iwai, H. Yoneda, and T. Honda. Sliding wear behavior of SiC whisker-reinforced aluminum composite. *Wear*, 181-183:594–602, 1995.

[93] M.J. Ghazali, W.M. Rainforth, and M.Z. Omara. A comparative study of mechanically mixed layers (MMLs) characteristics of commercial aluminium alloys sliding against alumina and steel sliders. *Journal of Materials Processing Technology*, 201:662–668, 2008.

[94] A. Mahato, T.A. Perry, V. Jayaram, and S.K. Biswas. Pressure and thermally induced stages of wear in dry sliding of a steel ball against an aluminium-silicon alloy flat. *Wear*, 268:1080–1090, 2010.

[95] Yves Berthier. *Handbook of Materials Behavior Models*, chapter Background on friction and wear, pages 676–697. Academic Press, 2001.

[96] T. Miyajima and Y. Iwai. Effects of reinforcements on sliding wear behavior of aluminum matrix composites. *Wear*, 255:606–616, 2003.

[97] Aleksandar Vencl, Ilija Bobic, Milan T. Jovanovic, Miroslav Babic, and Slobodan Mitrovic. Microstructural and tribological properties of A356 Al-Si alloy reinforced with Al_2O_3 particles. *Tribology Letters*, 32:159–170, 2008.

[98] C. Subramanian. Effects of sliding speed on the unlubricated wear behaviour of Al-12.3wt. *Wear*, 151:97–110, 1991.

[99] ASTM G77-98(2004) "standard test method for ranking resistance of materials to sliding wear using block-on-ring wear test".

[100] P. Blau. *Friction Science and Technology: From Concepts to Applications.* CRC Press, 2008.

[101] ASTM G99-05(2010) "standard test method for wear testing with a pin-on-disk apparatus".

[102] Z.N. Farhat, Y. Ding, D.O. Northwood, and A.T. Alpas. Effect of grain size on friction and wear of nanocrystalline aluminum. *Materials Science and Engineering A*, 206:302–313, 1996.

[103] X. Meng-Buranya, T.A. Perry, A.K. Sachdev, and A.T. Alpas. Subsurface sliding wear damage characterization in Al-Si alloys using focused ion beam and cross-sectional TEM techniques. *Wear*, 270:152–162, 2011.

[104] S.K. Dey, T.A. Perry, and A.T. Alpas. Micromechanisms of low load wear in an Al-18.5 *Wear*, 267:515–524, 2009.

[105] P.W. Bridgman. On torsion combined with compression. *Journal of Applied Physics*, 14:273–283, 1943.

[106] P.W. Bridgman. *Studies in Large Plastic Flow and Fracture.* McGraw-Hill Book Company, Inc., 1952.

[107] R. Z. Valiev, O.A. Kaibyshev, R.I. Kuznetsov, R.S. Musalimov, and N.K. Tsenev. The low-temperature superplasticity of metallic materials. *Doklady Akademii Nauk SSSR*, 301:864, 1988.

[108] R.Z. Valiev and T.G. Langdon. Principles of equal-channel angular pressing as a processing tool for grain refinement. *Progress in Materials Science*, 51:881–981, 2006.

[109] Y. Saito, N. Tsuji, H. Utsunomiya, T. Sakai, and R.G. Hong. Ultra-fine grained bulk aluminum produced by accumulative roll-bonding (ARB) process. *Scripta Materialia*, 39:1221–1227, 1998.

[110] D. Kuhlmann-Wilsdorf, B.C. Cai, and R.B. Nelson. Plastic flow between Bridgman anvils under high pressures. *Journal of Materials Research*, 6(12):2547–2564, 1991.

[111] A. P. Zhilyaev, T. R. McNelley, and T. G. Langdon. Evolution of microstructure and microtexture in FCC metals during high-pressure torsion. *Journal of Materials Science*, 42:1517–1528, 2007.

[112] Sylvie Descartes, C. Desrayaud, and E.F. Rauch. Inhomogeneous microstructural evolution of pure iron during high-pressure torsion. *Materials Science & Engineering, A*, 528:3666–3675, 2011.

[113] D.S. Fields and W.A. Backofen. Determination of strain-hardening characteristics by torsion testing. *ASTM Proceeding*, 57:1259–1272, 1957.

[114] John J. Jonas, Frank Montheillet, Laszlo S. Toth, and Chiradeep Ghosh. Effects of varying twist and twist rate sensitivities on the interpretation of torsion testing data. *Materials Science & Engineering A*, 591:9–17, 2014.

[115] John J. Jonas, Chiradeep Ghosh, and Laszlo S. Toth. The equivalent strain in high pressure torsion. *Materials Science and Engineering: A*, 607:530–535, 2014.

[116] A. P. Zhilyaev, T.R. McNelley, and T.G. Langdon. Evolution of microstructure and microtexture in fcc metals during high-pressure torsion. *Journal of Materials Science*, 42:1517–1528, 2007.

[117] Cheng Xu, Zenji Horita, and Terence G. Langdon. The evolution of homogeneity in processing by high-pressure torsion. *The evolution of homogeneity in processing by high-pressure torsion*, 55:203–212, 2007.

[118] A.P. Zhilyaev, K. Oh-ishi, T.G. Langdon, and T.R. McNelley. Microstructural evolution in commercial purity aluminum during high-pressure torsion. *Materials Science and Engineering A*, 410-411:277–280, 2005.

[119] Y. Todaka, M. Umemoto, A. Yamazaki, J. Sasaki, and K. Tsuchiya. Influence of high-pressure torsion straining conditions on microstructure evolution in commercial purity aluminum. *Materials Transactions*, 49:7–14, 2008.

[120] Genki Sakai, Zenji Horita, and Terence G. Langdon. Grain refinement and superplasticity in an aluminum alloy processed by high-pressure torsion. *Materials Science and Engineering: A*, 393:344–351, 2005.

[121] R.K Islamgaliev, N.F Yunusova, I.N Sabirov, A.V Sergueeva, and R.Z Valiev. Deformation behavior of nanostructured aluminum alloy processed by severe plastic deformation. *Materials Science and Engineering: A*, 319-321:877–881, 2001.

[122] B.B Straumal, B Baretzky, A.A Mazilkin, F Phillipp, O.A Kogtenkova, M.N Volkov, and R.Z Valiev. Formation of nanograined structure and decomposition of supersaturated solid solution during high pressure torsion of Al-Zn and Al-Mg alloys. *Acta Materialia*, 52:4469–4478, 2004.

[123] Rusland Z. Valiev, Rinat K. Islamgaliev, Nina F. Kuzmina, Yong Li, and Terence G. Langdon. Strengthening and grain refinement in an Al-6061 metal matrix composite through intense plastic straining. *Scripta Materialia*, 40(1):117–122, 1998.

[124] Ceren Gode, Hakan Yilmazer, Ismail Ozdemir, and Yoshikazu Todaka. Microstructural refinement and wear property of Al-Si-Cu composite subjected to extrusion and high-pressure torsion. *Materials Science and Engineering: A*, 618:377–384, 2014.

[125] C. Xu, Z. Horita, and T.G. Langdon. Mechanical properties of Al-6061 and an Al-6061 metal matrix composite processed by high-pressure torsion. *Materials Science Forum*, 667-669:689–694, 2011.

[126] J.L. Young, D. Kuhlmann-Wilsdorf, and R. Hull. The generation of mechanically mixed layers (MMLs) during sliding contact and the effects of lubricant thereon. *Wear*, 246:74–90, 2000.

[127] Y.-L. Shen. *Constrained Deformation of Materials, Chapter 2: Mechanics Preliminaries.* Springer, 2010.

[128] Jean Lemaitre. A continuous damage mechanics model for ductile fracture. *Journal of Engineering Materials and Technology*, 107:83–89, 1985.

[129] H. Qing. 2D micromechanical analysis of SiC/Al metal matrix composites under tensile, shear and combined tensile/shear loads. *Materials & Design*, 51:438–447, 2013.

[130] Michael Brunig and Steffen Gerke. Simulation of damage evolution in ductile metals undergoing dynamic loading conditions. *International Journal of Plasticity*, 27:1598–1617, 2011.

[131] Yingbin Bao and Tomasz Wierzbicki. On the cut-off value of negative triaxiality for fracture. *Engineering Fracture Mechanics*, 72(7):1049–1069, 2005.

[132] Javier Bonet and Richard D. Wood. *Nonlinear continuum mechanics for finite element analysis.* Cambridge University Press, 1997.

[133] Y.-L. Shen. *Constrained Deformation of Materials.* Springer, 2010.

[134] Y.L. Shen, M. Finot, A. Needleman, and S. Suresh. Effective plastic response of two-phase composites. *Acta Metallurgica Et Materialia*, 43(4):1701–1722, 1995.

[135] S.G. Song, N. Shi, G.T. Gray III, and J.A. Roberts. Reinforcement shape effects on the fracture behavior and ductility of particulate-reinforced 6061-Al matrix composites. *METALLURGICAL AND MATERIALS TRANSACTIONS A*, 27A:3739–3746, 1996.

[136] N. Chawla, V.V. Ganesh, and B. Wunsch. Three-dimensional (3d) microstructure visualization and finite element modeling of the mechanical behavior of SiC particle reinforced aluminum composites. *Scrip*, 51:161–165, 2004.

[137] *DPV-2000 Reference Manual, Rev.5, TECNAR, St-Bruno, QC.*

[138] R. Morgan, P. Fox, J. Pattison, C. Sutcliffe, and W. O'Neill. Analysis of cold gas dynamically sprayed aluminium deposits. *Materials Letters*, 58:1317–1320, 2004.

[139] J.R. Davis, editor. *Aluminum and Aluminum Alloys*, chapter Corrosion Behavior, pages 579–622. ASM Specialty Handbook. ASM International, 1993.

[140] R. R. Chromik, H. W. Strauss, and T. W. Scharf. Materials phenomena revealed by in situ tribometry. *JOM*, 64(1):35–43, 2012.

[141] Anthony C. Fischer-Cripps. *Nanoindentation*. Mechanical Engineering Series. Springer, 2004.

[142] *Hysitron Triboindenter User Manual, Hysitron, Inc., Minneapolis USA*.

[143] W.C. Oliver and G.M. Pharr. An improved technique for determining hardness and elastic modulus using load and displacement sending indentation experiments. *Journal of Materials Research*, 7(6):1564–1586, 1992.

[144] W.G. Sawyer and K.J. Wahl. Accessing inaccessible interfaces: In situ approaches to materials tribology. *MRS Bulletin*, 33(12):1145, 2008.

[145] T.W. Scharf and I.L. Singer. Monitoring transfer films and friction instabilities with in situ Raman tribometry. *Tribology Letters*, 14(1):3, 2003.

[146] Holger W. Strauss, Richard R. Chromik, Salim Hassani, and Jolanta E. Klemberg-Sapieha. In situ tribology of nanocomposite Ti-Si-C-H coatings prepared by PE-CVD. *Wear*, 272(1):133–148, 2011.

[147] R.R. Chromik, A.L. Winfrey, J. LuingJ. Lun.J. Nemanich, and K.J. Wahl. Run-in behavior of nanocrystalline diamond coatings studied by in situ tribometry. *Wear*, 265(3-4):477, 2008.

[148] Pantcho Stoyanov, Holger W. Strauss, and Richard R. Chromik. Scaling effects between micro- and macro-tribology for a Ti-MoS2 coating. *Wear*, 274-275(0):149–161, 2012.

[149] Richard R. Chromik, Colin C. Baker, Andrey A. Voevodin, and Kathryn J. Wahl. In situ tribometry of solid lubricant nanocomposite coatings. *Wear*, 262(9):1239–1252, 2007.

[150] I.L. Singer, S.D. Dvorak, K.J. Wahl, and T.W. Scharf. Role of third bodies in friction and wear of protective coatings. *Journal of Vacuum Science & Technology A*, 21(5):S232–S240, 2003.

[151] S.K. Biswas. *Wear - Materials, Mechanisms and Practice*, chapter 3: Wear of Metals: A Material Approach, pages 21–36. John Wiley and Sons, Ltd., 2005.

[152] C.U.A. Cheong and P.C. Stair. In situ studies of the lubricant chemistry and frictional properties of perfluoropolyalkyl ethers at a sliding contact. *Tribology Letters*, 10(1-2):117, 2001.

[153] X. Ge and S. Schmauder. Elastic modulus and interface stress constraint of particle-reinforced composites. *Materials Science & Engineering, A*, 168:93, 1993.

[154] T.L. Schmitz, J.E. Action, D.L. Burris, J.C. Ziegert, and W.G. S. Wear rate uncertainty analysis. *Journal of Tribology*, 126(4):802, 2004.

[155] P. Morin, M. Pitaval, D. Besnard, and G. Fontaine. Scanning electron microscope observation of single defects in solid crystalline materials. *Philosophical Magazine A*, 40:511, 1979.

[156] Yongshan Tao, Tianying Xiong, Chao Sun, Huazi Jin, Hao Du, and Tiefan Li. Effect of Al-Al_2O_3 on the properties of cold sprayed Al-Al_2O_3 composite coatings on AZ91D magnesium alloy. *Applied Surface Science*, 256(1):261 – 266, 2009.

[157] U.S. Department of Defense, U.S. Army Research Laboratory: Materials Deposition, Cold Spray, Standard MIL-STD-3021, 2008.

[158] Victor K. Champagne. The Repair of Magnesium Rotorcraft Components by Cold Spray. *Journal of Failure Analysis and Prevention*, 8:164–175, 2008.

[159] Hong Jin Kim, Wolfgang Windl, and D.A. Rigney. Structure and chemical analysis of aluminium wear debris: Experiments and ab initio simulations. *Acta Materialia*, 55:6489–6498, 2007.

[160] S.V. Prasad, J.R. Michael, B.S. Majumdar, and C.C. Battaile. On the Evolution of Friction-Induced Microstructures in Single Crystal Nickel. *Microscopy and Microanalysis*, 14 (Supplement 2):906–907, 2008.

[161] J.M. Shockley, H.W. Strauss, R.R. Chromik, N. Brodusch, R. Gauvin, E. Irissou, and J.-G. Legoux. In situ tribometry of cold-sprayed al-Al_2O_3 composite coatings. *Surface and Coatings Technology*, 215:350–356, 2013.

[162] S. Descartes and Y. Berthier. Rheology and flows of solid third bodies: background and application to an MoS_1.6 coating. *Wear*, 253:546–556, 2002.

[163] K.J. Wahl, R.R. Chromik, and G.Y. Lee. Quantitative in situ measurement of transfer film thickness by a Newton‘s rings method. *Wear*, 264:731, 2008.

[164] H.-J. Kim, A. Emge, S. Karthikeyan, and D.A. Rigney. Effects of tribooxidation on sliding behavior of aluminum. *Wear*, 259:501–505, 2005.

[165] W.M. Rainforth. Microstructural evolution at the worn surface: a comparison of metals and ceramics. *Wear*, 245:162–177, 2000.

[166] Afrooz Barnoush, Markus T. Welsch, and Horst Vehoff. Correlation between dislocation density and pop-in phenomena in aluminum studied by nanoindentation and electron channeling contrast imaging. *Scripta Materialia*, 63:465–468, 2010.

[167] J.R. Davis, editor. *Corrosion Behavior*, pages 579–622. ASM International, Materials Park, Ohio, 1993.

[168] D.H. Buckley. Ceramic microstructure and adhesion. *Journal of Vacuum Science & Technology, A: Vacuum, Surfaces, and Films*, A3(3):762, 1985.

[169] S.V. Pepper. Shear strength of metal-sapphire contacts. *Journal of Applied Physics*, 47:801, 1976.

[170] K.H. Johnson and S.V. Pepper. Molecular-orbital model for metal-sapphire interfacial shear strength. *Journal of Applied Physics*, 53:6634, 1982.

[171] D.J. Siegel, L.G. Hector Jr, and J.B. Adams. Adhesion, atomic structure, and bonding at the Al(111)/alpha-Al_2O_3(0001) interface; a first principles study. *Physical Review B*, 65(8):854151–8541519, 2002.

[172] R.Z. Valiev, R.K. Islamgaliev, and I.V. Alexandrov. Bulk nanostructured materials from severe plastic deformation. *Progress in Materials Science*, 45:103–189, 2000.

[173] P.J. Apps, J.R. Bowen, and P.B. Prangnell. The effect of coarse second-phase particles on the rate of grain refinement during severe deformation processing. *Acta Mat*, 51:2811–2822, 2003.

[174] I. Gutierrez-Urrutia, M.A. Munoz-Morris, and D.G. Morris. Contribution of microstructural parameters to strengthening in an ultrafine-grained Al-7 *Acta Materialia*, 55:1319–1330, 2007.

[175] I. Gutierrez-Urrutia, M.A. Munoz-Morris, I. Puertas, C. Luis, and D.G. Morris. Influence of processing temperature and die angle on the grain microstructure produced by severe deformation of an Al-7 *Materials Science and Engineering A*, 475:268–278, 2008.

[176] N.A. Fleck, G.M. Muller, and J.W. Hutchison. Strain gradient plasticity: Theory and experiment. *Acta Metallurgica Et Materialia*, 42:475–487, 1994.

[177] J. Michael Shockley, S. Descartes, E. Irissou, J.-G. Legoux, and R. R. Chromik. Third body behavior during dry sliding of cold-sprayed al-Al_2O_3 composites: In situ tribometry and microanalysis. *Tribology Letters*, 54:191–206, 2014.

[178] A. Sova, D. Pervushin, and I. Smurov. Development of multimaterial coatings by cold spray and gas detonation spraying. *Surface & Coatings Technology*, 205:1108–1114, 2010.

[179] H. Getu, J.K. Spelt, and M. Papini. Conditions leading to the embedding of angular and spherical particles during the solid particle erosion of polymers. *Wear*, 292-293:159–168, 2012.

[180] C.-Y. Yang, S.-L. Lee, C.-K. Lee, and J.C. Lin. Effects of Sr and Sb modifiers on the sliding wear behavior of A357 alloy under varying pressure and speed conditions. *Wear*, 261:1348–1358, 2006.

[181] T. Christman, A. Needleman, and S. Suresh. An experimental and numerical study of deformation in metal-ceramic composites. *Acta Metallurgica*, 37(11):3029–3050, 1989.

[182] J. Michael Shockley, S. Descartes, P. Vo, E. Irissou, and R. R. Chromik. The influence of Al_2O_3 particle morphology on the coating formation and dry sliding wear behavior of cold-sprayed Al-Al_2O_3 composites. *Submitted*, Submitted, 2014.

[183] Y. Ivanisenko, W. Lojkowski, R.Z. Valiev, and H.-J. Fecht. The mechanism of formation of nanostructure and dissolution of cementite in a pearlitic steel during high pressure torsion. *Acta Materialia*, 51:5555–5570, 2003.

[184] Kaveh Edalati, Zenji Horita, and Terence G. Langdon. The significance of slippage in processing by high-pressure torsion. *Scripta Materialia*, 60:9–12, 2009.

[185] K.J. Hodder, J.A. Nychka, and A.G. McDonald. Comparison of 10 μm and 20 nm Al-Al_2O_3 metal matrix composite coatings fabricated by low-pressure cold gas dynamic spraying. *Journal of Thermal Spray Technology*, 23(5):839–848, 2014.

[186] Yves Berthier, Magali Busquet, A. Eleod, Laurent Baillet, Lionel Lafarge, Aurélien Saulot, and Sylvie Descartes. Rheos, caractérisation des matériaux sous sollicitations extrêmes (couplage pression - cisaillement). In *Séminaire Annuel MACODEV*, Lyon, France, 2008.

[187] J.M. Shockley, S. Descartes, and R.R. Chromik. Significance of Al_2O_3 particle morphology in the microstructure evolution of cold-sprayed al-al2o3 during unconstrained high-pressure torsion. *Submitted*, n/a:n/a, 2014.

[188] Dina Goldbaum, Jihane Ajaja, Richard R. Chromik, Wilson Wong, Stephen Yue, Eric Irissou, and Jean-Gabriel Legoux. Mechanical behavior of Ti cold spray coatings determined by a multi-scale indentation method. *Materials Science and Engineering: A*, 530:253–265, 2011.

[189] L Mishnaevsky, K Derrien, and D Baptiste. Effect of microstructure of particle reinforced composites on the damage evolution: probabilistic and numerical analysis. *Composites Science and Technology*, 64:1805–1818, 2004.

Appendix A

RHEOS standard operating procedure

This SOP is the original work of the author.

A.1 Introduction

RHEOS consists of two major components to conduct high pressure torsion experiments: a hydraulic pump to apply normal loading on the samples and an 8 kW electric motor to induce shear through rotation. Data monitoring during experiments includes rotational torque and vertical displacement. This document will explain the basic steps of RHEOS operation. The procedures in this document may NOT be complete and it is NOT a substitute for proper training.

A.1.1 Normal loading

SAFETY: Do not put your hands near moving parts when the hydraulic pump is on.

The hydraulic system includes a pump, an **electronic valve ("bypass")** controlling pressurization of the normal load, an **electronic valve ("bloquage")** controlling depressurization (and thus regulation) of the normal load, and a **manual valve** permitting human-controlled depressurization of the normal load. The "bypass" and "bloquage" electronic valves are controlled by an **electronic PID controller**, which may need to be tuned to the desired loading range. The desired normal loading segments during an experiment are programmed prior to experimentation using software called **iTools**.

A.1.2 Rotation

SAFETY: Do not put your hands near moving parts when the motor is "sous tension."

Rotation is driven by an 8 kW electric motor. The desired rotations (in terms of degrees of rotation, rotation speed, etc.) are programmed prior to experimentation using software called **Cockpit**. An individual rotation pattern is called a "**position**." The motor is turned on and off via a button that toggles between the states of "hors tension" and "sous tension."

A.1.3 Torque measurement

The couple during an experiment is measured using a static torque sensor. There are two available sensors with different ranges of measurement and maximum tolerable normal load. It requires about half a day to switch the sensors because they are very heavy; furthermore, some calibration steps are required after switching sensors.

A.1.4 Vertical height measurement

During an experiment, a set of three induction sensors spaced apart by 120° measure displacement with an accuracy of ± 0.01 µm, with a maximum range of 2.5 mm. A second sensor with an accuracy of ± 0.5 mm measures the displacements along the entire movement range of the top and bottom parts of the instruments.

A.1.5 Software for experimental control and data acquisition

A labview program called "RHEOS - mesure continue et enregistrement" is used to launch the pre-programmed experimental sequence(s) of normal loading and rotation. It is also used to monitor the sensor outputs and save them into ".tdms" files for further analysis.

A.2 System startup

A.2.1 Turning on the power sources

PC:

Username “exp306”, password “lamcosexp306”, while using “cet ordinateur” instead of “INSA-Lyon.” System software can be accessed from the desktop shortcut called “Raccourci vers Rheos acquisition.”

Motor drive (tall electronics rack behind the PC):

Turn the black rotary switch to “on,” then press the green pushbutton switch. Couple sensor (on top of the tall electronics rack): Turn the rocker switch to “on” for the larger box, and plug in the smaller box.

Hydraulics unit:

Turn the black pivot switch to “on.” For now, do not press any of the green pushbutton switches.

A.2.2 Starting and initial zeroing the motor

Clear every loose object from the motor area of RHEOS. Open the program called “Rheos acquisitions avec mesure continue.” Activate the motor by clicking the button labeled that toggles between “hors tension” and “sous tension.” When activated for the first time after being off, some jittery noises will be produced as part of its startup routine, then the motor will fall silent. Release the “hors/sous tension” button by clicking it, turning it from red back to gray. The second time the motor is activated after being off (i.e., the next time you click “hors/sous tension”), it will zero the motor to the nearest 5° increment. Optionally, before activating the motor again, you may manually turn the motor so that the small arrow on the motor points between the two arrows labelled “0°” on the stationary casing; this will allow you to track the degrees of rotation according to those drawn on the motor casing.

A.2.3 Lubricating the motor bearings

Start the motor by activating the “hors/sous tension” button. Select “Position 0: +10 tours” and click the “start” button.

The motor will now turn 10 cycles in the positive direction. Next, select “Position 1: -10 tours” and it will turn 20 cycles in the negative direction. Finally, select “Position 2 (retour zéro)” to return the motor to zero. After this step, the “hors/sous tension” button can be released as desired.

A.3 Running an experiment

If you have already programmed and tested the normal loading segments and rotation positions, proceed with this section. If you have not yet done this or are not sure, see Section 4 (Programming the Normal Loading Segments in iTools) and Section 5 (Programming the Rotation Positions in Cockpit).

3.1 Ensure that you have followed all of the startup steps in Section 2.

3.2 Install the anvils. (Instructions for anvil polishing, degreasing, etc. are not described in this document.) When tightening the screws, just turn them by hand until they are snug. **Do not over-tighten the screws, as this can bend the ring.** Turing testing, the anvils will be held in place by the compressive forces; the ring simply keeps the anvils from moving when they’re not loaded.

3.3 Place your sample in the desired location on the anvils. (Instructions for sample polishing, degreasing, etc. are not described in this document.)

3.4 Open the program called “RHEOS – mesure continue et enregistrement.” Input the parameters of the file (such as filename, location of file saving, operator name, comments, etc.).

3.5 Turn on the hydraulic pump and the bypass valve by pressing the left and middle green pushbutton switches. Close the manual hydraulic valve (if open).

3.6 Use the hanging green pushbutton switch to begin raising the lower portion of the machine. **Make sure you pause every 5-10 seconds while raising it to observe if the position continues to change after you release the button. If so, switch the PID regulator between “auto” and “manual” several times and this will usually correct the problem.**

3.7 Select which “rotation position” is to be used during the test. In the “Declenchement rotation” menu, select “rotation auto” if you want it to rotation to automatically start at the selected loading “segment de rotation” as defined in iTools, with an appropriate delay (usually 15 s) to ensure the load has stabilized. Click the “hors/sous tension” button to activate the motor.

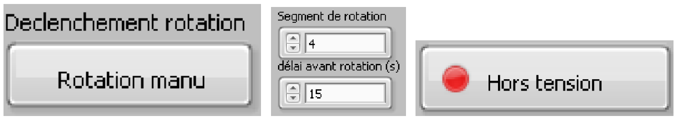

Segment de rotation 4
délai avant rotation (s) 15

3.8 When the anvils are roughly 0.5 mm away from contacting each other, stop the rise and launch the acquisition using the “Démarrer” button, answering “Oui” to the question “Est-ce que les paramètres sont bien enrégistrés?”

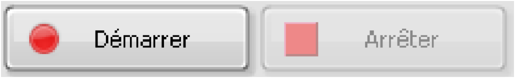

Check the signal coming from the vertical displacement sensors (“ecrasement1, etc.) and adjust each sensor using its screw, overlapping the three signals as close to 1.70 mm as possible. Then use the hanging green pushbutton switch to bring the top anvil into contact with the sample and apply a minor load of 2-3 kN.

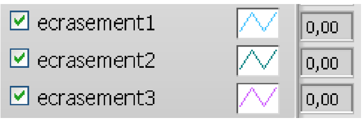

☑ ecrasement1 0,00
☑ ecrasement2 0,00
☑ ecrasement3 0,00

3.9 Stop (“Arrêter”) and then restart the acquisition to save all of the data until now into a separate file from that which will be collected during loading and rotation.

3.10 Start the test by clicking “run.” Open the “bloquage” valve by hitting the rightmost green pushbutton switch once the target load exceeds that of the measured load. Carefully monitor the loading and rotation cycles to ensure the test has completed successfully.

3.11 During the unloading cycle, you can open the manual valve to speed up unloading.

3.12 Stop the acquisition, turn off the valves and hydraulic pump, remove the sample, send the motor to “Position 2 (retour zéro),” and deactivate the motor by clicking the “hors/sous tension” button.

A.4 Programming the normal loading segments in iTools

The commercial software iTools allows for a loading cycle to be modified. Any change to a loading cycle will require testing and fine tuning to ensure it does not create too much overshoot. If fine tuning does not eliminate the overshoot, a new Autotune step may be necessary – which is a step that requires Edouard or another engineer to solve. This section will explain which loading parameters can be modified and how to test a new loading cycle.

A.4.1 Opening and using iTools

iTools will open without being connected to the hydraulic system electronics. To connect, click the icon labeled “Scrutation.” Once the system is connected, go to the “Programmateur” window and to the “Paramètres du segment” tab to modify the desired parameters.

Once all of the desired parameters have been modified, send them to the hydraulics control unit by pressing the designated button, shown below.

A.4.2 Modifying “Paramètres du segment” in iTools

Certain loading parameters can be changed in iTools, and these have drastic effects on the behavior of the loading cycle. A few of the most basic parameters are the following:

tYPE: This is the type of segment parameter. The most common choices are “RMP.T (2)” which is ramping the load as a function of time, and DWEL (3) which is remaining at the target load from the previous segment.

tGt: Target load in 0,1 kN. (i.e., 250,00 means 25,000 kN).

dur : Segment duration. Ramping segments may take longer than the input value if the load is outside the tolerances defined in the “Paramètres Programme” tab.

Modifying values in the “Paramètres Programme” tab requires expertise and will not be described in this document. It is a good idea to ask for help when varying these parameters, as the behavior of the system can be extremely unpredictable when parameters are changed.

Certain PID loop parameters must be “auto-tuned” by the machine according to the desired loading range to be used, but this procedure will not be described in this document.

A.4.3 Testing a new loading cycle

Any new loading cycle could result in unpredictable loading overshoot, which could cause damage to the torque sensor or fracture of the anvils. Therefore it is good practice to use very large diameter anvils for testing any new loading cycle. Once these are installed, put a spare sample between the anvils (there is usually a copper sample in the cabinet). **No Co-WC anvils can tolerate a load in excess of 5 GPa. In the center of the anvils, the maximum stress can be roughly twice that of the nominal average pressure. Therefore, be very careful to not load Co-WC anvils beyond 2.5 GPa.**

Once the desired loading cycle has been set, send the cycle to the control electronics by pressing the proper button in the software. If no errors are detected, use the hanging green pushbutton switch to bring the anvils into contact and apply a minor load of 2-3 kN. the loading cycle can be launched by following steps 3.11 and 3.12.

When finished with the iTools software, save the file and close iTools.

A.5 Programming the rotation positions in cockpit

The commercial software Cockpit allows for motor rotation patterns (called “Positions”) to be defined in terms of the degrees of rotation, the rotation speed, etc. This section will explain which rotation parameters can be modified and how to test a new rotation position.

A.5.1 Opening cockpit

Open Cockpit and under File, select the most recently used positions file (at this time there is only one). This will open a table, with “Positions” as rows and the variable parameters as columns. When the table cells are red, that means that they are only what is read in the file on the computer; after pressing the button with two curved arrows, the table cells will slowly turn black as the parameters on the drive motor are read by the computer.

Parameters can then be changed as desired. As soon as a position parameter has been modified, press enter to load it directly to the motor controller.

A.5.2 Position parameters

Index: This is the reference number of the position that will be selected in “RHEOS – mesure continue et enregistrement.”

Position (u): This is the number of rotations. 1 = 360° 2 = 720° 0.25 = 90°, etc.

Speed (% of nominal): This value can be set between 0 and 100. Speed 100 = 60 rotations per minute Speed 0.833 = 0.5 rotations per minute, etc.

Acceleration (% of nominal): This value is generally left at 10.

Deceleration (% of nominal): This value is generally left at 10.

Displacement: This can be toggled between absolute and incremental. Generally a test should be run in incremental. (If the motor has been zeroed before the test by executing “Position 2 (retour zéro)”, this shouldn’t make any difference, absolute and incremental will achieve the same results.)

Out in Position and **Out End Position**: Do not change these values.

A.5.3 Testing the positions

Rotations must be launched from “RHEOS – mesure continue et enregistrement.” Follow the instructions in step 2.3 using the desired position number.

Appendix B

Sample MATLAB code

All of the code in this appendix is original work of the author.

B.1 Wear rate calculation from Gwyddion output

```
fileToRead1 = input('Enter file name sans filetype extension:  ', 's');
fileToRead1 = strcat(fileToRead1, '.txt');
%IMPORTFILE(FILETOREAD1)
% Imports data from the specified file % FILETOREAD1:  file to read
% Auto-generated by MATLAB on 30-Nov-2012 16:57:20
DELIMITER = ' ';
HEADERLINES = 3;
%Import the file
newData1 = importdata(fileToRead1, DELIMITER, HEADERLINES);
% Create new variables in the base workspace from those fields.
vars = fieldnames(newData1);
for i = 1:length(vars)
 assignin('base', vars{i}, newData1.(vars{i}));
end
TrackLength = input('Enter track Length in mm:  ');
Cycles = input('Enter number of cycles:  ');
DownForce = input('Enter downforce in N: ');
DistanceSlid = TrackLength * Cycles *2*10^-3; %Units in m
DataColumns = size(data, 2);
WearAreaArrayColumns = DataColumns/2;
WearAreaArray=zeros(1,WearAreaArrayColumns);
PercentAboveTrackArray=zeros(1, WearAreaArrayColumns);
```

```
SumWearHeights = sum(data,1); %Units in m
%Assemble WearAreaArray, which is the wear area calculated from each
%profile
i=0;
for i=1:WearAreaArrayColumns
dx = data(3,2*i-1)-data(2,2*i-1);
WearAreaArray(1,i) = dx * SumWearHeights(1, 2*i);
PercentAboveTrackArray(1,i) = (sum(data(data(:,2*i)>0,
2*i)))/(sum(data(data(:,2*i)>0, 2*i))-sum(data(data(:,2*i)<0, 2*i)));

end
WearVolumeArray = TrackLength*WearAreaArray*10^6; %Units in mm^3
WearRateArray = WearVolumeArray / (DownForce*DistanceSlid);
%Units mm^3/N/m
disp('Wear Rates in mm^3/N/m')
[-WearRateArray' PercentAboveTrackArray']
disp('Mean and StDev Wear Rate in mm^3/N/m')
disp(fileToRead1)
disp(mean(-WearRateArray))
disp(std(-WearRateArray))
disp('Average Above Track')
disp(mean(PercentAboveTrackArray))
clear
```

B.2 Analysis of rheos HPT data

To use this code, the .tdms file output from RHEOS must be converted to a tab-delimited .txt file, which can then be opened by the code. One way of doing this is using the TDM Excel Add-In for Microsoft Excel, available from National Instruments.

```
%% Import data from text file.
% Script for importing data from the following text file:
%
% C:\Users\Shockley\Documents\E4 ANG50 Tab.txt
%
% To extend the code to different selected data or a different text
file,
% generate a function instead of a script.
% Auto-generated by MATLAB on 2013/11/26 15:03:02
%
% Initialize variables.
```

```
%filename = ’C:\Users\Shockley\Documents\E4 ANG50 Tab.txt’;
%filename = input(’Enter filename sans extension:  ’, ’s’);
%filename = strcat(filename, ’.txt’);
TestName = input(’Enter test name:  ’, ’s’);
filename = uigetfile(’*.*’);
delimiter = ’\t’;
startRow = 2;
%
formatSpec = ’%f%f%f%f%f%f%f%f%f%f%f%f%f%f%f%[^\n\r]’;
%% Open the text file.
fileID = fopen(filename,’r’);
%% Read columns of data according to format string.
% This call is based on the structure of the file used to generate
this % code.  If an error occurs for a different file, try regenerating
the code % from the Import Tool.  dataArray = textscan(fileID, formatSpec,
’Delimiter’, delimiter, ’EmptyValue’ ,NaN,’HeaderLines’ ,startRow-1,
’ReturnOnError’, false);
%% Close the text file.  fclose(fileID);
%% Post processing for unimportable data.
% No unimportable data rules were applied during the import, so no
post
% processing code is included.  To generate code which works for
% unimportable data, select unimportable cells in a file and regenerate
the
% script.
%% Allocate imported array to column variable names
%effortvertical = dataArray{:, 1};
couple = dataArray{:, 2};
%positionverin = dataArray{:, 3};
ecrasement1 = dataArray{:, 4};
ecrasement2 = dataArray{:, 5};
ecrasement3 = dataArray{:, 6};
Vitesse = dataArray{:, 7};
Rotation = dataArray{:, 8};
%ZroOK = dataArray{:, 9};
%MoteurOK = dataArray{:, 10};
%EntreNumrique_3 = dataArray{:, 11};
%EntreNumrique_4 = dataArray{:, 12};
%EntreNumrique_5 = dataArray{:, 13};
%EntreNumrique_6 = dataArray{:, 14};
%EntreNumrique_7 = dataArray{:, 15};
%% Clear temporary variables
clearvars filename delimiter startRow formatSpec fileID dataArray ans;
```

```
%clearvars -except Rotation Vitesse couple ecrasement1 ecrasement2
ecrasement3;
Degrees = input(’Enter degrees of rotation:  ’);
i=1;
while Rotation(i, 1) == 0
i=i+1;
end
rotationbegin = i;
i=rotationbegin+10;
while Rotation(i,1) == 1
 i=i+1;
end
rotationend=i;
clear i
RotationTime=rotationend-rotationbegin;
%Create array N
N = zeros(RotationTime, 1);
for i=1:RotationTime
 N(i, 1) = (i/(RotationTime))*(Degrees/360);
end
clear i
lnN = log(N);
clear rotationend
%Create Array of Torque, corrected by the "zero" offset
coupleoffsetcalc(1:100, 1) = couple(1:100, 1);
coupleoffset=mean(coupleoffsetcalc);
clear coupleoffsetcalc
radius = input(’Enter sample radius (mm):  ’);
InitialThickness = input(’Enter initial sample thickness (mm):  ’);

HeightCorrection = (mean(ecrasement1(1:10,1))+mean(ecrasement2(1:10,1))+
mean(ecrasement3(1:10,1)))/3 - InitialThickness;
Torque_Nm = zeros(RotationTime, 1);
Height_mm = zeros(RotationTime, 1);
nMorKNm = input(’Enter if couple data is in kNm instead of Nm, write
1000 here:  ’);
for i=1:RotationTime
Torque_Nm(i, 1)= couple(i+rotationbegin,1)*nMorKNm - coupleoffset*nMorKNm;

Height_mm(i, 1) = ((ecrasement1(i+rotationbegin,1)+ecrasement2(i+rotationbe
ecrasement3(i+rotationbegin,1))/3)-HeightCorrection;
end
clear i
lnTorque = log(Torque_Nm);
p=polyfit(lnN, lnTorque, 6);
```

```
p0 = p(1, 7);
p1 = p(1, 6);
p2 = p(1, 5);
p3 = p(1, 4);
p4 = p(1, 3);
p5 = p(1, 2);
p6 = p(1, 1);
DIFF5 = p6*6;
DIFF4 = p5*5;
DIFF3 = p4*4;
DIFF2 = p3*3;
DIFF1 = p2*2;
DIFF0 = p1*1;
Strain = zeros(RotationTime, 1);
Stress_MPa = zeros(RotationTime, 1);
dlnTdlnN = (DIFF5*lnN.^5 + DIFF4*lnN.^4 +
DIFF3*lnN.^3 + DIFF2*lnN.^2 + DIFF1*lnN.^1+DIFF0);
for i=1:RotationTime
Strain(i,1) = (2*pi*N(i,1)*radius)/(sqrt(3)*Height_mm(i,1));
Stress_MPa(i,1) = (sqrt(3)/(2*3.14159*(radius/1000)^3)
.*Torque_Nm(i,1).*(3+dlnTdlnN(i,1)))*10^-6;
end
lnTvslnNPlot(lnN, lnTorque, TestName);
figure StressStrainPlot(Stress_MPa, Strain, TestName);
tablename = strcat(TestName, ’ Rheos Processed Data’);
T = table(Strain, Stress_MPa, Height_mm, Torque_Nm);
writetable(T, tablename);
clearvars
```

Appendix C

Sample input file for Abaqus

The node, element, and set coordinates were redacted, as was the assembly step, for the sake of space.

```
*Heading
** Job name:  Job-116-square-small-compshear Model name:  Model with
Square Christophe-Shear
** Generated by:  Abaqus/CAE 6.11-1
*Preprint, echo=NO, model=NO, history=NO, contact=NO
**
** PARTS
**
*Part, name=Matrix
-------------------------------------------
NODE, ELEMENT, AND SET COORDINATES REDACTED
ASSEMBLY REDACTED
-------------------------------------------
**
** MATERIALS
**
*Material, name=Alumina
*Density
 4.1,
*Elastic
300., 0.2
*Material, name=Aluminum
*Density
 2.7,
*Elastic
```

```
70., 0.33
*Plastic
 0.2, 0.
 0.246, 0.0237
**
** INTERACTION PROPERTIES
**
*Surface Interaction, name=IntProp-1
1.,
*Friction
0.,
*Surface Behavior, no separation, pressure-overclosure=HARD
**
** INTERACTIONS
**
** Interaction:  Int-1
*Contact Pair, interaction=IntProp-1, type=SURFACE TO SURFACE, adjust=0.0
_PickedSet43_CNS_, Part-5-1.RigidSurface_
** Interaction:  Int-2
*Contact Pair, interaction=IntProp-1, type=SURFACE TO SURFACE, adjust=0.0
_PickedSet54_CNS_, Part-5-2.RigidSurface_
** ----------------------------------------------------------------
**
** STEP: Comp
**
*Step, name=Comp, nlgeom=YES
Shear
*Static
0.05, 1., 1e-05, 0.05
**
** BOUNDARY CONDITIONS
**
** Name:  BC- Bottom edge Type:  Displacement/Rotation
*Boundary
_PickedSet47, 2, 2
** Name:  BC-Top Edge Type:  Displacement/Rotation
*Boundary
_PickedSet48, 2, 2, -1.
** Name:  BC-VerticalMembers Type:  Displacement/Rotation
*Boundary
_PickedSet55, 2, 2
**
** OUTPUT REQUESTS
**
*Restart, write, frequency=0
```

```
*Print, solve=NO
**
** FIELD OUTPUT: F-Output-1
**
*Output, field
*Node Output
CF, COORD, RF, U
*Element Output, directions=YES
LE, PE, PEEQ, PEMAG, S, TRIAX
*Contact Output
CDISP, CSTRESS
**
** HISTORY OUTPUT: H-Output-2
**
*Output, history
*Node Output, nset=Set-RF
RF1, RF2
**
** HISTORY OUTPUT: H-Output-1
**
*Output, history, variable=PRESELECT
*End Step
** ----------------------------------------------------------------
**
** STEP: Shear
**
*Step, name=Shear, nlgeom=YES
*Static
0.05, 1., 1e-05, 0.05
**
** BOUNDARY CONDITIONS
**
** Name:  BC- Bottom edge Type:  Displacement/Rotation
*Boundary
_PickedSet47, 1, 1, 1.
_PickedSet47, 6, 6
** Name:  BC-Top Edge Type:  Displacement/Rotation
*Boundary
_PickedSet48, 1, 1
_PickedSet48, 6, 6
**
** OUTPUT REQUESTS
**
*Restart, write, frequency=0
*Print, solve=YES
```

```
**
** FIELD OUTPUT: F-Output-1
**
*Output, field
*Node Output
CF, COORD, RF, U
*Element Output, directions=YES
LE, PE, PEEQ, PEMAG, S, TRIAX
*Contact Output
CDISP, CSTRESS
**
** HISTORY OUTPUT: H-Output-2
**
*Output, history
*Node Output, nset=Set-RF
RF1, RF2
**
** HISTORY OUTPUT: H-Output-1
**
*Output, history, variable=PRESELECT
*End Step
```